UNIVERSITY OF CALIFORNIA, SAN DIEGO

Coastal ocean studies in southern San Diego using high-frequency radar derived surface currents

A dissertation submitted in partial satisfaction of the
requirements for the degree
Doctor of Philosophy

in

Oceanography

by

Sung Yong Kim

Committee in charge:

Bruce Cornuelle, Chair
Eric Terrill, Co-Chair
Teresa Chereskin
Myrl Hendershott
William Hodgkiss
Sutanu Sarkar

2009

The dissertation of Sung Yong Kim is approved, and it is acceptable in quality and form for publication on microfilm:

_____

_____

_____

_____

_____
Co-Chair

_____
Chair

University of California, San Diego

2009

DEDICATION

My family and Yu Jin

EPIGRAPH

"The chief source of ideas in oceanography comes, I think, from new observations... On the whole, when it comes to the phenomenology of the ocean, there are more discoveries than predictions. Most theories are about observations that have already been made."

— Henry Stommel

TABLE OF CONTENTS

LIST OF ABBREVIATION

ADCP	Acoustic doppler current profile
CTD	Conductivity temperature density
cpd	Cycles per day
EM	Expectation maximization
EOF	Empirical orthogonal function
FAWIRF	Frequency domain anisotropic WIRF
FIB	Fecal indicator bacteria
FIWIRF	Frequency domain isotropic WIRF
GDOP	Geometric dilution of precision
HF	High frequency
HSTD	Hourly standard deviation
MGD	Million gallon per day
MUSIC	Multiple signal classification
OI	Optimal interpolation
PDF	Probability density function
RMS	Root-mean-square
ROC	Receiver operating characteristic
RSB	Roberts-Snyder-Baumgartner
RWM	Random walk model
SSH	Sea surface height
SSHA	Sea surface height anomaly
SNR	Signal-to-noise ratio
TAWIRF	Time domain anisotropic WIRF
TIWIRF	Time domain isotropic WIRF
UWLS	Un-weighted least-squares fit
WIRF	Wind impulse response function
WLS	Weighted least-squares fit

LIST OF SYMBOLS

$\mathbf{u}$	Current vector
u	x-component of the current vector
v	y-component of the current vector
$\mathbf{m}$	Model coefficients
$\hat{\mathbf{m}}$	Estimated model coefficients
$\mathbf{P}$	Prior model covariance matrix
$\mathbf{R}$	Error covariance matrix
$\hat{\mathbf{P}}$	Posterior model covariance matrix
$\boldsymbol{\tau}$	Wind stress
τ_x	x-component of wind stress
τ_y	y-component of wind stress
η	Sea-level height
p	Sea-level pressure
f_c	Coriolis frequency
ρ	Sea water density
μ	Dynamic viscosity
ν	Kinematic viscosity
$\mathcal{Z}$	Integer number
$\mathcal{R}$	Real number
$\mathcal{C}$	Complex number

LIST OF FIGURES

LIST OF TABLES

ACKNOWLEDGEMENTS

I had a great opportunity to explore all kinds of oceanographic observation data in Scripps Institution of Oceanography (SIO). I have been in debt to work with Eric Terrill and Bruce Cornuelle as co-advisor, and thank them for their patience and generous support during my graduate study. I can not adequately express how deeply indebted I am to both of them. And I appreciate the valuable discussions and insightful comments from other thesis committee members – Teresa Chereskin, Myrl Hendershott, Bill Hodgkiss, and Sutanu Sarkar.

Especially, I would like to thank Mark Otero, Lisa Hazard, Paul Reuter, Jennifer Bowen, Joel Hazard, Tony de Paolo, Tom Cook, Edwin Beckenbach, Alex Pierson, Billy Middleton, Timothy Jenkins, and Timothy Harris in Coastal Observing Research and Development Center (CORDC, `http://cordc.ucsd.edu`), Diana Stockdale, Irina Tsimring, Evelyn Doudera, Courtney Wiley, and Monica Suimanjaya in Marine Physical Laboratory (MPL), Phil Moses and Dana Dahlbo in Climate Atmospheric Science and Physical Oceanography (CASPO), Jerome Wanetick, Ron Van Boxtel, Clive Dorman, and Melissa Carter in Integrative Oceanography Division (IOD), Jit Sarkar, Kaustubha Raghukumar, Melania Guerra, Claire Debever, and Ezra Miksic (Applied Ocean Science classmates), Jessica Lundquist, Daniel Birch, Stephanie Fried, and Peter Sutherland (officemates), Clay Clifton in Department of Environmental Health (DEH), County of San Diego, and Michelle Cordrey, Jeff Crooks, and Tammy Small at Tijuana River National Estuarine Research Reserve (TRNERR). I am very grateful to my friends, Marilyn Huckins, Belma Gumusoglu, Stringers, Maurice Loucks, and Dennis Lin, and their encouragements and supports. Special thanks to my wife Yu Jin Kim for her encouragements and patience.

I was sponsored by the graduate student fellowship provided by the California Institute of Telecommunication and Information Technology (CALIT2) during my second year study, and have been supported by both the State of California under the Coastal Ocean Currents Monitoring Program (COCMP), NOAA, and the International Boundary Water Commission (IBWC) for the rest of my graduate study.

Thanks to the efforts of people and groups to provide data used in this dissertation. Surface current data from Southern California Coastal Ocean Observing System (SCCOOS, `http://sccoos.ucsd.edu/`), wind records at Tijuana River (Tidal Linkage station) from System-Wide Monitoring Program at the TRNERR, Estuarine Reserves Division, NOAA, Centralized Data Management Office (CDMO, `http://cdmo.baruch.sc.edu/`), Baruch Marine Field Lab, and University of South Carolina, wind data at Scripps Pier from IOD at SIO, sea surface heights and harmonic constituents from Center for Operational Oceanographic Products and Services (CO-OPS) and Deep-ocean Assessment and Reporting of Tsunamis (DART) buoys in NOAA, atmospheric pressure data from NDBC (partially NCDC), directional wave spectra from Coastal Data Information Program (CDIP), rainfall data at San Diego Lindbergh Field from NCDC, the Tijuana River flow are from International Boundary and Water Commission (IBWC), CTD cast data and the water quality data from San Diego County, Department of Environmental Health (DEH), COAMPS wind model out-

puts from the Naval Research Laboratory (NRL) are used. A MATLAB compatible version of the RSB model developed by Philip J. Roberts in Georgia Institute of Technology is used as a courtesy of Burt Jones in the University of Southern California, the seawater MATLAB toolbox developed by Phil Morgan at CSIRO Marine and Atmospheric Research, and the HFRadarmapVer4.1 MATLAB toolbox developed by Mike Cook in Naval Postgraduate School are used.

Chapter 2, in part, is a reprint of the material as it appears in *Journal of Geophysical Research-Oceans*, 2007, Kim, S. Y., E. J. Terrill, and B. D. Cornuelle titled by 'Objectively mapping HF radar-derived surface current data using measured and idealized data covariance matrices', **112**, C06021, doi:10.1029/2006JC003756. The dissertation author was the primary investigator and author of this paper. Copyright (2007) American Geophysical Union.

Chapter 3, in part, is a reprint of the material as it appears in *Journal of Geophysical Research-Oceans*, 2008, Kim, S. Y., E. J. Terrill, and B. D. Cornuelle titled by 'Mapping surface currents from HF radar radial velocity measurements using optimal interpolation', **113**, C10023, doi:10.1029/2006JC004244. The dissertation author was the primary investigator and author of this paper. Copyright (2008) American Geophysical Union.

Chapter 4, in part, has been accepted for publication of the material as it is supposed to be appeared in *Journal of Physical Oceanography*, 2009, Kim, S. Y., B. D. Cornuelle, and E. J. Terrill titled by 'Anisotropic response of surface currents to the wind in a coastal region', doi: 10.1175/2009JPO4013.1. The dissertation author was the primary investigator and author of this paper.

Chapter 5, in part, has been submitted for publication of the material as it may appear in *Journal of Geophysical Research-Oceans*, 2009, Kim, S. Y., B. D. Cornuelle, and E. J. Terrill titled by 'Decomposing observations of high-frequency radar derived surface currents by their forcing mechanisms'. The dissertation author was the primary investigator and author of this paper.

Chapter 6 has been submitted for publication of the material as it my appear in *Environmental Science & Technology*, 2009, Kim, S. Y., E. J. Terrill, and B. D. Cornuelle titled by 'Assessing coastal plumes in a region of multiple discharges: the U.S.–Mexico border'. The dissertation author was the primary investigator and author of this paper.

VITA

1999	B.S., Naval Architecture and Ocean Engineering (Summa cum laude), Seoul National University Republic of Korea
2000–2003	Intelligence Officer Republic of Korea Navy Republic of Korea
2003–2009	Graduate Student Researcher Scripps Institution of Oceanography, University of California, San Diego U.S.A.
2009	Ph.D., Oceanography (Applied Ocean Science/Physical Oceanography), Scripps Institution of Oceanography, University of California, San Diego U.S.A.

PUBLICATIONS

Kim, S. Y., E. J. Terrill, and B. D. Cornuelle, 2007: Objectively mapping HF radar-derived surface current data using measured and idealized data covariance matrices. *J. Geophys. Res.*, **112**, C06021, doi:10.1029/2006JC003756

Kim, S. Y., E. J. Terrill, and B. D. Cornuelle, 2008: Mapping surface currents from HF radar radial velocity measurements using optimal interpolation. *J. Geophys. Res.*, **113**, C10023, doi:10.1029/2007JC004244

Hoteit, I., B. D. Cornuelle, S. Y. Kim, G. Forget, A. Kohl, and E. J. Terrill, 2008: Assessing 4D-VAR for dynamical mapping of coastal high-frequency radar in San Diego. *Dynam. Atmos. Oceans*, doi:10.1016/j.dynatmoce.2008.11.005

Kim, S. Y., B. D. Cornuelle, and E. J. Terrill, 2009: Anisotropic response of surface currents to the wind in a coastal region, *J. Phys. Oceanogr.*, doi: 10.1175/2009JPO4013.1, in press.

Kim, S. Y., B. D. Cornuelle, and E. J. Terrill, 2009, Decomposing observations of high-frequency radar derived surface currents by their forcing mechanisms. *J. Geophys. Res.*, submitted.

Kim, S. Y., E. J. Terrill, and B. D. Cornuelle, 2009, Assessing coastal plumes in a region of multiple discharges: the U.S.–Mexico border. *Environ. Sci. Tech.*, submitted.

PRESENTATIONS

Kim, S. Y., E. J. Terrill, and B. D. Cornuelle, 2005: Covariance decomposition of surface currents around San Diego. *Radio Oceanography Workshop–5*, Pescadero, California, U.S.A.

Kim, S.Y., E. J. Terrill, and B. D. Cornuelle, 2006: Decomposing observations of high-frequency radar derived surface current by their forcing mechanisms using covariance techniques. *Ocean Science Meeting 2006*, Honolulu, Hawaii, U.S.A. (Poster)

Kim, S. Y., E. J. Terrill, and B. D. Cornuelle, 2007: Mapping surface currents from HF radar radial velocity measurements using optimal interpolation. *Radio Oceanography Workshop-7*, Cancun, Mexico

Kim, S. Y., E. J. Terrill, and B. D. Cornuelle, 2007: A statistical model for water quality predictions from a river discharge using coastal observations. *American Geophysical Union Meeting 2007*, San Francisco, California, U.S.A (Poster)

Kim, S. Y., B. D. Cornuelle, and E. J. Terrill: 2008: Anisotropic response of surface currents to the wind in a coastal region. *Ocean Science Meeting 2008*, Orlando, Florida, U.S.A

Kim, S. Y., E. J. Terrill, B. D. Cornuelle, B. Jones, L. Washburn, M. A. Moline, J. D. Paduan, T. Garfield, and J. Largier, 2008: Poleward propagating features as observed in the California network of HF radar. *Radio Oceanography Workshop-8*, Honolulu, Hawaii, U.S.A.

Kim, S. Y., B. D. Cornuelle, and E. J. Terrill, 2008: Anisotropic response of surface currents to the wind in a coastal region. *Asia Oceania Geoscience Society 2008*, Busan, Republic of Korea

Kim, S. Y., 2008: Poleward propagating features as observed in the U.S. West Coast network of HF radar. *International Meeting of Students in Physical Oceanography 2008*, La Jolla, California, U.S.A.

Kim, S. Y., 2008: Coastal ocean studies using high-frequency radar derived surface currents. *Physical Oceanography Dissertation Symposium V*, Honolulu, Hawaii, U.S.A. (Invited)

Kim, S. Y., 2008: Poleward propagating features as observed in the U.S. West Coast network of HF radar. *Coastal ocean group seminar*, University of California, Los Angeles, Los Angeles, U.S.A. (Invited)

FIELDS OF STUDY

Major Fields : Applied Ocean Science/Physical Oceanography

Physical Oceanography
Professors Lynn Talley, Myrl Hendershott, and Paul Robinson

Data Analysis
Professors Robert Pinkel and Daniel Rudnick

Fluid Mechanics
Professor Clinton Winant

Ocean Waves
Professors Ken Melville and Robert Guza

Fundamentals of Wave Physics
Professors Bill Kuperman, Ken Melville, Dariuz Stramski, and Leroy Dorman

Ocean Turbulence and Mixing
Professor Laurence Armi

Array Processing
Professor Bill Hodgkiss

Ocean Color Remote Sensing
Professor Dariuz Stramski

Mathematics and Methods in Physics and Engineering
Professor Hans Wenzl

Marine Geology
Professors Steve Cande, David Hilton, and Christopher Charles

Biological Oceanography
Professor Peter Franks

Marine Chemistry
Professors Lihini Aluwihare, Kathy Barbeau, and Ralph Keeling

ABSTRACT OF THE DISSERTATION

Coastal ocean studies in southern San Diego using high-frequency radar derived surface currents

by

Sung Yong Kim

Doctor of Philosophy in Oceanography

University of California San Diego, 2009

Bruce Cornuelle, Chair

Eric Terrill, Co-Chair

Surface currents measured by high-frequency (HF) radars in southern San Diego are addressed from three perspectives: technical issues, physical interpretations, and environmental applications. Objective mapping (also known as optimal interpolation (OI)) is applied to the surface vector current using both observed and idealized covariance matrices. The mapping produces smooth fields and can fill in missing data. The covariance matrices calculated from the raw observations of surface currents show a roughly exponential form instead of the Gaussian shape which is often assumed.

The OI methods have been extended to map vector current directly from the radial velocities as an alternative to un-weighted least-squares fitting (UWLS), which has been the default method for the HF radar community. OI uses the expected covariance function in place of the arbitrary, discontinuous correlation function used in UWLS. Moreover, the OI approach reduces inconsistency along baselines between stations and provides superior uncertainty measures for the estimated current field.

In order to refine the covariance estimates and maps, the surface currents are decomposed according to their driving forces: tides, wind, low frequency pressure gradients, and several continuous frequency bands. The locally wind-driven currents are calculated by regression of the shore station winds on the observed surface currents to estimate the wind impulse response function. The response of surface currents to the wind in a coastal region is anisotropic due to the anisotropic bottom/coastline friction, pressure gradient, and boundary conditions. The frictional momentum balance between the gradient of sea surface elevation and the low frequency band currents is also considered. The spatial correlations of the components of surface currents exhibit a mix of Gaussian and exponential shapes with varying decorrelation length scales.

Finally, a data-driven model of the fate and transport of the plumes from three local discharges in southern San Diego has been developed using surface current observations. The statistical

model calculates particle trajectories which are compared with water quality samplings, and the skill of an alarm for low water quality is evaluated using receiver operating characteristic (ROC) analysis.

Chapter 1

Introduction

High-frequency (HF) radar using Bragg-backscattered radar signals ([Crombie(1955), Stewart and Joy(1974), Barrick et al.(1977)]) has matured as an oceanographic observation tool. It can provide hourly high resolution surface current fields covering 50 to 150 km from the coastline with 0.5–6 km spatial resolution. It can serve as part of the infrastructure of the coastal ocean observing system to integrate other in-situ observations and numerical modeling products. Research on surface current measurements using HF radars can be classified by technical issues, scientific interpretations, and environmental applications: the processing of the backscattered radar signal and the generation of the vector current map from multiple radial current measurements; understanding of the ocean surface circulation through analysis in time and space; water quality monitoring, larvae spreading, search and rescue, and oil spill tracking.

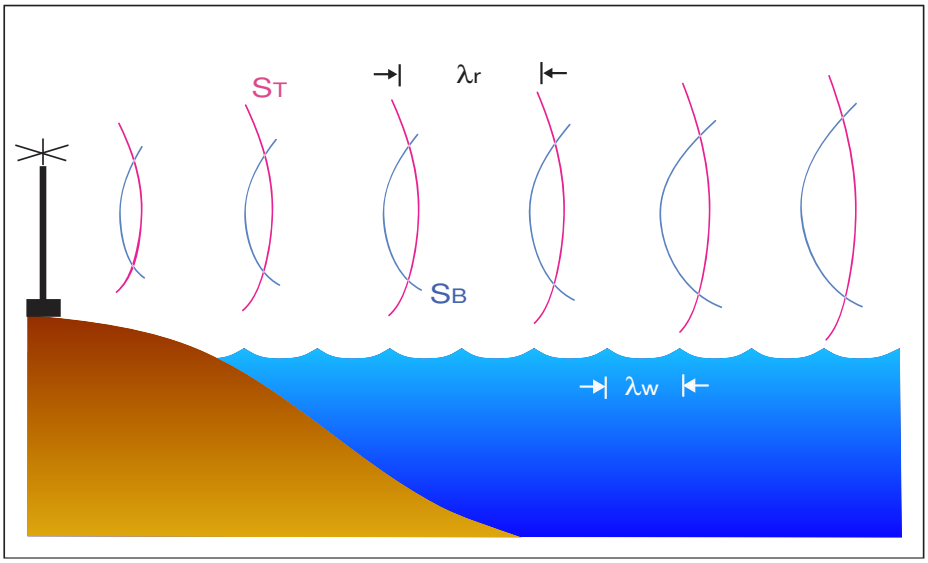

Figure 1.1: A schematic figure to show the transmitted (S_T) and backscattered (S_B) radar signals in the high-frequency radar operation. The radar signal is backscattered in phase when the wavelength of the surface gravity wave (λ_w) is half of the wavelength of the radar signal (λ_r).

The transmitted radar signal from the HF radar ranges from 3 to 30 MHz, and is backscattered in phase by surface gravity waves with the half wavelength of the radar signal, i.e., 5–50 m surface gravity waves are targets of this measurement (Figure 1.1). Received radar signals are processed in the form of the spectrum (Figure 1.2) in order to generate the radial current map (Figure 1.3a). At a given radar grid point, the radial current speed is calculated from the Doppler shift of the first order echo, and the radial current direction is computed from a direction finding method. The MUSIC algorithm (MUltiple SIgnal Classification, [Schmidt(1986), Barrick and Lipa(1996), de Paolo and Terrill(2007b)]) and the beam forming ([Johnson and Dudgeon(1993)]) are used for direction finding for compact array and phased array systems, respectively. Since the HF radar in this dissertation is based on the compact array system, the MUSIC algorithm is applied for direction finding. However, the MUSIC algorithm does not

provide a complete solution for all bearing angles, which leads to the missing data in the radial current map, consequently, and vector current map (Figure 1.3b). In addition, the estimate of vector currents along the baseline where the measurements of radial velocities are nearly aligned suffers from poor geometric dilution of precision and frequently results in spurious values.

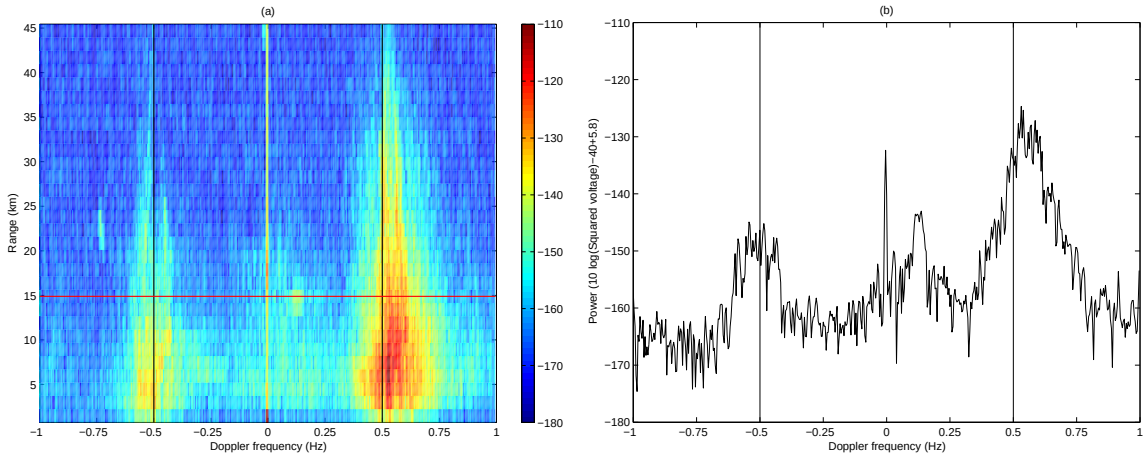

Figure 1.2: An example of the power spectrum of the backscattered signals (a) in all ranges and (b) at a single range (at the red line in (a)).

Coastal surface currents are a mixture of the oceanic responses to the local winds, remote wind forcing via eddies and coastal trapped waves, tides, pressure gradients, and meteorological fluxes of heat and fresh water ([Ewing(1950), Munk and Cartwright(1966), Essen et al.(1983), Alpers(1985), Price et al.(1986), Prandle(1987), Ng(1993a), Ng(1993b), Shay et al.(1995)]). In contrast to regions where circulation is dominated by a single forcing mechanism, in the San Diego region many superposed ocean responses are present as a result of the complicated topography, relatively weak winds, and intermittent eddies in the region (Figures 1.5, 1.4 and 2.5). The pure tides drive the coastal surface currents ([Munk et al.(1970), Hendershott and Munk(1970)]). The local wind response may not be symmetric due to the coastline and bottom topography ([Ekman(1905), Sverdrup(1938), Allen(1980), Beardsley et al.(1987), Overland and Pease(1988), Li and Weisberg(1999), Weisberg et al.(2001), Choi and Wilkin(2007)]). The shoreward steep bottom slope of the continental shelf/break regions in southern San Diego satisfies the necessary condition to generate M2 internal tides ([Cacchione and Wunsch(1974), Bratkovich(1985), Cacchione et al.(2002)]). The alongshore pressure gradient influences the surface currents as a low frequency forcing term ([Grant et al.(1984), Lentz and Winant(1986), Brink et al.(1987)]).

The border region coastlines of San Diego and Tijuana share similar environmental challenges with regards to impaired water quality resulting from local discharges. Water-borne materials discharged in the coastal zone are free to transport across political boundaries. While an understanding of the fate and transport of these discharged plumes has a broad audience in the management and general public alike, the spatial and temporal scales of the physical processes present nu-

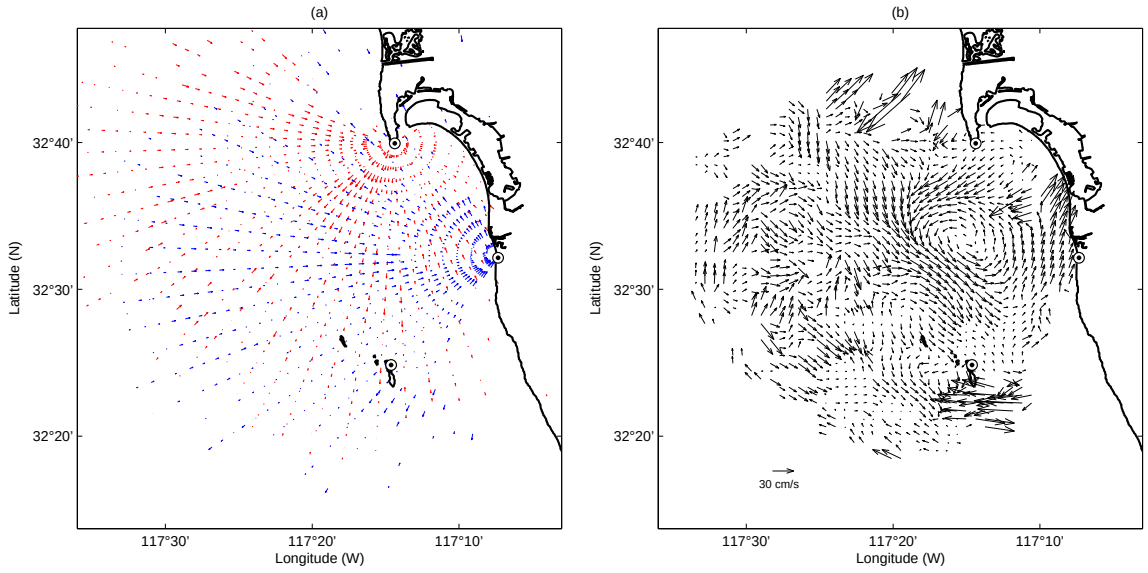

Figure 1.3: An example of the (a) multiple radial current maps (red: SDPL; blue: SDBP, see Figure 1.5) and (b) vector current map derived from HF radars in southern San Diego.

merous challenges in assessing with any fidelity ([Svejkovsky and Jones(2001), Largier et al.(2004), James and Groce(2006), Orozco-Borbon et al.(2006), Gersberg et al.(2008)]).

This dissertation is composed of five parts:

Chapter 2 presents objective mapping using observed and smoothed data covariance matrices computed directly from the observations of surface currents in order to fill the missing observations, and estimates the correlation functions and the decorrelation length scales of surface currents.

Chapter 3 investigates two methods – un-weighted least-squares fit (UWLS) and optimal interpolation (OI) – to compute the vector current map from multiple radial maps. The correlation function, the vector current map and its uncertainty, and the noise level of each method are discussed.

Chapter 4 focuses extensive statistical analysis on the physical relationship between surface currents and wind as a part of the forcing decomposition of surface currents. The anisotropic and asymmetric surface current response to the wind in a coastal region is presented.

Chapter 5 contains the decomposition of surface currents into components driven by pure tides, local wind, low frequency pressure gradient ($|\omega| \leq 0.4$ cycles per day) and cuspate tidal variances at the diurnal (K1) and semidiurnal (M2) frequencies. The variance distribution, the characteristics and variability of each forcing component are presented.

Chapter 6 presents a data-driven model using Lagrangian forward integration to understand the coastal surface circulation and to examine the connectivity between beach closure and fecal indicator bacteria (FIB).

The data analysis and processing technique described in the following chapters are appli-

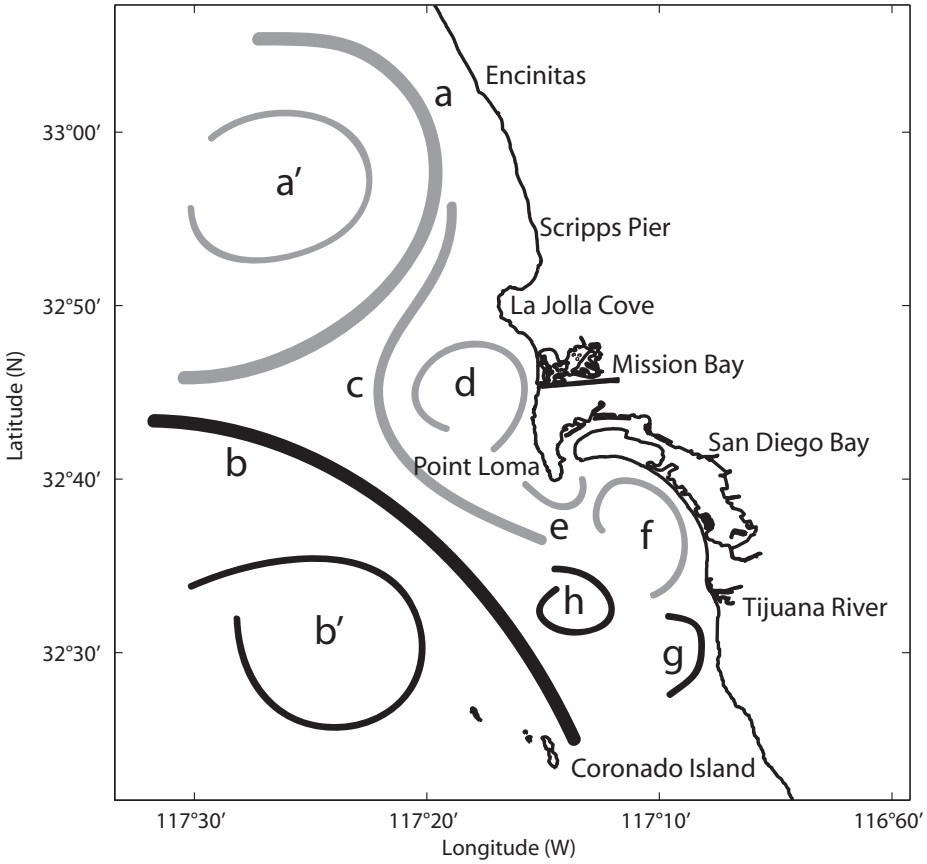

Figure 1.4: A schematic surface current pattern around San Diego. The flow strength is represented by the thickness of the flow. Some flows have consistent direction (black), and others can have reversing direction (gray). b is the southeastward flow, and b', g and h are clockwise flows.

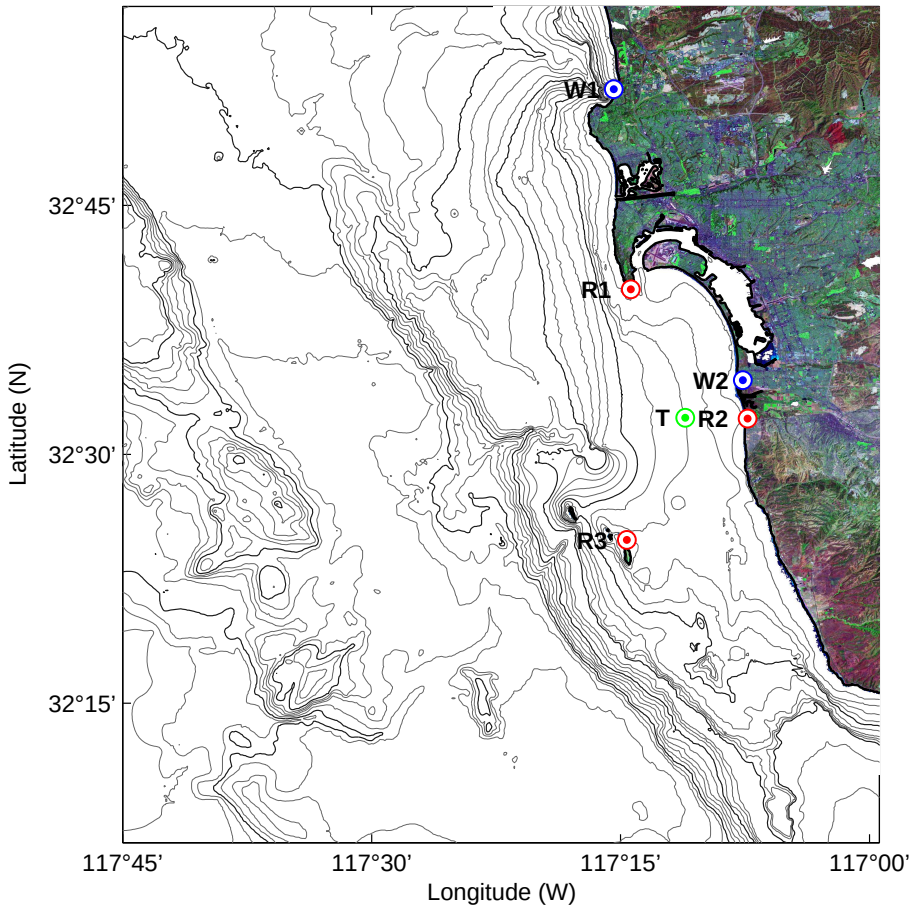

Figure 1.5: The study domain for the surface current: surface currents measured by three HF radars – Point Loma (R1: SDPL), Border Park (R2: SDBP), and Coronado Islands (R3: SDCI) – and winds observed at two shore stations – Scripps Pier (SIO, W1) and Tijuana River (TJR, W2). The temperature profile and the current profile (ADCP) are observed at the location T. The bottom bathymetry contours are indicated by the thin curves with 10 m ($0 < z < 100$ m) and 50 m ($100 < z < 1000$ m) contour intervals and the thick curves at the 50, 100, 500, and 1000 m depths.

cable for the any type of HF radar array system. u and v denote the current component in the x- and y-directions, respectively, and there is no rotation of the coordinate system throughout the dissertation.

Chapter 2

Objectively mapping high-frequency radar derived surface current data using measured and idealized data covariance matrices

Abstract

Surface currents measured by high-frequency radars are objectively mapped using covariance matrices computed from hourly surface vector currents spanning two years. Since retrievals of surface radial velocities are inherently gappy in space and time, the irregular density of surface current data leads to negative eigenvalues in the sample covariance matrix. The number and the magnitude of the negative eigenvalues depend on the degree of data continuity used in the matrix computation. In a region of 90% data coverage, the negative eigenvalues of the sample covariance matrix are small enough to be removed by adding a noise term to the diagonal of the matrix. The mapping is extended to regions of poorer data coverage by applying a smoothed covariance matrix obtained by spatially averaging the sample covariance matrix. This approach estimates a stable covariance matrix of surface currents for regions with the intermittent radar coverage. An additional benefit is the removal of baseline errors that often exist between two radar sites. The covariance matrices and the correlation functions of surface currents are exponential in space rather than Gaussian, as is often assumed in the objective mapping of oceanographic data sets. Patterns in the decorrelation length scale provide the variabilities of surface currents and the insights on the influence of topographic features (bathymetry and headlands). The objective mapping approach presented herein lends itself to various applications, including the Lagrangian transport estimates, dynamic analysis through divergence and vorticity of vector currents, and statistical models of surface currents.

2.1 Introduction

The surface current measurement by interpretation of radio waves (3–30 MHz) backscattered from surface gravity waves is quickly maturing as an oceanographic observational tool whose data is useful to a broad range of users. The shore-based antenna approach can provide continuous temporal and broad spatial surface current observations, facilitating the delivery of data in near realtime for various applications.

The complicated signal processing for extracting surface currents from the backscattered radar signals ([de Paolo and Terrill(2007b)]) yields radial velocities on polar coordinate grid points centered by each antenna location. Radial velocities measured by multiple antenna installations have been combined into a vector current field using unweighted least squares fitting ([Lipa and Barrick(1983)], Mike Cook's HFRadarmapVer4.1 MATLAB toolbox). The maps of ocean surface currents are gappy in space and time for three reasons. First, the MUSIC algorithm (MUltiple SIgnal Classification, [Schmidt(1986), Barrick and Lipa(1996), de Paolo and Terrill(2007b)]) on the measured Doppler spectrum does not provide a solution for all bearing angles. Second, the estimate of vector currents along the baseline between two radars where the measurements of radial velocities are nearly aligned suffers from poor geometric dilution of precision (GDOP), and frequently results in spurious vector currents. The region with radial velocities crossing at angles less than 15–20 degrees between two radars is commonly considered to produce unusable vector currents. Finally, hardware or software problems can lead to the temporary shutdown of individual radar sites.

Relevant applications of surface currents require time- and space-continuous data, which requires the interpolation of the gappy observations to a regularly spaced product. A popular approach involves projecting the observations on the dominant modes of the sample covariance matrix (EOFs) ([Boyd et al.(1994), Beckers and Rixen(2003), Alvera-Azcarate et al.(2005), Houseago-Stokes and Challenor(2004)]). The anomalies of the missing data are estimated iteratively, and the optimal number of EOFs and the number of iterations are determined by cross validation with randomly selected observations and their estimates. Since the data set of surface currents measured by high-frequency (HF) radars around San Diego is not pre-filtered and includes errors and uncertainties due to radar operations ([Graber et al.(1997)]), the first few EOFs may not explain the variability of observed surface currents effectively without elaborate quality control before computing the covariance matrix.

Another approach used with geophysical data is the expectation maximization (EM) method, which estimates the anomalies of the missing data with iteration using an error covariance matrix as the regularization matrix ([Orchard and Woodbury(1972), Schneider(2001), Beckenbach and Washburn(2004)]). The covariance matrix is estimated with the demeaned missing data substituted by zeros at the first iteration in order to avoid non-positive definiteness, and is updated with estimated missing data until convergence. Since the EM method estimates only missing data, the estimated covariance matrix may be discontinuous with nearby points in time and space.

Several approaches have been proposed for interpolation, such as normal mode

analysis ([Lipphardt Jr. et al.(2000)]), and objective analysis ([Bretherton et al.(1976), Denman and Freeland(1985), Hollingsworth and Lönnberg(1986), Brankart and Brasseur(1996)]). These methods are all closely related. In particular, objective analysis can be implemented as normal mode analysis or EOF analysis ([Davis(1985)]).

In this chapter, an objective mapping method is presented that applies the sample covariance matrix computed directly from observations of hourly-averaged surface vector currents during two years. This approach, although computationally cumbersome, is now technically feasible due to advances in computing power. It has a number of advantages, including: the covariance matrix is based directly on the observations, with no intermediate interpolation step; the calculation of the matrix is fast and simple, without iteration; and the method can include both time and space covariances. The main disadvantage of this method is the sensitivity to negative eigenvalues in the sample covariance matrix, which can arise from missing data. The negative eigenvalues can be mitigated by adding a noise term to the diagonal of the sample covariance matrix, effectively attenuating the components with negative eigenvalues. The EOF reconstruction approach was also tried, but needed to be severely limited in space because of outliers in the vector currents.

This chapter is organized into three sections. The outlier removal as a primitive data quality control process and basic statistics of the surface currents are presented: the standard deviation, the power spectrum, and the spatial structure of correlations (section 2.2). Then, the gridding using both sample and smoothed covariance matrices and the estimates of decorrelation scales of surface currents are presented (section 2.3). In particular, the approach used to estimate a smoothed homogeneous 2-dimensional data covariance matrix from the 4-dimensional sample data-data covariance matrix is described (section 2.3.5). Next, the decorrelation length scales across the coast and the uncertainty of objectively mapped vector current data are discussed. Examples of time series and vector fields of gridded surface currents are presented (section 2.4).

2.2 Observations

2.2.1 Data coverage

An array of high-frequency (about 25 MHz) direction-finding-style system for surface current measurements (Codar Ocean Sensors, Palo Alto, CA) has been deployed in the San Diego region since September 2002. Individual radar sites are located at Point Loma (SDPL), Border Field State Park on the U.S.–Mexico Border (SDBP), and an offshore station at the Coronado Islands (SDCI) (Figure 2.1).

The fractional data availability of surface vector currents at each vector grid point during a two-year period (April 2003 – March 2005) is shown in Figure 2.2a. The existence of vector current solutions depends strongly on the number and bearing angle diversity of the radial velocities within a search radius at each vector grid point. Since at least two radial velocities from different radar sites are required for a vector solution, the regions with overlapping radar range cells from multiple

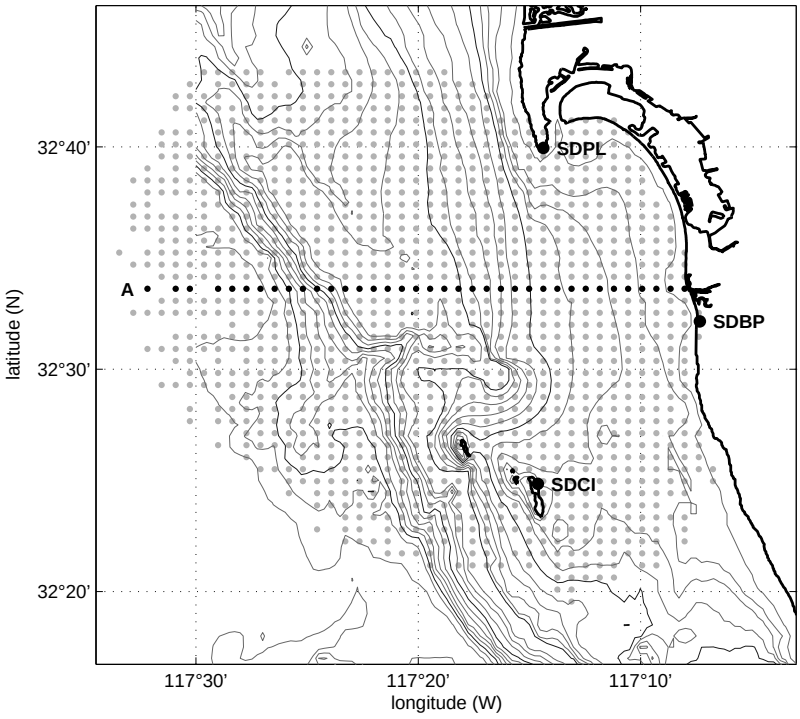

Figure 2.1: The observation domain of surface currents measured by HF radars deployed in southern San Diego. Three HF radar sites are SDPL (Point Loma), SDBP (Border Field State Park), and SDCI (Coronado Islands). The dotted area denotes the area with temporal coverage of at least 45% during two years (April 2003 – March 2005). Grid line A is the reference axis of decorrelation length scales in Figure 2.9. The bottom bathymetry contours are indicated by the thin lines with 10 m ($0 < z < 100$ m) and 100 m ($100 < z < 1000$ m) contour intervals and the thick lines at the 50, 100, 500, and 1000 m contours.

radar sites have better data coverage through time.

The timeline of available radial velocity data at each radar site is shown in Figure 2.3a. The surface vector currents derived from radial velocities using measured beam patterns at three sites (SDPL, SDBP, and SDCI) are used for this analysis. The percentage coverage relative to the vector grid points (Figure 2.1) through time is shown in Figure 2.3b. The temporary disruption of a single radar unit will reduce the coverage and the number of vector solutions.

The physical overview of surface currents is restricted to grid points with at least 45% vector current availability during the two years period, as indicated in Figure 2.1. The estimation of the data-data covariance matrix is limited to the domain of at least 90% coverage. Covariance matrices computed from regions with many missing data have unacceptably large negative eigenvalues (section 2.4.2 and Figure 2.10).

2.2.2 Outlier removal

The outliers in the surface current data lie in the tail of its probability density function. The identification of outliers follows as described below. A 2-day running mean of the time series, which is consistent with the duration of the local ocean's response to wind events, is subtracted to produce a high-pass filtered time series. The anomaly time series are then passed through a moving 5-day window in which the deviation from the 5-day running mean is compared to the 5-day running standard deviation. The hourly data during 5 days provide enough realizations for the detection of statistically anomalous data. Anomalies outside five standard deviations from the 5-day running mean are flagged as outliers. Figure 2.2b shows the percentage of identified outliers during two years. Outliers are typically clustered on the baseline and at the edges of radar coverage regions. Although most outliers are flagged in this process, a significant number remain behind.

The baseline, defined as the line of sight between two radars, is the place where it is difficult to resolve vector solutions from nearly parallel radial velocities which weakly constrain the vector current normal to the baseline. Vector current solutions using the standard unweighted least-squares fit can be spurious, which should be identified as outliers. The GDOP is determined by both the number of available radial velocities within the search radius of a vector grid point and their location relative to the radar, and it is typically high near the baseline ([Lipa and Barrick(1983), Gurgel(1994), Chapman et al.(1997), Levanon(2000)]).

The procedure for the preparation of the data set is to interpolate radial velocities across a radar range cell prior to vector combination if the radial velocities are missing within 15 degrees, and to remove the outliers among the combined vector currents using the approach described above. There are no other data quality assurance/quality control (QA/QC) processes beyond these two steps.

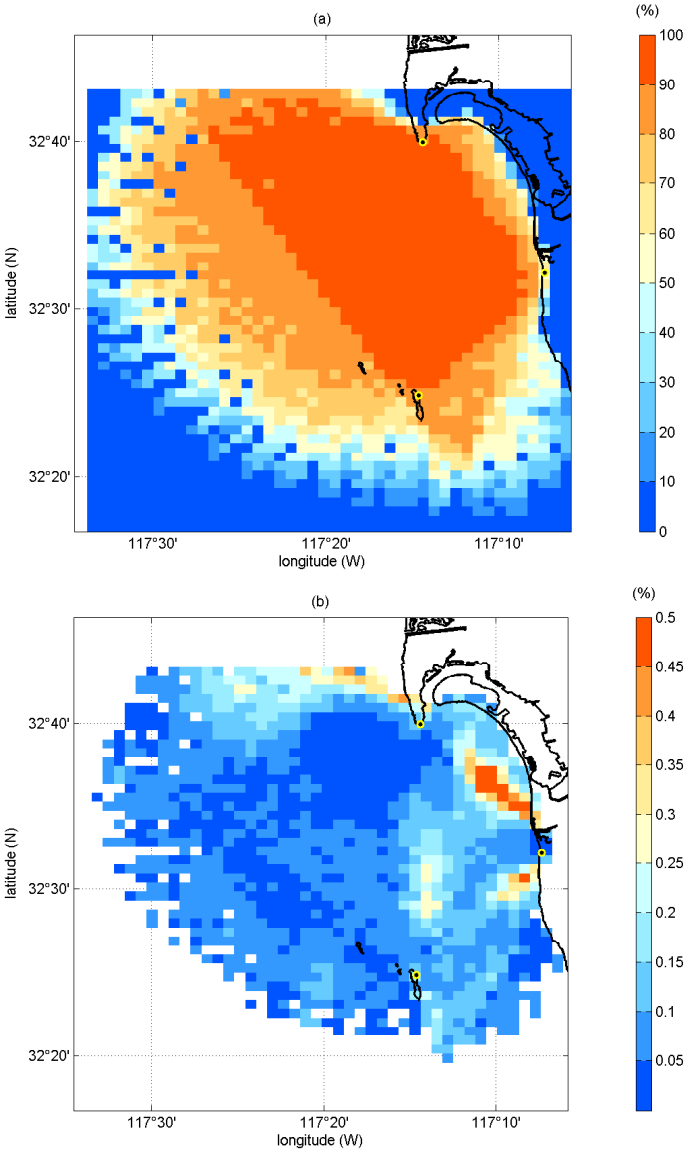

Figure 2.2: (a) A map of temporal data coverage at all grid points and (b) the percentage of the vector current solutions identified as outliers during two years of operation (April 2003 – March 2005).

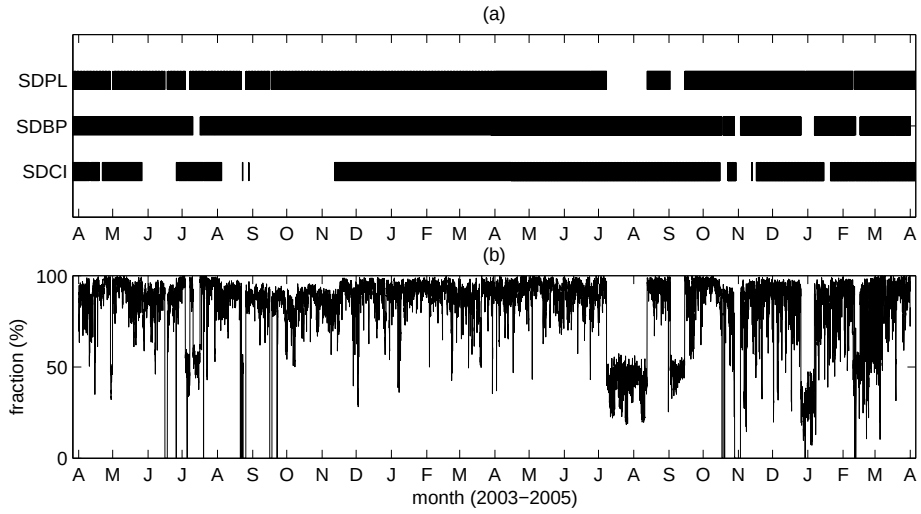

Figure 2.3: (a) The timeline of available radial velocities at each radar site. (b) The time series of percentage coverage relative to grid points that have at least 45% data availability of surface currents for two years.

2.2.3 Basic statistics

Southeastward flowing surface current is the typical current pattern in southern San Diego, as shown in Figure 2.4a. In general, the surface currents pass south of Point Loma and bend into the embayment created by the headland, with flow complications arising from San Diego Bay outflow, local gradients in wind forcing and eddies. The offshore currents are stronger than nearshore currents and are nearly unidirectional. The offshore is defined herein as the area farther than 30 km from the coast, and nearshore is the region within 30 km of the coast. During the analysis of the multi-year data set, the long term temporal mean (not shown) was found to exhibit a local artifact in a sector at approximately 287 degrees from true north at the SDBP site. Further investigation revealed that this artifact resulted from a bulge in the measured beam pattern of the SDBP site, which showed a bias in radial solutions across a 5-degree-wide angular bin ([de Paolo and Terrill(2007a)]). While the bias is visible in Figures 2.4b and 2.6c and the temporal mean currents as the discontinuous feature in this sector, it affects less than 8% of grid points. Since the smoothed covariance matrix and its decorrelation length scales presented herein are estimated from the spatial average of the sample data covariance matrix, the artifact has a minimal impact on this analysis.

The standard deviation of the surface current magnitudes is shown in Figure 2.4b. The standard deviations along the baselines are significantly larger than elsewhere due to the tendency of the baseline to generate spurious results. The standard deviation at the baseline between SDPL and SDBP shows some high values even after removal of outliers. The standard deviations of offshore currents are generally larger than nearshore currents, which may also be partly traceable to the inversion from radials.

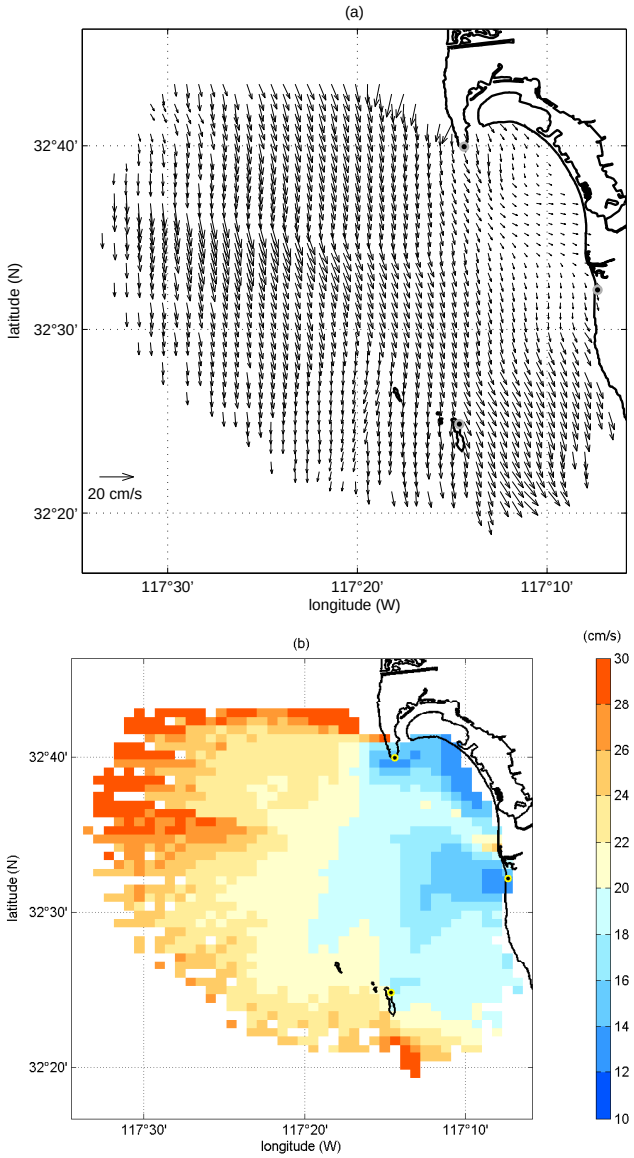

Figure 2.4: (a) A typical example of surface vector currents around San Diego. (b) The standard deviation of surface current magnitudes. Higher standard deviations along the baseline (SDPL–SDBP) result from the poor geometric dilution of precision.

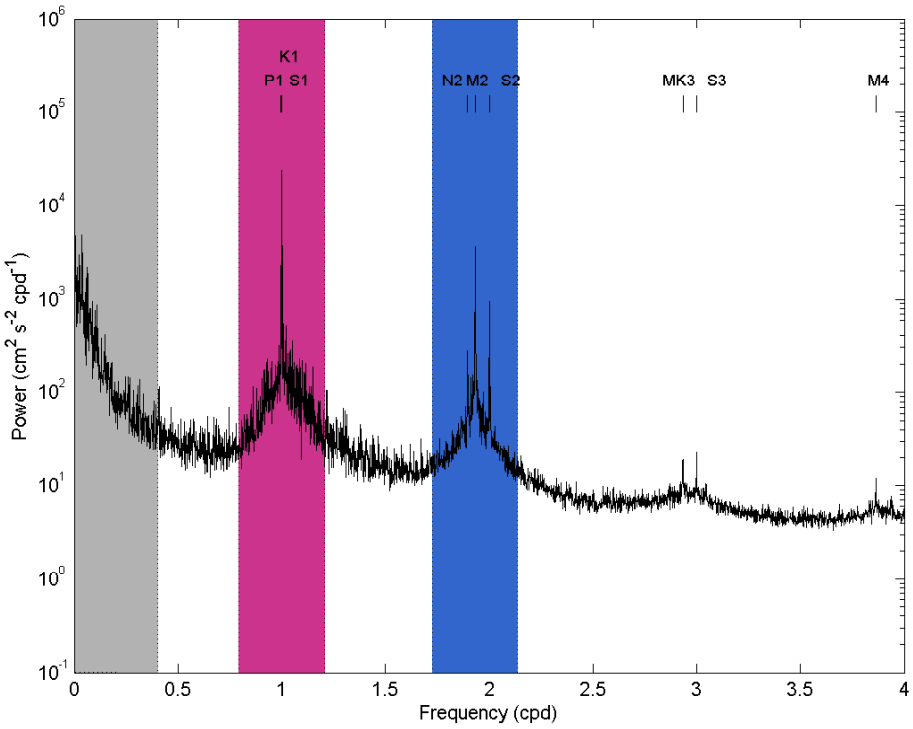

Figure 2.5: Regionally averaged power spectrum of hourly surface vector currents in the region with 45% or greater coverage (1337 grid points) shows that the dominant variances are at the low frequencies (less than 0.4 cpd), and the main tidal frequencies (K1 and M2) and their harmonics.

The regionally averaged power spectrum of the surface vector currents averaged over all grid points with at least 45% temporal coverage (Figure 2.1) is shown as Figure 2.5. Dominant variance appears at the low frequency band, defined herein as frequencies less than 0.4 cycles per day (cpd), the main tidal frequencies (K1 and M2) and their harmonics. The spreading of the energy around the tidal peaks is partly due to nonlinear interactions with the low frequency flow ([Munk and Cartwright(1966), Essen et al.(1983)]).

The correlation coefficients (equation 2.3) between surface currents at different grid points show the statistical spatial structure of surface currents such as the decorrelation length scale and the shape of the correlation function. The decorrelation length scale characterizes the typical scales of variability, and the correlation can identify inconsistent or abrupt features in the spatial domain and detect bad points.

The correlations of eastward currents (ρ_{uu}) between a reference grid point ($\mathbf{x}$) and all other grid points ($\mathbf{x}'$) are shown in Figure 2.6. In the same way, the correlations of northward currents (ρ_{vv}) are shown in Figure 2.7. Examples of the correlations are shown for two offshore grid points (Figures 2.6a, 2.6c, 2.7a and 2.7c) and two nearshore points (Figures 2.6b, 2.6d, 2.7b and 2.7d). The correlations at the offshore reference points show larger highly-correlated areas compared with the nearshore points. The north-south flows (v) have more directional preferences in their correlations

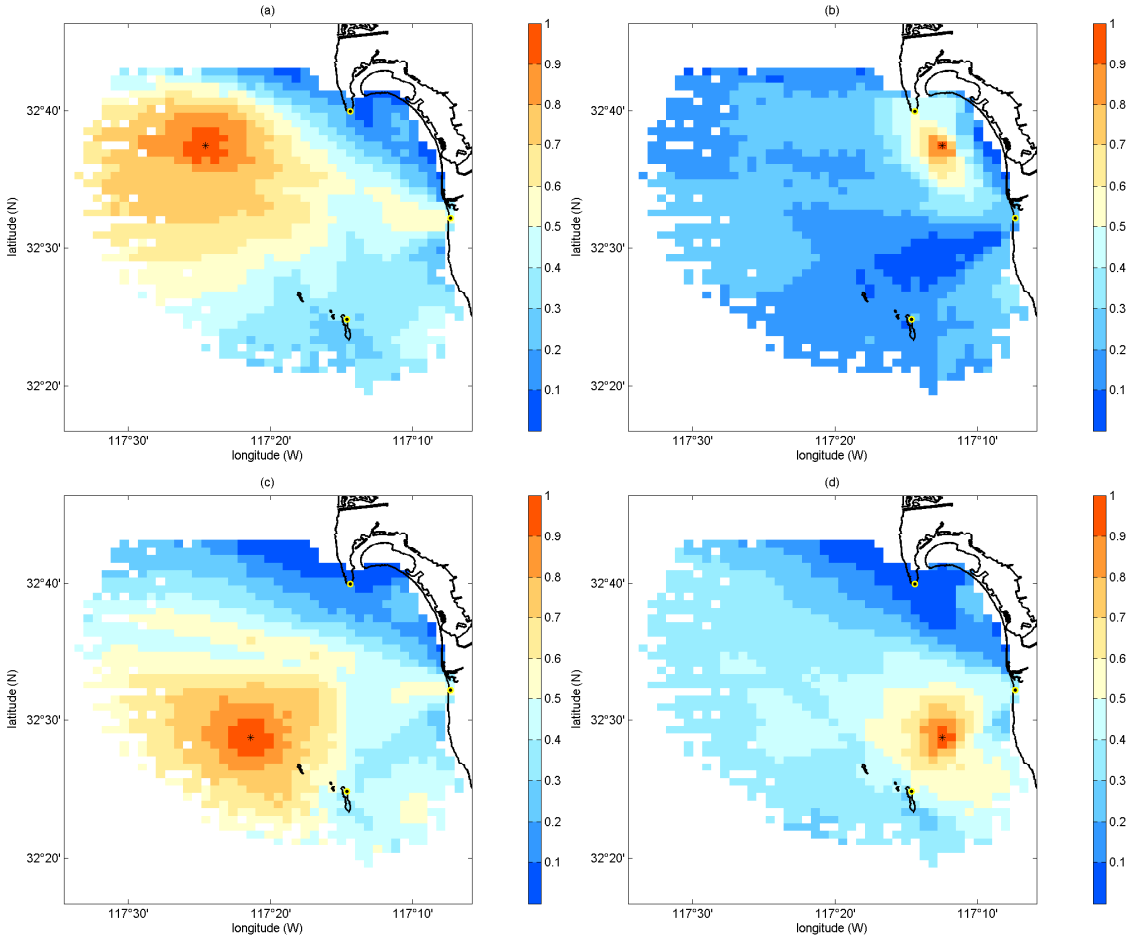

Figure 2.6: The correlations of eastward currents (ρ_{uu}) between a reference point ($\mathbf{x}$) and all other grid points ($\mathbf{x}'$). The four reference points are selected as the (a) offshore point A (32°37.40′N 117°24.55′W), (b) nearshore point B (32°37.40′N 117°12.47′W), (c) offshore point C (32°28.75′N 117°21.37′W), and (d) nearshore point D (32°28.75′N 117°12.47′W).

than the east-west flows (u). The cross-correlations (ρ_{uv} and ρ_{vu}) have complicated structures in space and vary within ± 0.3, which is not much above the level of no significance.

The cross sections of correlation in latitude (Figures 2.8a and 2.8b) and in longitude (Figures 2.8c and 2.8d) are shown for u and v, respectively. These cross sections are aligned to have a common origin and appear more exponential than Gaussian. The discontinuous lines result from data gaps within 45% coverage region (top row of Figure 2.8) and the Coronado Islands (bottom row of Figure 2.8).

Although the individual correlation functions of surface currents driven by a simple forcing such as wind, tides (diurnal and semi-diurnal tides, and their cuspate variances), and the low pressure gradient (Figure 2.5) are different (Chapter 5), we do not decompose the surface currents before mapping. Band-passing gappy data to isolate different physics adds significant complexity to the

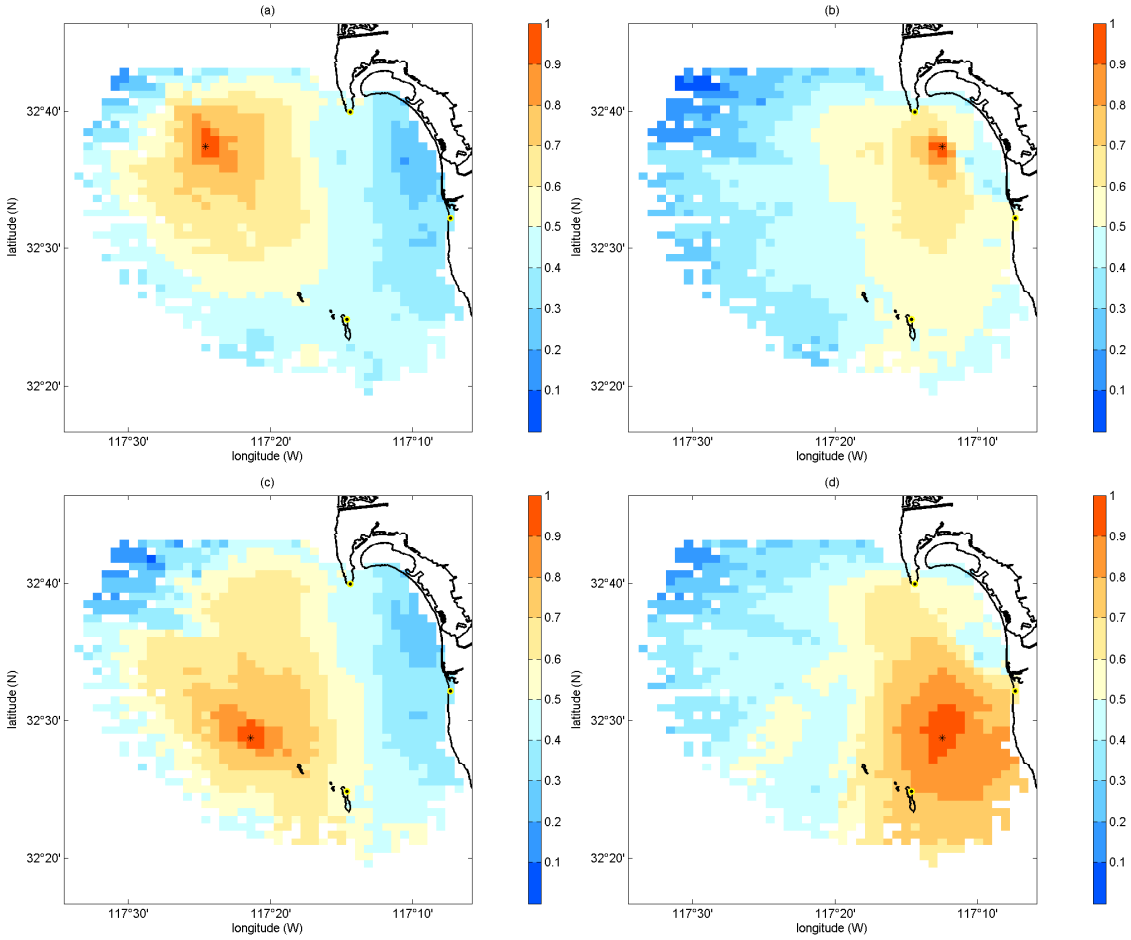

Figure 2.7: The correlations of northward currents (ρ_{vv}) between a reference point ($\mathbf{x}$) and all other grid points ($\mathbf{x}'$). The four reference points are selected as the (a) offshore point A (32°37.40′N 117°24.55′W), (b) nearshore point B (32°37.40′N 117°12.47′W), (c) offshore point C (32°28.75′N 117°21.37′W), and (d) nearshore point D (32°28.75′N 117°12.47′W).

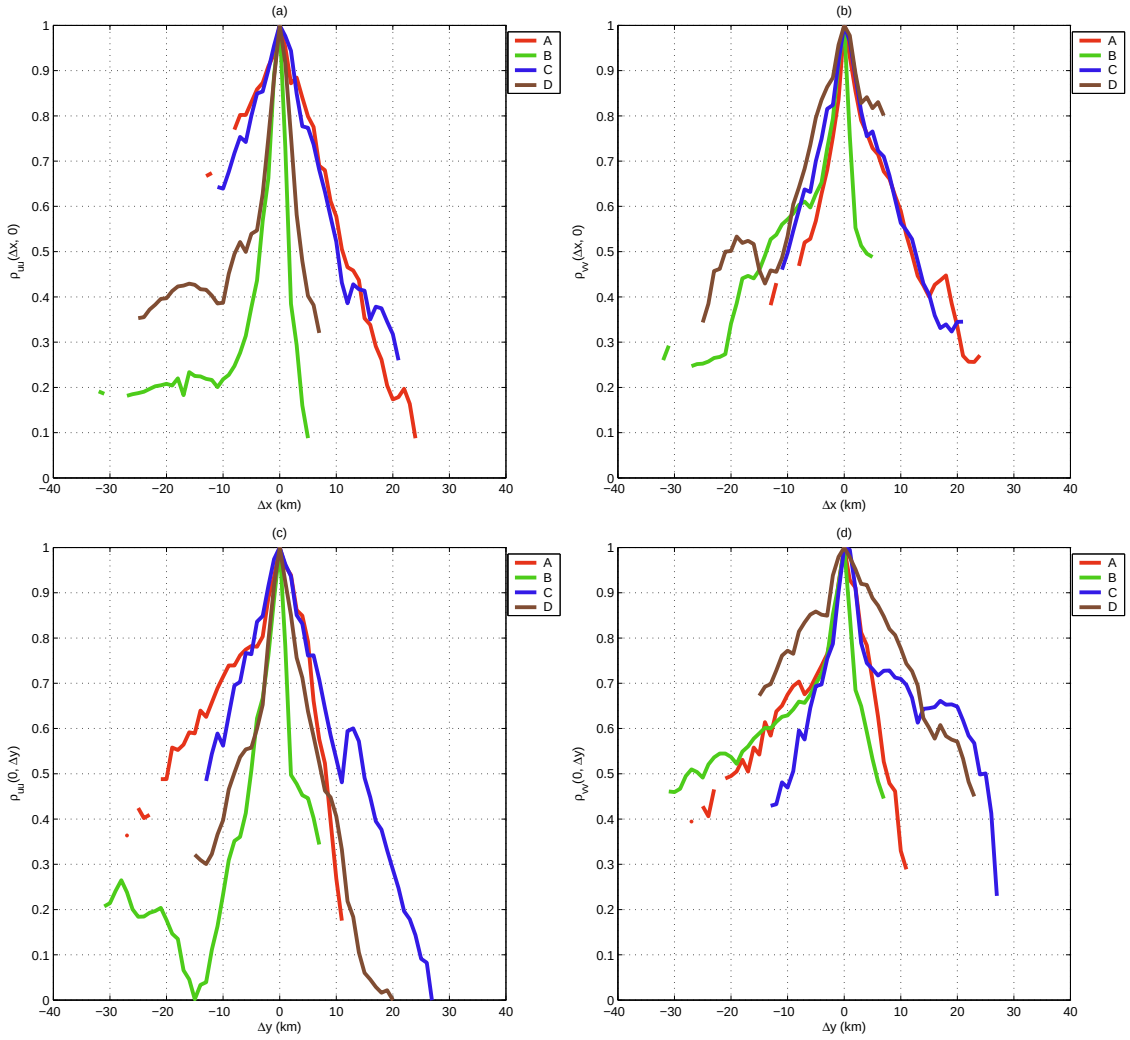

Figure 2.8: Latitudinal and longitudinal cross sections of two-dimensional correlations aligned to have a common origin on either Δx or Δy axis. (a) $\rho_{uu}(\Delta x, 0)$. (b) $\rho_{vv}(\Delta x, 0)$. (c) $\rho_{uu}(0, \Delta y)$. (d) $\rho_{vv}(0, \Delta y)$.

procedure. The sample data covariance matrix is the sum of the covariance matrix of all components.

2.3 Methods

2.3.1 Data covariance

The sample data covariance matrix ($\mathbf{C}$) with zero time lag is written as

$$\mathbf{C}(\mathbf{x},\mathbf{x}') = \frac{1}{\mathbf{N}(\mathbf{x},\mathbf{x}')} \sum_{t\in(\mathbf{x}\cap\mathbf{x}')} \mathbf{u}(\mathbf{x},t)\mathbf{u}^{\mathrm{T}}(\mathbf{x}',t), \tag{2.1}$$

where $\mathbf{u}(\mathbf{x},t) = [u(\mathbf{x},t)\, v(\mathbf{x},t)]^{\mathrm{T}}$ denotes the concatenated vector current observations, which have $2M \times L$ element (for 90% coverage during the two year time span, there are 510 grid points, so $2M = 1020$ and $L = 17544$). M and L are the number of grid points and time points, respectively. $\mathbf{N}(\mathbf{x},\mathbf{x}')$ is the number of time with observations at both grid points ($\mathbf{x}$ and $\mathbf{x}'$), and is less than L due to missing data.

The observed data covariance matrix is the sum of the true covariance matrix ($\mathbf{C}_t$) and the error covariance ($\mathbf{Q}$), which includes the observation errors owing to measurement noises and the statistical errors due to missing data:

$$\mathbf{C} = \mathbf{C}_t + \mathbf{Q}. \tag{2.2}$$

2.3.2 Correlation coefficients

The correlation coefficient (ρ) of surface currents between any two grid points is,

$$\boldsymbol{\rho}(\mathbf{x},\mathbf{x}') = \begin{bmatrix} \frac{1}{\sigma_u(\mathbf{x})} & 0 \\ 0 & \frac{1}{\sigma_v(\mathbf{x})} \end{bmatrix} \mathbf{C}(\mathbf{x},\mathbf{x}') \begin{bmatrix} \frac{1}{\sigma_u(\mathbf{x}')} & 0 \\ 0 & \frac{1}{\sigma_v(\mathbf{x}')} \end{bmatrix} = \begin{bmatrix} \rho_{uu} & \rho_{uv} \\ \rho_{vu} & \rho_{vv} \end{bmatrix}, \tag{2.3}$$

where $\boldsymbol{\sigma}(\mathbf{x}) = [\sigma_u(\mathbf{x})\, \sigma_v(\mathbf{x})]^{\mathrm{T}}$ is the time-averaged standard deviation of u and v, respectively.

2.3.3 Gridding using sample covariance matrix

Since the sample data covariance matrix is calculated by the anomalies from the time mean of a given time span, the mapping of anomalies is considered.

$$\tilde{\mathbf{d}} = (\mathrm{cov_{dm}})^{\mathrm{T}} (\mathrm{cov_{dd}})^{-1} \mathbf{d}, \tag{2.4}$$

where $\mathrm{cov_{dm}}$, $\mathrm{cov_{dd}}$, $\mathbf{d}$, and $\tilde{\mathbf{d}}$ denote the sample data-model covariance matrix, the sample data-data covariance matrix, the observed demeaned vector currents, and the estimated demeaned vector currents, respectively. The mapping grid coincides with the observation grid, so the two covariance matrices are the same, except that the data-model covariance matrix does not include the observational error. An observational error covariance matrix ($\mathbf{R}$) is added to the sample data covariance matrix which already includes error due to the finite and gappy sampling (equation 2.2):

$$\mathrm{cov}_{\mathrm{dm}}(\mathbf{x}, \mathbf{x}') = \mathbf{C}(\mathbf{x}, \mathbf{x}') \tag{2.5}$$

and

$$\mathrm{cov}_{\mathrm{dd}}(\mathbf{x}, \mathbf{x}') = \mathbf{C}(\mathbf{x}, \mathbf{x}') + \mathbf{R}. \tag{2.6}$$

In the mapping using the sample covariance matrix ($\mathbf{C}$), the regularization matrix ($\mathbf{R}$) is usually defined by the noise level of the observed data relative to the current variance. Since the sample covariance matrix is not positive definite due to missing data, the regularization matrix makes the data-data covariance matrix ($\mathrm{cov}_{\mathrm{dd}}$) invertible. It is assumed that the regularization matrix is a scaled identity matrix,

$$\mathbf{R} = \gamma^2 \mathbf{I}. \tag{2.7}$$

The mean eigenvalue (γ^2) of the regularization matrix should be greater than the magnitude of the smallest negative eigenvalue of the sample covariance matrix (equation 2.10), which is decomposed into orthogonal eigenvectors ($\mathbf{p}_k$) and eigenvalues (λ_k):

$$\mathbf{C}(\mathbf{x}, \mathbf{x}') = \sum_k \mathbf{p}_k \lambda_k \mathbf{p}_k^{\mathrm{T}}. \tag{2.8}$$

The mapping matrix is approximated schematically by,

$$\mathrm{cov}_{\mathrm{dm}}^{\mathrm{T}} \mathrm{cov}_{\mathrm{dd}}^{-1} = \sum_k \mathbf{p}_k \left(\frac{|\lambda_k|}{|\lambda_k| + \gamma^2} \right) \mathbf{p}_k^{\mathrm{T}}, \tag{2.9}$$

where $\mathbf{p}_k^{\mathrm{T}} \mathbf{p}_k = \mathbf{p}_k \mathbf{p}_k^{\mathrm{T}} = \mathbf{I}$ ($k = 1, 2, ..., 2M$) (equation 2.9 is valid only when all observations are present):

$$|\min(\lambda_k)| < \gamma^2. \tag{2.10}$$

The substitution of positive for negative eigenvalues in equation 2.9 does not change the covariance matrix by a significant amount compared to the statistical uncertainty in the 90% coverage regions. Maps using the sample covariance matrix without changing the sign of the eigenvalues are similar to those using equation 2.9. However, the simple sign change is not a general solution, because, for example, the variance becomes larger than in the sample covariance matrix.

2.3.4 Decorrelation length scale

The composite averaged correlation coefficients ($\tilde{\rho}$) are the spatial average of the correlations at the local grid points ($\hat{\mathbf{x}}$) within r_0 radius from a reference grid point ($\mathbf{x}$), and are fitted with the exponential function ($f(\Delta\mathbf{x})$):

$$\tilde{\boldsymbol{\rho}}(\mathbf{x}, \Delta\mathbf{x}) = \frac{\sum_{\forall \hat{\mathbf{x}}} \mathbf{N}(\hat{\mathbf{x}}, \hat{\mathbf{x}} + \Delta\mathbf{x}) \boldsymbol{\rho}(\hat{\mathbf{x}}, \hat{\mathbf{x}} + \Delta\mathbf{x})}{\sum_{\forall \hat{\mathbf{x}}} \mathbf{N}(\hat{\mathbf{x}}, \hat{\mathbf{x}} + \Delta\mathbf{x})} \tag{2.11}$$

and

$$f(\Delta\mathbf{x}) = e^{-\sqrt{g(\Delta\mathbf{x})}}, \tag{2.12}$$

where $g(\Delta\mathbf{x}) = a(\Delta x)^2 + b(\Delta x)(\Delta y) + c(\Delta y)^2$. The composite averaged correlation for u and v are calculated only within spatial lags from a reference point ($\pm n\Delta x$ and $\pm n\Delta y$, $n \in \mathcal{Z}$), because the signal-to-noise-ratio drops for larger lags. The coefficients (a, b, and c) are directly determined from minimizing the residual (ϵ) between the composite averaged correlation coefficients and the exponential function with a given n:

$$\epsilon(\mathbf{x}) = \frac{1}{(2n+1)^2} \sum_{i=1}^{(2n+1)^2} \left[\tilde{\boldsymbol{\rho}}(\mathbf{x}, \Delta\mathbf{x}_i) - f(\Delta\mathbf{x}_i)\right]^2. \tag{2.13}$$

These coefficients in equation 2.12 can be converted to principal axes by

$$\lambda_x = \left(a\cos^2\theta - b\cos\theta\sin\theta + c\sin^2\theta\right)^{-\frac{1}{2}}, \tag{2.14}$$

$$\lambda_y = \left(a\sin^2\theta + b\cos\theta\sin\theta + c\cos^2\theta\right)^{-\frac{1}{2}}, \tag{2.15}$$

and

$$\theta = \frac{1}{2}\arctan\frac{b}{c-a}, \tag{2.16}$$

where θ is the rotation angle (positive clockwise) and the number of lags (n) is determined from stabilizing the decorrelation length scale, and is addressed with an example in section 2.4.1. Then the semi-major (Λ) and semi-minor (λ) axes of the ellipse are

$$\Lambda = \max(\lambda_x, \lambda_y) \tag{2.17}$$

and

$$\lambda = \min(\lambda_x, \lambda_y). \tag{2.18}$$

2.3.5 Smoothed (homogeneous) covariance matrix

The sample mean correlation coefficient ($\bar{\rho}$) is the average of correlation coefficients compositing the spatial lag ($\Delta\mathbf{x}$) across all grid points.

$$\bar{\boldsymbol{\rho}}(\Delta\mathbf{x}) = \frac{\sum_{\forall\mathbf{x}} \mathbf{N}(\mathbf{x}, \mathbf{x}+\Delta\mathbf{x})\boldsymbol{\rho}(\mathbf{x}, \mathbf{x}+\Delta\mathbf{x})}{\sum_{\forall\mathbf{x}} \mathbf{N}(\mathbf{x}, \mathbf{x}+\Delta\mathbf{x})} = \begin{bmatrix} \bar{\rho}_{uu} & \bar{\rho}_{uv} \\ \bar{\rho}_{vu} & \bar{\rho}_{vv} \end{bmatrix}. \tag{2.19}$$

The sample mean standard deviations ($\bar{\sigma}$) can be smoothed by fitting to a surface such as a plane,

$$\bar{\boldsymbol{\sigma}}(\mathbf{x}) = \begin{bmatrix} \bar{\sigma}_u(\mathbf{x}) \\ \bar{\sigma}_v(\mathbf{x}) \end{bmatrix} = \begin{bmatrix} a_1 x + b_1 y + c_1 \\ a_2 x + b_2 y + c_2 \end{bmatrix}, \tag{2.20}$$

or by using a constant, which is chosen as the median of the standard deviations in the observation domain. The smoothed covariance matrix ($\bar{\mathbf{C}}$) is

$$\bar{\mathbf{C}}(\mathbf{x}, \mathbf{x}') = \bar{\boldsymbol{\rho}}(\Delta\mathbf{x})\bar{\boldsymbol{\sigma}}(\mathbf{x})\bar{\boldsymbol{\sigma}}(\mathbf{x}'). \tag{2.21}$$

2.4 Results

2.4.1 Decorrelation length scale

The decorrelation length scale provides a basis for the physical interpretation of surface currents. The locally averaged correlation coefficients (equation 2.11) of the u (or v) are fit with an exponential function (equation 2.12), and the decay scales of the exponential function are represented by the semi-major and semi-minor axes as well as by the rotation of ellipses.

In order to examine the variability of surface currents across the coast, we focus on the grid points along a line of constant latitude shown as line A in Figure 2.1. The locally averaged correlation coefficients of u (or v) at grid points ($\hat{\mathbf{x}}$) within 4 km radius (r_0) from the reference grid points ($\mathbf{x}$) are fit with an exponential function. The maximum lag ($n = 3$) was chosen as the low end of a band of lags ($n = 2, 3, \cdots, 8$) from the residuals (equation 2.13), which all give similar decorrelation length scale estimates within 10–15%. The ellipses of u and v are shown in Figure 2.9Aa and Figure 2.9Ab, respectively, and the polarization of the axes is nearly constant along line A. The decorrelation length scale of u decreases from offshore to the coast in the x- and y-directions, at least partly due to the effects of decreasing depth and the boundary layer of of coastline as shown in Figure 2.9B. Dominant southeastward currents in the south of San Diego are parallel to the shoreline, resulting in a long decorrelation length scale in v. Peaks of the decorrelation length scale of v are shown at 13 km offshore in the x-direction and at 18 km offshore in the y-direction.

2.4.2 Uncertainty

The number and magnitude of negative eigenvalues of the sample data covariance matrix depend on how many data are missing in the data set used for the estimation of the covariance matrix. Figure 2.10 shows the eigenvalue spectrum for several threshold values of the data coverage (60, 70, 80, and 90%). As the estimate was restricted to regions of increasing coverage, the number of negative eigenvalues decreases as do their magnitudes. If the data were 100% present there would be no negative eigenvalues. The most negative eigenvalue is a measure of the error in the sample data covariance compared to the true covariance matrix which must be non-negative definite. A diagonal covariance matrix with uniform variance (γ^2) is added to the sample data covariance matrix in order to make the covariance matrix non-singular. This must be large enough to compensate for the worst negative eigenvalue to restore the positive definite condition for the matrix inversion as discussed above. In the standard objective mapping, where the covariance matrices are assumed to be known in advance and are positive definite, the regularization matrix controls the amount of filtering in the mapping. This regularization is an artificial addition to remove the negative eigenvalues in this application. This is not an elegant method compared to other methods, but is simple and allows some representative calculations.

The uncertainty of the objectively mapped vector currents differs from the GDOP. We assumed all data are equally good regardless of GDOP, and the mapping error is determined by

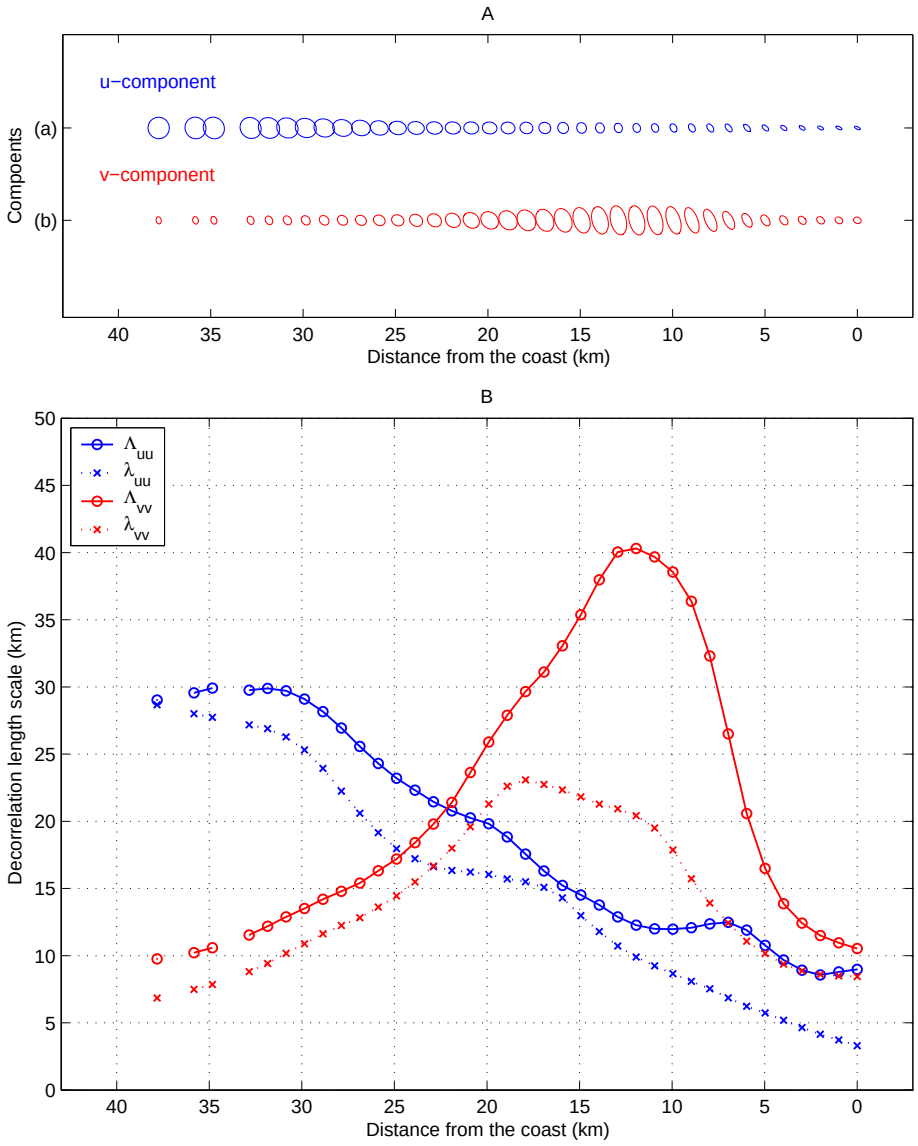

Figure 2.9: Decorrelation length scales of surface currents along grid line A in Figure 2.1. A. Ellipses of (a) u-component and (b) v-component. B. Decorrelation length scales of near-coast surface currents (Λ and λ denote the semi-major and semi-minor axes).

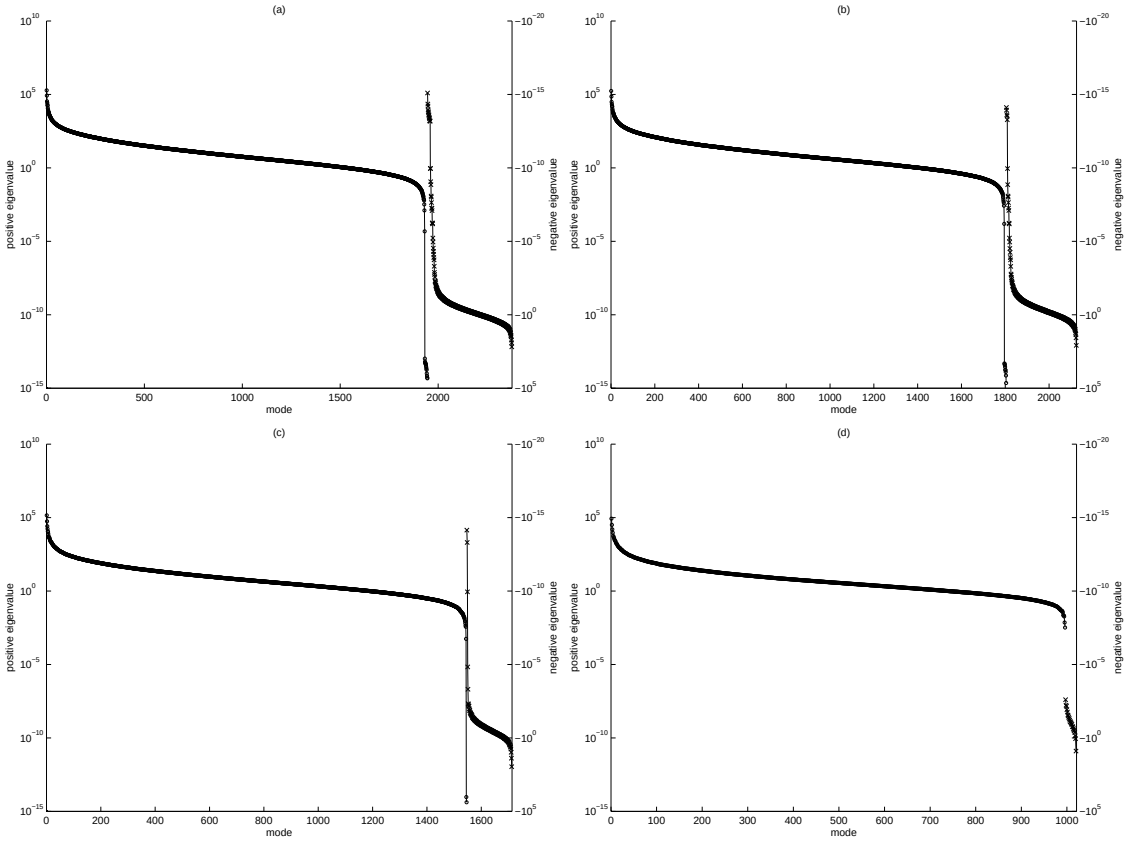

Figure 2.10: The eigenvalue spectrum of the sample data covariance matrix with varying data coverage. The positive and negative eigenvalues are indicated with circles and crosses, respectively. (a) 1188 grid points (60% coverage). (b) 1062 grid points (70% coverage). (c) 856 grid points (80% coverage). (d) 510 grid points (90% coverage).

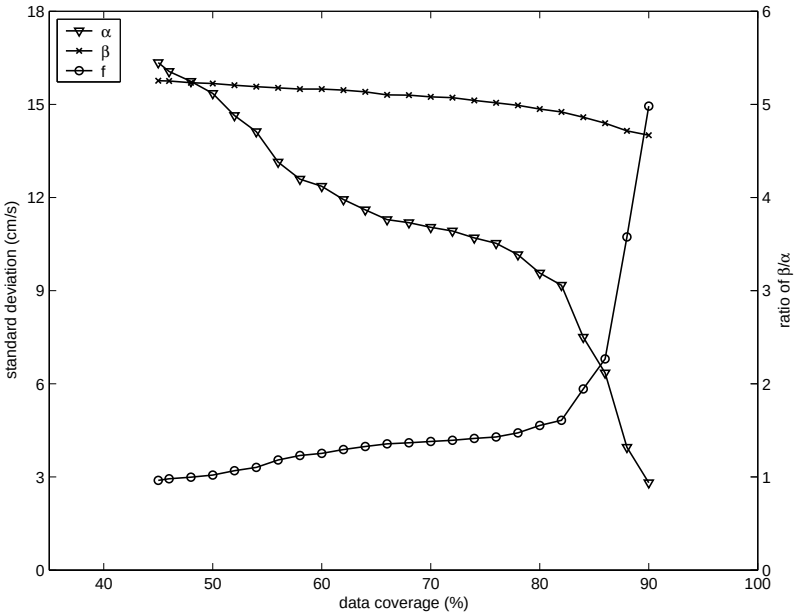

Figure 2.11: The square root of the magnitude of the most negative eigenvalue of the sample covariance matrix (α, triangle), the square root of the average variance of the surface current magnitudes at all grid points with the indicated data coverage (β, cross), and their ratio ($f = \beta/\alpha$, circle) are shown as a function of data coverage.

data coverage alone. The uncertainty presented here represents the expected uncertainty in the map due to missing data and measurement errors. The square root of the absolute value of the most negative eigenvalue of the sample covariance matrix as a function of data coverage (α, marked as triangle), the square root of the averaged variance of the surface current magnitudes at all grid points with the indicated data coverage (β, marked as cross), and their ratio ($f = \beta/\alpha$, marked as circle) are shown in Figure 2.11.

The sample covariance matrix with 90% coverage has a most negative eigenvalue of –7.9 $\mathrm{cm^2\,s^{-2}}$. In the objective mapping of this covariance matrix, a regularization matrix is applied as a diagonal matrix with 10% of the averaged variance of sample covariance matrix ($\gamma = 4.42\ \mathrm{cm\,s^{-1}}$), which is larger than the square root of the magnitude of the most negative eigenvalue. This γ is chosen arbitrarily as a 'reasonable' value, which leads to the estimation of surface currents with about 4 $\mathrm{cm\,s^{-1}}$ uncertainty. Qualitatively similar results are obtained for γ^2 in the range of 5–15% of the averaged variance of the sample covariance matrix.

2.4.3 Smoothed (homogeneous) covariance matrix

The contour plots of the sample mean correlation coefficients (equation 2.19) between u and v present the exponential structure as shown in Figures 2.12a and 2.12b, respectively. The mean correlation coefficients are constructed in order to exclude spurious small-scale structures

Table 2.1: (a) The coefficients (a, b, and c) of the exponential function fitted to the spatially averaged correlation coefficients (equation 2.12). (b) The decorrelation length scales (km) of u-component and v-component in the x- and y-directions.

(a)

	a	b	c
$\bar{\rho}_{uu}(\Delta x, \Delta y)$	0.0075	0.0038	0.007
$\bar{\rho}_{vv}(\Delta x, \Delta y)$	0.0036	0.0004	0.009

(b)

	x-direction	y-direction
u	13.7	10.4
v	16.6	34.6

due to missing data and to achieve a more robust estimate of the covariance matrix by horizontal averaging. The mean of the cross correlation term between u and v shows nearly flat structure varying within ± 0.2. Therefore the cross term of correlation for the smoothed covariance matrix is set to zero.

The mean correlation coefficients within $\pm 20\Delta x$ and $\pm 20\Delta y$ from the center are fitted with an exponential function (equation 2.12, $n = 20$). Since the mean correlation is smoother than the locally averaged correlation (equation 2.11), it is fitted with larger n and results in smaller residual variance. The contour plots of smoothed correlation coefficients are shown in Figures 2.12c and 2.12d, and the fitting coefficients (a, b, and c) and decorrelation length scales are shown in Table 2.1. These coefficients are a function of the spatial lag (Δx and Δy), getting flatter away from the center. However, for simplicity in calculations we assumed these coefficients as constant.

The standard deviation of surface currents might be assumed to depend on the bottom bathymetry in shallow water or the distance from the coastline (Figure 2.4b). Accordingly, the smoothed standard deviation of surface currents might be fitted by spatial functions such as bathymetry or distance from the coastline. However, since some standard deviations near baselines are high and are inconsistent with the nearby area, it could be difficult to avoid the influence of spurious data. Therefore the smoothed standard deviation of u (or v) is estimated from the median value of standard deviations at all observation grid points. The median value for $\bar{\sigma}_u$ and $\bar{\sigma}_v$ are 12.21 and 16.41 cm s^{-1}, respectively.

The smoothed covariance matrix of surface currents is reconstructed by multiplying the spatial mean correlation coefficients (equation 2.19) at the spatial lag (Δx and Δy) and the smoothed standard deviations at all grid points (x, y). The eigenvalue spectrum of the smoothed covariance matrix is shown in Figure 2.13. The smallest eigenvalue of the smoothed covariance matrix is 3.91 cm^2 s^{-2}, and a diagonal matrix with 10% of averaged variance is added as the regularization matrix ($\gamma = 4.57$ cm s^{-1}). The smoothed covariance matrix is positive definite, and the regularization has a reasonable noise level as discussed above.

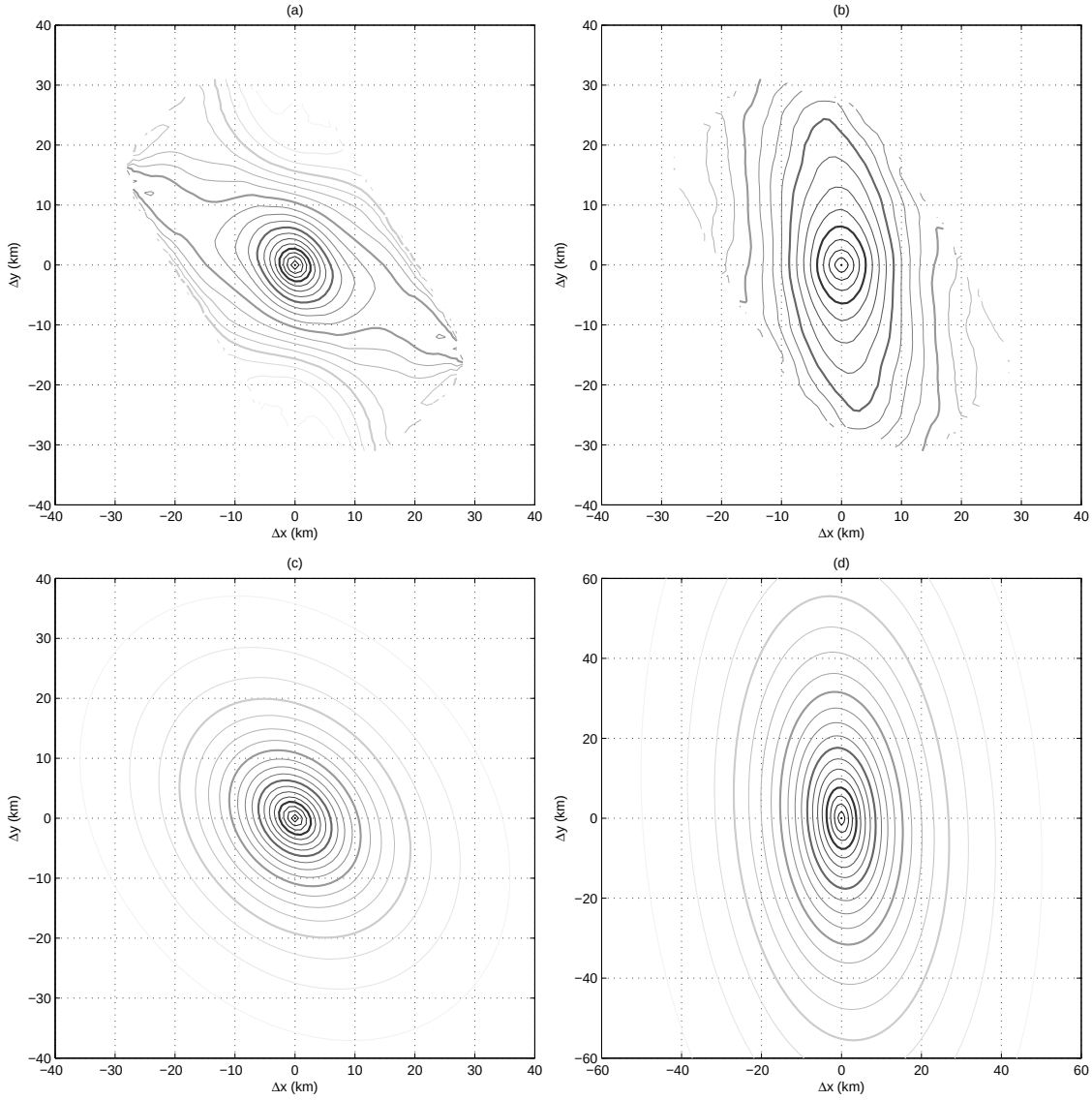

Figure 2.12: (a)-(b): The spatially averaged correlation coefficients (equation 2.19) for $\bar{\rho}_{uu}$ and $\bar{\rho}_{vv}$. (c)-(d): Exponential functions (equation 2.12) fitted to the spatially averaged correlation coefficients for $\bar{\rho}_{uu}$ and $\bar{\rho}_{vv}$. The spacing of thin contours is 0.05, and thick contours are at 0.2, 0.4, 0.6, and 0.8.

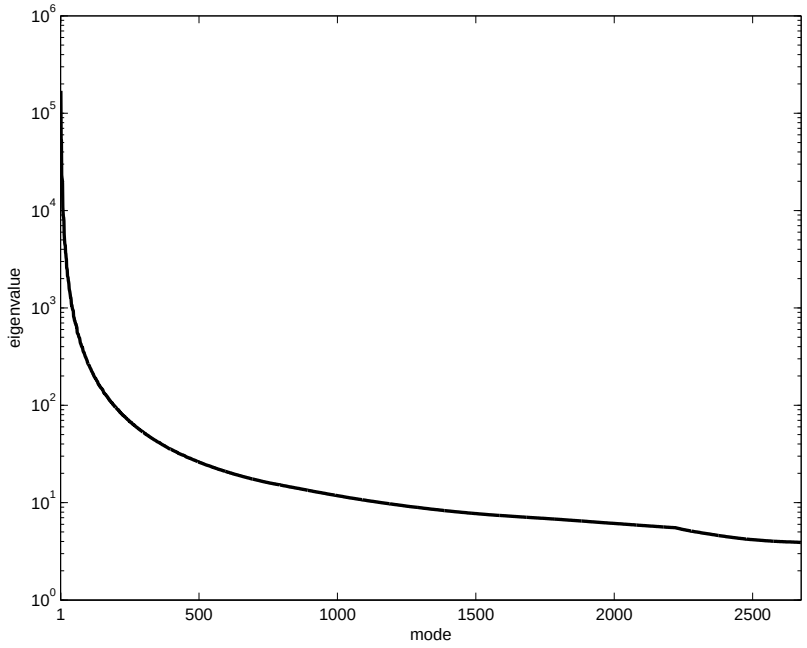

Figure 2.13: The eigenvalue spectrum of the smoothed covariance matrix.

2.4.4 Comparison of gridding

The surface vector currents measured at 510 grid points (90% spatial coverage) for one month were mapped objectively with both the sample covariance matrix during the two year time span and the smoothed covariance matrix. The sample covariance matrix can only map in the 90% coverage area, while the smoothed covariance matrix can be used for the expanded 45% coverage area.

Time domain

The observed and the objectively mapped surface current components (u and v) are shown in Figures 2.14a and 2.14b. As a random example having missing data, these time series are from a grid point within the 90% coverage area. The estimated data with both covariance matrices agree with the observations, and suppress the spurious data. Since the estimated data usually have less variance than the observations due to the regularization, a variance or covariance estimated from the objectively mapped surface currents will be biased.

Space domain

An example of the surface vector current field is shown with the 90% (dashed contour) and 45% (gray contour) coverage area in Figure 2.15. Spurious data can be seen on the baselines (SDPL and SDBP, SDPL and SDCI) and at the edge of the observation domain (at the west of

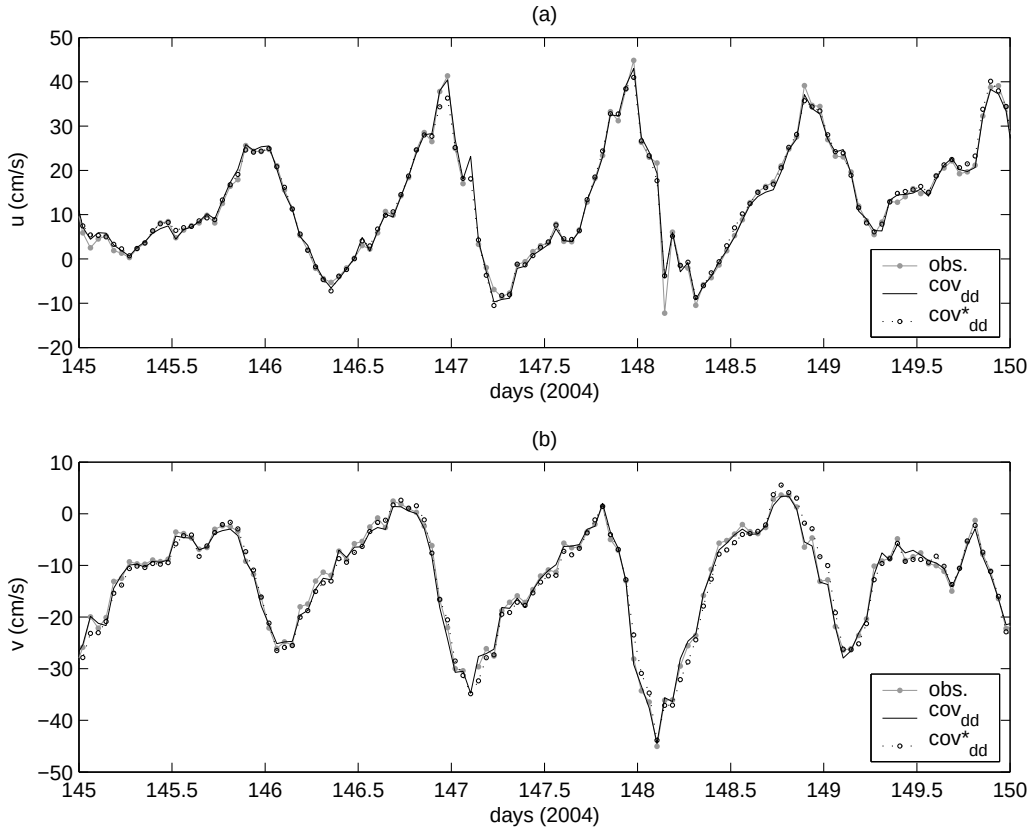

Figure 2.14: The sample time series for the raw data (gray dots), the objectively mapped data using the sample covariance matrix (black line), and the objectively mapped data using the smoothed covariance matrix (black dashdot). (a) u-component. (b) v-component.

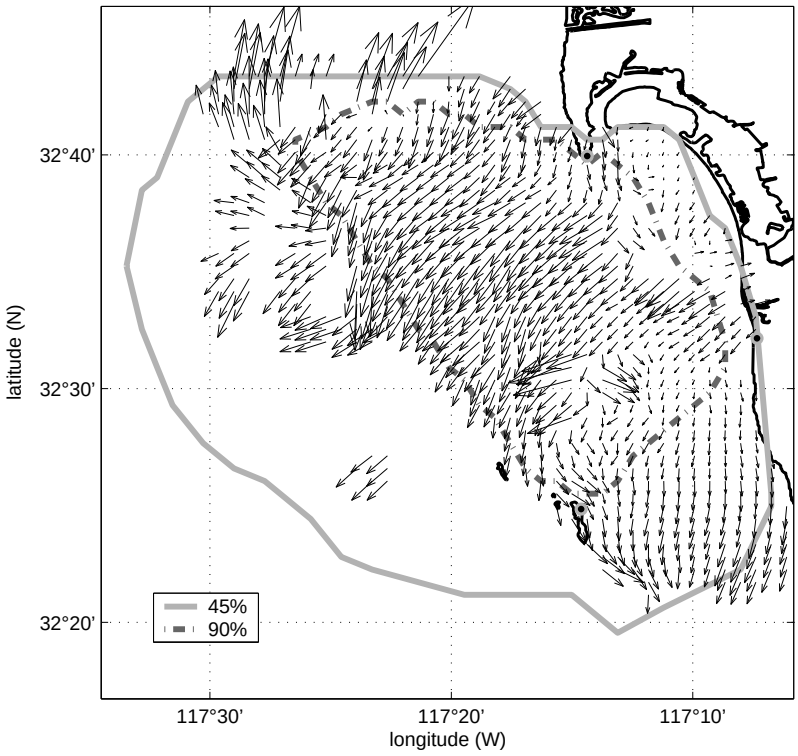

Figure 2.15: An example of the vector current field. The data coverage is indicated with contours.

Point Loma). Moreover, there are missing data on the baselines and at the west of the Coronado Islands.

The objectively mapped vector current field on grid points in the 90 and 45% coverage area is shown in Figures 2.16a and 2.16b, respectively. The spurious data are suppressed, and the gaps in space are filled with a consistent vector current field. The vector current field mapped with the smoothed covariance matrix shows a smoother field.

The objectively mapped uncertainty field for two coverage cases are shown in Figures 2.16c and 2.16d. The uncertainties normalized by the variance of the surface currents at each grid point are varying from 0 (more reliable) to 1 (more uncertain), and are represented as ellipses to include directional information. However, since the smoothed covariance matrix assumed no cross correlation between u and v, the ellipses are not tilted in Figure 2.16d. Higher uncertainty occurs in both the baseline of SDPL and SDBP (Figure 2.16c) and the area with fewer radial velocities (Figure 2.16d).

2.5 Discussion

There are a number of ways to map gappy observations to a complete grid. Some methods use prior estimates of covariance functions from either analytical functions or basis functions (or

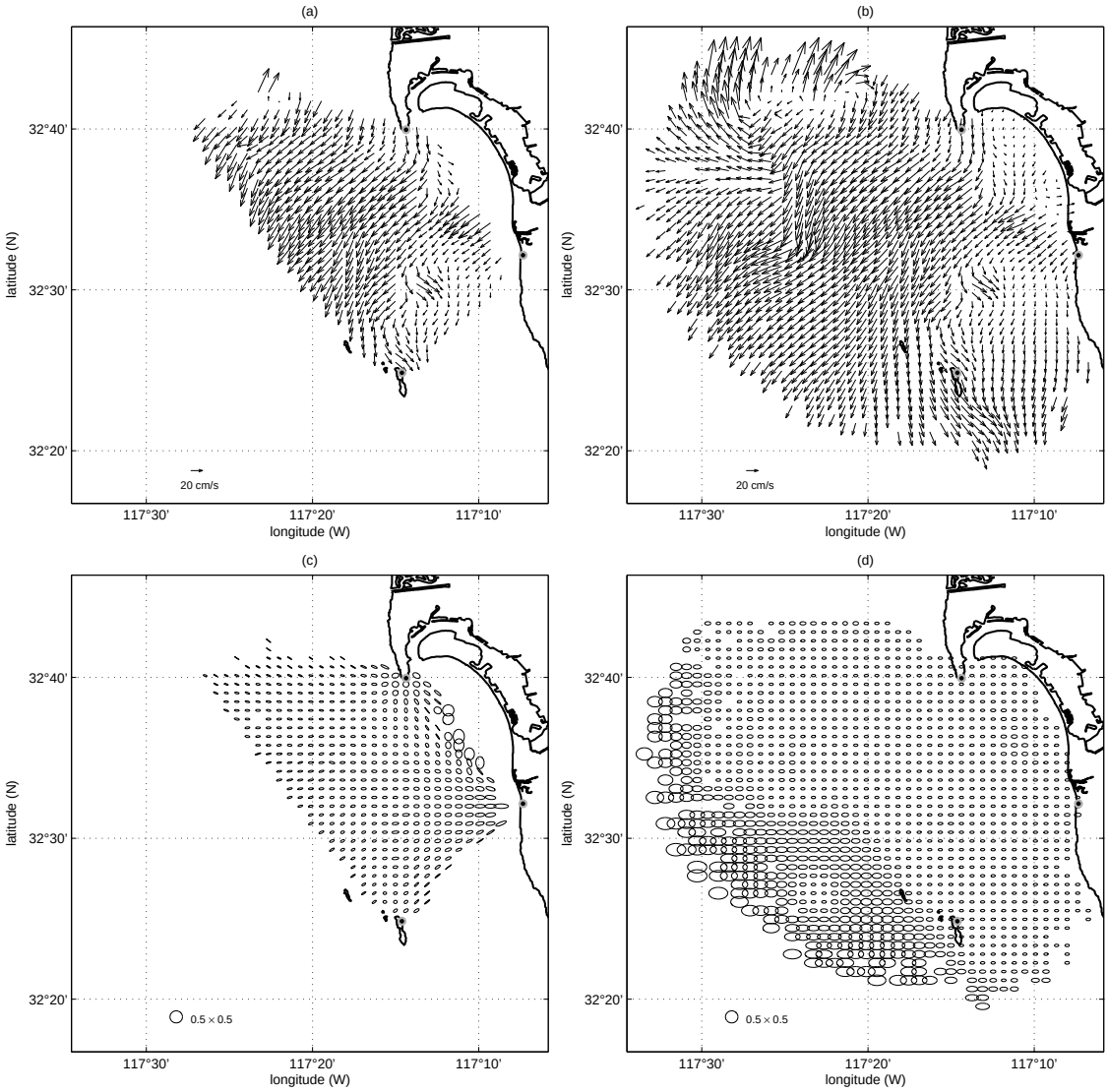

Figure 2.16: An example of the objectively mapped vector current field using (a) the data covariance matrix in the region with 90% data coverage and (b) the smoothed covariance matrix in the region with 45% data coverage. (c) and (d) are the normalized uncertainty ellipses corresponding to (a) and (b).

'normal modes') determined from models. The approach we have described involves the use of the observed covariance matrix in the objective mapping and the challenges faced when dealing with the negative eigenvalues of the sample covariance matrix.

There are several assumptions used in the objective mapping technique described in this chapter. First, the mean of the observations is assumed to be the same as the mean of the estimated data. Since the grid points where the vector currents are estimated are the same as where the vector currents are observed, this assumption is valid under the circumstances when there are sufficient number of unbiased observations to estimate mean currents. Second, since the fraction of missing observations is closely related to the size of the negative eigenvalues, there is a restriction in the estimation of the surface vector currents with reasonable uncertainty through the objective mapping using the sample covariance matrix. Finally, the cross correlations ($\bar{\rho}_{uv}$) between u and v are assumed zero in the smoothed covariance matrix. The decorrelation length scales and standard deviations are assumed as constant in the observation area as well. However, the smoothed covariance matrix might be improved by using locally-averaged decorrelation length scales and standard deviations related to the bottom bathymetry.

The objective mapping of surface currents enables us to get complete vector current fields for real time applications. The integration in time and the differentiation in space of surface currents are applicable to particle tracking for pollutants, rescue, and dispersion of larvae, and estimates of divergence and vorticity (e.g., upwelling and downwelling). As an ongoing application, the Tijuana River plume has been tracked with a random walk model based on the objectively mapped surface currents (Chapter 6). The decorrelation length scales and the correlation functions estimated from the observed surface currents provide the initial steps for the statistical surface current models. In order to build this model, the data covariance matrix should have enough realizations to include the response of surface currents to the various driving forces.

This job work was carried out in MATLAB on a dual Xenon CPU (4G RAM) machine running Linux. The hourly gridding for 1337 grid points takes about 20–30 seconds. The dominant computation is from the inversion of the covariance matrix.

This chapter, in part, is a reprint of the material as it appears in *Journal of Geophysical Research-Oceans*, 2007, Kim, S. Y., E. J. Terrill, and B. D. Cornuelle titled by 'Objectively mapping HF radar-derived surface current data using measured and idealized data covariance matrices', **112**, C06021, doi:10.1029/2006JC003756. The dissertation author was the primary investigator and author of this paper.

Chapter 3

Mapping surface currents from high-frequency radar radial velocity measurements using optimal interpolation

Abstract

An optimal interpolation (OI) method to compute surface vector current fields from radial velocity measurements derived from high-frequency (HF) radars is presented. The method assumes a smooth spatial covariance relationship between neighboring vector currents, in contrast to the more commonly used un-weighted least-squares fitting (UWLS) method, which assumes a constant vector velocity within a defined search radius. This OI method can directly compute any quantities linearly related to the radial velocities, such as vector currents and dynamic quantities (divergence and vorticity) as well as the uncertainties of those respective fields. The OI method is found to be more stable than the UWLS method and reduces spurious vector solutions near the baselines between HF radar installations. The OI method produces a covariance of the uncertainty of the estimated vector current fields. Three non-dimensional uncertainty indices are introduced to characterize the uncertainty of the vector current at a point, representing an ellipse with directional characteristics. The vector current estimation using the OI method eliminates the need for multiple mapping steps and optimally fills intermittent coverage gaps. The effects of angular interpolation of radial velocities, a commonly-used step in the pre-processing of radial velocity data prior to vector current computation in the UWLS method, are presented.

3.1 Introduction

The Doppler shifts of backscattered radio signals from surface gravity waves are used to estimate the current component in the direction of the bearing angle of the radar cell (Figure 3.1). The radial velocities on the radar grid points are estimated using either beam forming or direction finding (e.g. MUSIC) ([Lipa and Barrick(1983), Schmidt(1986), Barrick and Lipa(1996), Barrick and Lipa(1997), de Paolo and Terrill(2007b)]). Radial velocities measured from multiple radars are combined into vector currents on a rectangular grid, which is called vector grid, using a variety of methods. This computation is an independent step from the radial current estimation algorithm, and is applicable to the data obtained by high-frequency (HF) radar systems (e.g., WERA, CODAR).

An un-weighted least-squares fitting (UWLS) method has been used by many authors to extract the vector currents from the radial velocities ([Lipa and Barrick(1983), Gurgel(1994), Graber et al.(1997)]). Implicit in this approach is an assumption of a uniform vector velocity producing the radial velocities within the search radius for a given vector grid point. In other words, the correlation of the vector current is assumed to be one everywhere within the search radius and zero outside. The method also assumes an unlimited signal variance, which may create spurious estimates when combining nearly aligned noisy radial velocities due to the singularity of the geometric covariance matrix (equation 3.6). The terms 'signal variance' and 'error variance' are defined here as the expected variance of the surface currents and the expected observational error variance of the surface currents, respectively. In operation, spurious vector solutions most often occur near the baseline between two radars or near the maximum range. The segmented correlation function in the UWLS method can also produce a discontinuous current field. The proposed optimal interpolation (OI) method uses a correlation for the surface currents which more accurately describes the spatial relationship between radial velocity measurements.

The uncertainty of the estimated vector current has historically been addressed in two ways. The geometric dilution of precision (GDOP), which is calculated from the inverse of the geometric covariance matrix, has been used as an indicator of uncertainty ([Lipa and Barrick(1983), Chapman et al.(1997)]). In a slightly different way, the geometric covariance matrix is built with the cosine and sine function of the bearing angle inversely weighted by the hourly standard deviation (HSTD) of radial velocities ([Gurgel(1994), Lipa(2003)]). Since the GDOP has a different minimum depending on the number of available radial velocities (section 3.6.1), and the HSTD inversely weighted radial velocities follow different statistics compared to the raw (unconditioned) radial velocities, a unified definition of the uncertainty would be useful. In the OI method, an error covariance matrix is computed from the HSTD of radial velocities or the assumed error variance to provide an uncertainty for regularization. Three uncertainty indices are introduced as a normalized indicator for the quality of the solution.

This chapter is composed of four parts. First, we start with a general form of least-squares fitting, weighted least-squares fitting (WLS), which is used to calculate the vector currents.

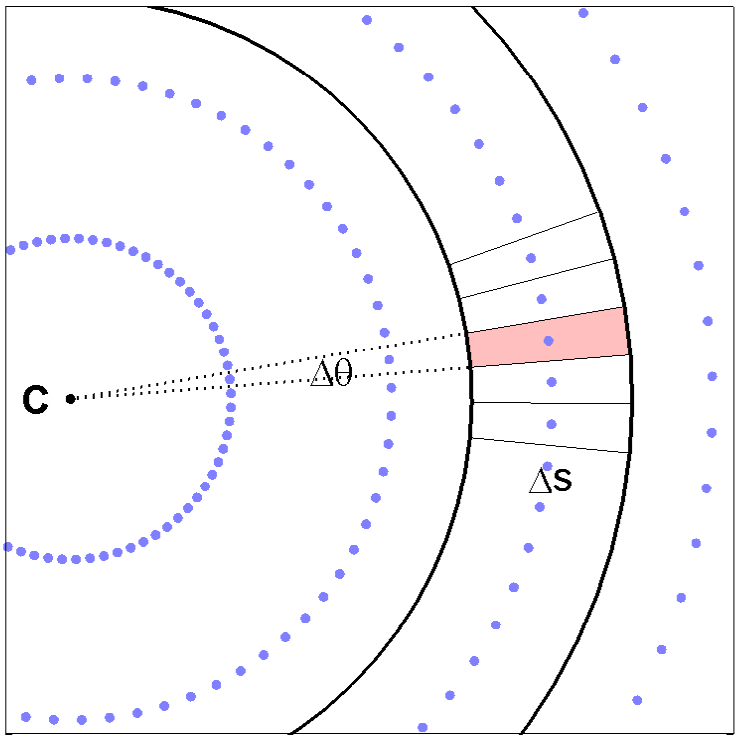

Figure 3.1: The radar grid structure for the radar located at point C. Each radar grid point (blue dot) is the center of a radar cell with the range resolution (Δs) and the azimuthal resolution ($\Delta\theta$). A radar cell (pink area) is the intersection of a range bin (annulus with thick curves) with an azimuthal bin (dotted lines).

We then show how to obtain the UWLS formula by allowing the signal variance to be infinite. Next, we describe the OI method using an averaging kernel with infinite basis (section 3.2.2), the algebraic derivation of the UWLS method from the OI method with finite basis (section 3.2.3), the implementation of the OI method (section 3.2.4), and the determination of parameters in the UWLS and OI methods (section 3.2.5). In the third part, the basic statistics of radial velocities and the radar uncertainty are addressed (section 3.3). Finally, examples and discussions using both methods are summarized (section 3.4).

3.2 Methods

The mean radial velocity (r) is the temporal average of N radial velocities (r_0) estimated from cross spectra of the backscattered signals during a given time span and in a given radar cell. (The time span in this chapter is an hour.) The hourly standard deviation (HSTD, ϵ) of the radial velocities is related to the uncertainty of the mean value (i.e., standard error):

$$\epsilon = \sqrt{\frac{1}{N}\sum_{i=1}^{N}\left(r_0^i - r\right)^2}\,, \tag{3.1}$$

where r_0^i is the radial velocity obtained at the ith time, and N is the sub-sampling rate during the given time span. The radial velocity referred to in this chapter is the hourly mean radial velocity (r), and its HSTD (ϵ) will be used in the construction of the error covariance of radial velocities.

3.2.1 Least-squares fitting

The weighted least-squares fitting (WLS, [Wunsch(1996)]) method to estimate the vector current ($\mathbf{u}$, 2×1 elements) at a vector grid point (x_k, y_k) assumes that each radial velocity is a linear combination of the vector current components. The radial velocities ($\mathbf{r}$, $L\times 1$ elements) within the search radius (d_0) of the vector grid point are expressed with the projection matrix ($\mathbf{G_a}$, $L\times 2$ elements) and the vector current ($\mathbf{u}$):

$$\mathbf{r} = \mathbf{G_a u} + \mathbf{n_a}, \tag{3.2}$$

where

$$\mathbf{G_a} = \begin{bmatrix} \mathbf{g}_1^{\mathrm{T}} \\ \mathbf{g}_2^{\mathrm{T}} \\ \vdots \\ \mathbf{g}_L^{\mathrm{T}} \end{bmatrix} = \begin{bmatrix} \cos\theta_1 & \sin\theta_1 \\ \cos\theta_2 & \sin\theta_2 \\ \vdots & \vdots \\ \cos\theta_L & \sin\theta_L \end{bmatrix},\ \mathbf{r} = \begin{bmatrix} r_1 \\ r_2 \\ \vdots \\ r_L \end{bmatrix}, \tag{3.3}$$

$\mathbf{g}_i = [\cos\theta_i\ \sin\theta_i]^{\mathrm{T}}$, θ_i denotes the bearing angle at the ith radar grid point (x_i, y_i) measured counterclockwise from East, $\mathbf{n_a}$ is the residual ($L\times 1$ elements) when the radial velocities are fit by a single vector current, and L is the number of radial velocities within the search radius ($^{\mathrm{T}}$ denotes the matrix transpose). The least-squares estimate for the vector current is

$$\hat{\mathbf{u}} = \left(\mathbf{G_a}^{\mathrm{T}}\mathbf{R}^{-1}\mathbf{G_a} + \mathbf{P}^{-1}\right)^{-1}\mathbf{G_a}^{\mathrm{T}}\mathbf{R}^{-1}\mathbf{r}. \tag{3.4}$$

The model covariance matrix $\left(\mathbf{P} \equiv \langle \mathbf{u}\mathbf{u}^{\mathrm{T}} \rangle\right)$ is the expected covariance of the unknown velocity, where $\langle \cdot \rangle$ denotes the expected value. The error covariance matrix $\left(\mathbf{R} \equiv \langle \mathbf{n_a}\mathbf{n_a}^{\mathrm{T}} \rangle\right)$ is the covariance matrix of the measurement uncertainty. In simple least-squares fitting, both $\mathbf{P}$ and $\mathbf{R}$ are assumed to be scaled identity matrices:

$$\mathbf{P} = \sigma_s^2 \mathbf{I} \text{ and } \mathbf{R} = \sigma_r^2 \mathbf{I}. \tag{3.5}$$

With the assumption of infinite signal variance ($\sigma_s^2 = \infty$) and unit error variance ($\sigma_r^2 = 1$), the WLS method matches the UWLS method, which is the standard method in the estimate of vector currents ([Lipa and Barrick(1983), Gurgel(1994), Graber et al.(1997)]). The UWLS method also assumes constant vector currents within the search radius (d_0) of the vector grid point, and the estimate becomes

$$\hat{\mathbf{u}} = \left(\mathbf{G}_\mathbf{a}^{\mathrm{T}} \mathbf{G}_\mathbf{a}\right)^{-1} \mathbf{G}_\mathbf{a}^{\mathrm{T}} \mathbf{r}, \tag{3.6}$$

where $\mathbf{G}_\mathbf{a}^{\mathrm{T}} \mathbf{G}_\mathbf{a}$ is called the geometric covariance matrix (2×2 elements), of which the inverse matrix is discussed with GDOP in section 3.6.1.

3.2.2 Averaging kernel with infinite basis

To begin a more general discussion of the computation of the vector current field, we consider the sampling function. The radial velocity ($\mathbf{r}$) is sampled by the kernel ($\mathbf{w}$) over a region (Ω) surrounding the nominal radar grid point (x_i, y_i) from a spatially continuous current field ($\mathbf{u}$).

$$\mathbf{r}(x_i, y_i) = \iint_\Omega \mathbf{w}(x_i, y_i, x, y)^{\mathrm{T}} \mathbf{u}(x, y)\, \mathrm{d}x\mathrm{d}y + \mathbf{n}, \tag{3.7}$$

where $\mathbf{r} = \mathbf{r}(x_i, y_i)$, $\mathbf{w} = \mathbf{w}(x_i, y_i, x, y)$, $\mathbf{u} = \mathbf{u}(x, y)$, and $\mathbf{n}$ is the measurement error of the radial velocity.

The kernel represents the sensitivity of the observed radial velocities to the surface vector current in the backscattering region. In other words, the kernel specifies the average over range and bearing angle of the HF radar measurements. If the bearing angle is constant over the local domain where the kernel ($\mathbf{w}(x_i, y_i, x, y)$) is defined, the kernel can be factored into separate coverage and angle components:

$$\mathbf{r}(x_i, y_i) = \iint_\Omega w(x_i, y_i, x, y) \mathbf{g}(x_i, y_i)^{\mathrm{T}} \mathbf{u}(x, y)\, \mathrm{d}x\mathrm{d}y + \mathbf{n}, \tag{3.8}$$

where $\mathbf{g}_i = \mathbf{g}(x_i, y_i) = [\cos\theta_i \ \sin\theta_i]^{\mathrm{T}}$, and θ_i denotes the bearing angle at the radar grid point. The weighting of the kernel ($w(x_i, y_i, x, y)$) is a function of the local radar grid point (x_i, y_i) and the point (x, y) being sampled. The kernel ($\mathbf{w}$) is normalized to unity,

$$\iint_\Omega |\mathbf{w}(x_i, y_i, x, y)|\, \mathrm{d}x\mathrm{d}y = 1. \tag{3.9}$$

The vector grid points to be mapped can be considered individually or as a grouped matrix. In this chapter, the UWLS and OI methods are described one by one.

The OI estimates ([Bretherton et al.(1976)]) for the vector current ($\hat{\mathbf{u}}$), the a posteriori uncertainty matrix ($\hat{\mathbf{P}}$), and the normalized uncertainty matrix ($\hat{\boldsymbol{\chi}}$) at a single point (x_k, y_k) are

$$\hat{\mathbf{u}} = \mathrm{cov}_{\mathrm{dm}}^{\mathrm{T}} \mathrm{cov}_{\mathrm{dd}}^{-1} \mathbf{r}, \tag{3.10}$$

$$\hat{\mathbf{P}} = \mathrm{cov}_{\mathrm{mm}} - \mathrm{cov}_{\mathrm{dm}}^{\mathrm{T}} \mathrm{cov}_{\mathrm{dd}}^{-1} \mathrm{cov}_{\mathrm{dm}}, \tag{3.11}$$

and

$$\hat{\boldsymbol{\chi}} = \mathbf{I} - \mathrm{cov}_{\mathrm{mm}}^{-1} \mathrm{cov}_{\mathrm{dm}}^{\mathrm{T}} \mathrm{cov}_{\mathrm{dd}}^{-1} \mathrm{cov}_{\mathrm{dm}}, \tag{3.12}$$

where these three matrices are:

$$\begin{aligned} (\mathrm{cov}_{\mathrm{dm}})_{ik} &= \langle \mathbf{r}_i \mathbf{u}^{\mathrm{T}} \rangle \\ &= \iint_{\Omega} w_i \, \mathbf{g}_i^{\mathrm{T}} \langle \mathbf{u}(x,y) \mathbf{u}^{\mathrm{T}}(x_k, y_k) \rangle \, \mathrm{d}x\mathrm{d}y, \end{aligned} \tag{3.13}$$

$$\begin{aligned} (\mathrm{cov}_{\mathrm{dd}})_{ij} &= \langle \mathbf{r}_i \mathbf{r}_j^{\mathrm{T}} \rangle + \langle \mathbf{n}_i \mathbf{n}_j^{\mathrm{T}} \rangle \\ &= \iint_{\Omega'} \iint_{\Omega} w_i w_j \, \mathbf{g}_i^{\mathrm{T}} \langle \mathbf{u}(x,y) \mathbf{u}^{\mathrm{T}}(x', y') \rangle \mathbf{g}_j \, \mathrm{d}x\mathrm{d}y \, \mathrm{d}x'\mathrm{d}y' + \langle \mathbf{n}_i \mathbf{n}_j^{\mathrm{T}} \rangle, \end{aligned} \tag{3.14}$$

and

$$(\mathrm{cov}_{\mathrm{mm}})_{kk} = \langle \hat{\mathbf{u}}_k \hat{\mathbf{u}}_k^{\mathrm{T}} \rangle, \tag{3.15}$$

where $(\mathrm{cov}_{\mathrm{dm}})_{ik}$ and $(\mathrm{cov}_{\mathrm{dd}})_{ij}$ denote the components at the ith row and kth (or jth) column of the data-model covariance matrix ($\mathrm{cov}_{\mathrm{dm}}$) and the data-data covariance matrix ($\mathrm{cov}_{\mathrm{dd}}$), respectively. The measurement uncertainty covariance matrix ($\langle \mathbf{n}_i \mathbf{n}_j^{\mathrm{T}} \rangle$) is a diagonal matrix if the radial velocity errors are independent. The error covariance is assumed to be

$$\langle \mathbf{n}_i \mathbf{n}_j^{\mathrm{T}} \rangle = \delta_{ij} \sigma_r^2, \tag{3.16}$$

where σ_r^2 includes the average measurement uncertainty (γ^2) of the radial velocity and the possibly time-dependent standard error (ϵ^2/N) of the mean radial velocity for N samples per hour:

$$\sigma_r^2 = \gamma^2 + \frac{\epsilon^2}{N}. \tag{3.17}$$

The number of samples during an hour in the radar operation is not recorded for each radar cell and varies in time and space between at least one and at most six in our dataset ($1 \leq N \leq 6$).

The average measurement uncertainty (γ^2) of the radial velocity is the sum of the representational error of the model ([Lorenc(1986), Daley(1993)]) and the errors in the radar measurements, and can be estimated by the variance of the sum of the radial velocities measured at nearby points by two opposing radars (section 3.3.3).

Although the radar measurement is not local, the form of the kernel ($\mathbf{w}$) is not well-defined. Therefore for simplicity the averaging kernel is hereafter assumed to be a delta function in space:

$$w_i = \delta(\mathbf{x} - \mathbf{x}_i). \tag{3.18}$$

The data-model covariance matrix (equation 3.13) and the data-data covariance matrix (equation 3.14) are

$$(\mathrm{cov}_{\mathrm{dm}})_{ik} = \mathbf{g}_i^{\mathrm{T}} \langle \mathbf{u}_i \mathbf{u}_k^{\mathrm{T}} \rangle \tag{3.19}$$

and

$$(\mathrm{cov}_{\mathrm{dd}})_{ij} = \mathbf{g}_i^{\mathrm{T}} \langle \mathbf{u}_i \mathbf{u}_j^{\mathrm{T}} \rangle \mathbf{g}_j + \delta_{ij} \sigma_r^2. \tag{3.20}$$

In this case each radial velocity can be considered as a point observation. The representational error may be adjusted to account for the covariance scale and the assumption that the kernel is a delta function.

3.2.3 Derivation of UWLS from OI

The OI method is a general approach to calculate vector currents. One can obtain the UWLS method from the OI method by making several simplifying assumptions. By default, the OI method assumes a continuous current field so that the radial velocities ($\mathbf{r}$, $M \times 1$ elements) are the projection of the collocated vector currents ($\mathbf{u}$) along the bearing angle (M is the total number of radial velocities):

$$\mathbf{r} = \mathbf{G}\mathbf{u}, \tag{3.21}$$

where $\mathbf{u}$ represents the vector currents at the radar grid points ($2M \times 1$ elements) and the projection matrix ($\mathbf{G}$, $M \times 2M$ elements) is

$$\mathbf{G} = \begin{bmatrix} \mathbf{g}_1^{\mathrm{T}} & \mathbf{0} & \mathbf{0} & \mathbf{0} \\ \mathbf{0} & \mathbf{g}_2^{\mathrm{T}} & \mathbf{0} & \mathbf{0} \\ \mathbf{0} & \mathbf{0} & \ddots & \mathbf{0} \\ \mathbf{0} & \mathbf{0} & \mathbf{0} & \mathbf{g}_M^{\mathrm{T}} \end{bmatrix}. \tag{3.22}$$

The continuous current field ($\mathbf{u}$) may be parameterized by a finite set of values ($\mathbf{m}$), and transformed to the radial velocities at the radar grid points by the interpolation matrix ($\mathbf{F_r}$):

$$\mathbf{u} = \mathbf{F_r}\mathbf{m}. \tag{3.23}$$

Therefore the radial velocities are

$$\mathbf{r} = \mathbf{G}\mathbf{F_r}\mathbf{m} + \mathbf{n} = \bar{\mathbf{G}}\mathbf{m} + \mathbf{n}, \tag{3.24}$$

where $\bar{\mathbf{G}} \equiv \mathbf{G}\mathbf{F_r}$ and $\mathbf{F_r}$ can represent a Fourier series expansion, a normal mode expansion ([Lipphardt Jr. et al.(2000), Kaplan and Lekein(2007)]), or an interpolation from a regular grid of vector current values. As before, $\mathbf{n}$ is the residual when the vector current is fit to the parameters. The use of the current values at the vector grid points as the parameters for a linear spline basis set makes for the simplest comparison to the discrete least-squares fitting method.

If the model is described with a finite basis as in equation 3.24 ([Davis(1985)]), the estimated vector current ($\hat{\mathbf{u}}$, equation 3.10) can be determined from the optimized parameters:

$$\hat{\mathbf{u}} = \mathbf{F_g}\hat{\mathbf{m}}, \tag{3.25}$$

where $\mathbf{F_g}$ is the mapping matrix of the vector currents to the vector grid point.

$$\hat{\mathbf{u}} = \mathbf{F_g}\mathbf{P}\bar{\mathbf{G}}^{\mathrm{T}}\left(\bar{\mathbf{G}}\mathbf{P}\bar{\mathbf{G}}^{\mathrm{T}} + \mathbf{R}\right)^{-1}\mathbf{r} \tag{3.26}$$

$$= \mathbf{F_g}\left(\bar{\mathbf{G}}^{\mathrm{T}}\mathbf{R}^{-1}\bar{\mathbf{G}} + \mathbf{P}^{-1}\right)^{-1}\bar{\mathbf{G}}^{\mathrm{T}}\mathbf{R}^{-1}\mathbf{r}, \tag{3.27}$$

If the parameters ($\hat{\mathbf{m}}$) in equation 3.23 are the estimated vector currents ($\hat{\mathbf{u}}$) on the vector grid points, then $\mathbf{F_g}$ in equation 3.25 becomes the identity matrix, and the model covariance matrix ($\mathbf{P}$) becomes $\langle \mathbf{u}\mathbf{u}^{\mathrm{T}} \rangle$. Equations 3.26 and 3.27 are interchangeable by the matrix inversion lemma ([Golub and Van Loan(1996)]). In a similar way, the a posteriori uncertainty matrix ($\hat{\mathbf{P}}$, equation 3.11) with a finite basis at a vector grid point is derived corresponding to equations 3.26 and 3.27 as

$$\hat{\mathbf{P}} = \mathbf{F_g}\mathbf{P}\mathbf{F_g}^{\mathrm{T}} - \mathbf{F_g}\mathbf{P}\bar{\mathbf{G}}^{\mathrm{T}}\left(\bar{\mathbf{G}}\mathbf{P}\bar{\mathbf{G}}^{\mathrm{T}} + \mathbf{R}\right)^{-1}\bar{\mathbf{G}}\mathbf{P}^{\mathrm{T}}\mathbf{F_g}^{\mathrm{T}} \tag{3.28}$$

$$= \mathbf{F_g}\left(\bar{\mathbf{G}}^{\mathrm{T}}\mathbf{R}^{-1}\bar{\mathbf{G}} + \mathbf{P}^{-1}\right)^{-1}\mathbf{F_g}^{\mathrm{T}}. \tag{3.29}$$

For comparison, the a posteriori uncertainty matrices in the WLS and UWLS methods are

$$\hat{\mathbf{P}} = \left(\mathbf{G_a}^{\mathrm{T}}\mathbf{R}^{-1}\mathbf{G_a} + \mathbf{P}^{-1}\right)^{-1} \tag{3.30}$$

and

$$\hat{\mathbf{P}} = \left(\mathbf{G_a}^{\mathrm{T}}\mathbf{G_a}\right)^{-1}, \tag{3.31}$$

respectively.

The normalized uncertainty matrix ($\boldsymbol{\varphi}$) is introduced in order to compare the uncertainty in the estimate between the UWLS and OI methods. The corresponding normalized uncertainty matrix in the OI method is the a posteriori uncertainty matrix (equation 3.29) divided by the observational error variance (σ_r^2):

$$\boldsymbol{\varphi} = \left(\bar{\mathbf{G}}^{\mathrm{T}}\bar{\mathbf{G}} + \mathbf{P}^{-1}\sigma_r^2\right)^{-1}, \tag{3.32}$$

(recall that $\mathbf{R} = \sigma_r^2\mathbf{I}$). On the other hand, since the UWLS method implies the unit error variance (1 cm^2 s^{-2}), the normalized uncertainty matrix is exactly the same as equation 3.31:

$$\boldsymbol{\varphi} = \left(\mathbf{G}_\mathbf{a}^\mathrm{T}\mathbf{G}_\mathbf{a}\right)^{-1}. \tag{3.33}$$

Motivated by the convenience of a unified definition of the uncertainty, we suggest an alternative non-dimensional uncertainty index matrix ($\hat{\boldsymbol{\chi}}$, equation 3.12), which is normalized by the signal variance (σ_s^2) instead of the error variance (σ_r^2). For the OI method, this is the a posteriori uncertainty covariance matrix normalized by the a priori model covariance ($\mathbf{P}$):

$$\hat{\boldsymbol{\chi}} \equiv \mathbf{P}^{-1/2}\left(\mathbf{P} - \mathbf{P}\bar{\mathbf{G}}^\mathrm{T}\left(\bar{\mathbf{G}}\mathbf{P}\bar{\mathbf{G}}^\mathrm{T} + \mathbf{R}\right)^{-1}\bar{\mathbf{G}}\mathbf{P}^\mathrm{T}\right)\mathbf{P}^{-1/2}. \tag{3.34}$$

This non-dimensional uncertainty index matrix does not exist in the UWLS method due to the assumption of the infinite signal variance ($\sigma_s^2 = \infty$), so the a priori model covariance matrix is not meaningful.

3.2.4 Implementing optimal interpolation

This section describes the approach taken to apply the OI method to the radial velocity data. The estimation of the vector current ($\hat{\mathbf{u}}$, equation 3.10) requires the data-model covariance matrix (equation 3.19) and the data-data covariance matrix (equation 3.20):

$$\left(\mathrm{cov}_\mathrm{dm}\right)_{ik} = \mathbf{g}_i^\mathrm{T}\sigma_s^2(x_k, y_k)\,\rho(\Delta x_{ik}, \Delta y_{ik}) \tag{3.35}$$

and

$$\left(\mathrm{cov}_\mathrm{dd}\right)_{ij} = \mathbf{g}_i^\mathrm{T}\sigma_s^2(x_k, y_k)\,\rho(\Delta x_{ij}, \Delta y_{ij})\mathbf{g}_j + \delta_{ij}\sigma_r^2, \tag{3.36}$$

where $\mathbf{g}_i = [\cos\theta_i\ \sin\theta_i]^\mathrm{T}$, $(\Delta x_{ik}, \Delta y_{ik}) = (x_i - x_k, y_i - y_k)$, $(\Delta x_{ij}, \Delta y_{ij}) = (x_i - x_j, y_i - y_j)$, and $\sigma_s^2(x_k, y_k)$ is the expected variance of surface currents at (x_k, y_k). $\rho(\Delta x, \Delta y)$ is the correlation function of the surface currents. Both exponential and Gaussian correlation functions are widely used.

Exponential:

$$\rho(\Delta x, \Delta y) = \exp\left(-\sqrt{\left(\frac{\Delta x}{\lambda_x}\right)^2 + \left(\frac{\Delta y}{\lambda_y}\right)^2}\right), \tag{3.37}$$

Gaussian:

$$\rho(\Delta x, \Delta y) = \exp\left(-\left(\frac{\Delta x}{\lambda_x}\right)^2 - \left(\frac{\Delta y}{\lambda_y}\right)^2\right), \tag{3.38}$$

where λ_x and λ_y are the decorrelation length scales in the x- and y-directions, respectively.

The normalized uncertainty matrix ($\boldsymbol{\varphi}$) and the uncertainty index matrix ($\hat{\boldsymbol{\chi}}$) are

$$\boldsymbol{\varphi} = \frac{1}{\sigma_r^2}\left(\mathrm{cov}_\mathrm{mm} - \mathrm{cov}_\mathrm{dm}^\mathrm{T}\mathrm{cov}_\mathrm{dd}^{-1}\mathrm{cov}_\mathrm{dm}\right) \tag{3.39}$$

and

$$\hat{\boldsymbol{\chi}} = \frac{1}{\sigma_s^2}\left(\mathrm{cov}_{\mathrm{mm}} - \mathrm{cov}_{\mathrm{dm}}^{\mathrm{T}}\mathrm{cov}_{\mathrm{dd}}^{-1}\mathrm{cov}_{\mathrm{dm}}\right). \tag{3.40}$$

3.2.5 Definition of parameters

Several parameters must be chosen, depending on the method: the search radius (d_0), the decorrelation length scales (λ_x and λ_y), the signal variance (σ_s^2), and the data error variance (σ_r^2). These parameters are functions of the range resolution (Δs) of the radar and the vector grid resolution (Δx and Δy). The vector grid resolution is determined by the spatial scales needed to resolve the surface currents of interest and limited by the radar resolution.

The implied correlation function of the surface currents in the least-squares fitting (UWLS and WLS) methods is one within the search radius (d_0) and zero outside. The search radius is typically chosen to be similar to the range resolution (Δs) of the radar, and so the observations at adjacent radar cells in range and azimuthal directions are assumed to be independent. In contrast to the least-squares fitting method, the correlation function of the OI method is controlled by the decorrelation length scales (λ_x and λ_y), which are set according to the scales of the surface currents to be resolved.

In order to avoid over-smoothing the data, the decorrelation length scale should be no longer than the expected length scale of the surface current. To resolve the variability, the grid resolution should be smaller than the expected length scale. In order to avoid too much redundancy, four times the vector grid resolution is suggested as the upper bound of the length scale, and the vector grid resolution is set to the length scale as the lower bound:

$$\Delta x \le \lambda_x \le 4\Delta x \text{ and } \Delta y \le \lambda_y \le 4\Delta y. \tag{3.41}$$

The radial velocities measured by the long range and short range high-frequency radars in Southern California are used to examine how the sensitivity and variability of the estimated current field depend on the decorrelation length scale. Although the variability of the estimated currents depends on the decorrelation length scale, the overall current variability is found to be varying only weakly within the suggested range.

3.3 Observations

3.3.1 Data coverage

While the approach described here can be applied to any radar system, the settings and data from an array of 25 MHz direction-finding style SeaSonde systems (Codar Ocean Sensors, Palo Alto, CA) are used. The radar cell is defined by a range resolution (Δs) of 1.49 km and an azimuthal resolution ($\Delta\theta$) of 5 degrees (Figure 3.1). The maximum range is less than 45 km and the effective bearing angles of individual radars are different due to the coastline geometry.

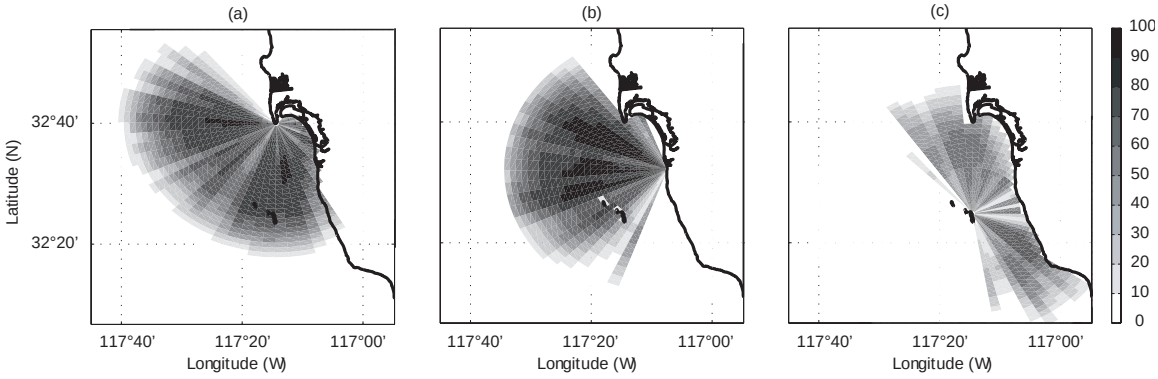

Figure 3.2: Percent availability of the radial velocities at each radar site during the 2-year study period (April 2003–March 2005). (a) SDPL. (b) SDBP. (c) SDCI.

The fractional availability of radial velocities of each radar during two years duration (April 2003–March 2005) is shown in Figure 3.2. The timeline of available radial velocities at each radar site is addressed elsewhere (Figure 2.3a). The radial velocities calculated with the measured antenna response function at three sites are analyzed in this chapter: Point Loma (SDPL), Border Field State Park on the U.S.–Mexico Border (SDBP), and Coronado Islands (SDCI).

3.3.2 Basic statistics

The two-year mean of the radial velocities measured by each radar is shown in Figure 3.3A. Since the radial velocity at a radar grid point is the projection of the vector current in the bearing angle, the contribution of the current component normal to the bearing angle is zero. The mean of the observed radial velocities is consistent with the typical south-eastward currents of this region (Figure 2.4).

The standard deviation (RMS) of radial velocities for each radar is shown in Figure 3.3B. Typical RMS of the surface current is $\sim$10 cm s^{-1} in the near shore and $\sim$20 cm s^{-1} in the offshore, respectively. Regions of low radial velocity variance are seen for all sites where the major axes of the surface current ellipses are normal to the direction of radial velocities. Higher RMS near land may result from abrupt changes of the radar signal strength due to land shadowing and the antenna response function. However, the higher values west of Point Loma for all three radar sites do not completely fit this explanation and need a separate investigation.

The probability density functions (PDFs) of the radial velocities measured by each radar during the 2-year study period, shown in Figure 3.4a, roughly resemble Gaussian distributions with fat tails. All three sites show similar e-folding scales and tails in the PDFs. The radial velocities in the tail of the PDF ($|r| > 90$ cm s^{-1}) are typically located at the edge of the radar coverage region, and therefore can be interpreted as outliers. Since the resolutions (Δr) of the radial velocity due to the first-order sea echo are 2.39, 2.29, and 2.36 cm s^{-1} for SDPL, SDBP, and SDCI, respectively, there are discontinuities in the PDFs where the magnitude of the radial velocity is less than 2 cm s^{-1}.

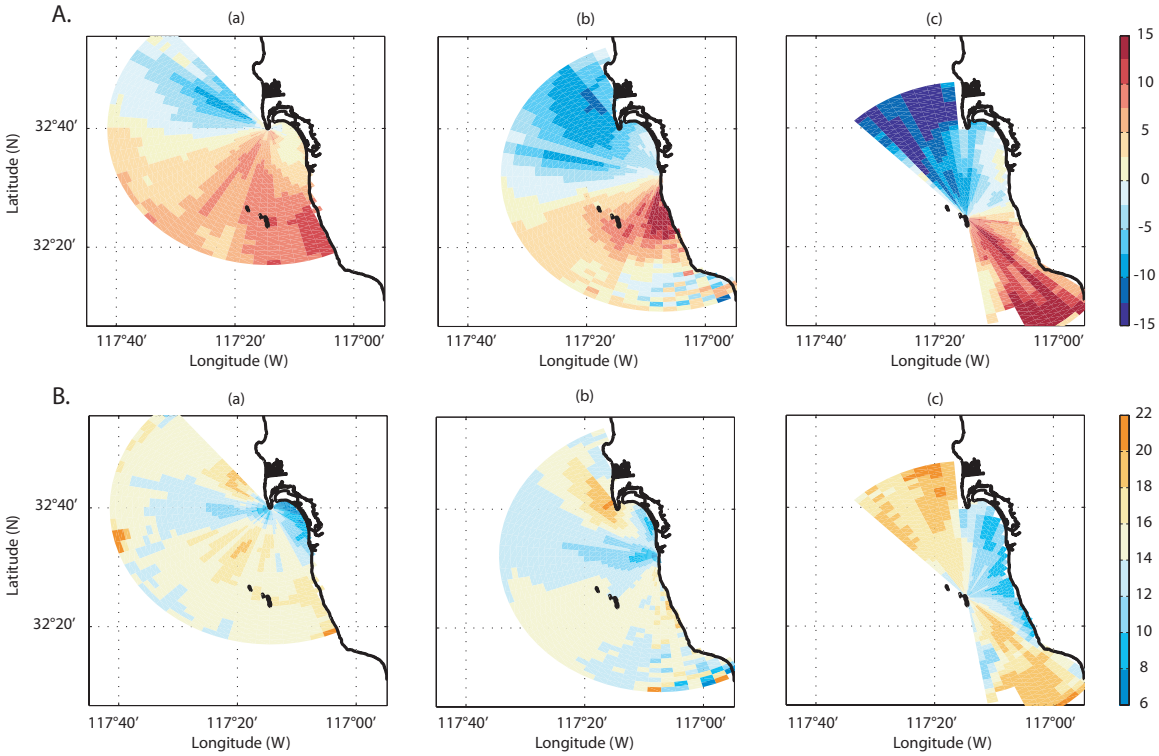

Figure 3.3: A. The time mean of the radial velocities ($\mathrm{cm\,s^{-1}}$). A negative (positive) velocity indicates the flow toward (away from) the radar. B. The standard deviations of the radial velocities ($\mathrm{cm\,s^{-1}}$). Column (a): SDPL. Column (b): SDBP. Column (c): SDCI.

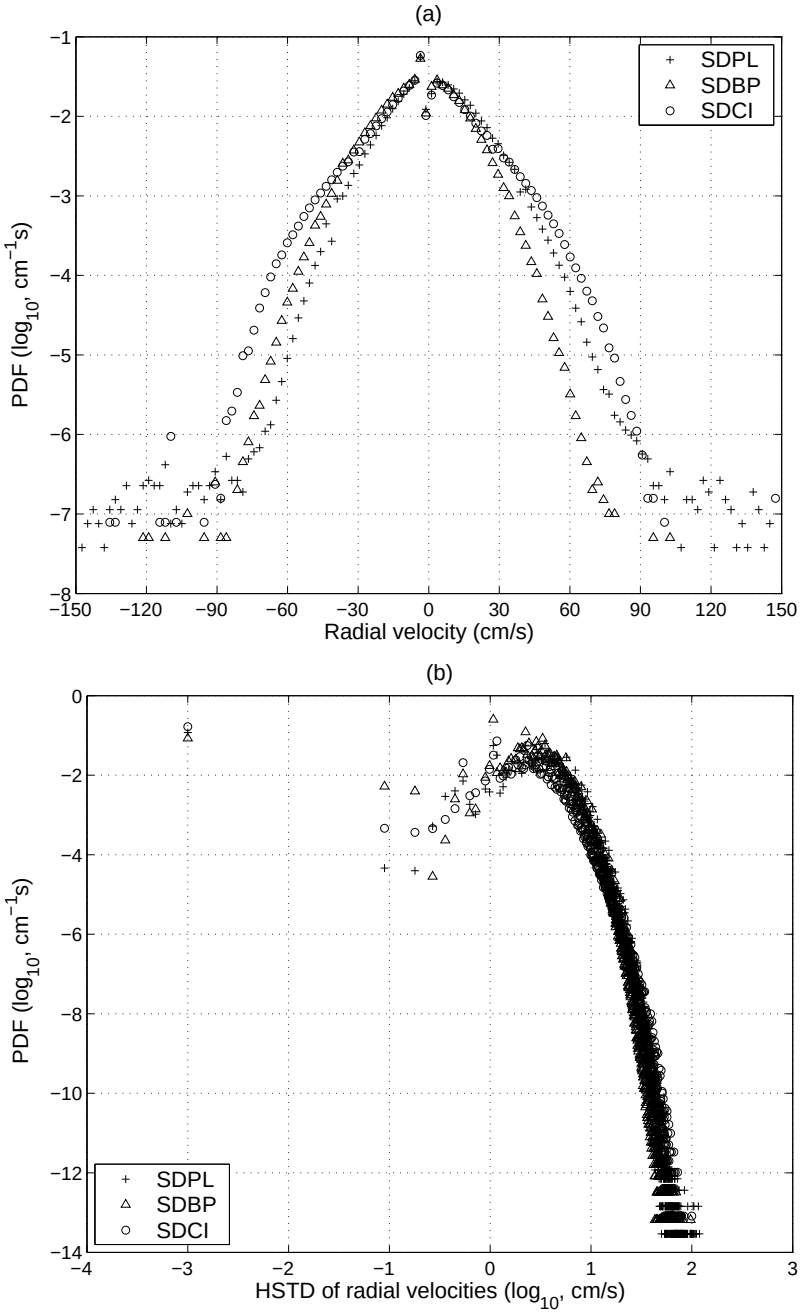

Figure 3.4: Probability density functions (PDFs) of (a) the radial velocities and (b) their hourly standard deviations (HSTDs) at each radar site during the 2-year study period (April 2003–March 2005).

The PDFs in log scale of the HSTD of the radial velocities are shown in Figure 3.4b. The optimal histogram bin size (w) of the HSTD is given by the formula ([Scott(1979)])

$$w = 3.49ab^{-1/3}\,, \tag{3.42}$$

where a and b denote the standard deviation of the HSTD and the number of available HSTD, respectively. The optimal histogram bin sizes are 0.07, 0.06, and 0.09 cm s^{-1} for each site. Most of the HSTD vary between 0.5 and 5 cm s^{-1}, with upper bounds of about 120 cm s^{-1}. The means of the HSTD are 5.47, 4.65, and 4.64 cm s^{-1} for each site. The mean HSTD is an estimate of the error variance of the surface currents. Since the number of samples (N) in each HSTD estimate is only known in a range ($1 \leq N \leq 6$), we assume that the time-dependent standard error is about 9 cm^2 s^{-2} as a constant, corresponding to $N = 3$.

The spatial and temporal distributions of radial velocities with magnitudes greater than 90 cm s^{-1} are shown in Figures 3.5a and 3.5b, respectively. They are located in the distant range bins of SDPL and SDCI sites and along the edge of the azimuthal bin of the measured beam pattern of SDCI site. Some of the radial velocities with large magnitude in SDBP site may not necessarily be outliers. The occurrences of outliers are more frequent during the winter than the summer.

The two-dimensional joint PDF of radial velocities (r) and their HSTDs (ϵ) at each radar site shows that there is no significant correlation between them:

$$P(r, \epsilon) \approx P(r)P(\epsilon). \tag{3.43}$$

The HSTDs of the radial velocities with magnitudes less than 30 cm s^{-1} have roughly chi-square distributions.

3.3.3 Validation of radial velocities

One method for determining the uncertainty of the radar measurements is the comparison of nearby radial velocities from two radars. Three requirements are recommended to find the pairs of radial velocities for this validation: The radar grid points where the radial velocities are measured are nearly collinear with the radar sites, separated by less than the radar range resolution, and nearly equidistant from the two sites. In the ideal case where the vector current is the same in both radar cells (or at coincident radar grid points), the correlation coefficients of those pairs would be a function of the difference between bearing angles. The two radial velocity measurements are

$$r_1(t) = \mathbf{g}_1^{\mathrm{T}}\mathbf{u}_1(t) + \epsilon_1(t) = u_1(t)\cos\theta_1 + v_1(t)\sin\theta_1 + \epsilon_1(t), \tag{3.44}$$

$$r_2(t) = \mathbf{g}_2^{\mathrm{T}}\mathbf{u}_2(t) + \epsilon_2(t) = u_2(t)\cos\theta_2 + v_2(t)\sin\theta_2 + \epsilon_2(t), \tag{3.45}$$

where r_i denotes the measured radial velocity, $\mathbf{g}_i = [\cos\theta_i \;\; \sin\theta_i]^{\mathrm{T}}$ is the directional unit vector, θ_i is the bearing angle, ϵ_i is the radial measurement error at the ith radar, and $\mathbf{u}_i = [u_i \;\; v_i]^{\mathrm{T}}$ is the vector components of the surface current, so $\mathbf{g}_i^{\mathrm{T}}\mathbf{u}_i$ is an inner product ($i = 1, 2$). Assuming the measurement errors are independent ($\langle\epsilon_1\epsilon_2^{\mathrm{T}}\rangle = 0$), the covariance of a pair of radial velocities is

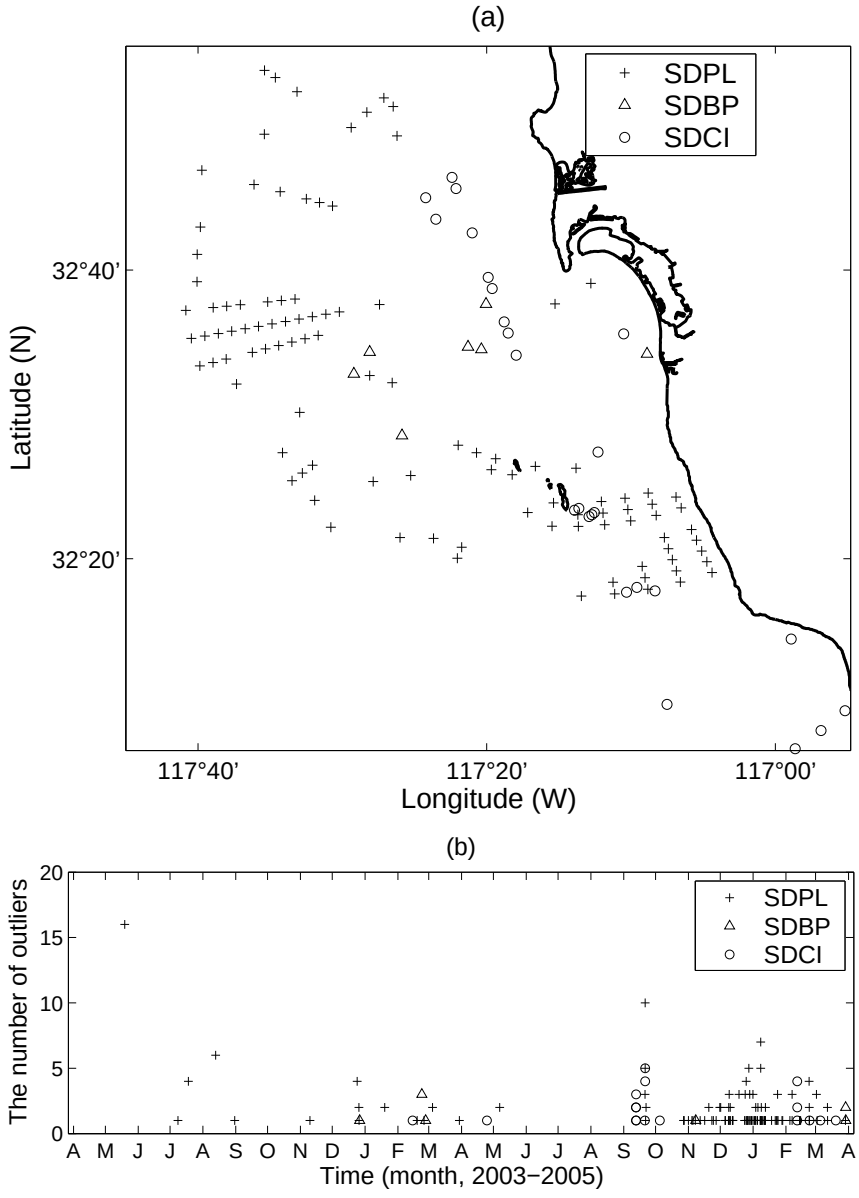

Figure 3.5: (a) The spatial distribution and (b) the temporal occurrence of radial velocities with magnitudes greater than 90 cm s^{-1}.

$$\langle r_1 r_2^{\mathrm{T}} \rangle = \mathbf{g}_1^{\mathrm{T}} \langle \mathbf{u}_1 \mathbf{u}_2^{\mathrm{T}} \rangle \mathbf{g}_2 = \begin{bmatrix} \cos\theta_1 & \sin\theta_1 \end{bmatrix} \langle \mathbf{u}_1 \mathbf{u}_2^{\mathrm{T}} \rangle \begin{bmatrix} \cos\theta_2 \\ \sin\theta_2 \end{bmatrix}. \tag{3.46}$$

If $\langle \mathbf{u}_1 \mathbf{u}_2^{\mathrm{T}} \rangle = \sigma^2 \mathbf{I}$, so u and v are independent with same variance, then the covariance is

$$\langle r_1 r_2^{\mathrm{T}} \rangle = \sigma^2 \left(\cos\theta_1 \cos\theta_2 + \sin\theta_1 \sin\theta_2 \right) = \sigma^2 \cos(\theta_1 - \theta_2). \tag{3.47}$$

Converting the covariance to the correlation coefficient,

$$\rho(r_1, r_2) = \frac{\langle r_1 r_2^{\mathrm{T}} \rangle}{\sqrt{\langle r_1^2 \rangle} \sqrt{\langle r_2^2 \rangle}} = \frac{\sigma^2}{\sigma^2 + \gamma^2} \cos(\theta_1 - \theta_2), \tag{3.48}$$

where $\langle r_1^2 \rangle = \langle r_2^2 \rangle = \sigma^2 + \gamma^2$ and $\langle \epsilon_1^2 \rangle = \langle \epsilon_2^2 \rangle = \gamma^2$.

From the observed radial velocities, 58 pairs are selected for which the distance between the pair of radar grid points is less than 150 m, which is a tenth of the range resolution (Δs). The correlation coefficients of these pairs with two years time span are shown as a function of the difference between bearing angles in Figure 3.6a. They are distributed somewhat like the cosine function of the difference of the bearing angles ($\gamma^2 = 0$), which is the expected value for ideal radial velocity measurements.

In a similar way, the averaged measurement uncertainty (γ^2) of the radial velocity can be estimated by assuming that two radial velocities (r_1 and r_2) are measured by two different radars at the same time for the same current field (equations 3.44 and 3.45):

$$u_1 = u_2 = u \text{ and } v_1 = v_2 = v. \tag{3.49}$$

The variance of the sum of the two radial velocities is a function of the difference of the bearing angle if u and v are independent:

$$\langle (r_1 + r_2)^2 \rangle = \langle u^2 \rangle \left(\cos\theta_1 + \cos\theta_2 \right)^2 + \langle v^2 \rangle \left(\sin\theta_1 + \sin\theta_2 \right)^2 + \langle \epsilon_1^2 \rangle + \langle \epsilon_2^2 \rangle. \tag{3.50}$$

If the current variance and the error variance in the x- and y-directions are the same (isotropic current field), respectively:

$$\langle u^2 \rangle = \langle v^2 \rangle = \sigma^2 \text{ and } \langle \epsilon_1^2 \rangle = \langle \epsilon_2^2 \rangle = \gamma^2, \tag{3.51}$$

the variance of the sum of the radial velocities is

$$\langle (r_1 + r_2)^2 \rangle = 4\sigma^2 \cos^2 \left(\frac{\theta_1 - \theta_2}{2} \right) + 2\gamma^2, \tag{3.52}$$

where $\sqrt{2}\gamma$ is the RMS error of the sum of oppositely-directed radial velocities ($|\theta_1 - \theta_2| = \pi$). From the observations of the nearby radial velocity pairs, the current variance and the error variance are estimated using least-squares fitting, and their square roots are 13.5 and 5.5 cm s^{-1}, respectively (Figure 3.6b). Although this assumes the surface current field has uniform and unpolarized variability, these can be used as the averages for the radial velocity measurements in the study domain. Therefore the average measurement uncertainty of the radial velocity (γ^2) is assumed to be 30 cm^2 s^{-2}.

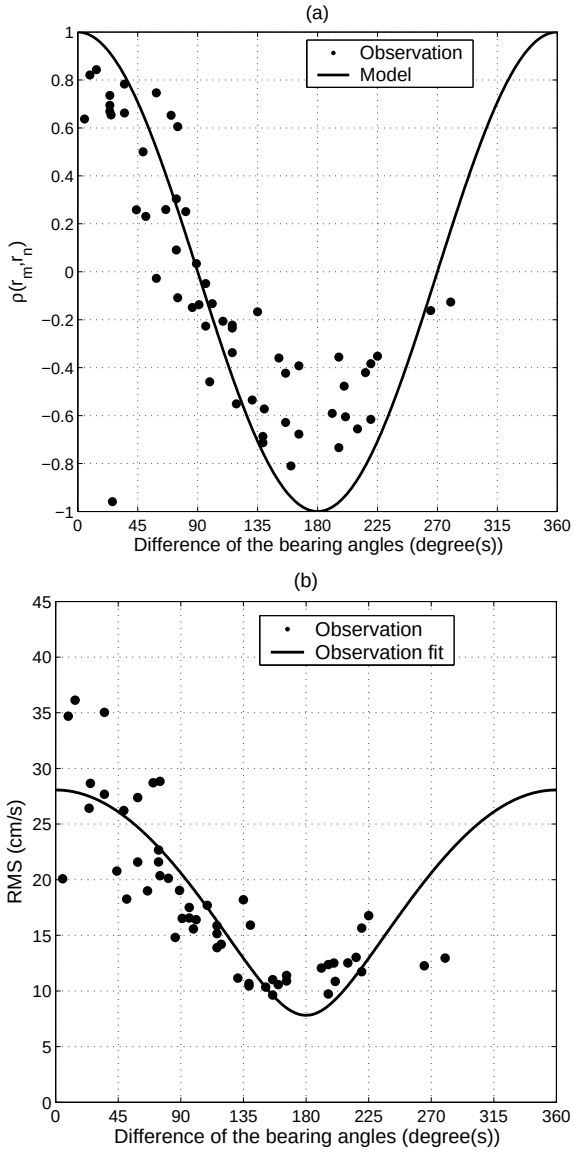

Figure 3.6: (a) Correlation coefficients of 58 radial velocity pairs $(\mathbf{r}_n, \mathbf{r}_m)$ nearby radar grid points (points separated by less than 150 m) and the model correlation coefficients as a cosine function of the difference between bearing angles ($\gamma^2 = 0$). (b) The variance of the sum of nearby radial velocity pairs is fitted with a cosine square function, and the RMS error of the sum of the oppositely-directed radial velocities is 7.8 cm s^{-1} ($\gamma = 5.5$ cm s^{-1}). The difference of the bearing angles is measured as the degrees clockwise from one bearing angle to the other.

Table 3.1: The comparisons of the singularity in the inversion of the covariance matrix and the structure of the correlation function for the UWLS, WLS, and OI methods.

	UWLS	WLS	OI
singularity	singular	nonsingular	nonsingular
correlation function	uniform	uniform	nonuniform

3.4 Results

Un-weighted least-squares fitting (UWLS), weighted least-squares fitting (WLS), and optimal interpolation (OI) are applied to the hourly radial velocities over a one month period (May 2004) in order to examine the estimated vector currents (section 3.4.3), their uncertainties (section 3.4.4), the effects of angular interpolation (section 3.4.5), and the calculation time and noise levels (section 3.4.6) under the assumed parameters. This one month data set has fewer missing data than those during other time periods, which allows a better estimate of the vector current and gives an upper bound on calculation time. The three methods are classified by the nature of the singularity in the inversion of the covariance matrix and the structure of the correlation function (Table 3.1).

3.4.1 Parameter selection

The search radius (d_0) in the UWLS and WLS methods is set to 1.5 km, which is the same as the radar range resolution (Δs). The segmented correlation function is shown in Figure 3.7a. The signal variance (σ_s^2) for the UWLS method is infinite and the error variance (σ_r^2) is implied as 1 $\mathrm{cm^2\ s^{-2}}$ from $\mathbf{R} = \mathbf{I}$ (equation 3.5). In the WLS method, the signal variance and the error variance are assumed the same as the OI method as below.

The correlation function for the OI method is chosen as an exponential function based on the spatially averaged correlation coefficients of surface currents (Figures 2.8, 2.12, and 5.14A). In order to avoid smoothing the estimated current field, the decorrelation length scales of the spatially averaged correlation coefficients ares considered to be an upper bound, which are 10–14 km in u and 16–35 km in v. The decorrelation length scales (λ_x and λ_y) in the x- and y-directions of the correlation function in the OI method are chosen to be 2 km, respectively, twice of the 1 km vector grid resolution (Δx and Δy). The vector current estimated using the exponential correlation function is less sensitive to the decorrelation length scale than that with Gaussian correlation function, because the exponential correlation falls off more quickly from the center. The exponential correlation function is shown in Figure 3.7b. For simplicity in the estimate of the surface current field the decorrelation length scales are assumed as a constant in space and all frequency bands. The variation of decorrelation length scales in space and frequency bands can be addressed with the complete dataset of estimated vector currents.

The search radius (d_0) in the OI method is 5 km, at which range the correlation is 0.08, which can be considered to be a reasonably small spatial weighting. The signal variance (σ_s^2) and the

error variance (σ_r^2) are assumed to be 400 and 40 $\mathrm{cm^2\,s^{-2}}$, respectively, constant over the observation domain. The error variance (σ_r^2, equation 3.17) is the sum of the average measurement uncertainty ($\gamma^2 \approx 30$ $\mathrm{cm^2\,s^{-2}}$, section 3.3.3) and the average standard error of the surface currents ($\epsilon^2/N \approx 9$ $\mathrm{cm^2\,s^{-2}}$, section 3.3.2). This tends to overestimate the error variance because the average standard error contributes to the average measurement uncertainty, and this produces estimates that err on the side of smoothness.

3.4.2 Radial velocities

The PDFs of the radial velocities measured by each radar site during a one month period (May 2004) are shown in Figure 3.8. Most radial velocities have magnitudes less than 70 $\mathrm{cm\,s^{-1}}$. One radial velocity with magnitude greater than 90 $\mathrm{cm\,s^{-1}}$ was measured by the SDPL site. The bin size of PDFs is the same as the resolution of radial velocity (Δr). The PDFs also show consistent discontinuities where the magnitude of radial velocity is less than 2 $\mathrm{cm\,s^{-1}}$ (Figure 3.4a).

3.4.3 Extracted vector currents

The PDFs of the vector current components (u and v) estimated using the UWLS, WLS, and OI methods without angular interpolation are compared in Figure 3.9 (Section 3.4.5 will explore the effects of angular interpolation of the radial velocity before mapping). The PDFs of the estimated vector components using the OI method are almost the same as the PDFs of radial velocities during the same period (Figure 3.8). However, the PDFs of the estimated vector components using the least-square fitting (WLS and UWLS) methods deviate from the PDFs of the OI method at a current magnitude of about 45 $\mathrm{cm\,s^{-1}}$. These vector components take up about 0.8 and 1.6% (UWLS) and 0.1 and 0.2% (WLS) of the number of total vector components for u and v, respectively. They are clustered in the areas having higher GDOP, which are the edges of the coverage of radars and the baselines. The WLS method removes the singularity of the geometric covariance matrix, but is still vulnerable to large errors in the radial velocities. Using a larger search radius in the WLS method reduces them, but generates too smooth a current field. The OI result is less sensitive to the error variance because of the larger averaging region. The OI method yields significantly more zero magnitudes than the UWLS and WLS methods, because the estimator tends to zero where there is insufficient data.

An arbitrarily chosen example of a vector current field estimated from the radial velocities using the UWLS and OI methods is shown in Figures 3.10a and 3.10b. When the number of radial velocities at a given vector grid point is insufficient to extract the vector current (e.g., near baselines and at the edges of the observation domain), the UWLS approach consistently yields inconsistent vectors as shown in Figure 3.10a, and the OI method tapers the solutions toward zero as shown in Figure 3.10b. The effective coverage area, defined by the spatial region in which vector solutions are generated, is found to vary with the mapping method, with the OI method yielding 30–40% more vector current solutions than the UWLS method when using the same input data sets. In

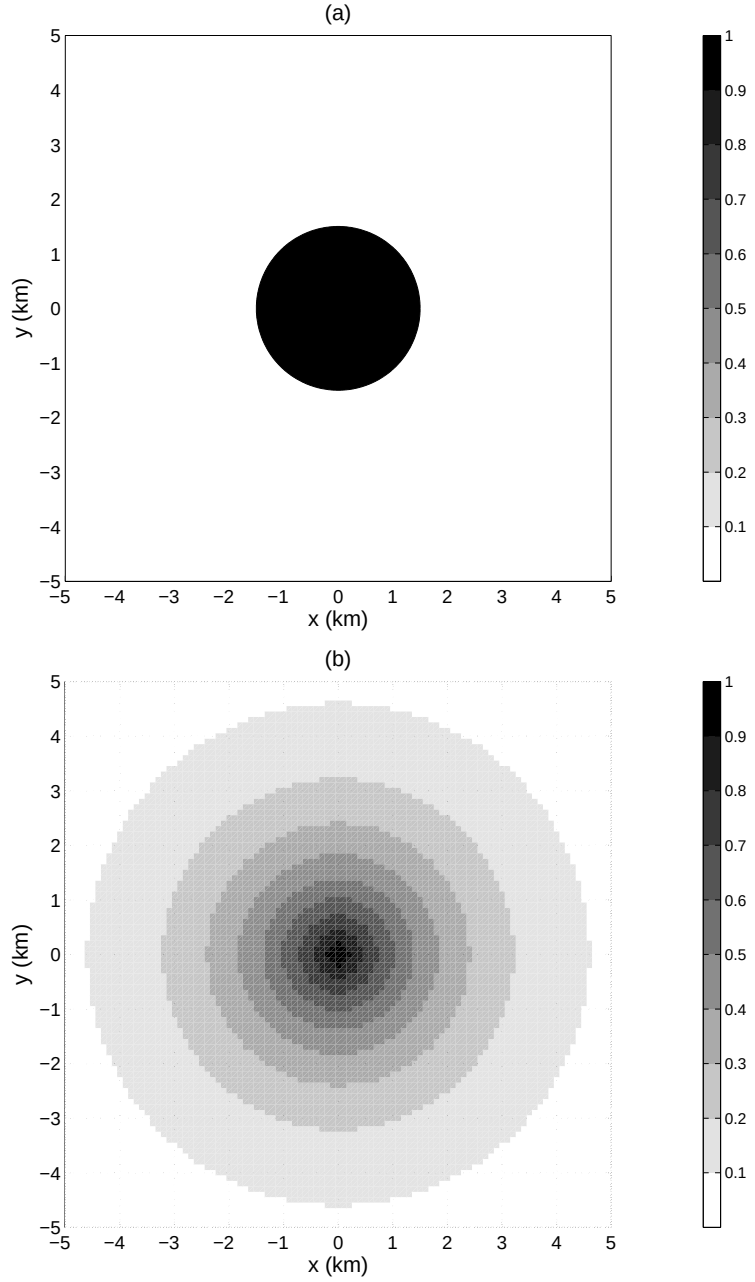

Figure 3.7: The spatial correlation functions in (a) least-squares fitting (UWLS and WLS) ($d_0 = 1.5$ km) and (b) optimal interpolation (OI) ($d_0 = 5$ km and $\lambda_x = \lambda_y = 2$ km).

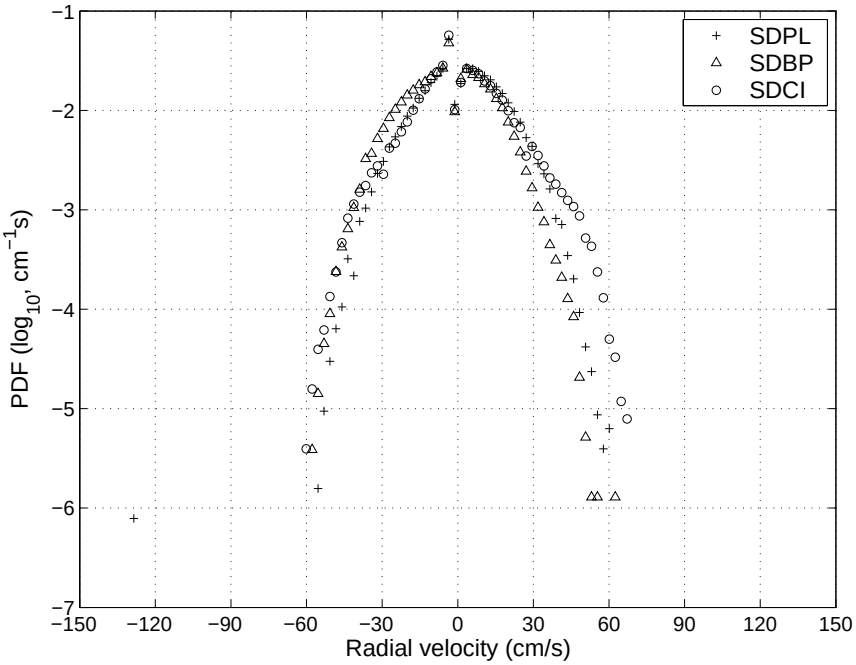

Figure 3.8: PDFs of the radial velocities at each radar site during one month (May 2004).

addition, the OI method generates smoother current fields than the UWLS method. The number and magnitude of the outliers along the baselines (SDBP and SDPL, SDPL and SDCI) are reduced in the current field estimated by the OI method, because of the non-singularity in the matrix inversion due to the added error variance and the contribution of the non-parallel radial velocities within the search radius. Although the baseline consistency can be improved in the WLS method, its correlation function is segmented and differs from the observed correlation.

An example of vector current time series estimated using the UWLS and OI methods is shown in Figure 3.11. The location of the grid point is 32°35.72′N 117°10.56′W, which is on the baseline between SDPL and SDBP sites in a nearshore region with about 20 m water depth. The vector components estimated using the UWLS method have both missing and spurious data. On the other hand, the vector components estimated using the OI method show the smoothly-varying current variance and improved consistency on the baseline.

A series of maps estimated using the OI method with the actual HSTD for each radar cell at each time did not seem to differ greatly from the maps estimated with the assumed error variance. However, the OI method using the actual HSTD enables us to make the most use of the available observations.

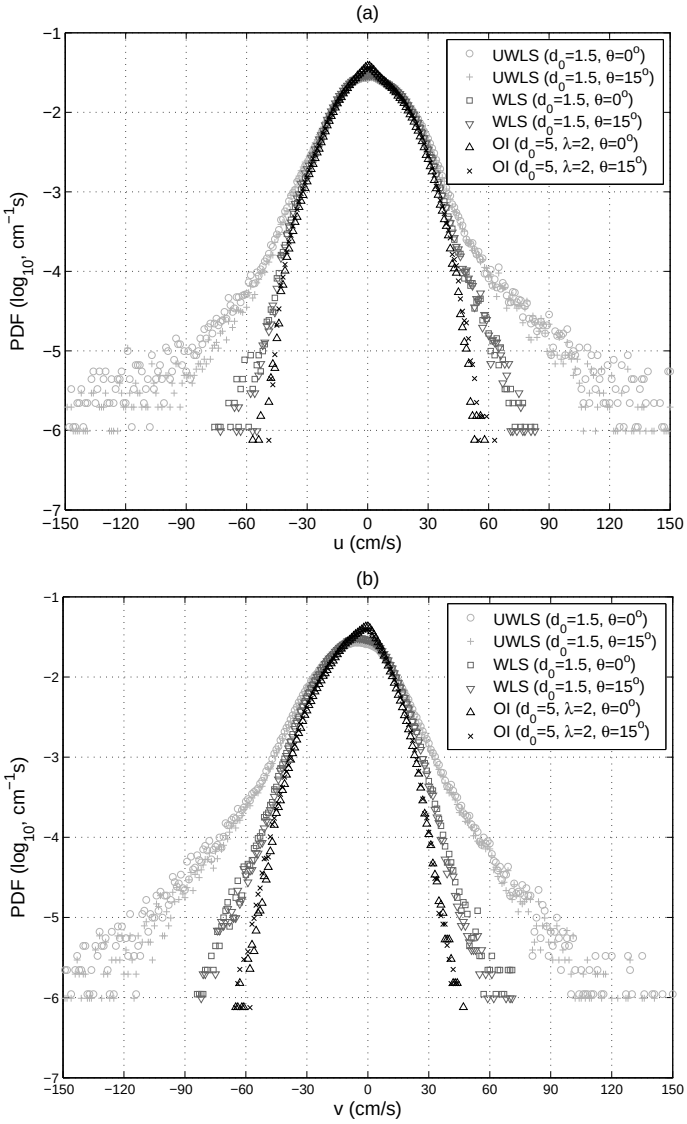

Figure 3.9: PDFs of the vector current components (u and v) estimated from the radial velocities during one month (May 2004) using each method (UWLS, WLS, and OI). d_0 denotes the search radius and θ is the swath width for angular interpolation (No angular interpolation is done, if θ is equal to zero degree). (a) u-component. (b) v-component.

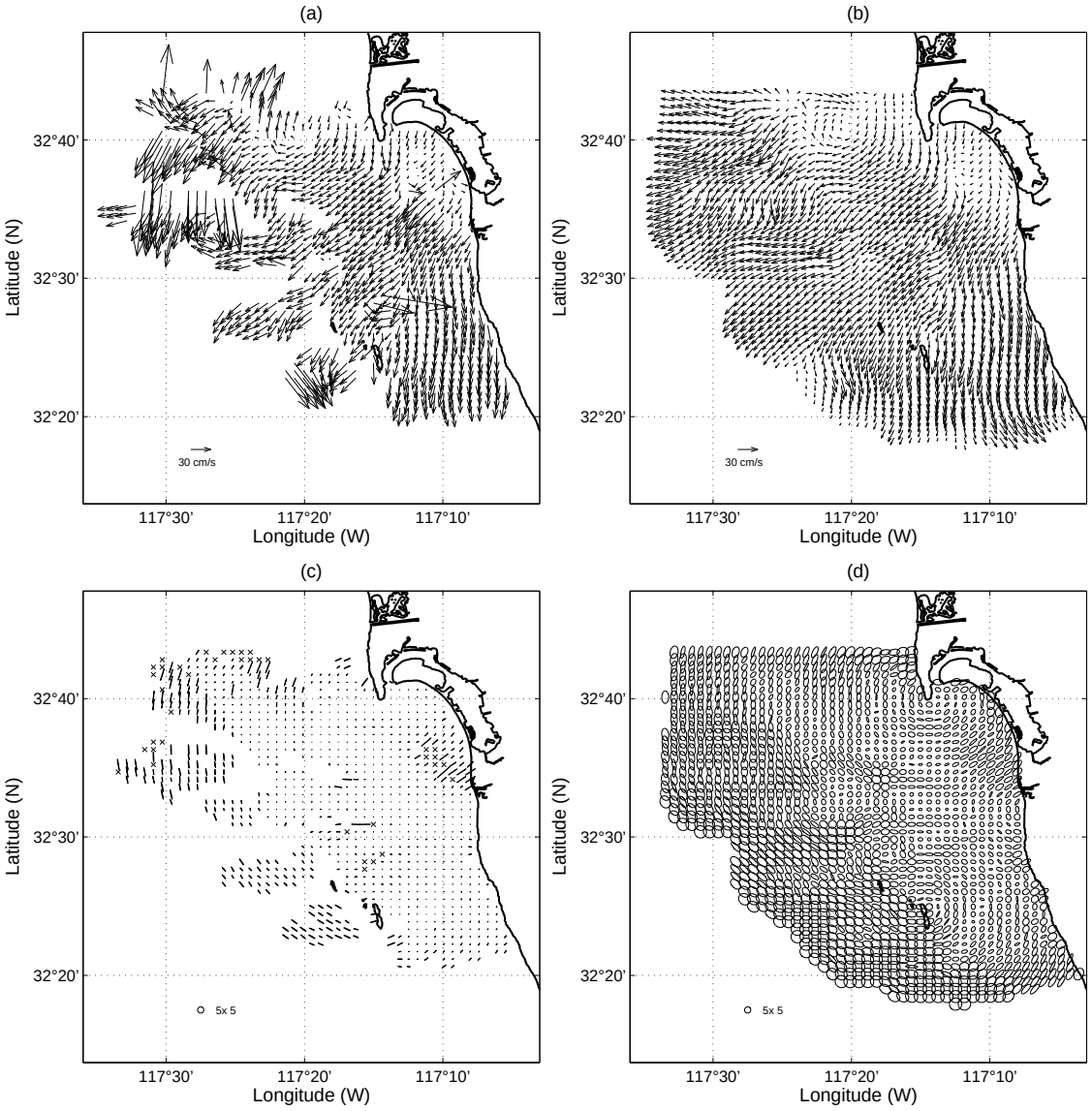

Figure 3.10: An example of the surface vector current field estimated using (a) the UWLS method ($d_0 = 1.5$ km) and (b) the OI method with the assumed error covariance matrix ($d_0 = 5$ km, $\lambda_x = \lambda_y = 2$ km, $\sigma_s^2 = 400$ cm^2 s^{-2}, and $\sigma_r^2 = 40$ cm^2 s^{-2}). (c) and (d) are normalized uncertainty ellipses corresponding to (a) and (b), respectively. The vector grid points having the error level greater than the cut-off error level are indicated with cross marks.

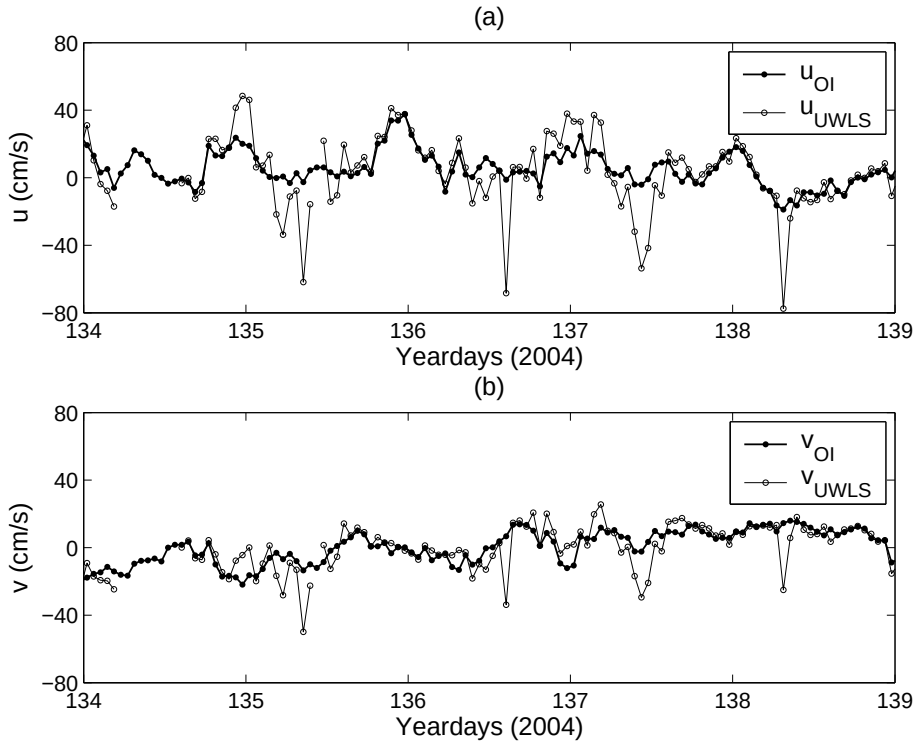

Figure 3.11: An example of the vector current time series estimated using the OI (closed) and UWLS (open) methods. The grid point is located at 32°35.72′N 117°10.56′W, which is the one of grid points on the baseline between SDPL and SDBP sites in a nearshore region with about 20 m water depth. (a) u-component. (b) v-component.

3.4.4 Uncertainties

The uncertainty in the surface current measurements of the high-frequency radar usually results from the observation errors, the vector current estimation, and the radar system itself such as the misalignment and the poor radar frequency signal-to-noise-ratio ([Graber et al.(1997), Lipa(2003)]). The uncertainty estimated from the comparison with independent in-situ observations is not included in this chapter; the discussion focuses on how the uncertainty of the radial velocities is propagated into the uncertainty of the vector currents.

Since the error variances (σ_r^2) in the UWLS and OI methods are 1 and 40 $\mathrm{cm^2\,s^{-2}}$, respectively, a re-scaling of uncertainty is required to compare the uncertainties ($\boldsymbol{\varphi}$) of the UWLS and OI methods (equations 3.33 and 3.32). Three normalized uncertainty components (φ^{uu}, φ^{vv}, and φ^{uv}) are illustrated with ellipses in Figures 3.10c and 3.10d. The cross term (φ^{uv}) provides the directional uncertainty. The cut-off error level, which is defined by the ratio of the a posteriori uncertainty matrix ($\hat{\mathbf{P}}$) to the expected observational error variance (σ_r^2), is used as the upper limit of the normalized uncertainty in the UWLS method. The vector grid points having errors greater than the cut-off error level are indicated by the cross marks in Figure 3.10c, and are typically near baselines and at the edges of the radar coverage region. The ellipses in Figure 3.10d are larger than those in Figure 3.10c, which shows that the OI method has greater uncertainty. However, the uncertainties of the UWLS and OI methods have different statistics (e.g., PDFs as shown in Figure 3.12) based on different signal and error variance assumptions. In other words, the uncertainty ($\boldsymbol{\varphi}$) normalized by the error variance is only comparable at the lower uncertainty levels, and differs at the higher levels. The normalized uncertainty in the UWLS and OI methods varies from zero to infinity and from zero to the ratio of the signal variance to the error variance, respectively.

The two-dimensional joint PDFs of the normalized uncertainty and estimated vector current components (u and v) for the UWLS and OI methods are shown in Figure 3.12. The normalized uncertainties greater than the cut-off error level in the UWLS method are not shown in Figures 3.12a and 3.12b, and take up about 1.3 and 3.6% of the number of total vector current solutions during a month for u and v, respectively. There is no obvious relationship between the normalized uncertainty and the magnitude of the estimated current components. However, the outliers due to singularity of the geometric covariance matrix in the UWLS method have higher normalized uncertainty (Figures 3.12a and 3.12b). The current components with higher uncertainty in the OI method are clustered near zero magnitude (Figures 3.12c and 3.12d). This is an important positive feature of the OI method.

A new set of uncertainty indices ($\hat{\boldsymbol{\chi}}$), comprised of three components ($\hat{\chi}^{uu}$, $\hat{\chi}^{vv}$, and $\hat{\chi}^{uv}$) of the a posteriori uncertainty matrix normalized by the signal variance (σ_s^2), have values approaching zero for an estimate with zero uncertainty and one for an estimate with no information. The ellipse can be tilted, which represents the directional uncertainty that results from the GDOP at a given vector grid point. The uncertainty indices ($\hat{\chi}^{uu}$ and $\hat{\chi}^{vv}$) in the UWLS method have Rayleigh distributions, which typically represent two orthogonal components with normal and independent

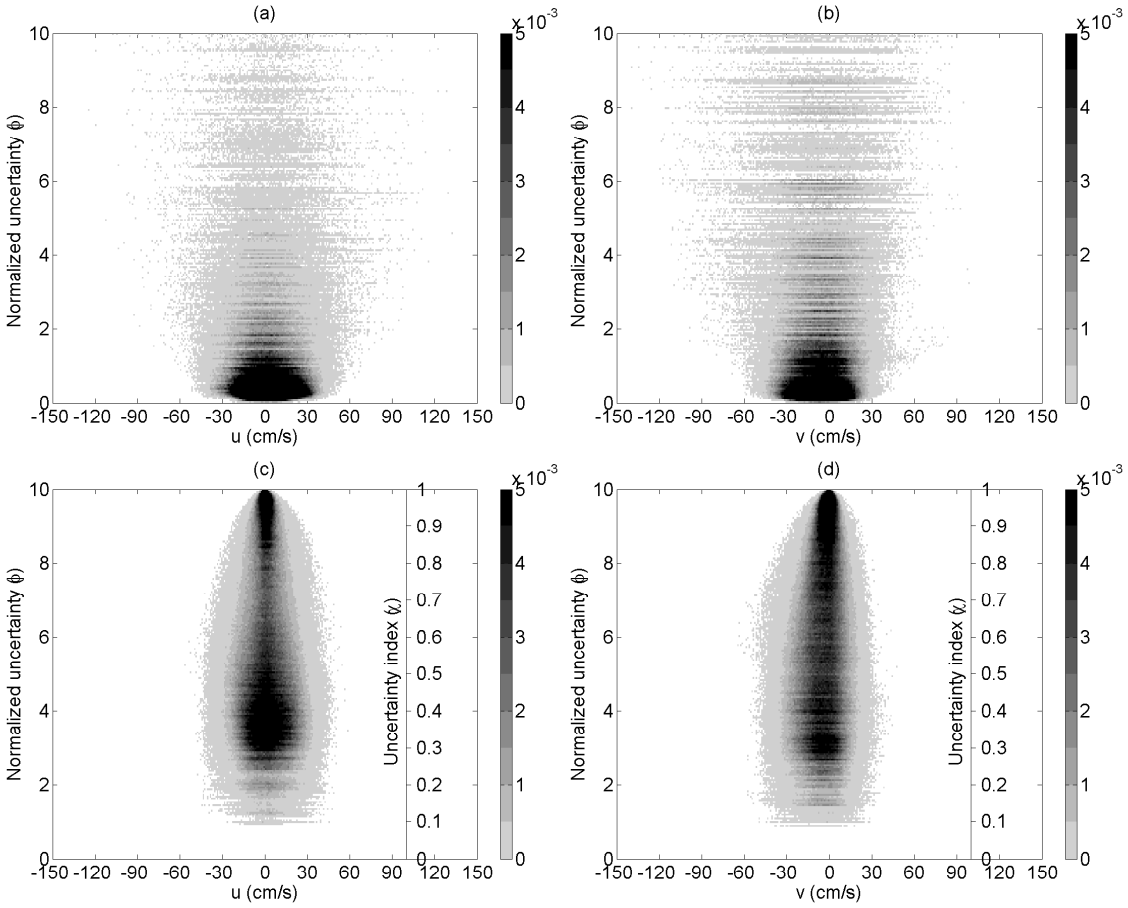

Figure 3.12: The two-dimensional joint PDFs of the vector current components (u and v) and their normalized uncertainties (φ^{uu} and φ^{vv}) during one month (May 2004). The assumed axis is for the uncertainty index ($\hat{\boldsymbol{\chi}}$). (a) φ^{uu} and u (UWLS). (b) φ^{vv} and v (UWLS). (c) φ^{uu} and u (OI). (d) φ^{vv} and v (OI).

distributions. The uncertainty indices ($\hat{\chi}^{uu}$ and $\hat{\chi}^{vv}$) in the OI method have uneven bimodal distributions, which have a higher peak near the center and a lower peak at the end, and the cross-term ($\hat{\chi}^{uv}$) has an exponential distribution. Moreover, the uncertainty indices vary in time except that higher uncertainty indices occur consistently around baselines and at the edges of the domain.

3.4.5 Effects of angular interpolation

A commonly-used process to fill gaps in MUSIC-derived radial velocity data is to interpolate (or average) across a 15-degree swath using a boxcar filter. The vector currents estimated from the radial velocities preprocessed with a 15 degree angular interpolation as well as their uncertainties were considered on the UWLS and OI methods during the analysis period. Angular interpolation increases the spatial extent of the vector currents estimated by the UWLS method. For example, the 15 degree angular interpolation typically increases the number of good estimates by 10%. However, angular interpolation is found not to generate any appreciable change in spatial coverage for the OI method. In addition, angular interpolation is not consistent with the assumptions of the statistics of the field, and does not provide the uncertainty (HSTD).

3.4.6 Calculation time and noise levels

The calculation time for each method (UWLS, WLS, and OI) to estimate the hourly vector current field is shown in Figure 3.13. On a per-grid-point perspective, the calculation time depends on the size of the square matrix to be inverted, which is equal to the number of available radial velocities within the defined search radius in the OI method and two in the least-squares fitting (UWLS and WLS) method (geometric covariance matrix in equation 3.6). For a dual Xenon 3.2 GHz processor computer with 2 gigabytes of RAM, the OI method takes about 0.0125 seconds per grid point, which is approximately three times longer than the least-squares fitting method. The calculation time of the OI method is reasonable for modern computers dedicated to real-time monitoring of hourly surface currents.

In order to examine the high frequency noise, the regionally averaged power spectra of vector current magnitudes estimated using the UWLS, WLS, and OI methods in areas with low and high fractional data availabilities (45 and 90%) over the one month period are shown in Figures 3.14a and 3.14b, respectively. At high frequencies (greater than 8 cycles per day, cpd), the power spectrum of the OI method goes flat at about 10 cpd, while that of the UWLS method is closer to about 8 cpd. However, the amount of the variance at frequencies less than 2.5 cpd, which explains most of the variance of the surface currents in the study domain, is almost identical for all three methods.

We assume that the difference between UWLS and WLS is only significant for incompatible or poorly determined points (e.g. the vector currents estimated in the poor GDOP areas), so the difference between these spectra should represent errors. The difference between WLS and OI results from both noise and small scale variance removed by spatial smoothing. We also assume that the

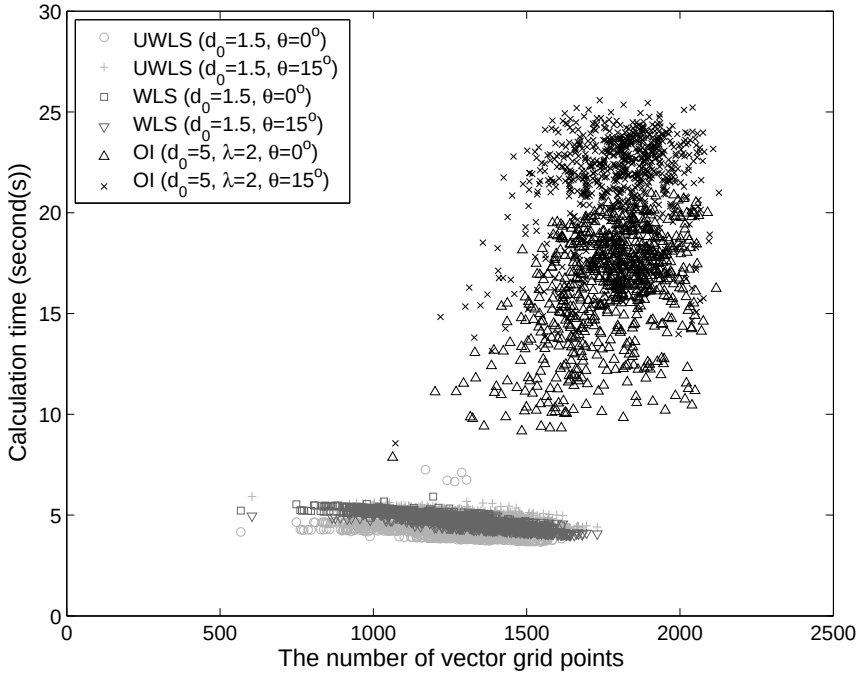

Figure 3.13: The calculation time and the number of vector grid points resolved from the radial velocities during one month (May 2004) using each method (UWLS, WLS and OI). d_0 denotes the search radius and θ is the swath width of angular interpolation (No angular interpolation is done, if θ is equal to zero degree).

variances in the frequency band above about 6 cpd contain only noise. The average noise levels in the area with over 45% coverage are about 8.92, 3.51, and 1.44 $cm^2\,s^{-2}\,cpd^{-1}$ for the UWLS, WLS, and OI methods, respectively, which correspond to 10.34, 6.49, and 4.15 $cm\,s^{-1}$ standard deviations. The vector current data with 45% coverage have higher errors than the data with 90% coverage, because they have more missing data in areas of marginal coverage and have outliers. In the area of with 45% coverage, the power spectra of the WLS and OI methods differ above about 2 cpd, while in the 90% coverage region, they only differ above about 5 cpd. This suggests that the OI method is not significantly smoothing the current field and is reducing the noise level. The average noise levels in the area with over 90% coverage are 5.62, 4.48, and 3.82 $cm\,s^{-1}$, respectively. Thus the assumed error variance ($\sim$6.3 $cm\,s^{-1}$, section 3.4.1) is acceptable compared to the noise levels of the OI method in both cases (45 and 90% fractional data availabilities).

3.5 Discussion

In the computation of vector currents from radial velocities measured by multiple high-frequency radars, the optimal interpolation (OI) method is suggested as a method to replace the unweighted least-squares fitting (UWLS) method. The OI method uses realistic correlation functions and the HSTD of the radial velocities, resolves the baseline inconsistency, and provides statistically consistent and well-defined uncertainty and increased coverage area. Moreover, the OI method produces currents with a similar PDF to that of the PDF of the radial velocities. The power spectrum of vector currents estimated using the OI method shows a lower level of high-frequency noise than the UWLS method, which is consistent with the assumed error covariance.

The OI method can directly calculate the vector currents, the divergence and vorticity of surface currents from the radial velocities, and eliminate the need for multiple mapping steps for the subsequent applications of surface currents. The computational expense of the OI method is reasonable for supporting real-time observation system, even the size of Southern California (about 300×300 km^2 region). The continuity equation and boundary conditions can be applied as constraints of the OI method, but this is beyond the scope of this chapter.

Although the covariance matrix used for the OI method is often derived from an isotropic spatial correlation function, the observed (possibly smoothed) covariance matrix of the surface currents (section 2.4.3) can be used, or a covariance representing a sum of normal modes ([Lipphardt Jr. et al.(2000), Kaplan and Lekein(2007)]). The variability of the estimated vector currents is weakly sensitive to the assumptions of the cut-off error level and the decorrelation length scales of the correlation function. Lower cut-off error level and longer decorrelation length scales generate vector currents with the reduced variability and a spatially smoother field.

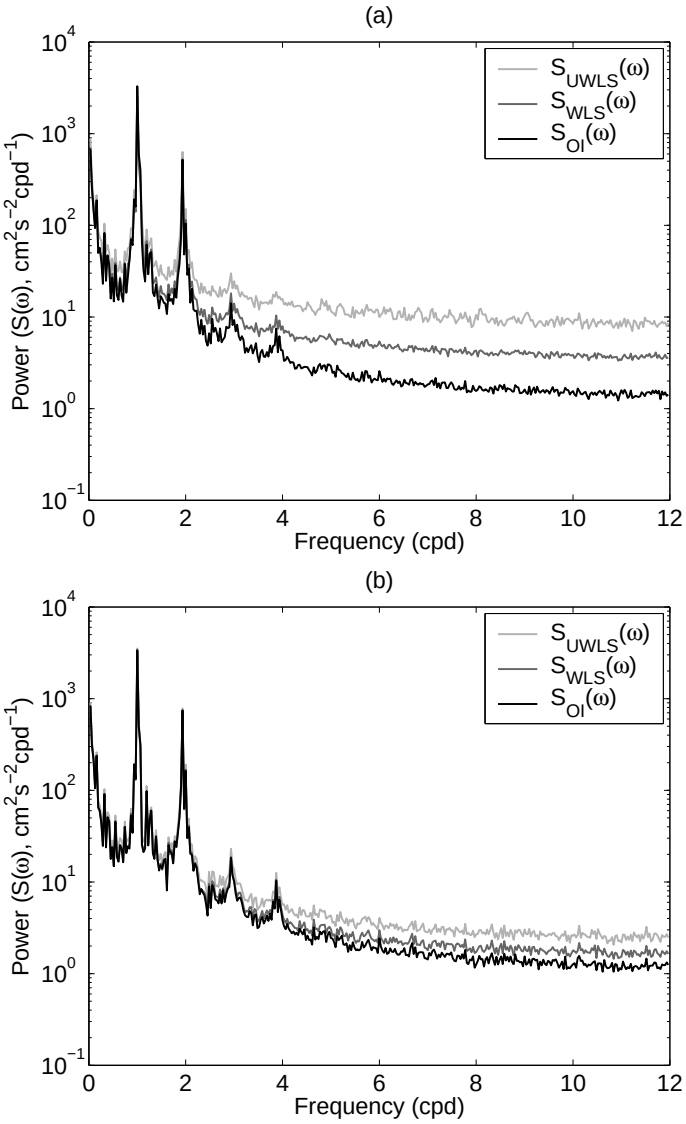

Figure 3.14: Regionally averaged power spectra of the surface vector current magnitudes estimated using the UWLS, WLS, and OI methods during the one month period (May 2004) over the area with (a) 45% fractional data availability (1337 vector grid points) and (b) 90% fractional data availability (510 vector grid points).

3.6 Appendix

3.6.1 Geometric dilution of precision (GDOP)

The geometric dilution of precision (GDOP) vector is defined as the diagonal components of the inverse of the geometric covariance matrix. The GDOP at a vector grid point generated by L radial velocities is

$$\left(\mathbf{G}_{\mathbf{a}}^{\mathrm{T}}\mathbf{G}_{\mathbf{a}}\right)^{-1} = \begin{bmatrix} \alpha_{uu} & \alpha_{uv} \\ \alpha_{vu} & \alpha_{vv} \end{bmatrix}, \tag{3.53}$$

where α_{uu} and α_{vv} are the GDOP components in the x- and y-directions (u and v), respectively, and α_r is the GDOP of the total current:

$$\alpha_{uu} = \frac{1}{\det\left(\mathbf{G}_{\mathbf{a}}^{\mathrm{T}}\mathbf{G}_{\mathbf{a}}\right)} \sum_{l=1}^{L} \sin^2\theta_l \geq \frac{1}{L}, \tag{3.54}$$

$$\alpha_{vv} = \frac{1}{\det\left(\mathbf{G}_{\mathbf{a}}^{\mathrm{T}}\mathbf{G}_{\mathbf{a}}\right)} \sum_{l=1}^{L} \cos^2\theta_l \geq \frac{1}{L}, \tag{3.55}$$

and

$$\alpha_r = \alpha_{uu} + \alpha_{vv} \geq \frac{4}{L} \tag{3.56}$$

(det denotes the determinant of the matrix). The GDOP depends on the number of available radial velocities within the search radius and their bearing angles. For an appropriate comparison of the GDOP, the GDOP should be normalized with the lowest GDOP in 2-dimensional space ([Levanon(2000)]). In the case of two radial velocities, the GDOP components are

$$\alpha_{uu} = \frac{\sin^2\theta_1 + \sin^2\theta_2}{\sin^2(\theta_1 - \theta_2)} \geq \frac{1}{2}, \tag{3.57}$$

$$\alpha_{vv} = \frac{\cos^2\theta_1 + \cos^2\theta_2}{\sin^2(\theta_1 - \theta_2)} \geq \frac{1}{2}, \tag{3.58}$$

and

$$\alpha_r = \frac{2}{\sin^2(\theta_1 - \theta_2)} \geq 2, \tag{3.59}$$

respectively. In the same way, the GDOP components by three radial velocities are

$$\alpha_{uu} = \frac{\sum \sin^2\theta_l}{\det\left(\mathbf{G}_{\mathbf{a}}^{\mathrm{T}}\mathbf{G}_{\mathbf{a}}\right)} \geq \frac{1}{3}, \tag{3.60}$$

$$\alpha_{vv} = \frac{\sum \cos^2\theta_l}{\det\left(\mathbf{G}_{\mathbf{a}}^{\mathrm{T}}\mathbf{G}_{\mathbf{a}}\right)} \geq \frac{1}{3}, \tag{3.61}$$

and

$$\alpha_r = \frac{3}{\det\left(\mathbf{G}_{\mathbf{a}}^{\mathrm{T}}\mathbf{G}_{\mathbf{a}}\right)} \geq \frac{4}{3}, \tag{3.62}$$

respectively. The GDOP in high-frequency radar measurements is more localized and time dependent due to the sparse solutions of the MUSIC algorithm compared to the GDOP in satellite remote sensing.

This chapter , in part, is a reprint of the material as it appears in *Journal of Geophysical Research-Oceans*, 2008, Kim, S. Y., E. J. Terrill, and B. D. Cornuelle titled by 'Mapping surface currents from HF radar radial velocity measurements using optimal interpolation', **113**, C10023, doi:10.1029/2006JC004244. The dissertation author was the primary investigator and author of this paper.

Chapter 4

Anisotropic response of surface currents to the wind in a coastal region

Abstract

Analysis of coastal surface currents measured off the coast of San Diego during two years suggests an anisotropic and asymmetric response to the wind, probably as a result of bottom/coastline boundary effects including pressure gradients. In a linear regression the statistically estimated anisotropic response explains approximately 20% more surface current variance than an isotropic wind-ocean response model. After steady wind forcing for 3 days, the isotropic surface current response veers 42 ± 2 degrees to the right of the wind regardless of wind direction while the anisotropic analysis suggests that the upcoast (onshore) wind stress generates surface currents with 10 ± 4 (71 ± 3) degrees to the right of the wind direction. The anisotropic response thus reflects the dominance of along-shore currents in this coastal region. Both analyses yield wind-driven currents with 3–5% of the wind speed as expected. In addition nonlinear isotropic and anisotropic response functions are considered, and the asymmetric current responses to the wind are examined. These results provide a comprehensive statistical model of the wind-driven currents in the coastal region, which has not been well identified in previous field studies, but is qualitatively consistent with descriptions of the current response in coastal ocean models.

4.1 Introduction

Surface current dynamics encompass a complex mixture of forcing terms including wind, tides, pressure gradients, and internal waves ([Ewing(1950), Munk and Cartwright(1966), Essen et al.(1983), Alpers(1985), Prandle(1987), Ng(1993a), Ng(1993b)]). Generally, the wind is a dominant driving source of energy for currents, which have been considered to have an isotropic response in the open ocean ([Ekman(1905), Gonella(1972), Weller(1981), Price et al.(1987), Rio and Hernandez(2003)]) and the coastal region ([Pidgeon and Winant(2005)]). The coastline and bottom topography produce horizontal pressure gradients and friction so that the coastal wind response of surface currents can depend on the wind direction. [Ekman(1905)] introduced this anisotropy by including pressure gradients in the analysis, and [Winant(2004)] has made three-dimensional calculations for basins with idealized topography. However, a complete wind-ocean response model to reflect this phenomena has not been addressed with observations.

The wind impulse response function (WIRF) provides a comprehensive representation of the link between the wind and currents from diurnal responses to upwelling events in the coastal region. The WIRF in the frequency domain ($\mathbf{H}$) is defined as the ratio of the Fourier coefficients of the current ($\hat{\mathbf{u}}$) to wind stress ($\hat{\boldsymbol{\tau}}$) at each frequency:

$$\mathbf{H}(z,\omega) = \frac{\hat{\mathbf{u}}(z,\omega)}{\hat{\boldsymbol{\tau}}(\omega)}. \tag{4.1}$$

[Gonella(1972)] derived the WIRF and its phase relationship at infinite and finite depth, and [Weller(1981)] observed the current shear and matched it with the Ekman theory. [Rio and Hernandez(2003)] investigated the surface currents estimated by drifting buoys and altimetry data along with atmospheric model (ECMWF) wind stress over the global ocean. These studies ([Gonella(1972), Weller(1981), Rio and Hernandez(2003)]) found a consistent phase relationship between surface currents and the wind. [Pidgeon and Winant(2005)] found negative phases between the diurnal currents and the diurnal wind at several moorings in the Santa Barbara Channel which were quantitatively consistent with previous studies. [Hyder et al.(2002)] used a depth-integrated slab model to examine the WIRF of the diurnal currents near the critical latitude where the response is resonant with the diurnal wind forcing.

The time domain WIRF ($\mathbf{g}$) between the wind stress ($\boldsymbol{\tau}$) and the current ($\mathbf{u}$) at a point is defined as a convolution ([Bendat and Piersol(2000)]):

$$\mathbf{u}(z,t) = \int_{t'} \mathbf{g}(z, t-t')\boldsymbol{\tau}(t')\,\mathrm{d}t'. \tag{4.2}$$

[Ekman(1905), Gonella(1971), Kundu(1984), Blackford(1978)] derived the time dependent current response for a step function wind using linear and slab models. [Lewis and Belcher(2004)] examined the time-dependent Ekman solutions coupled with Stokes drift using Laplace transforms to include evanescent solutions. [Prandle(1987), Essen(1993), Ng(1993a), Zelenke(2005), Rabinovich et al.(2006)] parameterized the observations of the wind stress and currents using linear/nonlinear models, and performed a time domain regression. Although [Ng(1993a)] and

[Rabinovich et al.(2006)] introduced the possibility of an anisotropic current response, the statistical models lacked physical interpretation and the difference in skill between isotropy and anisotropy was not explored.

[Li and Weisberg(1999), Weisberg et al.(2001), Overland and Pease(1988)] discussed the anisotropic and asymmetric current (or sea-ice current) response due to the sea surface height set up by the wind in the coastal regions using numerical models. [Simpson et al.(2002)] explained the in-phase strong current variability with an analytical two-layer model using the pressure gradient set up by the diurnal wind. [Sverdrup(1938), Allen(1980), Beardsley et al.(1987), Huyer and Kosro(1987), Choi and Wilkin(2007)] also have examined the upwelling in the coastal region and the dependency of the response on the wind direction.

The three-dimensional Ekman theory including pressure gradients induced by boundaries can produce anisotropy, but it is difficult to apply to the realistic cases with open boundaries, complicated bathymetry, and sparse wind observations. A statistical model that substantiates the anisotropy and asymmetry of the surface current response is presented in this chapter without having to build a numerical model.

This chapter is organized into three sections. First, the Ekman solutions with depth-independent viscosity are obtained for the isotropic and anisotropic WIRFs in the frequency domain (section 4.2). Next, the isotropic and anisotropic WIRFs are statistically estimated in both frequency and time domains using observations of surface currents and the wind (sections 4.3, 4.4, and 4.5.2). Finally, nonlinear WIRFs are considered for their asymmetrical responses (section 4.5.3).

4.2 Theoretical background

4.2.1 Momentum equations

Adjustment terms (A_x and A_y) in the momentum equations are introduced that are only related to the wind-driven currents modeling both bottom drag and pressure gradient set up along the coast:

$$\frac{\partial u}{\partial t} - f_c v + A_x = \frac{1}{\rho}\frac{1}{\partial z}\left(\mu \frac{\partial u}{\partial z}\right), \tag{4.3}$$

$$\frac{\partial v}{\partial t} + f_c u + A_y = \frac{1}{\rho}\frac{1}{\partial z}\left(\mu \frac{\partial v}{\partial z}\right), \tag{4.4}$$

where f_c, ρ, and μ denote the Coriolis frequency, the sea water density, and the dynamic viscosity, respectively. z is the depth coordinate (upward positive). Assuming μ is independent of depth, the adjustment terms are composed of pressure gradients and the anisotropic part of the stress divergence:

$$A_x = \frac{1}{\rho}\frac{\partial p}{\partial x} - \nu_a \frac{\partial^2 u}{\partial z^2}, \tag{4.5}$$

$$A_y = \frac{1}{\rho}\frac{\partial p}{\partial y} - \nu_a \frac{\partial^2 v}{\partial z^2}, \tag{4.6}$$

where ν and ν_a denote the isotropic and anisotropic kinematic viscosity.

For the statistical analysis on the observations, the adjustment terms are considered as convolutions of the time history of currents:

$$A_x = a_{xx} * u + a_{xy} * v = \int_{-\infty}^{\infty} a_{xx}(\xi)u(t-\xi) + a_{xy}(\xi)v(t-\xi)\mathrm{d}\xi, \tag{4.7}$$

$$A_y = a_{yx} * u + a_{yy} * v = \int_{-\infty}^{\infty} a_{yx}(\xi)u(t-\xi) + a_{yy}(\xi)v(t-\xi)\mathrm{d}\xi, \tag{4.8}$$

where a_{xx}, a_{xy}, a_{yx}, and a_{yy} represent the effects of the bottom and coastline boundary friction and the pressure gradient set up near the coast. They are convolved in the time domain with the current components (u and v) in the x- and y-directions, respectively ($*$ is the time domain convolution operator).

Since the system is linear and time-invariant, it is natural to work in the frequency domain, and the equations transformed into the frequency domain are simpler because convolutions become products:

$$(i\omega + a_{xx})\,\hat{u} + (-f_c + a_{xy})\,\hat{v} = \nu\frac{\partial^2 \hat{u}}{\partial z^2}, \tag{4.9}$$

$$(f_c + a_{yx})\,\hat{u} + (i\omega + a_{yy})\,\hat{v} = \nu\frac{\partial^2 \hat{v}}{\partial z^2}. \tag{4.10}$$

The isotropic and anisotropic WIRFs in the frequency domain are calculated explicitly (sections 4.2.2 and 4.7.1) and numerically (sections 4.2.3 and 4.7.1), respectively. The isotropic WIRF is represented by a single complex function in both frequency and time domains, and the anisotropic WIRF consists of four complex functions in the frequency domain or four real functions in the time domain.

4.2.2 Isotropic approach

If an isotropic response is expected, the momentum equations can be combined using complex numbers to represent the surface currents ($\mathbf{u} = u + iv$) and wind stress ($\boldsymbol{\tau} = \tau_x + i\tau_y$). The frequency domain isotropic WIRF (FIWIRF) at finite depth with the depth-independent viscosity and adjustment terms is reviewed in section 4.7.1.

As a simpler form, the FIWIRF for water of infinite depth without adjustment terms ($A_x = A_y = 0$) was derived as in [Ekman(1905)] or text books:

$$\mathbf{H}(z,\omega) = \frac{\hat{\mathbf{u}}(z,\omega)}{\hat{\boldsymbol{\tau}}(\omega)} = \frac{e^{\lambda z}}{\lambda\rho\nu}, \tag{4.11}$$

where $\lambda = \sqrt{i(\omega + f_c)/\nu}$. The depth at which the current is directed oppositely to the surface current at zero frequency is $\delta_E = \pi\sqrt{2\nu/f_c}$ ([Ekman(1905)]), which we call the Ekman depth. Typical eddy viscosity (ν) values for the upper ocean used in these calculations have ranged from 10^{-5} to 10^{-1} $\mathrm{m^2\,s^{-1}}$ ([Santiago-Mandujano and Firing(1990), Chereskin(1995), Weller and Plueddemann(1996), Schudlich and Price(1998), Rio and Hernandez(2003)]). The analysis below is not sensitive to the choice of eddy viscosity, so 1×10^{-4} $\mathrm{m^2\,s^{-1}}$ is chosen as an example.

The magnitude and phase of the FIWIRF at quarter fractions of the Ekman depth ranging from the surface to the Ekman depth are shown in Figures 4.1A and 4.1C, respectively. The current response is infinite at $\omega = -f_c$ ($f_c = 1.07$ cycles per day (cpd) in the study domain) and weakens with depth due to the decreasing momentum flux divergence (Figure 4.1A). The veering of surface currents is to the left of the wind stress with positive phase ($\omega < -f_c$) and is to the right of the wind stress with negative phase ($\omega > -f_c$) ([Gonella(1972), Weller(1981), Rio and Hernandez(2003)]). The phase of the FIWIRF at the surface is a step function with a jump from 45 to -45 degrees at $\omega = -f_c$ (Figure 4.1C). The veering of the current profile under steady wind ($\omega = 0$) is 45 degrees to the right of the wind at the surface and opposite to the surface current (225 degrees) at the Ekman depth ([Ekman(1905), Gonella(1971)]). The current rotates clockwise ($\omega < -f_c$) with depth and counterclockwise ($\omega > -f_c$), respectively.

The WIRF is dependent on the viscosity as expressed by δ_E in the simple cases. The WIRF with lower viscosity has a stronger response at the surface and decays faster with depth yielding shallow momentum penetration into the water column. For example, a well-stratified water column with a shallow pycnocline is likely to have a strong wind impulse response confined near the surface as with diurnal jets ([Price et al.(1986)]) or in the summer. In the same way, the current response due to the wind in a water column with higher viscosity is weaker at the surface and penetrates more deeply, as with well-mixed layers in the winter.

The difference between WIRFs for the surface current assuming infinite or finite depth is small. The adjustment terms generally reduce the magnitude of the WIRF due to damping, removing the singularity at the Coriolis frequency.

4.2.3 Anisotropic approach

The bottom friction and pressure set up in the momentum equations can be different in the x- and y-directions, and lead to an anisotropic current response, referred to in the following as 'extended Ekman theory'. The surface currents and the wind are considered as two-dimensional vectors as in [Pedlosky(1992)] instead of scalar complex variables. Although the adjustment terms can be functions of frequency, for many of the following examples they are assumed to be constant in the frequency domain corresponding to Rayleigh friction in the time domain: $a_{xx} = r_{xx}\delta(t)$, $a_{yy} = r_{yy}\delta(t)$, and $a_{xy} = a_{yx} = 0$ ($\delta(t)$ denotes the Dirac Delta function). The frequency domain anisotropic WIRF (FAWIRF) at finite depth is calculated algebraically in section 4.7.1.

As an introduction to the form of the anisotropic solutions, the FAWIRF at infinite depth

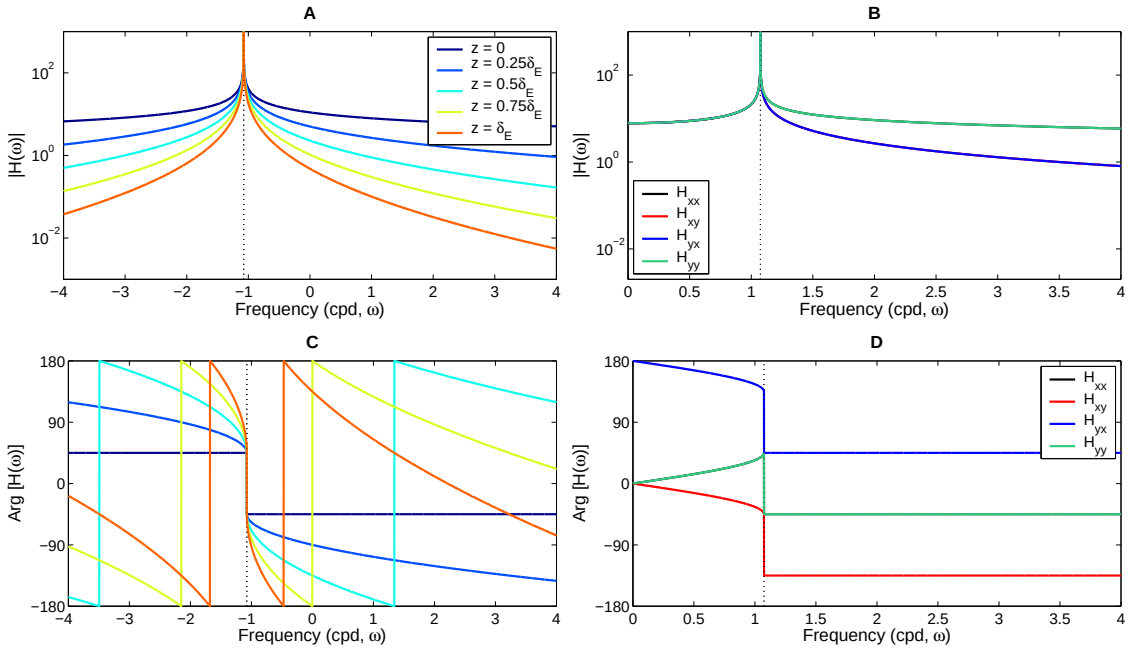

Figure 4.1: A and C: The magnitude and phase of the linear FIWIRF in the Ekman theory at each $0.25\delta_E$ depth increment from the surface ($z = 0$) to the Ekman depth ($z = \delta_E$). B and D: The magnitude and phase of the four functions of the linear FAWIRF at the surface for a parameter choice as the Ekman theory. The FIWIRF and FAWIRF are calculated assuming infinite water depth with depth-independent viscosity ($\nu = 1 \times 10^{-4}$ m^2 s^{-1}) and no friction ($r_{xx} = 0$ and $r_{yy} = 0$). H_{xx} and H_{yy} in B and D are superposed, and H_{xy} and H_{yx} in B are superposed. The vertical dot line indicates the inertial frequency ($\omega = \pm 1.07$ cpd) in the study domain.

with no adjustment terms was calculated, and its magnitude and phase are shown in Figures 4.1B and 4.1D, respectively. The current responses due to two wind impulses and four components of the FAWIRF are presented as

$$\hat{u}(z,\omega) = H_{xx}(z,\omega)\hat{\tau}_x(\omega) + H_{xy}(z,\omega)\hat{\tau}_y(\omega), \tag{4.12}$$

$$\hat{v}(z,\omega) = H_{yx}(z,\omega)\hat{\tau}_x(\omega) + H_{yy}(z,\omega)\hat{\tau}_y(\omega), \tag{4.13}$$

where H_{xx}, H_{xy}, H_{yx}, and H_{yy} are complex functions in the frequency domain. This solution is the same as the Ekman solution. Although the anisotropic responses are not as convenient to interpret, they can be converted to rotary spectra for comparisons with the isotropic response. In this FAWIRF, the magnitudes of all four terms are the same for $\omega < f_c$, and the magnitudes of the diagonal terms (H_{xx} and H_{yy}) and the cross terms (H_{xy} and H_{yx}) are the same for $\omega > f_c$, respectively (Figure 4.1B). The cross terms are out of phase while the diagonal terms are in phase for all frequencies. The phase slopes ($\partial\theta/\partial\omega$) of the cross terms and diagonal terms have an opposite sign for $\omega < f_c$ and zero for $\omega > f_c$ (flat phase).

The anisotropic WIRF can be represented in the same way as the isotropic WIRF by computing the response to each directional wind component separately. For example, the surface current responses ($\hat{u}$ and $\hat{v}$) can be expressed as the combination of the four functions of the FAWIRF multiplied by the wind stress components ($\hat{\tau}_x$ or $\hat{\tau}_y$) in the negative frequency (clockwise, $\omega < 0$) and the positive frequency (counterclockwise, $\omega > 0$) domains:

$$\hat{\mathbf{u}}(\omega < 0) = \left(H_{xx}^{\dagger} + iH_{yx}^{\dagger}\right)\hat{\tau}_x(\omega), \tag{4.14}$$

$$\hat{\mathbf{u}}(\omega > 0) = \left(H_{xx} + iH_{yx}\right)\hat{\tau}_x(\omega), \tag{4.15}$$

$$\hat{\mathbf{u}}(\omega < 0) = \left(H_{xy}^{\dagger} + iH_{yy}^{\dagger}\right)\hat{\tau}_y(\omega), \tag{4.16}$$

and

$$\hat{\mathbf{u}}(\omega > 0) = \left(H_{xy} + iH_{yy}\right)\hat{\tau}_y(\omega), \tag{4.17}$$

where † denotes the complex conjugate, and $\hat{\mathbf{u}}$ is the rotary Fourier coefficients for u and v. This enables plotting the FAWIRF in Figures 4.2B and 4.2D as the FIWIRF for Ekman theory (Figures 4.1A and 4.1C). As an example, the surface current response at $\omega = 0$ is 45 degrees to the right of the wind stress:

$$\hat{u} + i\hat{v} = H_{xx}(0)\hat{\tau}_x + H_{xy}(0)\hat{\tau}_y + i\left(H_{yx}(0)\hat{\tau}_x + H_{yy}(0)\hat{\tau}_y\right) \tag{4.18}$$

$$= |H_{xx}(0)|e^{-\frac{\pi}{4}}(\hat{\tau}_x + i\hat{\tau}_y), \tag{4.19}$$

where $H_{xx}(0) = H_{yy}(0) = H_{xy}(0) = -H_{yx}(0)$ as shown in Figures 4.1B and 4.1D. The FIWIRF and FAWIRF in Figure 4.1 are used for comparison to the WIRFs estimated from the observation data (Figures 4.6, 4.7, 4.12, and 4.13).

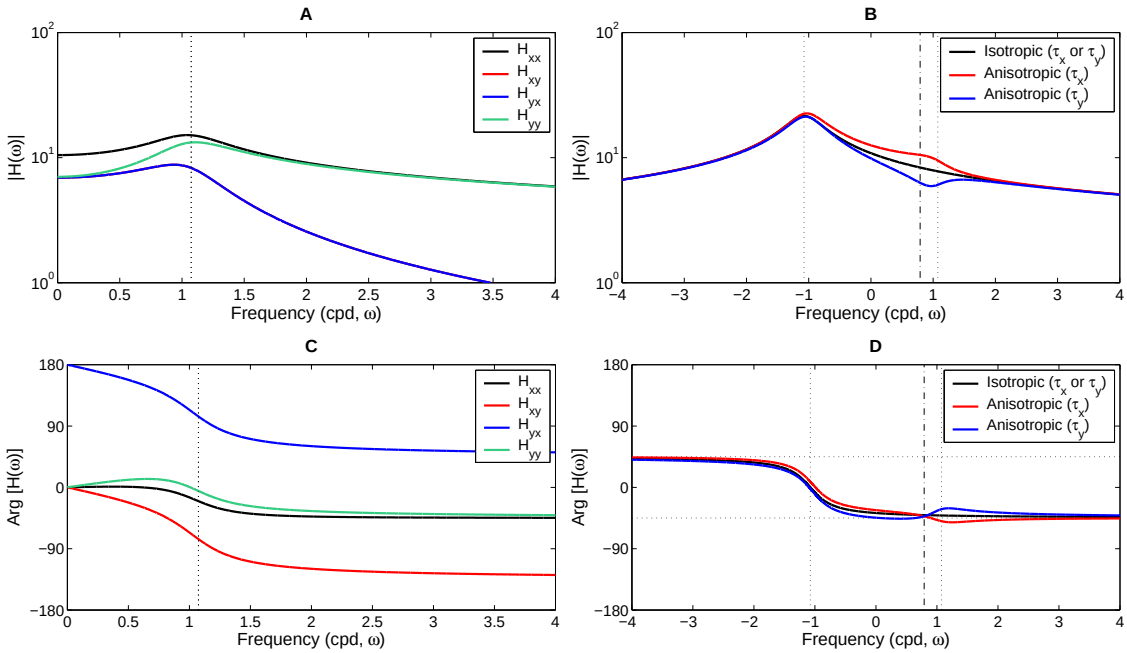

Figure 4.2: The linear FAWIRF based on the extended Ekman theory with depth-independent viscosity ($\nu = 1 \times 10^{-4}$ m^2 s^{-1}) and two different frictions in the x- and y-directions ($r_{xx} = 1 \times 10^{-6}$ s^{-1} and $r_{yy} = 4 \times 10^{-5}$ s^{-1}). A. The magnitude of the FAWIRF. B. The magnitude of the FIWIRF with same viscosity and the friction as the arithmetic mean of two frictions ($r = (r_{xx} + r_{yy})/2$), and the magnitude of the FAWIRF when wind stress (τ_x or τ_y) is applied in each direction. C. The phase of the FAWIRF. D. The phase of the FIWIRF and FAWIRF. The phase transition frequency (ω_0) is 0.7909 cpd (a vertical dashdot line in B and D) for the selected parameters. H_{xy} and H_{yx} in A are overlapped, and the vertical dot line indicates the inertial frequency ($\omega = \pm 1.07$ cpd) in the study domain.

When the adjustment terms are different in the x- and y-directions ($r_{xx} < r_{yy}$ in this example), the response to either x- or y-directional wind stress using the FAWIRF is compared with that of the FIWIRF with friction equal to the arithmetic mean of the two frictions ($r = (r_{xx} + r_{yy})/2$). The symmetry in the FAWIRF is broken by the differing friction (Figures 4.2A and 4.2C) although the magnitudes of the cross terms (a_{xy} and a_{yx}) of the adjustment terms are included as the identical amount. The peaks of the FAWIRF are spread and the phases become smooth. Using equations 4.14–4.17, the FAWIRF for each wind stress component is converted to compare with the FIWIRF (Figures 4.2B and 4.2D). The magnitude and phase of the isotropic WIRF stay between the two components of the anisotropic WIRF. Due to the damping by the friction, the magnitude of the FAWIRF in the direction with more friction is smaller than that in the direction with less friction (Figure 4.2B).

The phase transition of the FAWIRF can be examined in three frequency bands as shown in Figure 4.2D: The current response in the direction with less friction is more to the left of the wind than that in the direction with more friction for $\omega < -f_c$. The current response in the direction

with more friction is more to the right of the wind than that in the direction with less friction for $\omega > -f_c$ but less than the frequency ω_0 where the phase curves cross ($-f_c < \omega < \omega_0$). In other words, more friction leads to more veering angle in the low frequency band ($|\omega| < f_c$) as expected. The phase transition frequency (ω_0) varies between $f_c/2$ and f_c, as a function of the two frictions (not shown). Above the transition frequency, the current in the direction with less friction is more to the right of the wind than the current response in the direction with more friction. Both anisotropic surface current responses converge to -45 degrees as $\omega \to \infty$.

When the adjustment terms are isotropic ($r_{xx} = r_{yy}$), the solution is isotropic, so the FIWIRF and FAWIRF are identical. The magnitude of the four terms of the FAWIRF show similar patterns to the Ekman theory except for a blunt peak at the Coriolis frequency and smoothly changing phase due to the non-zero friction. The phase slope at $\omega = -f_c$ of the FIWIRF and FAWIRF (all four functions) is reduced in magnitude as the friction coefficient (r) increases:

$$\left.\frac{\partial\theta(\omega, r=0)}{\partial\omega}\right|_{\omega=-f_c} = -\infty \tag{4.20}$$

and

$$\left.\frac{\partial\theta(\omega, r\to\infty)}{\partial\omega}\right|_{\omega=-f_c} \to 0. \tag{4.21}$$

As the friction increases, the phase at $\omega = 0$ becomes bigger than -45 degrees, which means the surface wind-driven currents head less than 45 degrees to the right of the wind.

4.3 Methods

4.3.1 Statistical linear estimate of WIRFs

The isotropic and anisotropic WIRFs in both frequency and time domains are estimated using the observations of surface currents and wind stress. Four cases are considered: frequency domain isotropic and anisotropic WIRFs (FIWIRF and FAWIRF) and time domain isotropic and anisotropic WIRFs (TIWIRF and TAWIRF). Although in ideal cases the frequency and time domain estimates should be equivalent, the treatment of missing data leads to differences, and so both methods are used as a check on the results and as a measure of uncertainty. This statistical estimate employs a form of ridge regression ([Hoerl and Kennard(1970), Marquardt(1970), Snee(1977), Golub et al.(1979)]) using regularization. The wind stress and surface currents with bold font in the following equations means either a complex number in the isotropic case or a two-element vector in the anisotropic case.

Frequency domain

From equation 4.1, the linear regression equation in the frequency domain is

$$\hat{\mathbf{u}}(z,\omega) = \mathbf{H}(z,\omega)\hat{\boldsymbol{\tau}}(\omega). \tag{4.22}$$

The frequency domain WIRF ($\mathbf{H}$) is computed from the (time) ensemble covariance average of the Fourier coefficients of surface currents ($\hat{\mathbf{u}}$) and wind stress ($\hat{\boldsymbol{\tau}}$) at each frequency (ω):

$$\mathbf{H}(z,\omega) = \Big(\langle \hat{\mathbf{u}}(z,\omega)\, \hat{\boldsymbol{\tau}}^{\dagger}(\omega)\rangle\Big)\, \Big(\langle \hat{\boldsymbol{\tau}}(\omega)\, \hat{\boldsymbol{\tau}}^{\dagger}(\omega)\rangle + \mathbf{R_a}\Big)^{-1}, \tag{4.23}$$

where † indicates the complex conjugate transpose, and $\mathbf{R_a}$ is the regularization matrix and is assumed the noise level of the wind stress.

Time domain

From equation4.2, the covariance of currents and wind stress is

$$\langle \mathbf{u}\boldsymbol{\tau}^{\dagger}\rangle = \int_{t'} \mathbf{g}(z, t-t')\, \langle \boldsymbol{\tau}(t')\boldsymbol{\tau}(t)^{\dagger}\rangle\, \mathrm{d}t', \tag{4.24}$$

and is truncated and discretized as a finite sum:

$$\langle \mathbf{u}\boldsymbol{\tau}^{\dagger}\rangle = \sum_{k=0}^{N} \mathbf{g}(z, k\Delta t)\, \langle \boldsymbol{\tau}(t-k\Delta t)\boldsymbol{\tau}(t)^{\dagger}\rangle. \tag{4.25}$$

In other words,

$$\langle \mathbf{u}(z,t)\, \boldsymbol{\tau}_N^{\dagger}(t)\rangle = \mathbf{G}(z)\langle \boldsymbol{\tau}_N(t)\, \boldsymbol{\tau}_N^{\dagger}(t)\rangle. \tag{4.26}$$

where $\boldsymbol{\tau}_N(t) = [\boldsymbol{\tau}(t-N\Delta t)\ \cdots\ \boldsymbol{\tau}(t-\Delta t)\ \boldsymbol{\tau}(t)]^{\dagger}$ is the wind stress stacked with N hours time lag.

The time domain WIRF ($\mathbf{G}$) is computed from the covariance matrix between surface currents ($\mathbf{u}$) and time lag wind stress ($\boldsymbol{\tau}_N$).

$$\mathbf{G}(z) = \Big(\langle \mathbf{u}(z,t)\, \boldsymbol{\tau}_N^{\dagger}(t)\rangle\Big)\, \Big(\langle \boldsymbol{\tau}_N(t)\, \boldsymbol{\tau}_N^{\dagger}(t)\rangle + \mathbf{R_b}\Big)^{-1}, \tag{4.27}$$

where $\mathbf{G} = [\mathbf{g}_1\, \mathbf{g}_2\, \cdots\, \mathbf{g}_N]^{\dagger}$, and $\mathbf{R_b}$ is the regularization matrix, which compensates for the sample error in the covariance matrix by suppressing small or negative eigenvalues.

4.3.2 Statistical nonlinear estimate of WIRFs

Since the responses of the linear WIRFs to oppositely directed wind are symmetric, nonlinear WIRFs are needed to break the symmetry of the response. The nonlinear WIRFs are calculated in the frequency and time domains similarly to the linear WIRFs. The magnitude of the wind stress is used in the regression to provide the nonlinear term as one of a number of ways to do the nonlinear regression. In the frequency domain the nonlinear regression equation is

$$\hat{\mathbf{u}}(z,\omega) = \mathbf{H_1}\hat{\boldsymbol{\tau}} + \mathbf{H_2}|\hat{\boldsymbol{\tau}}|, \tag{4.28}$$

where $\mathbf{H_1} = \mathbf{H_1}(z,\omega)$ and $\mathbf{H_2} = \mathbf{H_2}(z,\omega)$. In the time domain, the regression equation becomes

$$\mathbf{u}(z,t) = \mathbf{G_1}\boldsymbol{\tau}_N + \mathbf{G_2}|\boldsymbol{\tau}_N|, \tag{4.29}$$

where $\mathbf{G_1} = \mathbf{G_1}(z)$ and $\mathbf{G_2} = \mathbf{G_2}(z)$. These are performed in practice by appending the vector of $|\hat{\boldsymbol{\tau}}|$ or $|\boldsymbol{\tau}_N|$ to the existing vector data and regressing as usual.

4.3.3 Residual variance ratio estimate

The variance ratio of the wind-driven currents to the total currents at each frequency is the coherence (γ^2). The residual variance ratio (β^2) is its complement ($\beta^2 = 1 - \gamma^2$) ([Bendat and Piersol(2000)]). The total residual variance ratio (ϵ^2) is defined as the variance of the residual currents after the wind regression to the total currents for all frequencies or time lags, and is convenient to compare the performance of the WIRFs.

Frequency domain

The residual variance ratio (β^2) in the frequency domain is

$$\beta^2(\omega) = \frac{|\hat{\mathbf{r}}(\omega)|^2}{|\hat{\mathbf{u}}(\omega)|^2}, \tag{4.30}$$

where $\hat{\mathbf{r}}(\omega) = \hat{\mathbf{u}}(\omega) - \mathbf{H}(\omega)\hat{\boldsymbol{\tau}}(\omega)$. $\mathbf{H}(\omega)$ can be the FIWIRF or FAWIRF. For the linear FAWIRF, the residual variance ratios (β_u^2 and β_v^2) for the current components (u and v) are

$$\beta_u^2(\omega) = \frac{|H_{xx}\hat{\tau}_x + H_{xy}\hat{\tau}_y - \hat{u}|^2}{|\hat{u}|^2} \tag{4.31}$$

and

$$\beta_v^2(\omega) = \frac{|H_{yx}\hat{\tau}_x + H_{yy}\hat{\tau}_y - \hat{v}|^2}{|\hat{v}|^2}, \tag{4.32}$$

respectively, where H_{xx}, H_{xy}, H_{yx}, and H_{yy} are the four response functions of the FAWIRF. The residual variance ratio of total currents is estimated:

$$\beta^2(\omega) = \frac{|H_{xx}\hat{\tau}_x + H_{xy}\hat{\tau}_y - \hat{u}|^2 + |H_{yx}\hat{\tau}_x + H_{yy}\hat{\tau}_y - \hat{v}|^2}{|\hat{u}|^2 + |\hat{v}|^2}. \tag{4.33}$$

The total residual variance ratio (ϵ^2) in the frequency domain is

$$\epsilon^2 = \frac{\sum_k |\hat{\mathbf{r}}(\omega_k)|^2}{\sum_k |\hat{\mathbf{u}}(\omega_k)|^2}. \tag{4.34}$$

Time domain

The total residual variance ratio (ϵ^2) in the time domain is

$$\epsilon^2 = \frac{\sum_k \langle \mathbf{r}(t_k) \rangle^2}{\sum_k \langle \mathbf{u}(t_k) \rangle^2}, \tag{4.35}$$

where $\mathbf{r}(t) = \mathbf{u}(t) - \mathbf{G}(z)\boldsymbol{\tau}_N(t)$, $\mathbf{G}(z)$ denotes the TIWIRF or TAWIRF, and $\boldsymbol{\tau}_N(t)$ is the N hours time lag stacked wind stress. In the ideal case, the total residual variance ratio in both frequency and time domains should be identical.

4.4 Observations

Surface currents used for this study were observed by high-frequency (∼25 MHz) radars during two years (April 2003–March 2005) over a 40 km region from the coast of southern San Diego county (Chapters 2 and 3). A time series of spatially averaged hourly surface currents (u and v) over the area shown as the black curve in Figure 4.3 is used in this analysis. This area indicates grid points with data present for at least 70% of the two years. The spatially averaged surface current is smoother and more reliable, having only 2.2% missing data. Regional averages or point measurements can be used to investigate the horizontal structure of the WIRF. The effective averaging depth for surface current measurements by high-frequency (HF) radar has been estimated as 5–16% of the wave length of the backscattering surface waves ([Stewart and Joy(1974), Barrick et al.(1977), Ha(1979), Fernandez et al.(1996)]), but the range accepted in the HF radar community is 8–16% (Don Barrick 2008, personal communication). Therefore the averaging depth in this study is assumed to be approximately 1 m. The two year surface current time series is detided at the main tidal constituents (O1, P1, K1, M2, and S2) using least squares fitting. The S2 component of the surface current is removed even though the harmonic forcing of the diurnal wind can be ambiguous with the S2 tide. The amplitude of the S1 surface tide in San Diego is nearly zero (harmonic constituents of surface tides from [NOAA(2006)] and Table 5.1), so most of the diurnal variability of surface currents is assumed to result from the diurnal wind.

The wind observed at Tijuana River (Tidal Linkage station, Figure 4.3) during the same period as the surface current is hourly averaged and has 8.5% missing data. The hourly composite mean of the wind (regardless of local sunrise and sunset) (not shown) shows about 2.5 times stronger variance of the east-west wind than the north-south wind. The wind stress is estimated from the drag coefficient as described in [Large and Pond(1981)], and the overall results are not sensitive to the choice of the drag coefficient except for a compensating shift in magnitude of the WIRF.

The rotary power spectra of the detided surface current and the wind are shown in Figures 4.4A and 4.4C, respectively, which are estimated from 90 subsamples with the same record length, and missing observation values have been filled with zeros. Both have a red spectrum and the wind spectrum shows dominant clockwise diurnal variance. Although the variance of the surface current has been reduced by the tidal fit, the resolution ($\Delta\omega = 0.1244$ cpd) of the subsample power spectrum is not enough to isolate the tidal lines, so there are broad variance peaks around the K1 and M2 frequencies due to nonlinearity.

The coherence and phase between each component of the surface current and wind stress are shown in Figures 4.4B and 4.4D, which are estimated in the same way as the power spectra in Figures 4.4A and 4.4C. The x-directional wind stress (τ_x) is coherent with surface current components (u and v) as ∼0.7 near 1 cpd, and the coherence of the y-directional wind stress (τ_y) is ∼0.3 at the same frequency but high at low frequencies (less than 1 cpd) (Figure 4.4B). The phases fluctuate at the frequencies with low coherence (Figure 4.4D).

The coastline in the south of San Diego is aligned roughly north-south and faces west

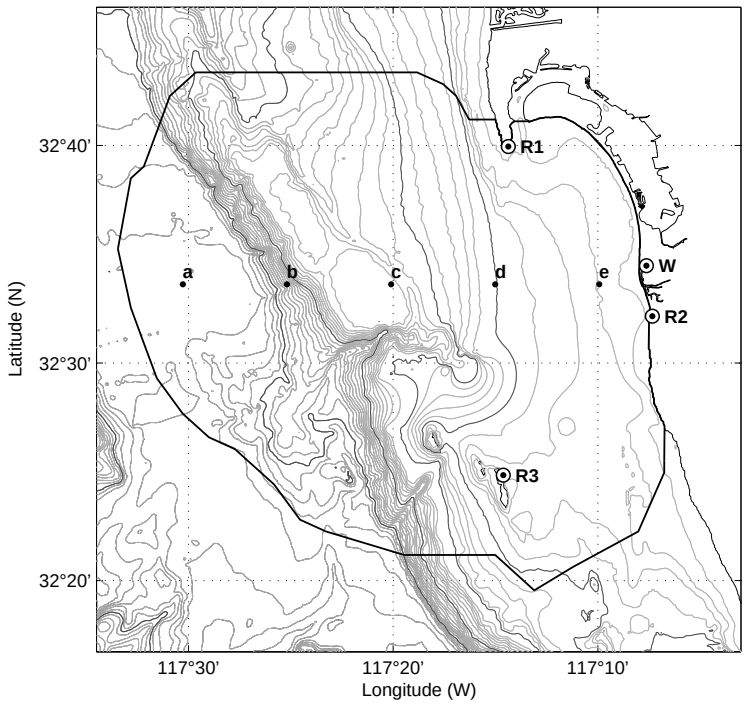

Figure 4.3: The study domain of surface currents and the wind. The effective spatial coverage area where the high-frequency radars (R1, R2, and R3) observed is indicated with black curve. Three high-frequency radar sites are Point Loma (R1), Border Park (R2), and Coronado Island (R3). The Tijuana River wind station (W) is located near the Tijuana River valley. Five evenly spaced grid points are chosen as the offshore (**a**) and onshore (**e**) locations in the cross shelf direction to examine the spatial variation of WIRFs (see section 4.5.2). The bottom bathymetry contours are indicated by the thin curves with 10 m ($0 < z < 100$ m) and 50 m ($100 < z < 1000$ m) contour intervals and the thick curves at the 50, 100, 500, and 1000 m depths.

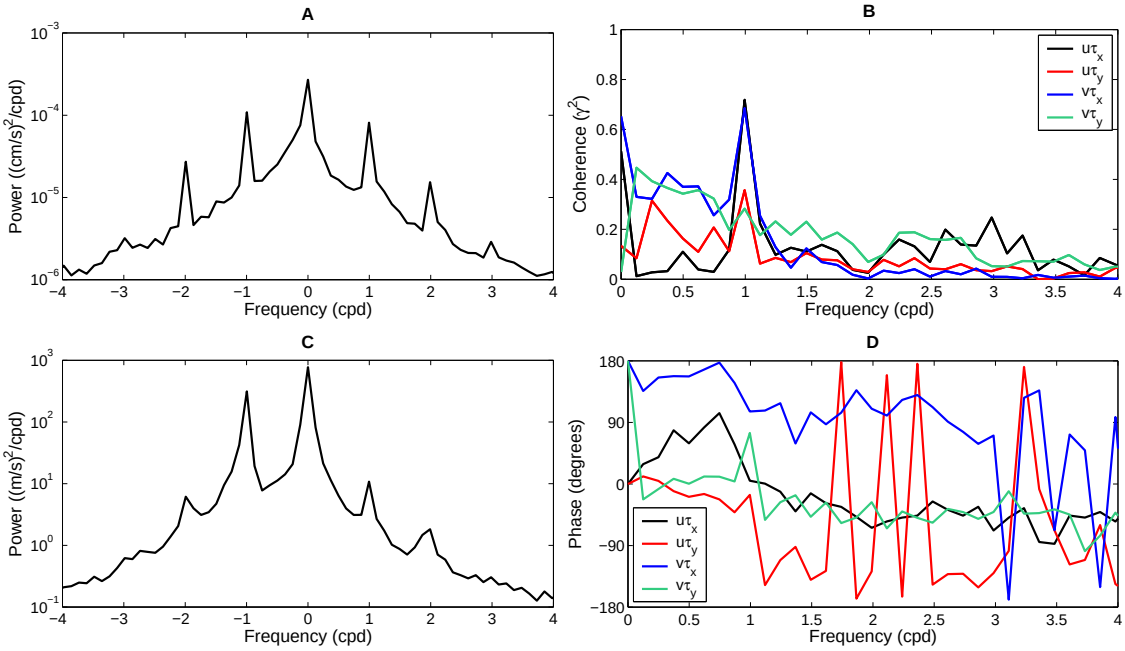

Figure 4.4: A and C: The rotary power spectra of the detided surface current (A) and the wind (C) are estimated from 90 subsamples with the same record length (8.12 days) and averaged across each frequency. B and D: Coherence (B) and phase (D) between the surface current and wind stress are estimated using the same spectra.

(Figure 4.3). The Coronado embayment (San Diego Bay) and the headland (Point Loma) are located near the northeast boundary. The water depth of the continental shelf region is mostly less than 100 m.

4.5 Data analysis

4.5.1 Overview

The WIRF estimates are affected by the treatment of the missing data. The frequency domain WIRFs are estimated through replacing missing data with zeros. This leads to positive-definite matrices, but the variances are biased low and spurious high frequency energies are created. The time domain WIRFs are estimated from the covariance matrix of the observed data only. This reduces bias, but can create small or negative eigenvalues of the lagged covariance matrix. A regularization matrix can be added (equations 4.23 and 4.27) to limit the structure of the solutions and to make the sample autocovariance matrix of the wind stress invertible when it is non-positive definite. This regularization keeps the regression from overfitting the data, and is checked by cross-validation ([Efron and Gong(1983), LeBlanc and Tibshirani(1996)]). In other words, the model estimated from training data is applied to independent test data, and the difference between the estimated and observed data is called the cross-validation error. This error is a function of the regularization, and has a minimum value between underfitting and overfitting. The regularization matrix ($\mathbf{R_a} = \mathbf{R_a}(\omega)$) in the frequency domain can be justified as the statistical and observational noise contributions to the wind stress variance. The regularization matrix in the time domain compensates for the statistical and observational noise in the autocovariance matrix of the wind. For lack of better assumptions, it is assumed to be a scaled diagonal matrix with a fraction of the wind stress variance $\left(\mathbf{R_a} = \kappa^2\mathbf{I}\right)$. The effects of missing observations on the WIRF estimate are discussed in section 4.6.

The goal of the regularization is to ensure that the cross-validation error is no larger than the error on the training data by adjusting $\mathbf{R_a}$ to minimize the cross-validation error for every set of predicting variables ([Marquardt(1970), Hoerl and Kennard(1970)]). The number of subsamples in the frequency or time domain calculation increases as the length of data chunks decreases, and the degrees of freedom decrease with increasing Fast Fourier Transform (FFT) length or decreasing maximum time lag. The larger the maximum time lag, the more variables are available to fit the data, so the total residual variance ratio decreases, but the decrease is small after about 6 days (Figure 4.5B). Without cross-validation, the error using a small number of subsamples (many fitting variables) is artificially low ([Davis(1985)]) if regularization is not used, but the need for regularization decreases as the number of subsamples increases. As the fit is generalized from isotropic to anisotropic and then to nonlinear, the number of parameters available to fit the data increases, so the residual variance ratio without cross-validation decreases. The regularization is adjusted so that the training and test datasets yielded the nearly same error variance ratio. However, the residual variance ratio for the cross-validation data has larger uncertainty due to the limited number of realizations compared

to the training data when errors are estimated using the Jackknife ([Emery and Thomson(1997)]). The total residual variance ratios for the training data in the frequency and time domains are shown in Figures 4.5A and 4.5B, respectively. The Jackknife estimate for the impulse response function and its uncertainty are shown in the frequency domain for simplicity:

$$\mathbf{H}(\omega) = \frac{1}{M} \sum_{k=1}^{M} \left(\frac{\langle \hat{\mathbf{u}} \hat{\boldsymbol{\tau}}^{\dagger} \rangle}{\langle \hat{\boldsymbol{\tau}} \hat{\boldsymbol{\tau}}^{\dagger} \rangle} \right)_k \tag{4.36}$$

and

$$\sigma^2_{\mathbf{H}(\omega)} = \frac{1}{M-1} \sum_{k=1}^{M} \left[\left(\frac{\langle \hat{\mathbf{u}} \hat{\boldsymbol{\tau}}^{\dagger} \rangle}{\langle \hat{\boldsymbol{\tau}} \hat{\boldsymbol{\tau}}^{\dagger} \rangle} \right)_k - \mathbf{H}(\omega) \right]^2, \tag{4.37}$$

where M is the number of subsampled datasets.

Cross-validation ([Efron and Gong(1983), LeBlanc and Tibshirani(1996)]) is repeated 30 times with randomly chosen blocks of training data and test data taking 90 and 10% of the total data, respectively. The training data are chosen by subsampling with a uniform probability as opposed to a systematic choice of sequential contiguous blocks. Results of the two approaches (random or systematic) become nearly the same as the number of realizations increases, with little change in the results above 30 trials. In the frequency domain, the choice of the training data and test data is constrained because the data are divided into blocks with the same record length, and are Fourier transformed separately. In the time domain, each excluded datum removes many lags. If they are distributed randomly, too many data are removed. Therefore they are subsampled in blocks. The regularization ($\mathbf{R_b}$) necessary to minimize the cross-validation error in the time domain WIRFs is about 10% of the mean eigenvalue (averaged variance) of the wind stress autocovariance matrix. On the other hand, the regularization in the frequency domain used a constant noise level, which decreases as the number of subsamples increases. The relationship between the error in the observations and the uncertainty in the WIRF estimate is discussed in section 4.5.6.

The minimum number of subsamples and the maximum time lag are determined by the values at which the total cross-validated residual variance ratio averaged across all realizations (section 4.3.3) is a minimum (Figure 4.5). The number of subsamples is larger than the number of independent time series available from a given data set. The 6-day chunks are assumed to be mostly independent, although the low frequency components are not. The error bars on the WIRF and the residual variance are calculated using the Jackknife method (see for example [Emery and Thomson(1997)]) with 30 randomly subsampled data sets (M is equal to 30 in equations 4.36 and 4.37 and each subset is 90% of total data).

The FIWIRF and FAWIRF are calculated from an ensemble of 90 independent FFTs of 8.12-day period of the surface current and wind stress (section 4.3.1 and equation 4.28), and the TIWIRF and TAWIRF are computed from the wind stress stacked with hourly time lags up to 6 days regressed on the surface current (section 4.3.1 and equation. 4.29). These are approximately

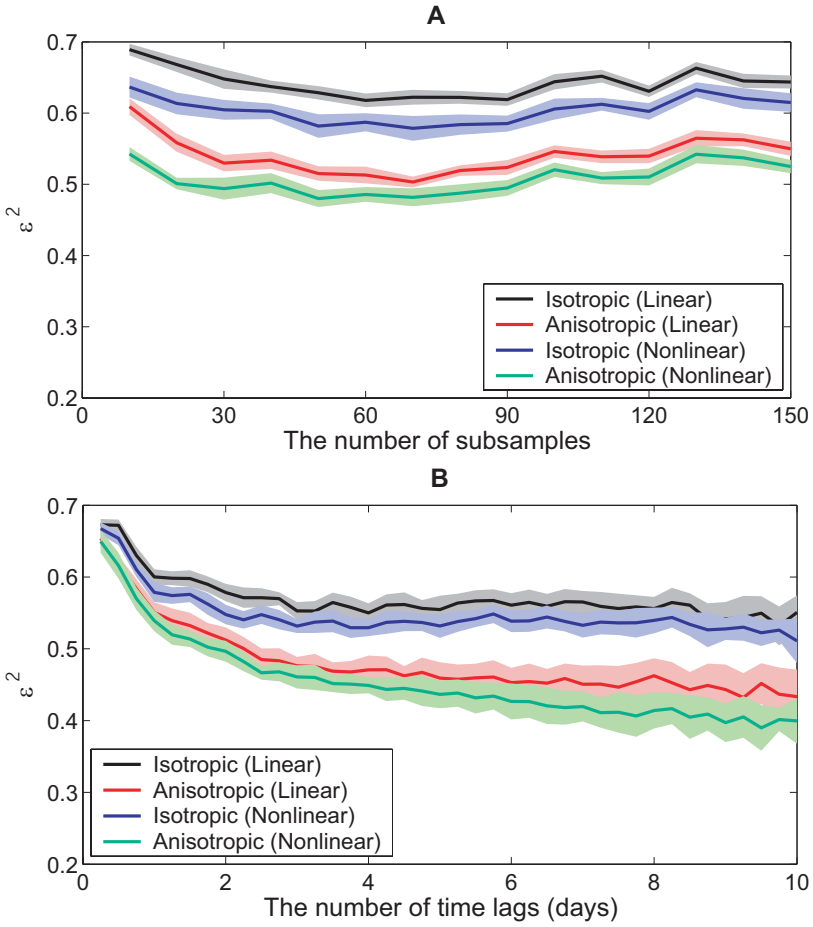

Figure 4.5: A. The total residual variance ratio (ϵ^2) of the linearly/nonlinearly estimated FIWIRFs and FAWIRFs for the training datasets in terms of the number of subsamples (equation 4.34). B. The total residual variance ratio of the linearly/nonlinearly estimated TIWIRFs and TAWIRFs for the training datasets in terms of the number of time lags (equation 4.35). The noise level of the wind stress and the 10% of mean eigenvalue of the wind stress autocovariance matrix are used as the regularization in the frequency domain WIRFs and the time domain WIRFs, respectively. The mean total residual variance ratios and the uncertainties (a shaded region is one standard deviation) are estimated from 30 realizations using the Jackknife method.

the minima of the cross-validated error (Figure 4.5). The estimated WIRFs include the current response to steady wind ($\omega = 0$).

The WIRFs in one domain are (inversely) Fourier transformed into the other domain, and each pair satisfies Parseval's theorem. For example, the estimated FIWIRF (Figures 4.6A and 4.6B) is inversely Fourier transformed into the time domain to represent a temporal amplitude (Figure 4.6C). The estimated TIWIRF (Figure 4.12C) is Fourier transformed into the frequency domain (Figures 4.12A and 4.12B) so that the FIWIRF and TIWIRF are comparable across the two domains, and a similar procedure can be applied to the FAWIRF (Figure 4.7) and TAWIRF (Figure 4.13). For the nonlinear WIRFs, only the linear regression coefficients ($\mathbf{H_1}$ in equation 4.28 and $\mathbf{G_1}$ in equation 4.29) are considered for the comparison between the two domains.

The isotropic and anisotropic WIRFs are compared both as the rotary power spectra in the frequency domain and as the time integrated response. For instance, the linear FIWIRF is plotted for only onshore wind (τ_x) because it is isotropic, but the linear FAWIRF is plotted for onshore and upcoast winds (τ_x and τ_y), respectively, as magnitude and phase in the frequency domain (Figures 4.8A and 4.8B, respectively). The time integration of temporal amplitudes of the FIWIRF (Figure 4.6C) and FAWIRF (Figure 4.7C) for steady wind are compared (Figure 4.9A). The TIWIRF and TAWIRF are also examined in the similar way (Figure 4.9B). The anisotropic response to upcoast wind is shifted 90 degrees down (Figures 4.8B and 4.14B) and rotated 90 degrees clockwise (Figure 4.9) to align with the other results. Moreover, the nonlinear anisotropic WIRFs are illustrated for steady winds with four directions: onshore ($\tau_x > 0$), offshore ($\tau_x < 0$), upcoast ($\tau_y > 0$), and downcoast ($\tau_y < 0$) winds.

Because of the ambiguity of WIRFs with tides at the S2 frequency, the linear WIRFs estimated with the surface current both including and excluding the S2 variance are compared. With the S2 variance included in the fit, the residual variance ratios of the WIRF at the S2 frequency is approximately 0.48, but the contribution of the S2 variance to the total variance is negligible. The WIRFs with and without the S2 variance overlap within errorbars and the S2 variance of the wind is small, so the surface current excluding the S2 variance is used. The variance removal at the S2 frequency is particularly evident in the plots of WIRFs (Figures 4.8A and 4.14A) as a drop in the response function at that frequency.

4.5.2 Linear WIRFs

Frequency domain

The magnitudes of the FIWIRF and FAWIRF have peaks near the diurnal frequency ($\omega = -1$ cpd for the FIWIRF and $\omega = 1$ cpd for the FAWIRF) instead of the Coriolis frequency ($\omega = \pm f_c$) as shown in Figures 4.6A and 4.7A. Because the variances of the diurnal surface currents and diurnal wind stress are much larger than those at the Coriolis frequency, the WIRFs do not have as good signal-to-noise-ratio (SNR) at the Coriolis frequency, and the regularized least squares estimate biases the response function toward zero so that the estimated FIWIRF and FAWIRF have

a maximum at the diurnal frequency ($\omega = -1$ or $\omega = 1$ cpd). There is also increasing uncertainty at higher frequency due to the dominance of the diurnal variance in the data (Figures 4.6A and 4.7A).

The phase of the FIWIRF is nearly zero at $\omega \cong -f_c$, and varies between -45 and 45 degrees (Figure 4.6B). The overall shapes of the FIWIRF (Figures 4.6A and 4.6B) agree with the FIWIRF at the ocean surface of the Ekman theory (Figures 4.1A and 4.1C) and as seen in other observations ([Gonella(1972), Weller(1981), Rio and Hernandez(2003)]). The temporal amplitude of the FIWIRF has diurnal fluctuations, and diminishes within 3–4 days with a clockwise rotation (Figure 4.6C). This time decaying amplitude is different from the evanescent solution for the step-function wind using the Laplace transform ([Ekman(1905), Lewis and Belcher(2004)]), because we measure a local response for a statistically steady state wind in the coastal region.

The FAWIRF is made up of four response functions, which gives twice the number of parameters as the FIWIRF. The cross terms (H_{xy} and H_{yx}) have more uncertainties in their magnitudes and phases than the diagonal terms (H_{xx} and H_{yy}) (Figures 4.7A and 4.7B). At $\omega = 0$, the phases of the FAWIRF are the same as the phases of the Ekman theory (Figures 4.7B and 4.1D). However, the magnitudes of four terms (H_{xx}, H_{xy}, H_{yx}, and H_{yy}) of the FAWIRF at $\omega = 0$ are not identical as they were in the isotropic case showing anisotropic response in the quasi-steady state (Figures 4.7A and 4.1B). The wind-current responses at all other frequencies are anisotropic although noise in the estimate certainly contributes. The viscosity (ν) and adjustment terms (a_{xx}, a_{xy}, a_{yx}, and a_{yy}) could be estimated as functions of frequency using the observations, and an example of the fit of adjustment terms to the data is presented in section 4.7.2. The temporal amplitude of the FAWIRF has approximately inertial periodicity and decays to zero within 3–4 days (Figure 4.7C).

Coherence calculations (not shown) find that 60–70% of the variances of the diurnal surface currents is explained by the diurnal land/sea breezes (equations 4.31 and 4.32). However, the y-directional surface current (v) in the low frequency band ($0 \leq \omega < 1$ cpd) has higher coherence with wind than the x-directional surface current (u) ($\beta_v^2 \approx 0.5$ and $\beta_u^2 \approx 0.3$). This is consistent with the hypothesis that the coastline in the study domain blocks flow to the east so that positive u is inhibited by the pressure set-up at long time scales.

The FAWIRF to each wind component (τ_x or τ_y) is compared with the FIWIRF as rotary spectra (Figure 4.8). The x-directional wind stress (τ_x) apparently generates a stronger response at both clockwise diurnal frequency and zero frequency than the y-directional wind stress (τ_y) (Figure 4.8A), partly because of higher SNR. The phases of the FAWIRF for τ_x and τ_y vary between -45 and 45 degrees, and bracket the phase of the FIWIRF (Figure 4.8B) as the extended Ekman theory does (Figure 4.2D). As an example, the temporal amplitudes of the FIWIRF and FAWIRF are integrated for 3 days under constant wind stress (0.013 $\mathrm{kg\,m^{-1}\,s^{-2}}$ for the typical wind speed in the study domain of 3 $\mathrm{m\,s^{-1}}$) as shown in Figure 4.9A. The FIWIRF generates surface currents 41$\pm$2 degrees to the right of steady wind, and the FAWIRF produces surface currents at 75$\pm$0.5 (τ_x) and 9$\pm$2 (τ_y) degrees to the right of the steady wind stress, respectively, which are identical of the phases at $\omega = 0$ in Figure 4.8B. The time integration of the steady wind response shows that the response is smaller cross-shore than along-shore as expected. The magnitudes of the wind-driven currents are 3–5% of

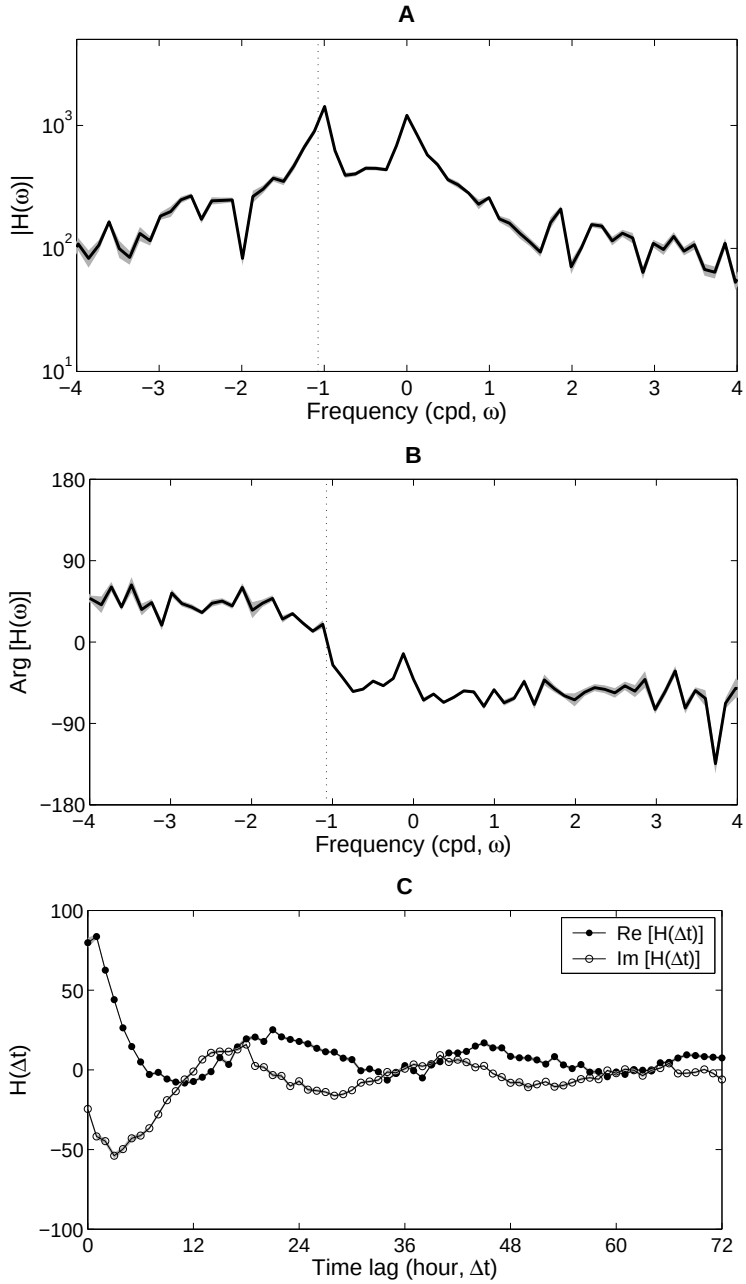

Figure 4.6: The linearly estimated FIWIRF. A. Magnitude. B. Phase. C. Temporal amplitudes. The FIWIRF is estimated with 90 subsamples, and the uncertainty shown as the gray-shaded region in A and B is calculated from 30 realizations using the Jackknife method. The vertical dot line indicates the inertial frequency ($\omega = -1.07$ cpd) in the study domain.

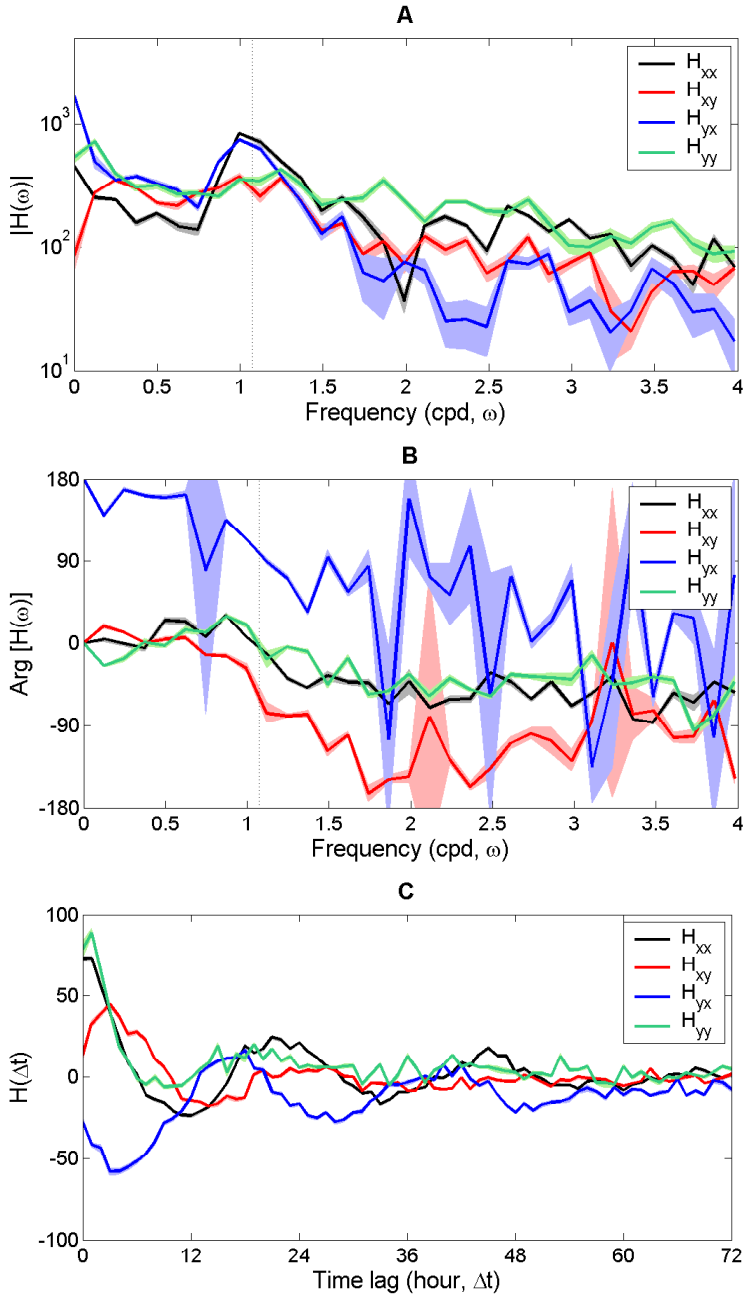

Figure 4.7: The linearly estimated FAWIRF. A. Magnitude. B. Phase. C. Temporal amplitudes. The FAWIRF and its errorbars are estimated in the same way of the FIWIRF (Figure 4.6). The vertical dot line indicates the inertial frequency ($\omega = 1.07$ cpd) in the study domain.

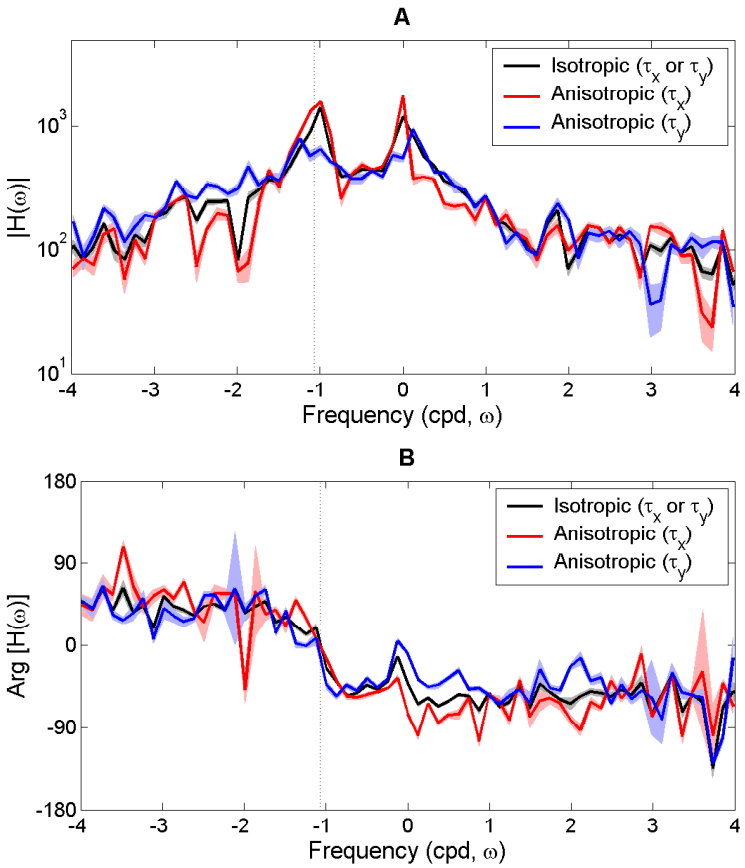

Figure 4.8: The magnitude and phase of the linearly estimated FIWIRF and FAWIRF for wind stress (τ_x and τ_y), respectively. A. Magnitude. B. Phase. The phase of the FAWIRF for the y-directional wind stress (τ_y) is shifted down by 90 degrees to align with the others. The solid curves in A and B are the same as in Figures 4.6A and 4.6B, respectively. The vertical dot line indicates the inertial frequency ($\omega = -1.07$ cpd) in the study domain.

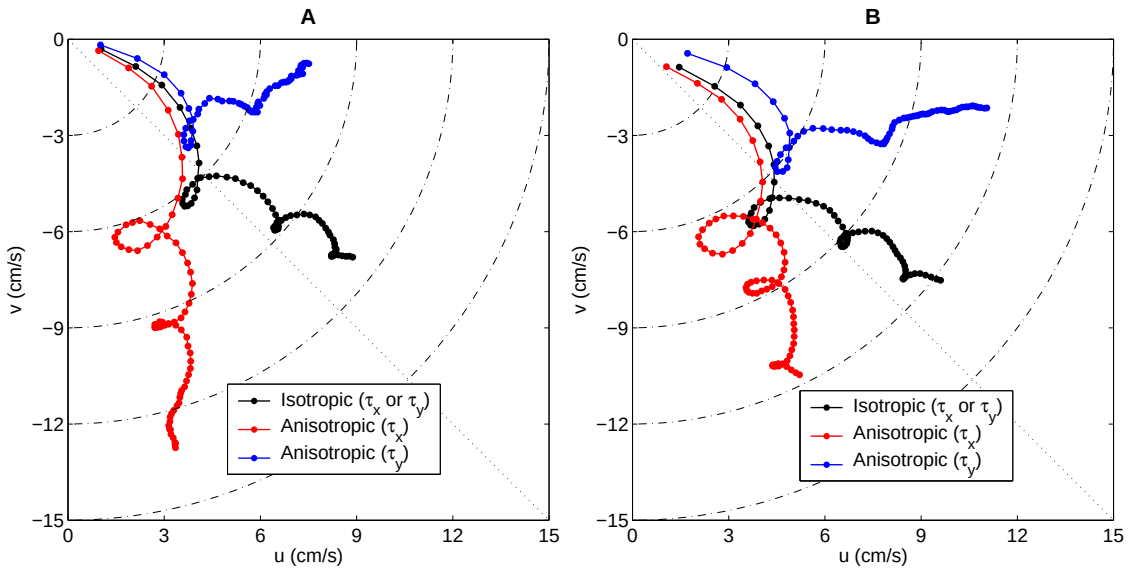

Figure 4.9: Time integrations of the temporal amplitudes of the linearly estimated WIRFs for a constant wind stress during 3 days. A. FIWIRF and FAWIRF. B. TIWIRF and TAWIRF. The wind stress at either direction (τ_x or τ_y) of the typical wind speed ($|\mathbf{u}| = 3\ \mathrm{m\,s^{-1}}$) in the study domain is applied. Anisotropic response for the y-directional wind stress (τ_y) is rotated 90 degrees clockwise to align with other responses. The thin dashdot quarter-circular curves denote the percentage of the wind-driven current speed to the wind speed, which are 1, 2, 3, 4, and 5% from the origin, and the thin dotted line indicates the direction of 45 degrees to the right of the wind stress.

the wind speed, which is consistent with other studies ([Bye(1965), Churchill and Csanady(1983), Wu(1983), Weber(1983)]). The total residual variance ratios by the FIWIRF and FAWIRF are 0.62 and 0.52, respectively (Figure 4.5A), indicating significant anisotropy.

The spatial variation of WIRFs is examined by computing the FIWIRF between the detided surface currents at five locations sampling the cross shelf direction in the study domain (grid points $\mathbf{a}-\mathbf{e}$ in Figure 4.3) and wind stress. Each FIWIRF is made from 90 subsamples with the same record length, and averaged over the realizations at each frequency. As an example of cross shelf variation of WIRFs, the magnitude and phase of the FIWIRF at five evenly spaced points sampling the cross shelf direction are shown in Figure 4.10A and 4.10B, respectively. The FIWIRF shows larger response onshore than offshore. To show the response to a steady wind, the temporal amplitude of the FIWIRF is integrated in time for three days with a constant typical wind speed in San Diego (Figure 4.11). As the point considered moves from offshore to onshore, the veering angle changes from 70 degrees (offshore) to 30 degrees (onshore) to the right of the wind. The slower rotation with depth inshore may imply that less of full Ekman layer may be fit into the shallow water depth ([Ekman(1905), Lentz(2001), Kirincich et al.(2005)]).

Time domain

The TIWIRF and TAWIRF are shown in Figures 4.12C and 4.13C, respectively, and the magnitude and phase of the Fourier transformed TIWIRF and TAWIRF are shown in Figures 4.12A–4.12B and 4.13A–4.13B, respectively. The TIWIRF shows approximately inertial oscillations with slowly decreasing amplitude (Figure 4.12C), which are slightly larger than that of the FIWIRF (Figure 4.6C). However, the energy of the TIWIRF and the FIWIRF is nearly equal when the time lag and the data record length are same. The energy of the TAWIRF and the FAWIRF is also approximately the same within the estimation errors. The SNR of the TAWIRF is again relatively lower at the Coriolis frequency than at the diurnal frequency so the peaks are found close to 1 cpd.

The magnitude of the TIWIRF in the frequency domain is large at the diurnal frequency (Figure 4.12A), and its phase stays between -45 and 45 degrees with phase shift of nearly zero degree at $\omega \cong -f_c$ (Figure 4.12B). The phase of the TIWIRF at zero frequency is -43 ± 2 degrees (Figure 4.6B or 4.14B), which is consistent with the phase of the FIWIRF (-41 ± 2 degrees, Figure 4.8B). The TAWIRF (Figure 4.13) has similar features to the FAWIRF (Figure 4.7).

The Fourier transformed TIWIRF and TAWIRF for each wind component (τ_x and τ_y) are compared as rotary spectra (Figure 4.14), and also show the peak at the diurnal frequency, the drops at the S2 frequency, and the bracketing phases of the TAWIRF as with the frequency domain WIRFs.

The time-integrated responses (Figure 4.9B) of the TIWIRF and TAWIRF to typical constant wind stress in the study domain also shows similar patterns to those of the FIWIRF and FAWIRF (Figure 4.9A). In a quasi-steady state, the TAWIRF generates surface current responses of 67±1 (τ_x) and 12±3 (τ_y) degrees to the right of the wind stress, respectively, and the TIWIRF

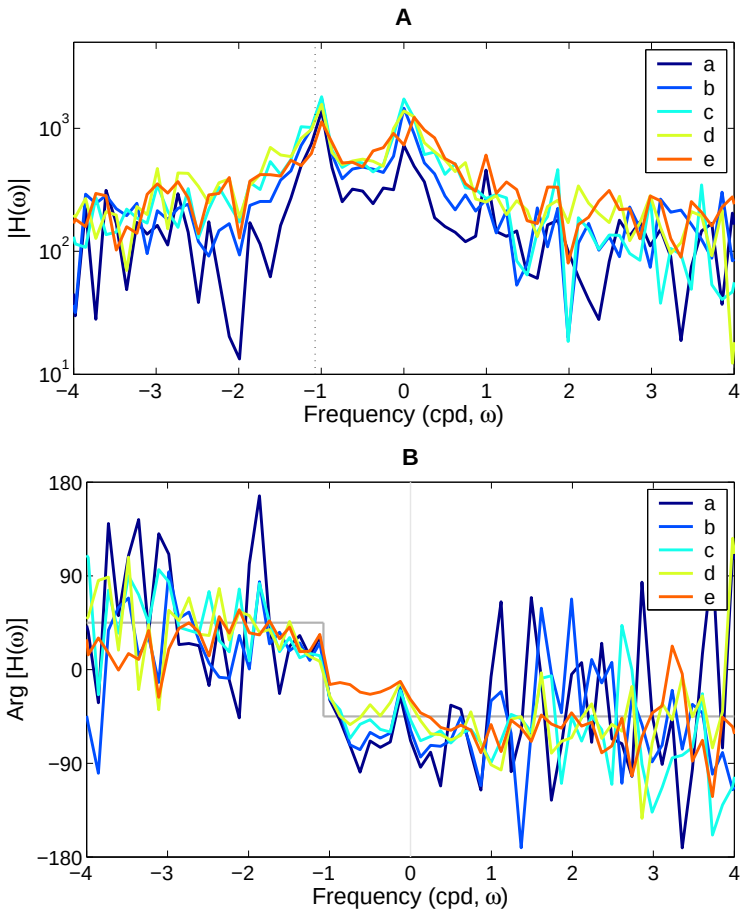

Figure 4.10: A and B: The magnitude and phase of the FIWIRF in the cross shelf direction. The gray line denotes the theoretical phase of the FIWIRF in the study domain. The vertical dot line indicates the inertial frequency ($\omega = -1.07$ cpd) in the study domain.

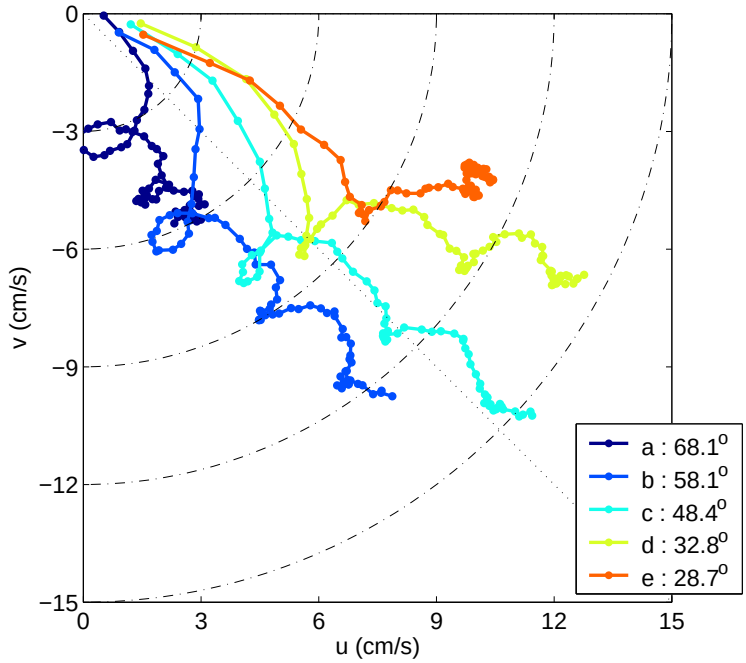

Figure 4.11: Time integration of the temporal amplitude of the FIWIRF in the cross shelf direction (offshore (**a**) and onshore (**e**) locations) for a constant wind stress during 3 days. The x-directional wind stress (τ_x) of the typical wind speed ($|\mathbf{u}| = 3\ \mathrm{m\,s^{-1}}$) in the study domain is applied. The veering angles from offshore to onshore are 68.1, 58.1, 48.4, 32.8, and 28.7 degrees to the right of the steady wind. The thin dashdot quarter-circular curves denote the percentage of the wind-driven current speed to the wind speed, which are 1, 2, 3, 4, and 5% from the origin, and the thin dotted line indicates the direction of 45 degrees to the right of the wind stress.

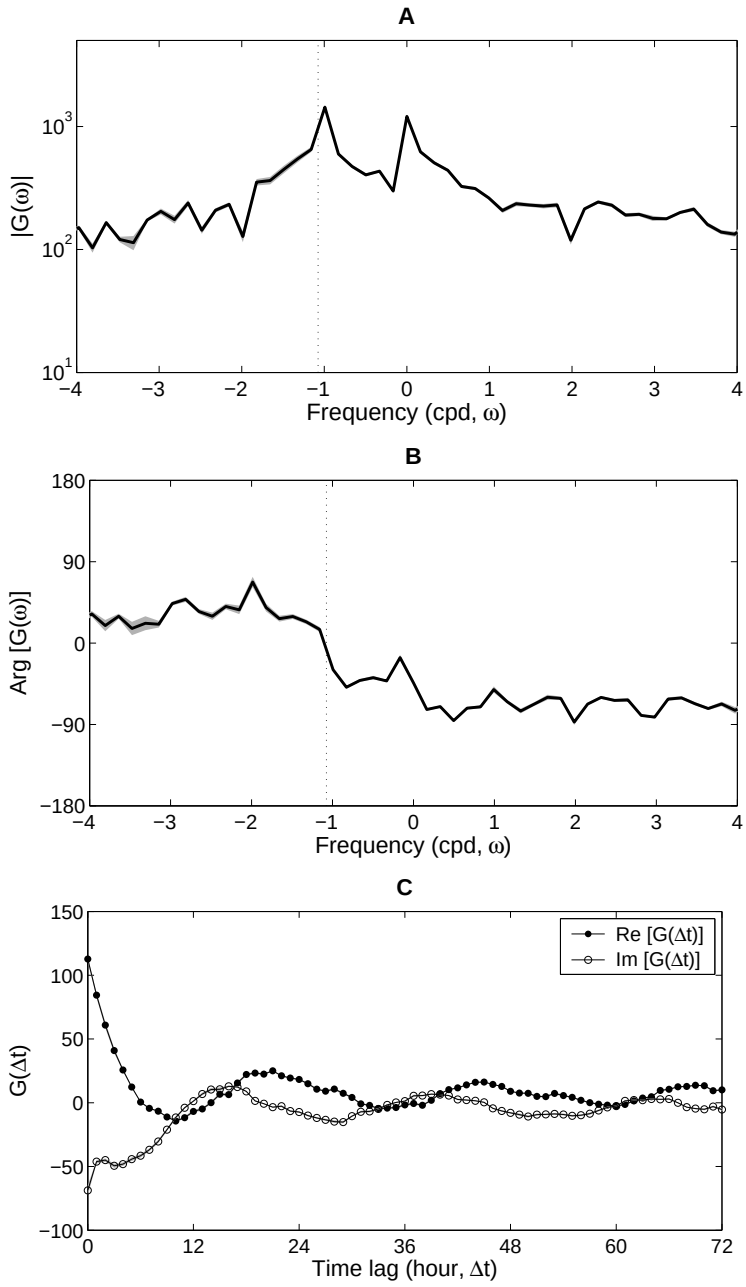

Figure 4.12: The linearly estimated TIWIRF. A and B: The magnitude and phase of the inversely Fourier transformed TIWIRF. C. Amplitude. The TIWIRF is estimated with the surface currents and 6 days time lag stacked wind stress, and the uncertainty is calculated from 30 realizations using the Jackknife method. The vertical dot line indicates the inertial frequency ($\omega = -1.07$ cpd) in the study domain.

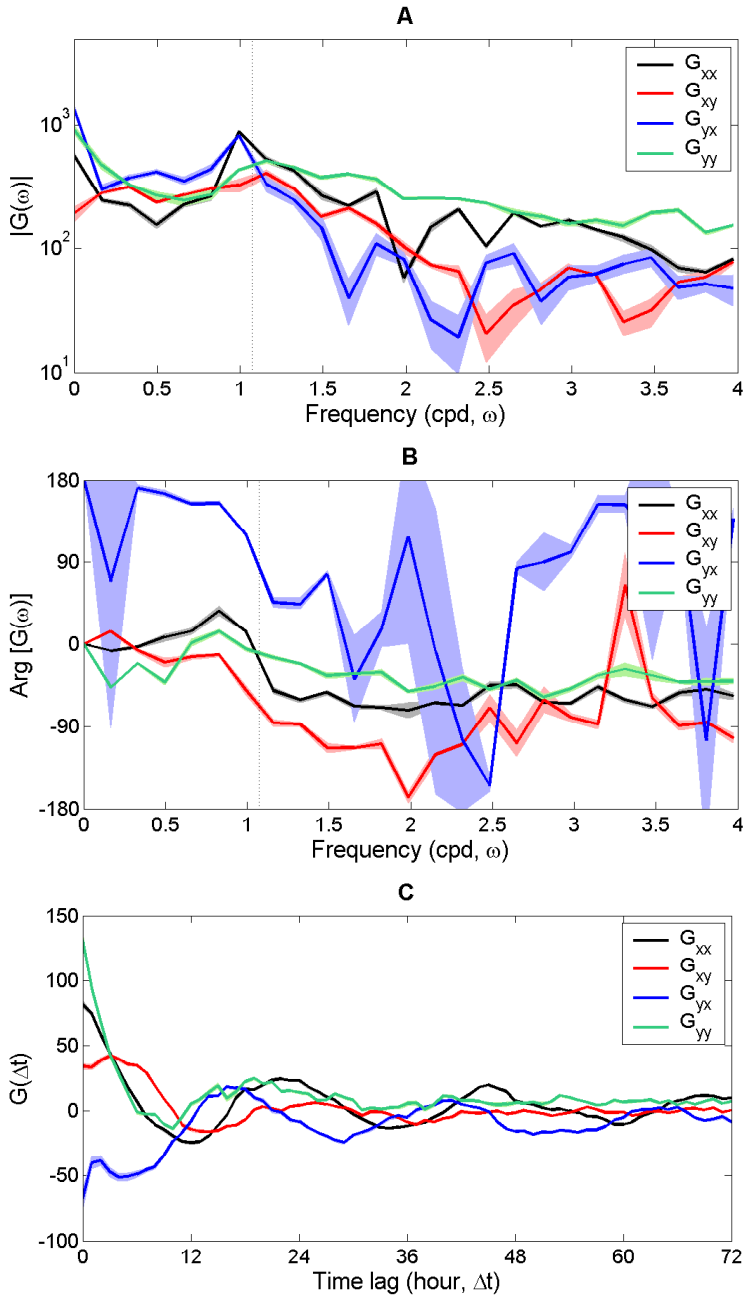

Figure 4.13: The linearly estimated TAWIRF. A and B: The magnitude and phase of the inversely Fourier transformed TIWIRF. C. Amplitude. The TAWIRF and its error bar are estimated in the same way of the TIWIRF (Figure 4.12). The vertical dot line indicates the inertial frequency ($\omega = 1.07$ cpd) in the study domain.

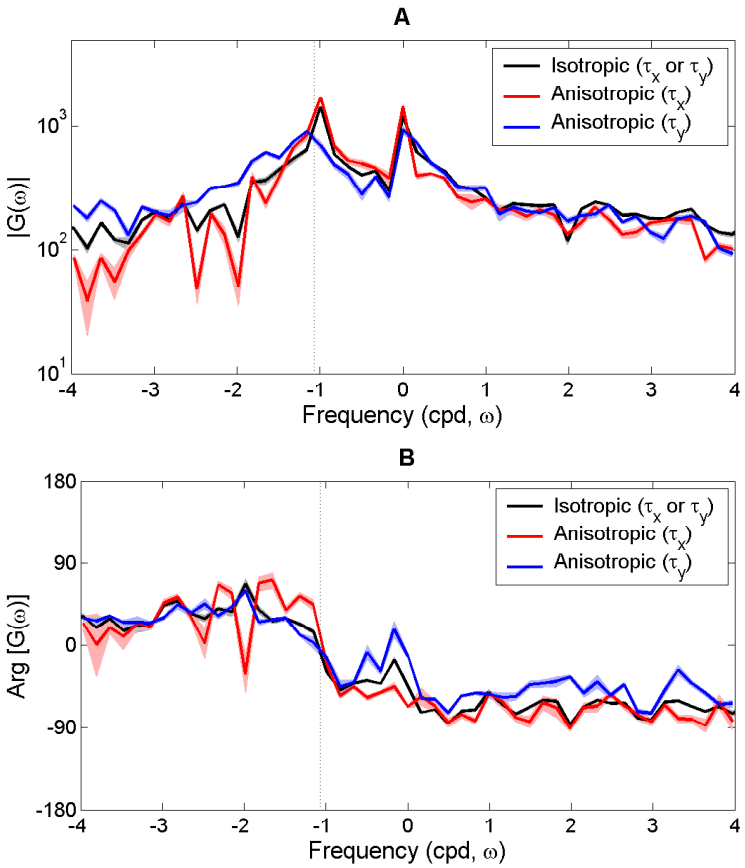

Figure 4.14: The magnitude and phase of the linearly estimated TIWIRF and TAWIRF for wind stress (τ_x and τ_y), respectively. A. Magnitude. B. Phase. The phase of the TAWIRF for the y-directional wind stress (τ_y) is shifted down 90 degrees to align with others. The solid curves in A and B are the same as in Figures 4.12A and 4.12B, respectively. The vertical dot line indicates the inertial frequency ($\omega = -1.07$ cpd) in the study domain.

yields surface currents at 43±2 degrees to the right of the wind direction. The suppression of the crossshore response is still evident, as the veering angle of the response rotates the current away from the crossshore direction when compared to the isotropic response. The fraction of surface current variance explained by the TIWIRF and TAWIRF with 6-day time lag are 43.9 and 54.7% of the total current variance, respectively (Figure 4.5B).

Although the linear WIRFs show anisotropy in the wind response, the responses to onshore and offshore winds (or upcoast and downcoast winds) are identical.

4.5.3 Nonlinear WIRFs

The magnitude and phase of the WIRF ($\mathbf{G}$ or $\mathbf{H}$) in the linear regression are similar to those of the linear part ($\mathbf{G_1}$ or $\mathbf{H_1}$, respectively) in the nonlinear regression (not shown). The nonlinear term ($\mathbf{G_2}$ or $\mathbf{H_2}$) controls the asymmetric current response. However, their contributions can not be simply presented in the form of the linearly estimated WIRFs (e.g., magnitude and phase in Figures 4.8 and 4.14) because of nonlinearity .

The time integrations of the temporal amplitudes of the linear and nonlinear WIRFs are shown in Figure 4.15 to examine the anisotropic and asymmetric responses to four different steady winds. While the linear FIWIRF (Figure 4.15A) has an isotropic response, the nonlinear FIWIRF shows a different response to onshore and offshore winds. The response of the nonlinear FIWIRF to onshore wind is closer to alongcoast compared to the onshore wind response of the linear FIWIRF, and the offshore wind generates a much stronger response at about 40 degrees to the right of the wind direction. Because of the isotropy assumption, the response of the nonlinear FIWIRF to the upcoast wind is identical to that to the onshore wind, and the same for the offshore wind and downcoast wind.

The time integrated responses of the linear and nonlinear FAWIRFs are shown in Figures 4.15B and 4.15C, respectively. The response of the linear FAWIRF was discussed in Figure 4.9A, but is plotted with all four quadrants for easier comparison to the nonlinear results with the current suppressed in the onshore direction and enhanced in the offshore direction (Figure 4.15B). The response of the nonlinear FAWIRF shows asymmetric features in the coastal region (Figure 4.15C).

The time integrated responses of the linear/nonlinear TIWIRFs and TAWIRFs are shown in Figures 4.15D–4.15F, and those have nearly the same pattern as the frequency domain WIRFs.

4.5.4 Wind-driven surface circulation

One of the benefits of the WIRF is to provide a complete description of the wind-driven flow. The complexity of the wind-driven surface current was examined (not shown) using the nonlinear FAWIRF and two wind cases: constant wind and diurnal wind (hourly composite mean wind stress). The responses to the steady wind from multiple directions (not shown) reflect coastline and bathymetry effects. The surface current response to the onshore wind is inhibited by coastline and veers either up- or down-coast. The response to the down-coast wind within 160–240T is 30–40%

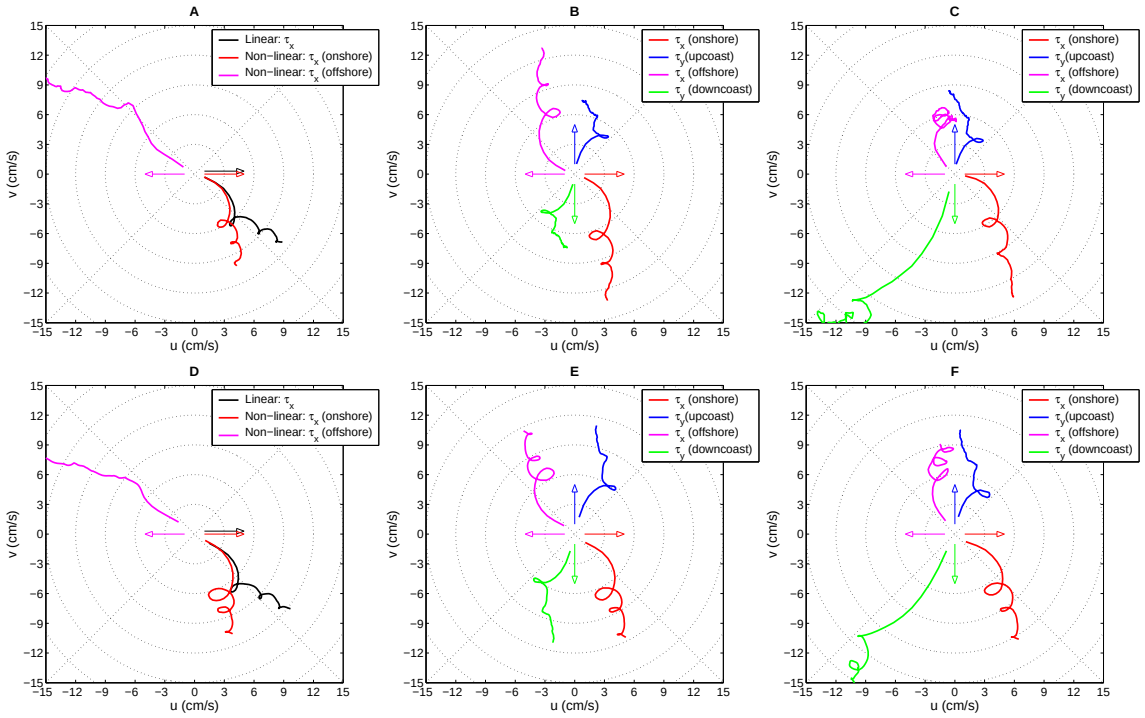

Figure 4.15: Top row: Time integrations of the temporal amplitudes of the frequency domain WIRFs for a constant wind stress during 3 days. A. Linear FIWIRF ($\hat{\mathbf{u}} = \mathbf{H}\hat{\boldsymbol{\tau}}$) and nonlinear FIWIRF ($\hat{\mathbf{u}} = \mathbf{H_1}\hat{\boldsymbol{\tau}} + \mathbf{H_2}|\hat{\boldsymbol{\tau}}|$). B. Linear FAWIRF, which is a four quadrant plot of Figure 4.9A. C. Nonlinear FAWIRF. Bottom row: Time integrations of the time domain WIRFs for a constant wind stress during 3 days. D. Linear TIWIRF ($\mathbf{u} = \mathbf{G}\boldsymbol{\tau}_N$) and nonlinear TIWIRF ($\mathbf{u} = \mathbf{G_1}\boldsymbol{\tau}_N + \mathbf{G_2}|\boldsymbol{\tau}_N|$). E. Linear TAWIRF, which is a four quadrant plot of Figure 4.9B. F. Nonlinear TAWIRF. The constant wind stress is presented as an arrow for each direction: up (upcoast), down (downcoast), right (onshore), and left (offshore). The thin dashdot circular curves denote the percentage of the wind-driven current speed to the wind speed, which are 1, 2, 3, 4, and 5% from the origin, and the thin dotted lines indicate the direction of 45 degrees to the right of the wind stress.

stronger than response to the wind in other directions. The diurnal wind generates rotating currents with the elliptical or skewed responses by the coastline with different phases (not shown) resulting from varying time lags.

4.5.5 Residual variance ratio

The total residual variance ratio of the nonlinearly estimated WIRFs plotted against the number of subsamples (Figure 4.5A for the FIWIRF and FAWIRF) and the number of time lags (Figure 4.5B for the TIWIRF and TAWIRF) show improvement over the linear fits. Compared with the linear estimate, the total residual ratio is reduced by about 5% in the frequency domain estimates (FIWIRF and FAWIRF) and by about 4% for the time domain estimates (TIWIRF and TAWIRF). This is not significant beyond one standard deviation, but it is greater than that expected for adding red noise parameters and the physical results are sensible (Figure 4.15).

4.5.6 Errors in the WIRF

The error in the estimated WIRF can result from several sources: the measurement errors of surface currents and wind, statistical uncertainty, and errors introduced by the parameterization of the WIRF. The measurement error of surface currents in the study domain is about 5.5 $\mathrm{cm\,s^{-1}}$ (section 3.3.3), and is assumed to be uncorrelated in time so that averaging over many realizations reduces the effects of this error. The wind measurement error is reported as $\pm 2\%$ of the wind speed (0.04–0.18 $\mathrm{m\,s^{-1}}$). The statistical uncertainty is estimated using the Jackknife method, but that does not completely characterize the error. Least-squares methods include error estimates, which account for missing information.

The contamination of the observed currents by the measurement noise and other processes is modeled by a white noise spectrum used to calculate a SNR at each frequency. The estimated linear frequency domain WIRF (equation 4.23) can be rewritten as

$$\mathbf{H} = \left(\hat{\boldsymbol{\tau}}^{\dagger}\mathbf{R_a}^{-1}\hat{\boldsymbol{\tau}} + \mathbf{P}^{-1}\right)^{-1}\hat{\boldsymbol{\tau}}^{\dagger}\mathbf{R_a}^{-1}\hat{\mathbf{u}} \tag{4.38}$$

$$= \left(\hat{\boldsymbol{\tau}}^{\dagger}\hat{\boldsymbol{\tau}} + \mathbf{P}^{-1}\kappa^2\right)^{-1}\hat{\boldsymbol{\tau}}^{\dagger}\hat{\mathbf{u}}, \tag{4.39}$$

where $\mathbf{R_a} = \kappa^2\mathbf{I}$ is the noise level assumed as a constant, and $\mathbf{P}$ is the prior uncertainty of the WIRF.

The posterior uncertainty covariance ($\hat{\mathbf{P}}$) of the WIRF is

$$\hat{\mathbf{P}} = \left(\hat{\boldsymbol{\tau}}^{\dagger}\mathbf{R_a}^{-1}\hat{\boldsymbol{\tau}} + \mathbf{P}^{-1}\right)^{-1} = \kappa^2\left(\hat{\boldsymbol{\tau}}^{\dagger}\hat{\boldsymbol{\tau}} + \mathbf{P}^{-1}\kappa^2\right)^{-1}. \tag{4.40}$$

The amplitude of the uncertainty is somewhat arbitrary, because the choice of a white noise spectrum is oversimplified and poorly constrained, but the posterior uncertainty (not shown) has larger errors away from the frequencies with strong driving.

This error analysis does not account for systematic errors in the wind or current measurements. The errors in the wind measurements translate to model errors in the regression, so that the

problem becomes deconvolution, for solution by total least squares ([Golub and Van Loan(1980), Van Huffel and Vandewalle(1991)]) or other methods, which are outside the scope of this work.

4.6 Discussion

Wind impulse response functions are statistically estimated from spatially averaged observed surface currents and shore station wind in both frequency and time domains to examine anisotropic and nonlinear current response in the coastal area. The surface current response due to coastal wind forcing is found to be anisotropic, i.e., dependent on wind direction, in contrast to the isotropic response in the open ocean. Bottom and coastline boundaries including islands and headlands support local sea level gradients due to wind and may also yield anisotropic bottom drag. For steady wind forcing for 3 days, the linear isotropic current response estimated in the frequency or time domain is 42 ± 2 degrees to the right of wind direction regardless of the wind direction. However, the linear anisotropic current response in both domains is 10 ± 4 degrees to the right of the upcoast wind and 71 ± 3 degrees to the right of the onshore wind. The linearly estimated FAWIRF and TAWIRF by construction produce the same response to onshore and offshore winds (or upcoast and downcoast winds). Only the nonlinear WIRFs can show asymmetric current response. The surface current response discussed in this chapter includes the wind-driven components coupled with the bottom and depth effects.

The instantaneous acceleration of the current is proportional to wind stress, friction, and pressure gradients. The direct correlation of the wind stress and the acceleration of surface currents ($\partial \mathbf{u}/\partial t$) is relatively low due to noise in the derivatives. Instead of the momentum balance, the regression is used, which implies time integration of the momentum equations. The response to the wind includes sea surface set up due to the cumulative effects of currents interacting with topography. Thus the wind response we consider here can include currents accelerated by the pressure gradients due to sea surface set up, as considered by [Ekman(1905)]. The anisotropy of the coastline and bathymetry leads to an anisotropic response of the currents both through pressure set up and frictional effects.

For the comparison of estimated WIRFs, the total residual variance ratio is calculated by cross-validation for the training data and the uncertainty is estimated using the Jackknife method. The regularization in the frequency and time domain WIRF estimates is picked to optimize the cross-validation performance. The error bars of the isotropic and anisotropic WIRFs do not overlap, so the improvement in fitting attained by allowing anisotropy is robust.

The advantages in the use of spatially averaged surface currents are to avoid the ambiguity in the spatial decorrelation of both surface currents and wind stress, to increase the SNR in the surface currents with less missing data, and to provide a representative view of the study domain. In addition, the effects of missing data are potentially represented in the error bars calculated by the Jackknife method. Missing data are less of a problem for the time domain calculation of the WIRF. Because the correlation uses only the data available, and no interpolation or zero-filling is used. This

comes at the expense of non-positive-definite covariance matrices, and the crude regularization we apply may affect the results. Similar results for both frequency and time domains estimates show that missing data are not a dominant effect.

While the data and methodology presented document the anisotropic wind response of the ocean near San Diego, it is noteworthy to emphasize that the response is a combination of both directly wind-driven flow and alongshore geostrophic response to upwelling/downwelling favorable winds. Given the site specific nature of the latter dynamics, a logical extension of this work would be a broad area examination of the response function along the U.S. West Coast (USWC), taking advantage of the growing HF radar mapped surface currents records (Figure 7.1A). It is expected that the spatially varying USWC wind climate, coupled with a complex coastline geometry, will introduce gradients in the geostrophic response that can be diagnosed in those data sets using the wind impulse response functions described in this chapter.

The anisotropic wind response in coastal waters has broad ranging implications to the understanding and prediction of the transport of biologics, contaminants, spilled oil, and other water-borne constituents in the coastal zone, especially for those scenarios where 'rule of thumb' estimates of wind drift are used for predicting the Lagrangian behavior of the upper ocean. This is especially prevalent in operational communities dealing with oil spills and search/rescue response. In addition, anisotropic surface current response suggests that coastal upwelling indices and estimates based upon wind climatology may have biases that need further investigation. The previously mentioned study would be a first step in this direction, and assist in growing interests in including ocean dynamics in simple coastal productivity models and fisheries research.

4.7 Appendix

4.7.1 WIRFs in Ekman theory

The Ekman theory at finite depth is considered in the frequency domain.

Isotropic approach

The momentum equations with depth-independent viscosity (ν) in physical space,

$$\frac{\partial u}{\partial t} - f_c v + a_{xx} * u = \nu \frac{\partial^2 u}{\partial z^2}, \tag{4.41}$$

$$\frac{\partial v}{\partial t} + f_c u + a_{yy} * v = \nu \frac{\partial^2 v}{\partial z^2}, \tag{4.42}$$

are combined and Fourier transformed into the frequency domain assuming an isotropic friction coefficient ($a_{xx} = a_{yy} = r\delta(t)$ and $a_{xy} = a_{yx} = 0$):

$$\lambda^2 \hat{\mathbf{u}}(z,\omega) = \frac{\partial^2 \hat{\mathbf{u}}(z,\omega)}{\partial z^2}, \tag{4.43}$$

where $\lambda = \sqrt{[i(\omega + f_c) + r]/\nu}$. $\hat{\boldsymbol{\tau}}(\omega)$ and $\hat{\mathbf{u}}(z,\omega)$ denote the wind stress and currents in the frequency domain. When boundary conditions at the surface ($z = 0$) and finite depth ($z = -h$) are applied, the upper boundary condition sets viscous stress equal to wind stress,

$$\left.\frac{\partial \hat{\mathbf{u}}(z,\omega)}{\partial z}\right|_{z=0} = \frac{\hat{\boldsymbol{\tau}}(\omega)}{\rho\nu}. \tag{4.44}$$

If the lower boundary condition sets flow to zero,

$$\hat{\mathbf{u}}(z,\omega)|_{z=-h} = 0, \tag{4.45}$$

the FIWIRF is

$$\mathbf{H}(z,\omega) = \frac{\hat{\mathbf{u}}(z,\omega)}{\hat{\boldsymbol{\tau}}(\omega)} = \frac{\sinh\lambda(z+h)}{\lambda\rho\nu\cosh(\lambda h)}. \tag{4.46}$$

If the lower boundary condition enforces zero deep stress,

$$\left.\frac{\partial \hat{\mathbf{u}}(z,\omega)}{\partial z}\right|_{z=-h} = 0, \tag{4.47}$$

the FIWIRF becomes

$$\mathbf{H}(z,\omega) = \frac{\hat{\mathbf{u}}(z,\omega)}{\hat{\boldsymbol{\tau}}(\omega)} = \frac{\cosh\lambda(z+h)}{\lambda\rho\nu\sinh(\lambda h)}, \tag{4.48}$$

and its magnitude and phase are identical to equation 4.46.

Anisotropic approach

The momentum equations in the frequency domain are

$$\alpha_{xx}\hat{u} + \alpha_{xy}\hat{v} = \nu\frac{\partial^2\hat{u}}{\partial z^2}, \tag{4.49}$$

$$\alpha_{yx}\hat{u} + \alpha_{yy}\hat{v} = \nu\frac{\partial^2\hat{v}}{\partial z^2}, \tag{4.50}$$

where $\alpha_{xx} = i\omega + a_{xx}$, $\alpha_{xy} = -f_c + a_{xy}$, $\alpha_{yx} = f_c + a_{yx}$, and $\alpha_{yy} = i\omega + a_{yy}$. When equation 4.49 is used to solve for $\hat{v}(z,\omega)$,

$$\hat{v} = \frac{1}{\alpha_{xy}}\left(\nu\hat{u}^{(2)} - \alpha_{xx}\hat{u}\right), \tag{4.51}$$

and substituted into equation 4.50, the fourth order ordinary differential equation results:

$$\nu^2\hat{u}^{(4)} - \nu(\alpha_{xx} + \alpha_{yy})\hat{u}^{(2)} + (\alpha_{xx}\alpha_{yy} - \alpha_{xy}\alpha_{yx})\,\hat{u} = 0, \tag{4.52}$$

where $B^{(n)}$ is the n-th order of derivative with respect to z. Assuming that the solution of equation 4.52 is

$$\hat{u}(z,\omega) = \sum_{j=1}^{4} c_j(\omega)e^{\lambda_j(\omega)z}, \tag{4.53}$$

and this assumption works only when ν is depth-independent. From the characteristic equation of equation 4.52,

$$\hat{u}^{(4)} + p\hat{u}^{(2)} + q\hat{u}^{(1)} + s\hat{u} = 0, \tag{4.54}$$

$$\lambda^4 + p\lambda^2 + q\lambda + s = 0, \tag{4.55}$$

where $p = -\left(\alpha_{xx} + \alpha_{yy}\right)/\nu$, $q = 0$, and $s = \left(\alpha_{xx}\alpha_{yy} - \alpha_{xy}\alpha_{yx}\right)/\nu^2$. The quartic equation can be solved by Ferrari-Cardan's method ([Smith(1959)]). An additional parameter (m) is introduced,

$$(\lambda^2 + p + m)^2 = (p + 2m)\lambda^2 + (p^2 - s + 2pm + m^2), \tag{4.56}$$

and three m are found to satisfy that determinant of the right hand side of equation 4.56 is equal to zero $\left[D = -4(p + 2m)(p^2 - s + 2pm + m^2) = 0\right]$:

$$m_1 = -\frac{p}{2} \text{ and } m_{2,3} = -p \pm \sqrt{s}. \tag{4.57}$$

For each m, four characteristic roots (λ) exist. When $m = -p/2$,

$$\lambda^2 = -\frac{p}{2} \pm \sqrt{\frac{p^2}{4} - s} \tag{4.58}$$

$$= \frac{\alpha_{xx} + \alpha_{yy}}{2\nu} \pm \frac{1}{\nu}\sqrt{\frac{\left(\alpha_{xx} - \alpha_{yy}\right)^2}{4} + \alpha_{xy}\alpha_{yx}}. \tag{4.59}$$

When $m = -p \pm \sqrt{s}$,

$$\lambda_{1,2} = \frac{1}{2}\left(\sqrt{-p + 2\sqrt{s}} \pm \sqrt{-p - 2\sqrt{s}}\right) \tag{4.60}$$

and

$$\lambda_{3,4} = \frac{1}{2}\left(\sqrt{-p - 2\sqrt{s}} \pm \sqrt{-p + 2\sqrt{s}}\right). \tag{4.61}$$

The boundary conditions at the top (wind stress) and bottom (zero deep stress) are applied,

$$\left.\frac{\partial \hat{u}(z,\omega)}{\partial z}\right|_{z=0} = \frac{\hat{\tau}_x(\omega)}{\rho\nu}, \tag{4.62}$$

$$\left.\frac{\partial \hat{v}(z,\omega)}{\partial z}\right|_{z=0} = \frac{\hat{\tau}_y(\omega)}{\rho\nu} \Longrightarrow \left.\frac{1}{\alpha_{xy}}\left(\nu\hat{u}^{(3)} - \alpha_{xx}\hat{u}^{(1)}\right)\right|_{z=0} = \frac{\hat{\tau}_y(\omega)}{\rho\nu}, \tag{4.63}$$

$$\left.\frac{\partial \hat{u}(z,\omega)}{\partial z}\right|_{z=-h} = 0, \tag{4.64}$$

and

$$\left.\frac{\partial \hat{v}(z,\omega)}{\partial z}\right|_{z=-h} = 0 \Longrightarrow \left.\frac{1}{\alpha_{xy}}\left(\nu\hat{u}^{(3)} - \alpha_{xx}\hat{u}^{(1)}\right)\right|_{z=-h} = 0. \tag{4.65}$$

Equation 4.52 can be solved as an inverse problem ([Wunsch(1996)]).

$$\mathbf{Ac} = \mathbf{d}, \tag{4.66}$$

where $\mathbf{c} = \begin{bmatrix} c_1 \\ c_2 \\ c_3 \\ c_4 \end{bmatrix}$, $\mathbf{d} = \begin{bmatrix} \frac{\hat{\tau}_x(\omega)}{\rho\nu} \\ \frac{\hat{\tau}_y(\omega)}{\rho\nu}\alpha_{xy} \\ 0 \\ 0 \end{bmatrix}$, and

$$\mathbf{A} = \begin{bmatrix} \lambda_1 & \lambda_2 & \lambda_3 & \lambda_4 \\ \nu\lambda_1^3 - \alpha_{xx}\lambda_1 & \nu\lambda_2^3 - \alpha_{xx}\lambda_2 & \nu\lambda_3^3 - \alpha_{xx}\lambda_3 & \nu\lambda_4^3 - \alpha_{xx}\lambda_4 \\ e^{-\lambda_1 h} & e^{-\lambda_2 h} & e^{-\lambda_3 h} & e^{-\lambda_4 h} \\ (\nu\lambda_1^3 - \alpha_{xx}\lambda_1)e^{-\lambda_1 h} & (\nu\lambda_2^3 - \alpha_{xx}\lambda_2)e^{-\lambda_2 h} & (\nu\lambda_3^3 - \alpha_{xx}\lambda_3)e^{-\lambda_3 h} & (\nu\lambda_4^3 - \alpha_{xx}\lambda_4)e^{-\lambda_4 h} \end{bmatrix}.$$

The anisotropic response functions in the x-direction (H_{xx} and H_{xy}) are estimated by solving equation 4.66 numerically at each finite frequency and substituting the model efficient ($\mathbf{c}$) into equation 4.53. Then, the anisotropic response functions in the y-direction (H_{yx} and H_{yy}) are estimated from equation 4.51. All FAWIRFs for three choices of m in equation 4.57 show the identical magnitude and phase.

4.7.2 Estimate of adjustment terms

The parameters of the Ekman model, including kinematic viscosity (ν) and adjustment terms (a_{xx}, a_{xy}, a_{yx}, and a_{yy}), can be estimated from data-derived WIRFs. However, there are limitations in the estimate due to the errors in the estimated WIRFs. In addition, the transformation between the parameters and the WIRF is nonlinear, and must be inverted iteratively. As the simplest case, constant adjustment terms and viscosity are varied to approximately fit the width and the magnitude of the peak at the Coriolis frequency. The peak of the WIRF near zero frequency is not predicted by the Ekman model, and may indicate frequency-dependent adjustment terms and Ekman layer parameters. The magnitude of the model WIRF is scaled by a constant for a compensating shift in magnitude of the data-derived WIRFs, which provides a clue for the viscosity estimate. The magnitude and phase of the FIWIRF and the model fit are shown in Figures 4.16A and 4.16C, respectively. The estimated viscosity (ν) is 2.1×10^{-5} m^2 s^{-1} in both FIWIRF and FAWIRF, and is within the typical viscosity range (section 4.2.2). The isotropic friction coefficient (r) is equal to 3.16×10^{-6} s^{-1}. The anisotropic adjustment terms based on the data-derived FAWIRF are $r_{xx} = 1 \times 10^{-9}$ s^{-1}, $r_{xy} = -8 \times 10^{-6}$ s^{-1}, $r_{yx} = 0$, and $r_{yy} = 1 \times 10^{-5}$ s^{-1} (Figures 4.16B and 4.16D). Although the adjustment terms can be a function of frequency, this is beyond the scope of this dissertation.

This chapter, in part, has been accepted for publication of the material as it is supposed to be appeared in *Journal of Physical Oceanography*, 2009, Kim, S. Y., B. D. Cornuelle, and E. J. Terrill titled by 'Anisotropic response of surface currents to the wind in a coastal region', doi: 10.1175/2009JPO4013.1. The dissertation author was the primary investigator and author of this paper.

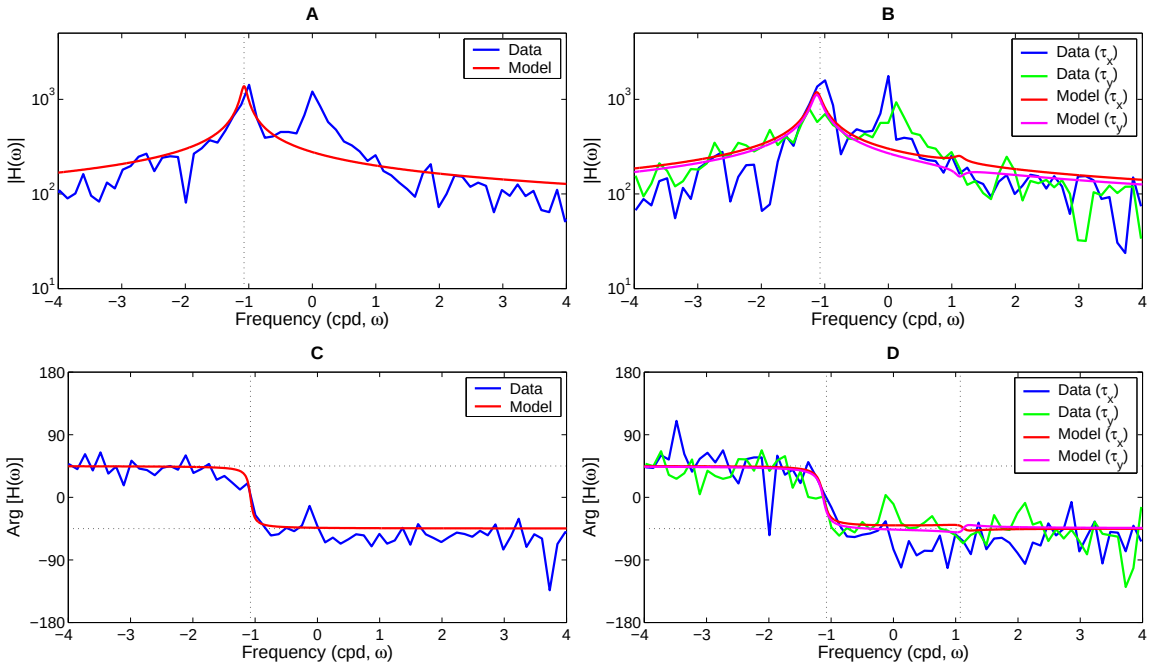

Figure 4.16: Comparison of the model WIRF (thick line) and the data-derived WIRF (thin line). A and C: Magnitude and phase of the FIWIRF ($r = 3.16 \times 10^{-6}$ s^{-1}). B and D: Magnitude and phase of the FAWIRF ($r_{xx} = 1 \times 10^{-9}$ s^{-1}, $r_{xy} = -8 \times 10^{-6}$ s^{-1}, $r_{yx} = 0$, and $r_{yy} = 1 \times 10^{-5}$ s^{-1}). The estimated viscosity (ν) is 2.1×10^{-5} m^2 s^{-1} in both FIWIRF and FAWIRF. The vertical dot line indicates the inertial frequency ($\omega = -1.07$ cpd) in the study domain.

Chapter 5

Decomposing observations of high-frequency radar derived surface current by their forcing mechanisms

Abstract

Surface current observations from a high-frequency radar network deployed in southern San Diego are decomposed according to their driving forces: pure tides, local winds, low frequency pressure gradient, and several continuous frequency bands. In contrast to regions where circulation is dominated by a single forcing mechanism, in the San Diego region many superposed ocean responses are present as a result of the complicated topography and relatively weak winds in the region. This necessitates the application of a statistical decomposition approach. Surface currents driven by pure tides are calculated using harmonic analysis. The locally wind-driven surface currents are estimated by regression of observed winds on observed surface currents (Chapter 4). The surface currents with the wind forced component removed are then filtered by weighted least-squares fitting assuming three colored signals and white noise: low frequency band ($|\omega| \leq 0.4$ cycles per day) and cuspate tidal peaks at the diurnal (K1) and semidiurnal (M2) frequencies. The power spectrum of the locally wind-driven surface currents shows a strong diurnal peak superposed on a red spectrum, similar to the power spectrum of the observed winds. The magnitude of the locally wind-driven surface currents is typically 3–5% of the wind speed, and their veering angles vary 30–50 degrees to the right of the wind at zero time lag. The frictional momentum balance is explored by calculating the coherence between the atmospherically-adjusted sea-surface height difference and the surface currents within a distinctive low frequency band. The spatial correlations of each part of the decomposed surface currents exhibit Gaussian and exponential shapes with varying decorrelation length scales.

5.1 Introduction

Coastal surface currents are a mixture of the oceanic responses to the local winds, remote wind forcing via eddies and coastal trapped waves, tides, pressure gradients, and meteorological fluxes of heat and fresh water ([Ewing(1950), Munk and Cartwright(1966), Essen et al.(1983), Alpers(1985), Price et al.(1986), Prandle(1987), Ng(1993a), Ng(1993b), Shay et al.(1995)]).

Surface currents driven by the local wind are classified into two kinds of currents by the nature of the mechanical coupling: wind-drift currents due to friction of the wind ([Ekman(1905), Bye(1965), Price et al.(1987)]) and wave-drift currents (Stokes drift) due to surface waves ([Bye(1967), Kenyon(1969)]). Wind-drift currents (called wind-driven currents herein) remain in the wall layer ([Csanady(1982)]) or the inertial sublayer ([Leibovich(1977)]), which is a logarithmic boundary layer ($O(1)$ m) between the air-sea interface and the top of Ekman layer ([Bye(1965), Wu(1975)]). The veering angles of wind-driven currents within the wall layer range from zero to 45 degrees to the right of the wind direction ([Csanady(1982), Fernandez et al.(1996)]), and their magnitudes are 2–3% of the wind speed ([Bye(1965), Churchill and Csanady(1983), Wu(1983), Weber(1983), Spaulding(1999)]). In statistical analyses of the wind and currents, the locally wind-driven currents have been parameterized by the wind velocity or wind stress using linear and nonlinear models ([Prandle(1987), Essen(1993), Ng(1993a), Rabinovich et al.(2006)]). Meanwhile, the wind impulse response function (WIRF) between wind stress and currents within the Ekman layer has been studied in a complementary way ([Ekman(1905), Gonella(1972), Weller(1981), Rio and Hernandez(2003)] and Chapter 4). The wind-driven surface layer jet within the mixing layer depends on the heat flux and the surface wind stress ([Phillips(1966), Price et al.(1986)]), and seasonal and daily stratification changes can induce a signal of 1–3 $\mathrm{cm\,s^{-1}}$ ([Graber et al.(1997)]) and larger ([Cronin and Kesseler(2008)]). On the other hand, Stokes drift is dependent on the directional wave spectrum ([Kenyon(1969), Essen(1993)]), and has been reported as 7–14 $\mathrm{cm\,s^{-1}}$ at the surface and $\sim$2 $\mathrm{cm\,s^{-1}}$ at 1 m depth as an exponentially decayed profile under typical wind speed ([Graber et al.(1997)]). Because the high-frequency (HF) radar observes only the averaged currents of the upper one meter, the surface layer jet and Stokes drift in this chapter will not be distinguishable from the Ekman response (section 5.6.1).

Tidal forcing produces phase-locked pure tidal currents and near-tidal-band currents ([Munk et al.(1965), Munk et al.(1970), Hendershott and Munk(1970), Hendershott(1973)]). The phase-locked tidal currents are the sum of the barotropic tides and the baroclinic internal tides. The near-tidal-band currents arise from modulation of the tides by nonlinear interactions (e.g. cuspate tidal peaks) or due to slowly varying parameters (e.g., stratification) in linear dynamics. From surface current observations the barotropic and baroclinic tides may be distinguishable by the spatial variation of the amplitude and phase due to changes in topography or stratification.

Besides tidal forcing, alongshore pressure gradients, typically generated by large scale atmospheric forcing, can drive the subtidal surface currents ([Chelton and Davis(1982), Allen and Denbo(1984), Lentz and Winant(1986)]). These subtidal currents may include

coastally trapped waves ([Chapman(1983), Brink et al.(1987), Brink(1991)]) and other climate signals such as El-Nino, Southern Oscillation Index (SOI), and Pacific Decadal Oscillation (PDO) ([Enfield and Allen(1980), Chelton and Enfield(1986), Johnson and O'Brien(1990), Trenberth and Hurrell(1994)]).

Finally, the residual currents not explained by the other forcing terms are considered to be a result of intermittent local eddies, high-frequency tidal harmonic surface currents, outliers, and observational errors. There is precedence in the literature of separating currents based upon their forcing such as decomposing tidal currents and residual currents using harmonic analysis or band-pass filters ([Prandle(1987), Shay et al.(1995)]). Moreover, the locally wind-driven surface currents were estimated from the de-tided surface currents in two ways: a simple regression between surface currents and winds ([Essen et al.(1983), Prandle and Player(1993)]) and a fit using rotary empirical orthogonal functions ([Ng(1993a)]). Surface currents off southern San Diego have a mixed response from several driving forces: tidal constituents, diurnal (plus harmonics) wind, broad-band wind, diurnal heat flux, and alongshore pressure gradient. Therefore the use of a band-pass filter before the separation of locally wind-driven currents and tidal currents can be problematic, because locally wind-driven currents can have similar spectral content as the tidal currents. Moreover, because of missing data, least-squares spectral analysis is needed instead of conventional band-pass filters.

The surface current decomposition is motivated by the following questions: How much surface current variance is explained by each forcing component? What are the characteristics and variability of the surface currents driven by each forcing component? How can these results be used to create a statistical surface current model based upon the observations?

This chapter is organized into three main sections. First, observations of winds, surface tides (sea-surface heights), and surface currents are described (section 5.2). Next, the decomposition techniques using a statistical regression between winds and surface currents (Chapter 4) and a weighted least-squares fitting method are addressed (section 5.3). Last, the characteristics of the decomposed surface currents are discussed including typical time series, the variance fraction attributed to each component, and the spatially averaged correlations (section 5.4).

5.2 Observations

Surface currents used in this analysis were observed by three HF radars ($\sim$25 MHz) deployed off southern San Diego (Figure 5.1): Point Loma, Border Park, and Coronado Islands. Winds are observed at two shore stations – Scripps Pier (SIO) and Tijuana River (TJR), and are converted into wind stress using the drag coefficient described in [Large and Pond(1981)]. For the estimate of the alongshore pressure difference, the sea-surface heights (SSHs) at San Diego Bay (SDB) and Los Angeles Harbor (LAH) and the atmospheric pressure data at San Diego Lindbergh Field (SAN) and Los Angeles International Airports (LAX) are used. Observations used in this study are hourly averages over two years (April 2003 – March 2005). The fractional data availability of the surface currents and winds is shown in Figure 5.2, and the SSH records are complete. The gray scale in

the data availability of surface currents indicates the ratio of the number of hourly vector current solutions to the number of grid points in Figure 5.1, which indicate the spatial coverage region with data at least 70% of the two-year period. The coastline of southern San Diego faces roughly west southwest (SWW), and the continental shelf break is nearly parallel to the coastline. The headland (Point Loma) is located near the northeast boundary.

5.2.1 Wind

The rotary power spectrum of the TJR wind estimated from two years of data is characterized by a diurnal peak and its harmonics superposed on a red spectrum (Figure 5.3a). The variance in the clockwise diurnal frequency is 3–4 times greater than that in the counterclockwise diurnal frequency. The SIO wind spectrum (not shown) is similar. The rotary coherence and phase between the two wind observations are estimated from 90 subsamples with 8.12-day record length, with missing observation values filled with zeros (Figures 5.3b and 5.3c, respectively). The highest coherence (0.6–0.8) is found at the diurnal (S1) and semidiurnal (S2) frequencies, and in the subdiurnal frequency band ($|\omega| < 1$ cycle(s) per day (cpd)). The phase in all significant frequencies is nearly zero.

In the time domain, the hodograph (not shown) of the hourly composite mean of the wind observations with respect to the local time shows dominant land/sea breezes and northeast-southwest polarization of the wind direction at both locations. A slight difference in the polarization between both sites is presumably due to the geography.

5.2.2 Sea surface heights (SSHs)

The SIO SSH shows lower coherence than SDB SSH (by roughly 0.1) with the SSHs at the other shore stations along the U.S. West Coast (USWC), especially in the subinertial frequency band. Moreover, the SIO SSH anomaly (SSHA) time series shows inconsistencies compared with SSHA at nearby stations. Therefore the SDB SSH is chosen to estimate the local pressure difference although it may be biased by inner harbor effects and less exposed to local wave setup.

The power spectrum of the SDB SSH (not shown) shows that the semidiurnal variance is stronger than the diurnal variance (M2>K1>O1$\simeq$S2) as shown by the SDB tidal constituents listed in Table 5.1. Since the SDB surface tide may be distorted by the frequency response of the bay, it is compared with the SSH observed at 190 NM west of San Diego (NDBC buoy, 46412). The SSH at the offshore station is 10–20% smaller and approximately 15 minutes later than that in the bay. The power spectra shape of the SSHs at two locations are similar. The atmospherically-adjusted SSHs are made by adding the algebraic sum of the atmospheric pressure and the SSH converted to decibars at each pair of stations: SAN–SDB and LAX–LAH ([Wunsch and Stammer(1997)]). While the atmospheric pressure and SSH are not observed at the same location, the atmospheric pressure is assumed to have large scale variability and the mismatch in the observed locations should be negligible.

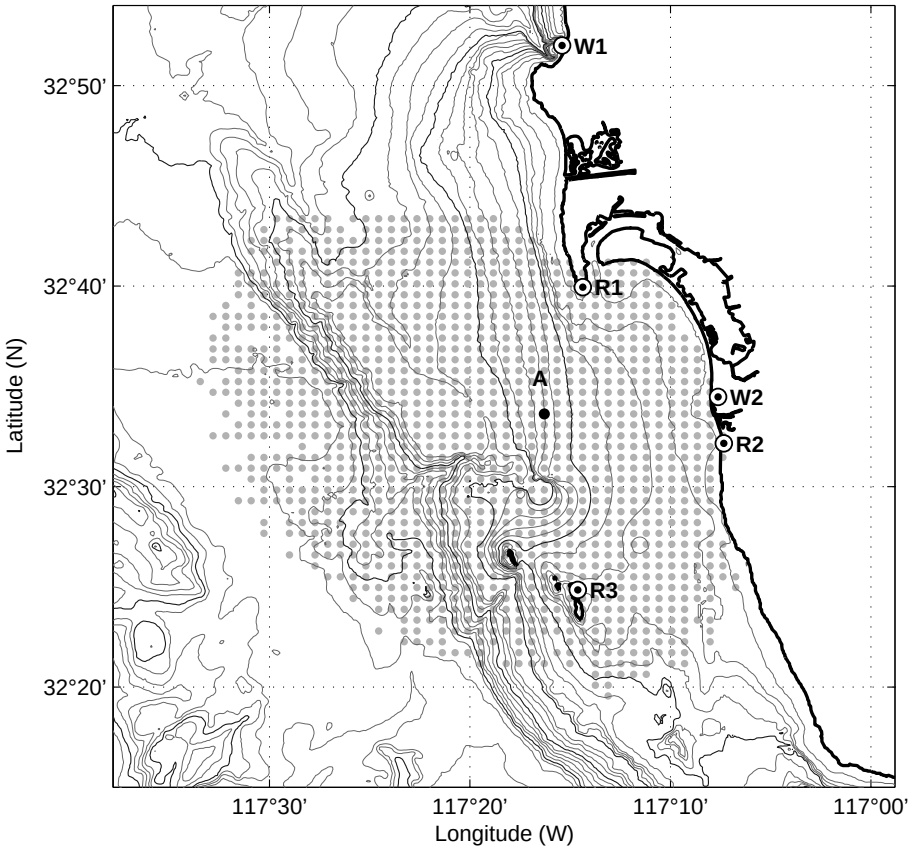

Figure 5.1: The study domain for the surface current decomposition: surface currents measured by three HF radars – Point Loma (R1), Border Park (R2), and Coronado Islands (R3) – and winds observed at two shore stations – Scripps Pier (SIO, W1) and Tijuana River (TJR, W2). The gray dots indicate the grid points that have at least 70% data availability of surface currents for two years (April 2003 – March 2005). The decomposed surface current time series at the location A are shown as an example in Figure 5.5. The bottom bathymetry contours are indicated by the thin curves with 10 m ($0 < z < 100$ m) and 50 m ($100 < z < 1000$ m) contour intervals and the thick curves at the 50, 100, 500, and 1000 m depths.

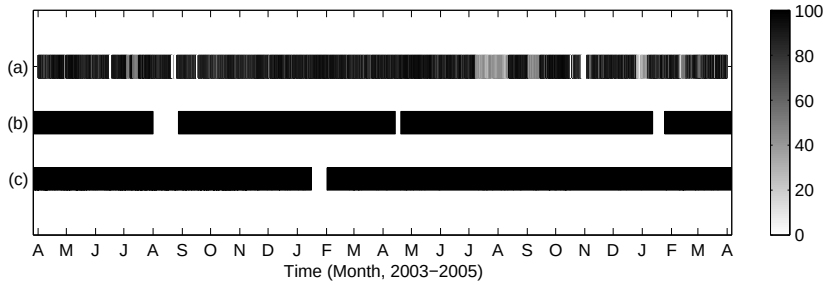

Figure 5.2: The data availability of the observations: (a) Surface currents. The gray scale indicates the spatial coverage relative to total grid points shown in Figure 5.1. (b) SIO wind (W1). (c) TJR wind (W2). The SSHs at San Diego Bay and Los Angeles Harbor and the atmospheric pressure data at San Diego Lindbergh Field (SAN) and Los Angeles International Airports (LAX) do not have missing data.

Table 5.1: The surface tide constituents and amplitudes at Los Angeles Harbor (LAH) and San Diego Bay (SDB) ordered by the amplitude at SDB.

Constituents	Constituents name	Frequency (cpd)	Amplitude (m)	
			LAH	SDB
M2	Principal lunar semidiurnal	1.9323	0.515	0.576
K1	Lunar solar diurnal	1.0027	0.343	0.352
S2	Principal solar semidiurnal	2.0000	0.203	0.233
O1	Principal lunar diurnal	0.9295	0.218	0.223
N2	Larger lunar elliptic semidiurnal	1.8960	0.121	0.136
P1	Principal solar diurnal	0.9937	0.107	0.109
S1	Solar diurnal	1.0000	0.003	0.000

5.2.3 Surface currents

Hourly surface currents optimally interpolated directly from radial velocities are used for the decomposition analysis (Chapter 3). As a part of the data quality control, the surface currents with the fractional error variance (called an uncertainty index) bigger than 0.95 in either x- or y-direction are filtered out. The fractional error variance is defined as the ratio of the posterior uncertainty to the expected current variance in the optimal interpolation, and is approaching zero for an estimate with zero uncertainty and one for an estimate with no information. A lower threshold for the fractional error variance generates more missing data, but a higher threshold can impose a bias in the surface current field. The surface currents in southern San Diego are typically southeastward, and their spatial correlations exhibit an exponential shape with different length scale in the x- and y-directions (Chapter 2).

The rotary power spectra of the surface currents are averaged over the grid points shown in Figure 5.1 using data filled with zeros for missing data. The averaged power spectrum shows clockwise-dominant tidal peaks, variance in the low frequency band (less than 0.4 cpd), frequency

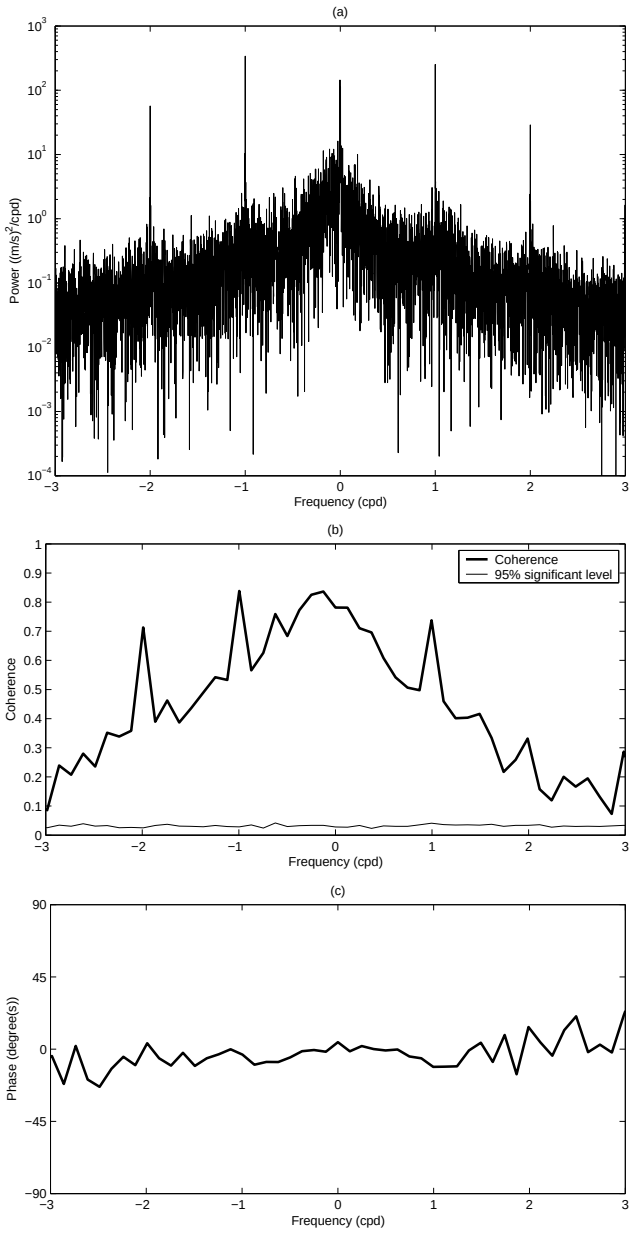

Figure 5.3: (a) Rotary power spectrum of TJR wind calculated from two years of data. (b) and (c): Coherence and phase between SIO and TJR winds estimated with 90 subsamples of two wind time series, and each one has 8.12-day record of length. The 95% significant level is calculated from the 95% percentile of the coherence between data and independent Gaussian random variables. The missing observation values have been filled with zeros in those estimates.

bands centered on diurnal and semidiurnal tides, their harmonics, and residuals (Figure 5.4a). However, the variance of surface currents at the inertial frequency ($1.06 \leq f_c \leq 1.08$ cpd in the study domain) is not significantly larger than the background ([Bratkovich(1985)]), which may be due to dissipation and blocking by the coastline. The weak inertial variance of surface currents in southern San Diego is not due to the limitation of record length because the two-year record length provides enough resolution to separate the inertial frequency (f_c) and the closest diurnal frequency (K1). In addition, the surface currents measured by the HF radar network along the entire USWC (Figure 7.1A) show a significant separation of the variance between those two frequencies, so the weak inertial variance appear to be local to San Diego. The diurnal variance of surface currents (K1 and S1) is approximately five times larger than the semidiurnal (M2) variance, in contrast to the amplitude distribution of the tidal constituents in SDB (Table 5.1) – likely a result of other diurnal forcing components, especially, diurnal winds and the diurnal stratification or heat flux.

The source of the surface current variance at the semidiurnal frequency (S2) is ambiguous, because it may be driven by both the diurnal wind and the S2 tide. Since the wind variance at the S2 frequency is about 10 times less than the S1 variance, we assume that the S2 variance of surface currents is dominantly driven by the S2 tide (section 4.5.1).

The effective averaging depth in the current measurements using HF radar is 8–16% wavelength of the surface gravity wave (Don Barrick 2008, personal communication; [Stewart and Joy(1974), Barrick et al.(1977), Ha(1979), Fernandez et al.(1996)]), and the averaging depth for the data in this chapter is assumed to be less than 1 m due to radar with ∼25 MHz operating frequency.

5.3 Methods

The surface currents ($\mathbf{u}$) are decomposed according to their driving forces:

$$\mathbf{u} = \mathbf{u}_{\mathrm{t}} + \mathbf{u}_{\mathrm{w}} + \langle \mathbf{u} \rangle + \mathbf{u}_{\mathrm{g}} \tag{5.1}$$

$$= \mathbf{u}_{\mathrm{t}} + \mathbf{u}_{\mathrm{w}} + \langle \mathbf{u} \rangle + \mathbf{u}_{\hat{\mathrm{L}}} + \mathbf{u}_{\hat{\mathrm{D}}} + \mathbf{u}_{\hat{\mathrm{S}}} + \mathbf{u}_{\mathrm{r}}, \tag{5.2}$$

where $\mathbf{u}_{\mathrm{t}}$, $\mathbf{u}_{\mathrm{w}}$, $\langle \mathbf{u} \rangle$, and $\mathbf{u}_{\mathrm{g}}$, respectively, denote the surface currents driven by pure tides, the locally wind-driven surface currents, the temporal mean surface currents, the surface currents with wind removed. The wind-free surface currents ($\mathbf{u}_{\mathrm{g}}$) are the sum of low frequency ($\mathbf{u}_{\hat{\mathrm{L}}}$), diurnal frequency band ($\mathbf{u}_{\hat{\mathrm{D}}}$), which include the inertial frequency surface currents, semidiurnal frequency band ($\mathbf{u}_{\hat{\mathrm{S}}}$) components, and residual surface currents ($\mathbf{u}_{\mathrm{r}}$).

Under the assumption that locally wind-driven surface currents and barotropic currents driven by pure tides (Table 5.1) do not interfere, the barotropic tidal currents including the S2 variance are filtered out first, then locally wind-driven surface currents are separated later.

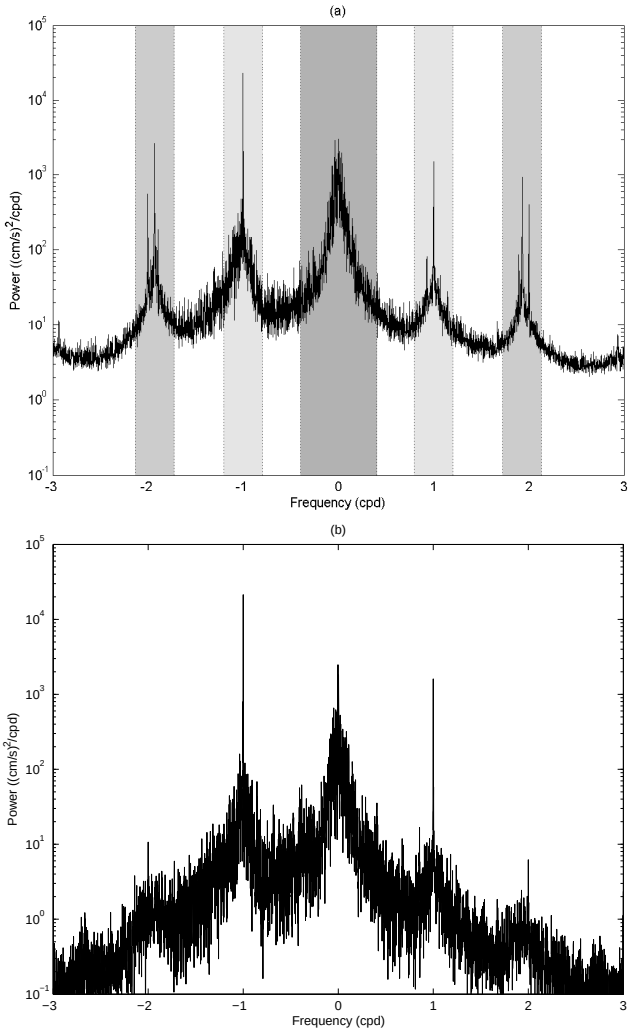

Figure 5.4: Regionally averaged rotary power spectra of (a) surface currents ($\mathbf{u}$), (b) locally estimated wind-driven surface currents ($\mathbf{u}_{\mathrm{w}}$), and (c) surface currents with the locally estimated wind-driven components removed ($\mathbf{u}_{\mathrm{g}}$).

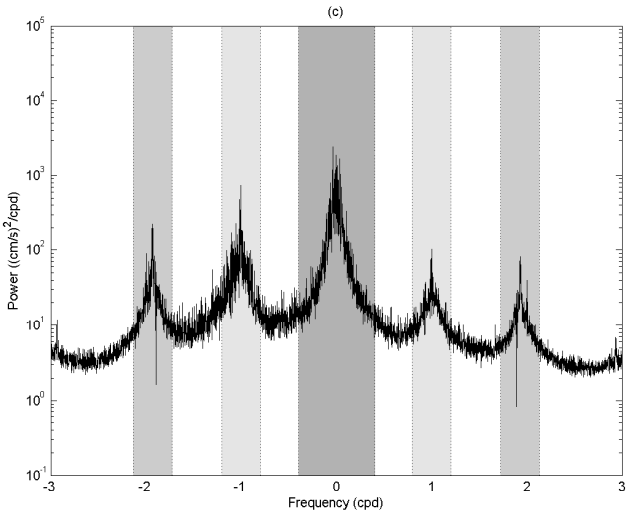

Figure 5.4: (Continued.)

5.3.1 Surface currents driven by pure tides

The current signal phased-locked with tidal constituents is filtered using least-squares fitting for the main tidal frequencies in Table 5.1 except the S1 frequency. The barotropic and baroclinic components are discussed with the tidal ellipses of surface currents at the K1 and M2 frequencies in section 5.4.1. Moreover, the baroclinic tidal currents and near tidal band currents may not be distinguishable in this analysis.

5.3.2 Locally wind-driven surface currents

The isotropic and anisotropic wind impulse response functions (WIRFs) in the frequency-domain and time-domain have been studied ([Ekman(1905), Gonella(1972), Weller(1981)] and Chapter 4). The frequency-domain WIRF describes the relationship between currents and wind stress as in the extended Ekman theory (Chapter 4). On the other hand, the time-domain WIRF is convenient for estimating wind-driven surface currents from the wind observations using the time convolution for applications such as surface current forecast models or upwelling index estimates. Although the frequency-domain and time-domain WIRF estimates should be equivalent, the two approaches differs in the treatment of missing observations and in the regularization of the inverse problem. The surface current response to wind in the coastal region has been reported as asymmetric and anisotropic in the numerical models and observations ([Sverdrup(1938), Allen(1980), Beardsley et al.(1987), Huyer and Kosro(1987), Overland and Pease(1988), Li and Weisberg(1999), Weisberg et al.(2001), Choi and Wilkin(2007)]). Therefore both the frequency-domain isotropic WIRF (FIWIRF) and the time-domain anisotropic WIRF (TAWIRF) are considered in this analysis. As the statistical estimates of the WIRFs were addressed thoroughly in Chapter 4, the essential part of the WIRF

estimate in two domains is described briefly.

Frequency domain

The FIWIRF ($\hat{\mathbf{H}}$) is computed from the time average covariance of the Fourier coefficients of the detided surface currents ($\hat{\mathbf{u}}_\mathrm{f}$) and wind stress ($\hat{\boldsymbol{\tau}}$) at each frequency ($\omega$), which are combined into complex numbers ($\hat{\boldsymbol{\tau}} = \hat{\tau}_x + i\hat{\tau}_y$, $\hat{\mathbf{u}} = \hat{u} + i\hat{v}$), respectively, for the isotropic estimate:

$$\hat{\mathbf{H}}(\mathbf{x},\omega) = \Big(\langle \hat{\mathbf{u}}_\mathrm{f}(\mathbf{x},\omega)\, \hat{\boldsymbol{\tau}}^\dagger(\omega)\rangle\Big)\, \Big(\langle \hat{\boldsymbol{\tau}}(\omega)\, \hat{\boldsymbol{\tau}}^\dagger(\omega)\rangle + \mathbf{R_a}\Big)^{-1}, \tag{5.3}$$

where † indicates the complex conjugate transpose and the regularization matrix ($\mathbf{R_a}$) is assumed to be the noise level of the wind stress. The averages are computed using 90 sub-intervals of the total data duration and the missing data are filled with zeros.

The Fourier coefficients of the locally wind-driven surface currents are given by the product of the transfer function with the wind stress

$$\hat{\mathbf{u}}_\mathrm{w}(\mathbf{x},\omega) = \hat{\mathbf{H}}(\mathbf{x},\omega)\hat{\boldsymbol{\tau}}(\omega). \tag{5.4}$$

Time domain

The TAWIRF ($\mathbf{H}$) of the detided surface currents ($\mathbf{u}_\mathrm{f}$) in the discrete time domain (Δt) is estimated from

$$\mathbf{H}(\mathbf{x}) = \Big(\langle \mathbf{u}_\mathrm{f}(\mathbf{x},t)\, \boldsymbol{\tau}_N^\dagger(t)\rangle\Big)\, \Big(\langle \boldsymbol{\tau}_N(t)\, \boldsymbol{\tau}_N^\dagger(t)\rangle + \mathbf{R_b}\Big)^{-1}, \tag{5.5}$$

where $\boldsymbol{\tau}_N(t) = [\boldsymbol{\tau}(t - N\Delta t)\ \cdots\ \boldsymbol{\tau}(t-\Delta t)\, \boldsymbol{\tau}(t)]^\dagger$ denotes the wind stress stacked with up to N-hour time lags. $\boldsymbol{\tau}(t)$ is a two-element vector to allow for anisotropic response, i.e., $\boldsymbol{\tau}(t) = [\tau_x(t)\, \tau_y(t)]^\dagger$. The regularization matrix ($\mathbf{R_b}$) is assumed to be a scaled identity matrix

$$\mathbf{R_b} = \gamma^2\mathbf{I}, \tag{5.6}$$

with γ adjusted to minimize the error in the cross-validated current estimates (section 4.5.1). The locally wind-driven surface currents are computed as the convolution of the TAWIRF and the wind time series:

$$\mathbf{u}_\mathrm{w}(\mathbf{x},t) = \sum_{n=0}^{N} \mathbf{h}(\mathbf{x}, n\Delta t)\, \boldsymbol{\tau}(t - n\Delta t). \tag{5.7}$$

The autocovariance of wind stress and the covariance of wind stress with surface currents in equation 5.5 are computed excluding the missing data.

5.3.3 Surface currents in frequency bands

The power spectrum of the surface currents ($\mathbf{u}_\mathrm{g}$) after removal of wind and tides is dominated by three frequency bands (Figure 5.4c). As the observation time series are not complete, band-pass filtering in the three frequency bands is accomplished by weighted least-squares fitting, in spite of the computational expense. The frequencies are equally-spaced and cover the bands just

as in conventional Fourier analysis, but the background spectrum outside the bands with enhanced energy is treated as noise and is not estimated directly:

$$\mathbf{u}_{\mathrm{g}} = \mathbf{u}_{\widehat{\mathrm{L}}} + \mathbf{u}_{\widehat{\mathrm{D}}} + \mathbf{u}_{\widehat{\mathrm{S}}} + \mathbf{u}_{\mathrm{r}} \tag{5.8}$$

$$= \begin{bmatrix} \mathbf{G}_{\widehat{\mathrm{L}}} & \mathbf{G}_{\widehat{\mathrm{D}}} & \mathbf{G}_{\widehat{\mathrm{S}}} \end{bmatrix} \begin{bmatrix} \mathbf{m}_{\widehat{\mathrm{L}}} \\ \mathbf{m}_{\widehat{\mathrm{D}}} \\ \mathbf{m}_{\widehat{\mathrm{S}}} \end{bmatrix} + \mathbf{u}_{\mathrm{r}} = \mathbf{G}\mathbf{m} + \mathbf{u}_{\mathrm{r}}, \tag{5.9}$$

where $\mathbf{G}$ denotes the regression basis, which are the stacked arrays of sine and cosine functions for regression on the low, diurnal, and semidiurnal frequency bands ($\mathbf{G}_{\widehat{\mathrm{L}}}$, $\mathbf{G}_{\widehat{\mathrm{D}}}$, and $\mathbf{G}_{\widehat{\mathrm{S}}}$). The model coefficients ($\mathbf{m}$) are estimated by

$$\widehat{\mathbf{m}} = \mathbf{P}\mathbf{G}^{\dagger} \left(\mathbf{G}\mathbf{P}\mathbf{G}^{\dagger} + \mathbf{R}_{\mathbf{c}} \right)^{-1} \mathbf{u}_{\mathrm{g}}, \tag{5.10}$$

or

$$= \left(\mathbf{G}^{\dagger} {\mathbf{R}_{\mathbf{c}}}^{-1} \mathbf{G} + \mathbf{P}^{-1} \right)^{-1} \mathbf{G}^{\dagger} {\mathbf{R}_{\mathbf{c}}}^{-1} \mathbf{u}_{\mathrm{g}}, \tag{5.11}$$

where $\mathbf{P}$ and $\mathbf{R}$ denote the model covariance matrix and the error covariance matrix, respectively ([Wunsch(1996)]). Equation 5.11 is applied in this chapter because of the computational expense for the matrix inversion, i.e, the number of frequencies to be estimated (951 frequencies) is less than the length of the time series (8771 time records).

The model covariance matrix ($\mathbf{P} = \langle \mathbf{m}\mathbf{m}^{\dagger} \rangle$) is the prior estimate of the spectral covariance matrix. The diagonal term of the model covariance matrix is the expected variance at each frequency, and the off-diagonal terms are the cross-correlation of Fourier coefficients between different frequencies. $\mathbf{P}$ is a diagonal matrix for a stationary process and can be separated into blocks by each frequency component:

$$\mathbf{P} = \begin{bmatrix} \mathbf{P}_{\widehat{\mathrm{L}}} & \mathbf{0} & \mathbf{0} \\ \mathbf{0} & \mathbf{P}_{\widehat{\mathrm{D}}} & \mathbf{0} \\ \mathbf{0} & \mathbf{0} & \mathbf{P}_{\widehat{\mathrm{S}}} \end{bmatrix}, \tag{5.12}$$

where $\mathbf{P}_{\widehat{\mathrm{L}}} = \langle \mathbf{m}_{\widehat{\mathrm{L}}} \mathbf{m}_{\widehat{\mathrm{L}}}^{\dagger} \rangle$, $\mathbf{P}_{\widehat{\mathrm{D}}} = \langle \mathbf{m}_{\widehat{\mathrm{D}}} \mathbf{m}_{\widehat{\mathrm{D}}}^{\dagger} \rangle$, and $\mathbf{P}_{\widehat{\mathrm{S}}} = \langle \mathbf{m}_{\widehat{\mathrm{S}}} \mathbf{m}_{\widehat{\mathrm{S}}}^{\dagger} \rangle$. The variance conservation between the discrete Fourier transform and the weighted least-squares fitting approach is discussed in sections 5.6.2 and 5.6.3.

The error covariance matrix ($\mathbf{R}_{\mathbf{c}} = \langle \mathbf{u}_{\mathrm{r}} \mathbf{u}_{\mathrm{r}}^{\dagger} \rangle$) is estimated from the power spectrum of the residual surface currents ($\mathbf{u}_{\mathrm{r}}$):

$$S(\omega) \propto \omega^{-\beta}, \tag{5.13}$$

which can be assumed as the power spectrum with white noise ($\beta = 0$) or Brownian/Gaussian noise ($\beta = 2$). The power spectrum of the background currents is approximately (Figure 5.4c)

$$S(\omega) = \frac{9^2}{(\omega + 3)^2}. \tag{5.14}$$

However, because of the conversion of the non-white error spectrum to a non-diagonal matrix in the time domain and the computational burden of matrix inversion, we assumed the power spectrum of the error covariance matrix to be white with $S(\omega) = 2\ \mathrm{cm^2\ s^{-2}\ cpd^{-1}}$, which is the floor level in Figure 5.4c.

5.3.4 Alongshore pressure gradient forcing

The frictionally dominated depth-averaged momentum balance ([Lentz and Winant(1986), Brink et al.(1987)]) is:

$$\frac{b}{H}\int_{-H}^{\eta}\mathbf{u}\,\mathrm{d}z = -gH\nabla\eta, \tag{5.15}$$

where b, g, and H, respectively, denote a linear bottom drag coefficient, gravitational acceleration ($9.8\ \mathrm{m\,s^{-2}}$), and the water depth. To relate this balance to the surface currents, two assumptions are needed. First, assume that the local pressure gradient ($\nabla\eta$) is proportional to the atmospherically-adjusted SSH difference between two shore stations ($\Delta\eta$) divided by the distance between them (Δc):

$$\nabla\eta \propto \frac{\Delta\eta}{\Delta c}, \tag{5.16}$$

and second, assume that the low-frequency-band surface currents are proportional to the depth-averaged currents:

$$\mathbf{u}_{\hat{\mathrm{L}}} \sim \frac{1}{H}\int_{-H}^{\eta}\mathbf{u}\,\mathrm{d}z. \tag{5.17}$$

At each frequency we regress SSH difference on surface current to find coherence and regression coefficients for u and v with $\Delta\eta$. The regression coefficients include bottom and form drag ([McCabe et al.(2006), Warner and MacCready(2008)]), corresponding to the $b/(gH)$ in equation 5.15. By multiplying by gH they can be compared to the bottom drag coefficients inferred by other studies. The time derivative of the low frequency band surface currents was found to be negligible compared with the two terms in the friction balance.

5.4 Results

A typical example of a time series of the decomposed surface currents at location A (Figure 5.1) is shown in Figures 5.5a–5.5h. The surface currents (Figure 5.5a) are decomposed into pure tide surface currents (Figure 5.5b), locally wind-driven surface currents (Figure 5.5c), temporal mean surface currents (Figure 5.5d), low frequency band surface currents ($|\omega| \leq 0.4$ cpd) (Figure 5.5e), diurnal band surface currents (Figure 5.5f), semidiurnal band surface currents (Figure 5.5g), and residual surface currents (Figure 5.5h). The variances partitioned into these components are summarized in Table 5.2. The low frequency surface currents and the locally wind-driven surface currents each have approximately one-third of the total variance. The variance of surface currents coherent with the alongshore pressure difference takes approximately 3% of the total variance (section 5.4.4). The pure tide surface currents and the surface currents in the diurnal and semidiurnal frequency

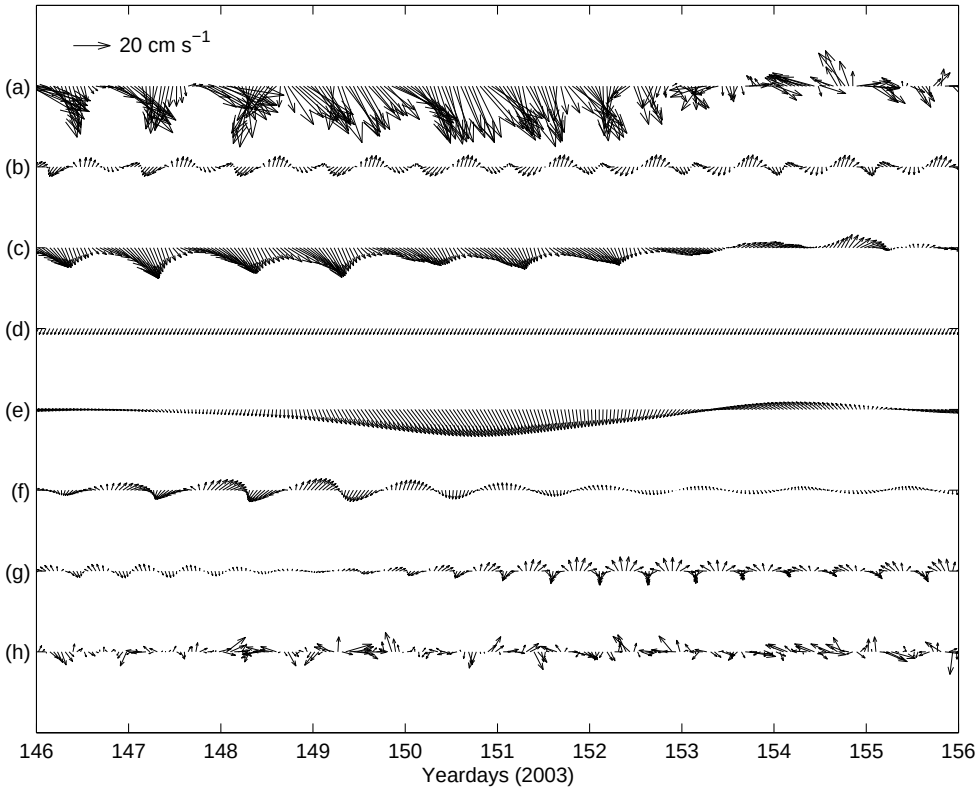

Figure 5.5: An example of a set of time series of decomposed surface currents at the location A in Figure 5.1. (a) Unconditioned surface currents ($\mathbf{u}$). (b) Surface currents driven by pure tides ($\mathbf{u}_{\mathrm{t}}$). (c) Locally wind-driven surface currents ($\mathbf{u}_{\mathrm{w}}$). (d) Mean surface currents ($\langle\mathbf{u}\rangle$). (e) Surface currents in the low frequency band ($\mathbf{u}_{\widehat{\mathrm{L}}}$). (f) Surface currents in the frequency band centered on diurnal frequency ($\mathbf{u}_{\widehat{\mathrm{D}}}$). (g) Surface currents in the frequency band centered on semidiurnal frequency ($\mathbf{u}_{\widehat{\mathrm{S}}}$). (h) Residual surface currents ($\mathbf{u}_{\mathrm{r}}$).

bands represents ∼20% of the total variance. The residual surface currents – some portion of the nonlinear interactions, the small scale structure, outliers, and noise – accounts for approximately 15% of total variance.

Table 5.2: The variance fraction (%) of the decomposed surface currents. The variance of surface currents coherent with alongshore pressure difference is approximately 3% of total variance (section 5.4.4).

Pure tide	Wind	Mean	Low	Diurnal	Semidiurnal	Residual
6.3	32.6	1.4	31.8	8.9	4.1	14.9

5.4.1 Surface currents driven by pure tides

The surface currents driven by the K1 and M2 tides are shown as ellipses in Figures 5.6a and 5.6b, respectively. The K1 tidal surface currents have a crossshore amplitude change from 2.5–

3 cm s^{-1} over the continental shelf break (offshore) to 0.5–1.0 cm s^{-1} nearshore suggesting depth and coastline effects (Figure 5.6a). The phases are nearly uniform but slightly rotate clockwise from south to north. The M2 tidal surface currents show a front between oppositely rotating flows, from clockwise in the north to counterclockwise in the south, with some clockwise ellipses around the Coronado Islands (Figure 5.6b). The front is robust and consistent with the M2 tidal ellipse structures estimated from shorter surface current time series (e.g. monthly data), and is likely connected with the surface signature of shoreward propagating internal waves. An ADCP and temperature mooring northeast of the Coronado Islands in 28 m water depth showed upward phase propagation in the current profile and M2 internal bores in the temperature profiles, supporting the existence of M2 internal tide signatures in the surface currents. The amplitude of the M2 tidal surface currents is 4.5–5 cm s^{-1} over the Loma Sea Valley (about 500 m water depth in the southwestern area of Point Loma) and is 1.5–2.5 cm s^{-1} in the rest of the domain. The clockwise ellipses near Coronado Islands maybe an island wake in the shoreward propagating surface features ([Ingram and Chu(1987)]). In addition, the alternating clockwise and counterclockwise flows in the area of Point Loma and SDB mouth may be influenced by the topography.

The phase propagation speeds of barotropic tides along the USWC have been reported as 210–220 and 140–152 m s^{-1} ([Munk et al.(1970), NOAA(2006)]) for K1 and M2 tides, respectively. Therefore the phase of barotropic tides across the study domain (about 40×40 km^2) are essentially constant, and the local phase changes in Figure 5.6 are assumed to be a result of the baroclinic component.

5.4.2 Locally wind-driven surface currents

Statistical overview

The FIWIRF is estimated using two wind observations (SIO and TJR) and surface currents at each grid point in Figure 5.1. The coherences in the frequency domain are computed from 90 sub-integrals of 8.12 days record length using the minimum cross-validated residual variance (section 4.5.1). The probability density functions (PDFs) of both magnitude and phase of the FIWIRF at each frequency for all grid points are shown in Figures 5.7a and 5.7c (SIO winds) and Figures 5.7b and 5.7d (TJR winds), respectively. The higher variance and the phase shift at near inertial frequency are consistent with previous studies ([Gonella(1972), Weller(1981), Rio and Hernandez(2003)] and Chapter 4). The removal of the S2 variance in the surface currents appears to cause the drop in the response function at that frequency (Figures 5.7a and 5.7b). The higher variance in the very low frequency band ($|\omega| \leq 0.2$ cpd in Figures 5.7a and 5.7b), which is the mismatched portion with the theoretical response function, may be ambiguous since it could be a result of geostrophic balance between currents and remotely or locally wind-driven pressure gradient. As the coherence (not shown) between the alongshore pressure difference (equation 5.16) and wind stress at SIO and TJR is $\sim$0.1 in this low frequency band, the local pressure setup is more likely. This higher variance also can be studied by estimating the adjustment terms in the momentum equations (equations

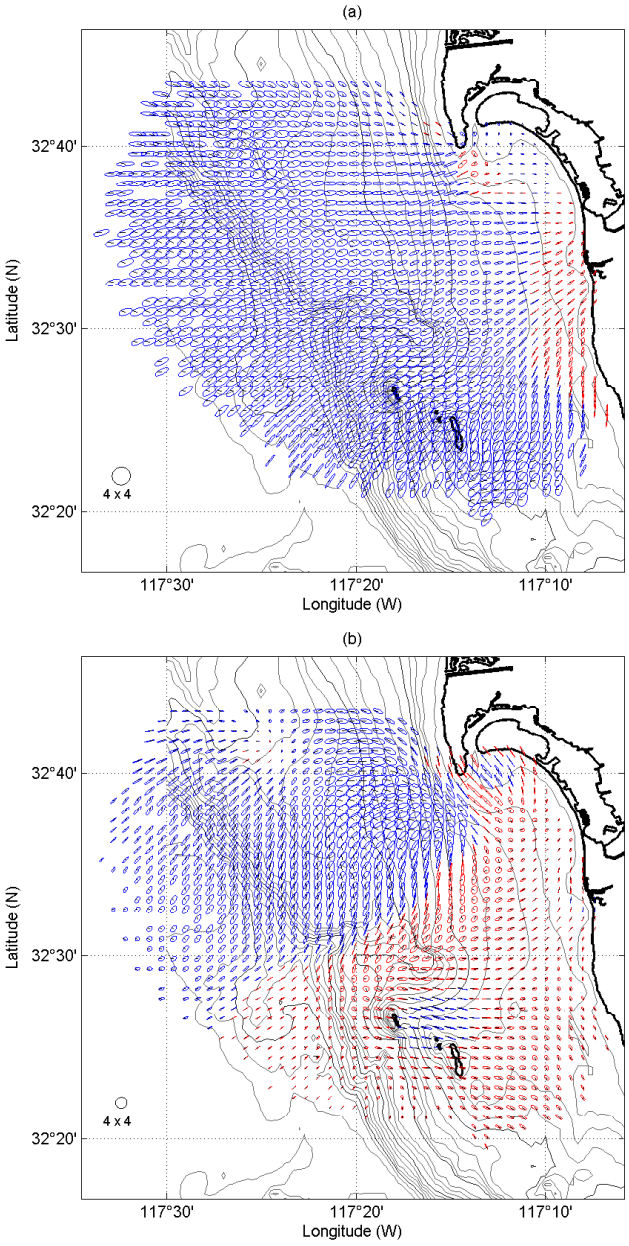

Figure 5.6: Tidal ellipses of surface currents estimated using the harmonic analysis for the (a) K1 and (b) M2 frequencies. The red and blue ellipses represent counterclockwise and clockwise rotations, respectively, and the phases are indicated with the black line in each ellipse. The units of the major and minor axes are cm s^{-1}.

4.3 and 4.4) as a function of frequency, representing the anisotropic current response to the wind. Although the phases in the high frequency band ($|\omega| > 2$ cpd) fluctuate, they seem consistent with the theoretical phase (gray line in Figure 5.7b). The TJR FIWIRF shows approximately three times higher response than the SIO FIWIRF, and its phase is more stable. This is thought to be due to its greater proximity to the region, and thus greater skill in representing the actual winds.

Coherence maps

The rotary coherence between detided surface currents and the individual wind is averaged for frequencies at and below 2 cpd ($|\omega| \leq 2$ cpd) (Figures 5.3a and 5.3b), which we call the spatial coherence map. The TJR coherence map shows radially decreasing coherence from the TJR wind station ($\sim$0.4) to offshore ($\sim$0.1), and the SIO coherence map has a lower coherence level (0.1–0.2) but with a similar tendency. The decrease in the coherence could be explained by reduced skill of the wind at the shore station in estimating offshore wind or by less coherent offshore surface currents. In spite of the distance between the two wind stations, the radial decay shown by the SIO wind suggests that both shore station are measuring similar large scale winds and land/sea breezes (Figure 5.3c).

In a similar way, the coherence maps (Figures 5.7c and 5.7d) calculated from the locally estimated wind-driven surface currents ($\hat{\mathbf{u}}_\mathrm{w}$ in equation 5.4) using the FIWIRF estimated with two winds simultaneously show radially decreasing features away from the TJR wind station with higher coherence levels than the coherence map of detided surface currents: 0.6–0.8 (SIO, Figure 5.8c) and 0.7–0.95 (TJR, Figure 5.8d). The spatial structure in the locally wind-driven surface currents shows the contribution of the local wind observations as a foot print. Coherence maps (not shown) using only individual winds (SIO or TJR) show perfect coherence at all frequencies by definition, because the locally wind-driven currents calculated from a single wind at a single frequency are perfectly coherent with the wind. Since maps of coherence do not appear biased by areas of missing data (Figures 5.8a–5.8d), we assume that the coherence estimates are not strongly influenced by missing observations.

Locally wind-driven surface current estimate

The TAWIRF is computed from the surface currents at each grid point and both wind observations together (SIO and TJR) (equation 5.5). The regularization level is set at 10% of the mean eigenvalue of the autocovariance of the wind stress with 6 days time lag, which is 1.41×10^{-5} $\mathrm{kg^2\ m^{-2}\ s^{-4}}$. Then, the locally wind-driven surface currents ($\mathbf{u}_\mathrm{w}$) are calculated with the estimated TAWIRF and the two wind time series (equation 5.7). The regionally averaged power spectrum of the locally wind-driven surface currents characterizes the response to the diurnal wind (land/sea breezes) and its harmonics with red spectrum as the power spectrum of the wind (Figure 5.4b).

The mean wind-driven surface currents vary slowly over the study domain from 7–10 $\mathrm{cm\ s^{-1}}$ south of Point Loma to 1–5 $\mathrm{cm\ s^{-1}}$ offshore and nearshore (Figure 5.9). Notably, the response is

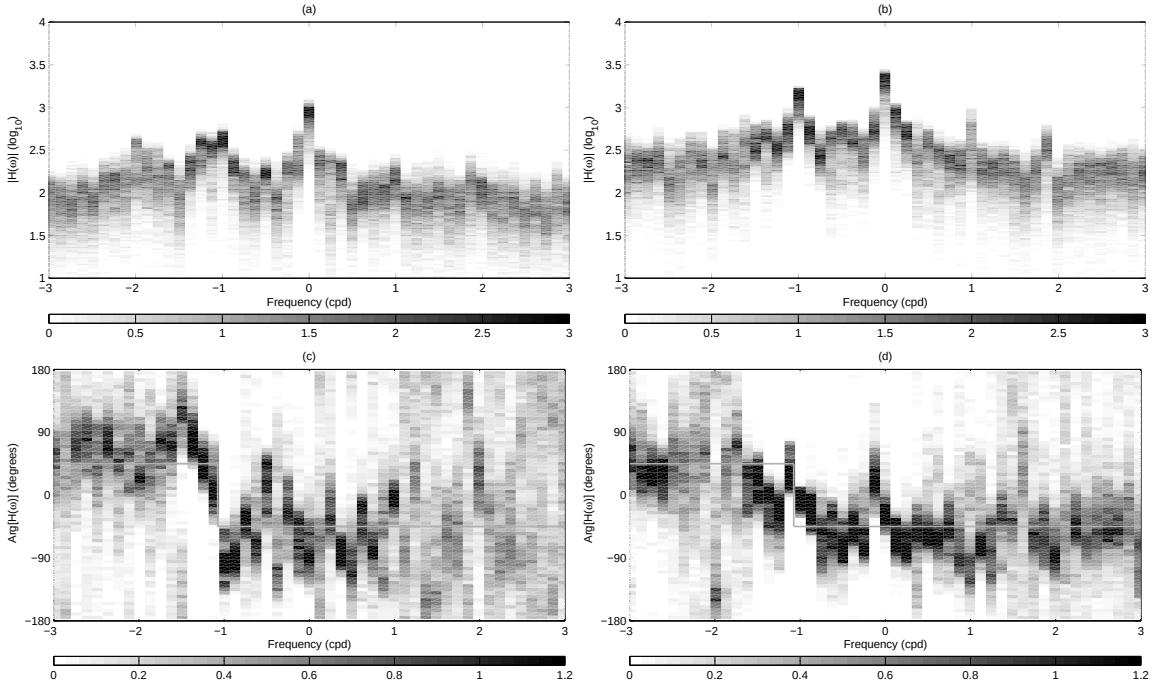

Figure 5.7: PDF of the magnitude and phase of the FIWIRFs. Each FIWIRF is estimated with two wind observations (SIO and TJR) together and surface currents at each grid point in Figure 5.1, which have 8.12 days record length (90 subsamples). The gray line denotes the theoretical phase of surface currents ([Gonella(1972)] and Figure 4.1C). (a) and (c): The magnitude and phase of the SIO FIWIRF. (b) and (d): The magnitude and phase of the TJR FIWIRF.

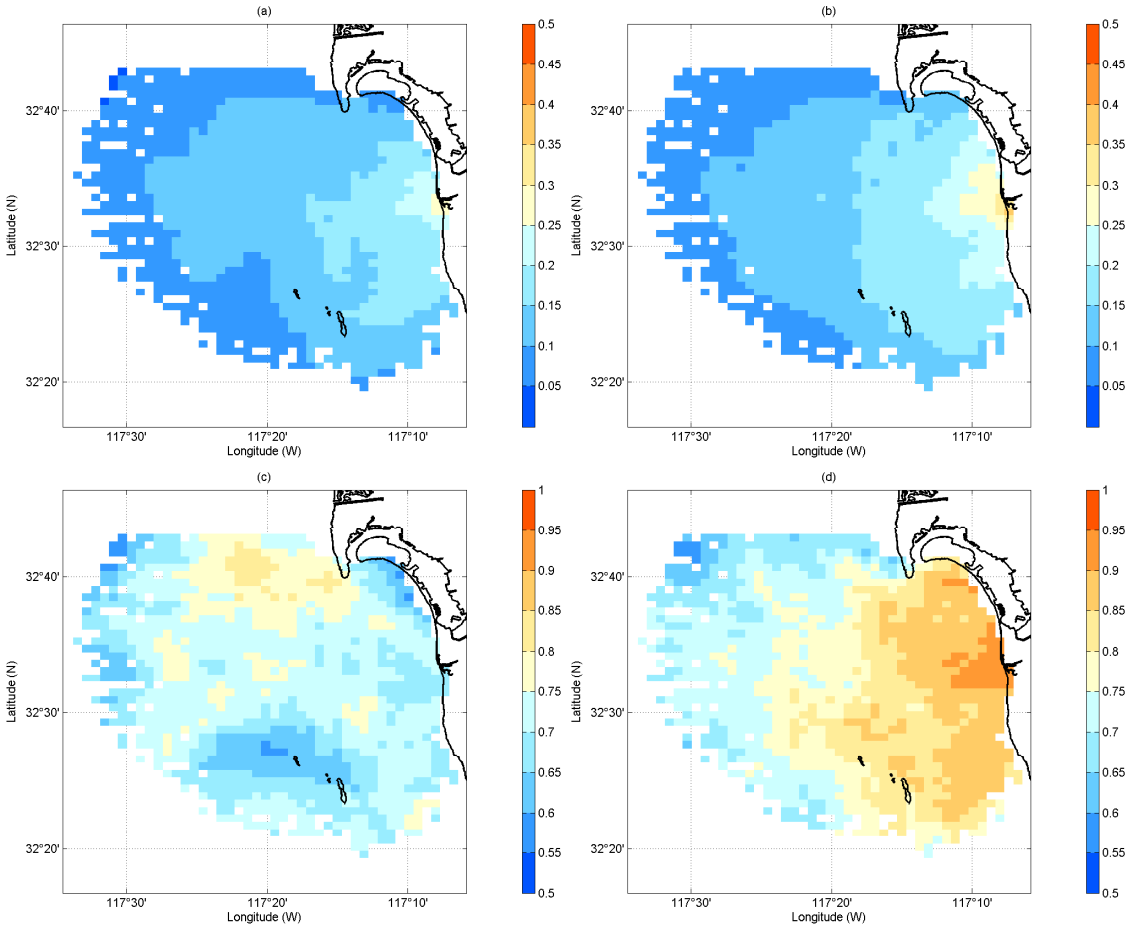

Figure 5.8: (a)–(b): Averaged coherence of the detided surface currents ($|\omega| \leq 2$ cpd) and wind stress at the individual shore station wind: (a) SIO wind. (b) TJR wind. (c)–(d): Averaged coherence of the locally wind-driven surface currents ($|\omega| \leq 2$ cpd) estimated using FIWIRF and wind stress at the individual shore station: (c) SIO wind. (d) TJR wind. The colorbars in (a)–(b) and (c)–(d) have different bounds with same scale unit.

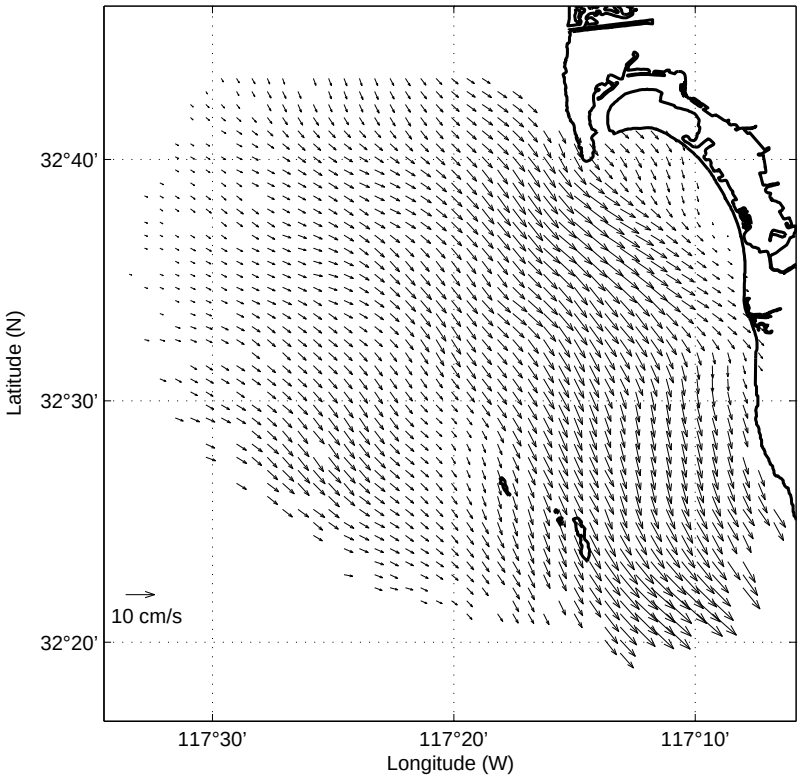

Figure 5.9: Time mean of the locally wind-driven surface currents, which are estimated using the TAWIRF and the wind stress time series for 6 days.

weaker along the continental shelf break region. A possible explanations for this spatial gradient is the wind offshore decorrelates from the observed wind at the coast. The directions of the mean wind stress are 29 (SIO) and 42 (TJR) degrees from true north, and the overall wind-driven surface current responses are less than 90 degrees to the right of the wind direction (Figure 5.9).

The 2D PDF of the ratio of the spatially averaged wind-driven surface current speed ($|\bar{\mathbf{u}}_{\mathrm{w}}|$) over the study domain to the TJR wind speed ($|\mathbf{u}^{\mathrm{w}}|$) with respect to the TJR wind speed with zero hour time lag is considered (not shown). The ratio in low wind speed (less 1 $\mathrm{m\,s^{-1}}$) is very scattered, and varies with 2–5% intermediate wind speed (between 1 and 5 $\mathrm{m\,s^{-1}}$). At high speed (more than 5 $\mathrm{m\,s^{-1}}$ and this occupies ∼1% of total wind data) the ratio converges about 4%. The dominant ratio over all speeds stays within 1.5–3%, which is consistent with other studies ([Bye(1965), Churchill and Csanady(1983), Wu(1983), Weber(1983), Spaulding(1999)]). Moreover, the directional PDF of the veering angle at zero time lag shows the dominance at 55±25 (SIO) and 48±20 (TJR) degrees, which implies the direction of the locally wind-driven response to a quasi-steady wind.

5.4.3 Mean surface currents

We examine the time averaged surface current signal that has the computed wind-driven surface current removed and find that the flow in the western domain of the region examined has strong variance (5–9 $\mathrm{cm\,s^{-1}}$).. This is consistent with the large scale surface current variability measured by two long range HF radars (∼5 MHz) off San Diego and San Clemente Island. Two surface flows with opposite rotation are bifurcated near Tijuana River, which move northward (counterclockwise) and southward (clockwise) along the coastline (Figure 5.10). The northward surface currents hit the northern boundary (SDB mouth), and return via southeastward flows. A local artifact found along an azimuthal bin at approximately 287 degrees from true north of the SDBP site results from the radial velocity solutions derived from an abrupt change in the measured beam pattern of the SDBP site (section 2.2.3), which causes an ambiguity in the bearing solution calculated from the MUSIC algorithm ([de Paolo and Terrill(2007a)]).

5.4.4 Low frequency surface currents

The coherence and phase between the alongshore pressure difference between LAH and SDB and the spatially averaged low frequency band surface currents ($\bar{\mathbf{u}}_{\widehat{\mathrm{L}}}$) are computed from 25 subsamples in the x- and y-directions, separately (Figure 5.11). The only coherence and phase with higher than 80% significant levels are shown. The frequency band having the relatively higher coherence (0.2–0.3) above the significant levels and approximately constant phase (45 degrees) is less than 1/7 cpd for $\bar{v}_{\widehat{\mathrm{L}}}$. Although the coherence and phase with 90 subsamples also produce consistent results, the results estimated with 25 subsamples are used to provide better resolution in the low frequency band. Since $\bar{u}_{\widehat{\mathrm{L}}}$ is not significantly coherent with the alongshore pressure difference, $\bar{v}_{\widehat{\mathrm{L}}}$ in low frequency band ($|\omega| \leq 1/7$ cpd) becomes the alongshore surface current.

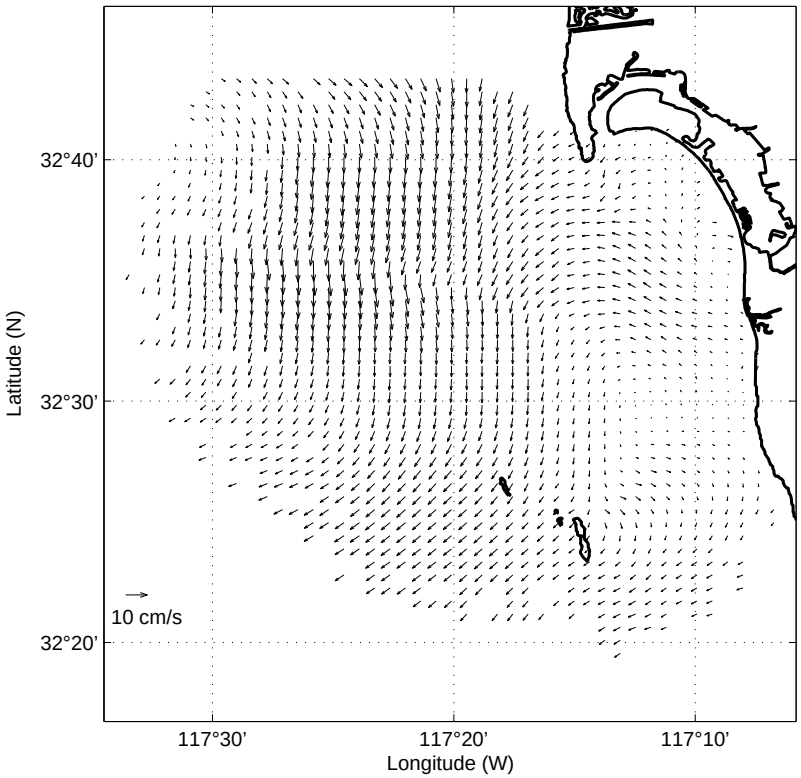

Figure 5.10: Time mean surface currents with estimated wind-driven surface currents removed.

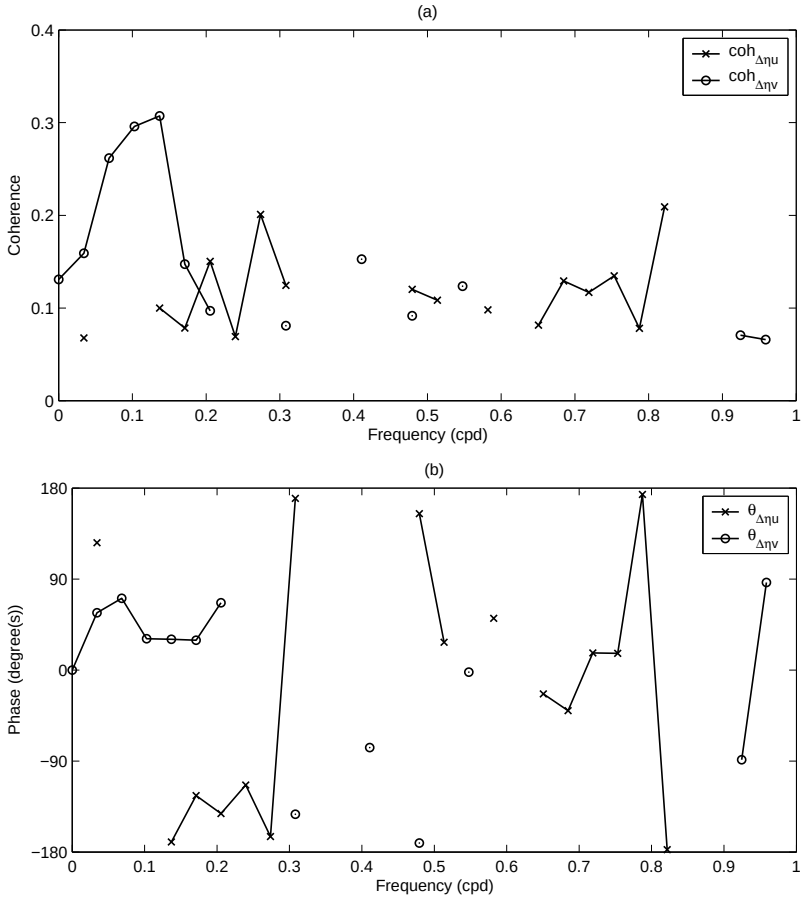

Figure 5.11: (a) and (b): Coherence and phase between the atmospherically-adjusted pressure difference and the spatially averaged low frequency band surface currents ($\bar{\mathbf{u}}_{\widehat{\mathrm{L}}}$) in the x- and y-directions, separately. Both are computed with 25 subsampled elements, and cross and circle marks indicates 80% significant levels for u and v, respectively

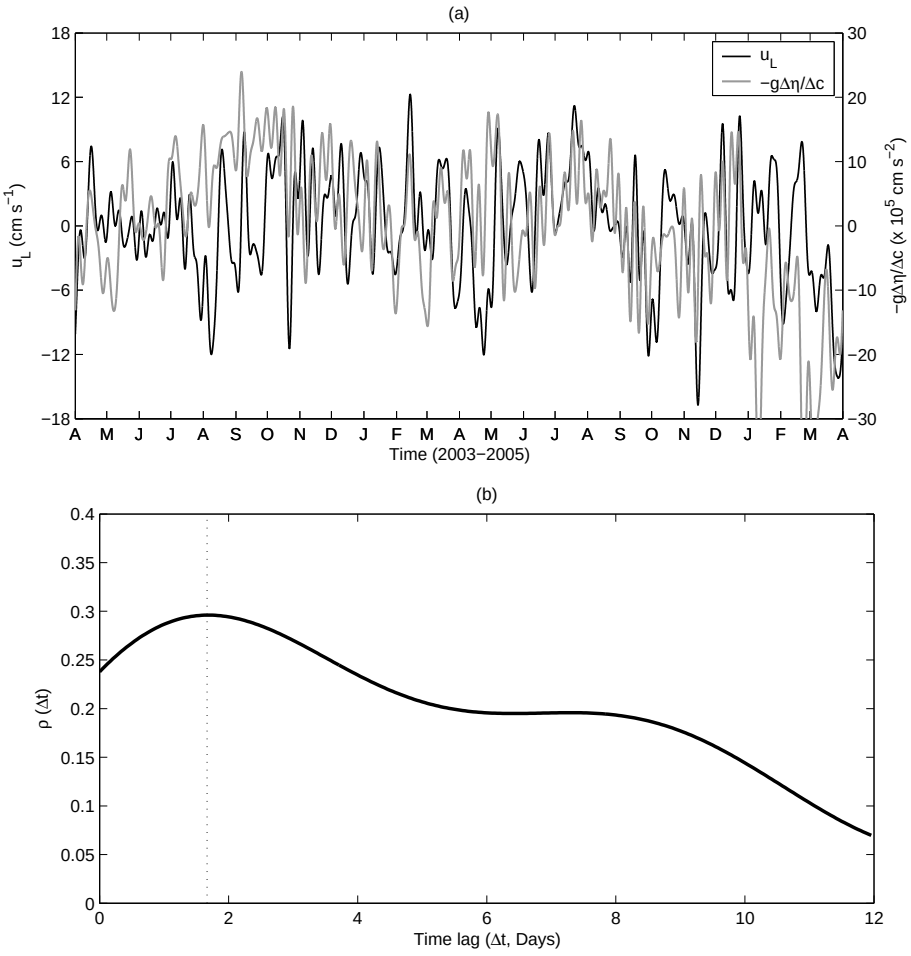

Figure 5.12: (a) The time series and (b) the time lag correlation of the alongshore pressure difference and the spatially averaged alongshore surface current within the coherent frequency band ($|\omega| \leq 1/7$ cpd). The time lag correlation has a maximum ($\sim$0.3) at 1.75 days advanced time lag of the alongshore pressure difference to the alongshore surface current (a dotted line in (b)).

The time series of two terms in the frictional balance (equations 5.16 and 5.17) are shown in Figure 5.12a, and the time lag correlation between them has ∼0.3 as a maximum with 1.75 days advanced time lag of the alongshore pressure difference to the alongshore surface current (Figure 5.12b). The time lag may not be constant, however, the dominant low frequency variability can be governed by the nearly constant time lag. At the time lag of maximum correlation, the frictional coefficient (r) is calculated using linear regression to be 0.724×10^{-6} $\mathrm{m^{-1}s}$. The alongshore pressure difference explains approximately 10% of the low frequency band surface currents, which is 3% of total variance.

The computed frictional coefficient (r) may be interpreted as $b/\left(gH\right)$, which corresponds to 0.07–0.7 $\mathrm{cm\,s^{-1}}$ in the $O(10-100)$ m depth – consistent with the other bottom drag studies in Table 5.3.

Table 5.3: The bottom drag studies using the conventional depth averaged momentum balance.

Studies	Frictional balance	Drag coefficient (b)
[Grant et al.(1984)]	$\tau_B = \rho b v \lvert\mathbf{u}\rvert$	0.005–0.011 (no unit)
[Lentz and Winant(1986)]	$\tau_B = \frac{\rho b}{H}\int_{-H}^{\eta} v\mathrm{d}z$	0.05 $\mathrm{cm\,s^{-1}}$
[Brink et al.(1987)]	$\tau_B = \rho b \lvert\mathbf{u}\rvert$	0.05–0.1 $\mathrm{cm\,s^{-1}}$

5.4.5 Diurnal band surface currents

The main driving forces for the diurnal band surface currents are considered as the diurnal tidal constituents (K1, O1, and P1) and the diurnal wind (S1) modulated by the components in the low frequencies ([Munk et al.(1965)]). The diurnal band surface currents in southern San Diego is the dominantly clockwise flow with the order of 3 ± 2 $\mathrm{cm\,s^{-1}}$.

5.4.6 Semidiurnal band surface currents

The M2 surface current signal is expected to contain signatures of the internal tide at the same frequency as the region is conducive for their generation. The seasonal buoyancy frequency (∼50 and ∼200 cpd for winter and summer, respectively) and the shoreward steep bottom slope of the continental shelf/break region in southern San Diego satisfies the necessary condition to generate the M2 internal tides ([Cacchione and Wunsch(1974), Bratkovich(1985), Cacchione et al.(2002)]). Independent studies have found internal tides observed in SAR images ([Jackson(2004)]). This topic is outside of the scope of this publication, and will be addressed in subsequent research. Moreover, the surface currents in the semidiurnal frequency band are considered to be minimally influenced by the wind.

5.4.7 Residual surface currents

The residual surface currents are considered to include the component of the signal driven by non-linear forcing terms, small scale variability, intermittent local eddies, observational noise and outliers. The significant higher variances of residual surface currents are shown in west/south of Point Loma, the offshore edge of the radial bin of Coronado Islands site (R3 in Figure 5.1), and the lee of the Coronado Islands (Figure 3.3). The spatial mean and RMS of the residual surface currents are nearly constant in space with 2–3 and 4–6 cm s^{-1}, respectively. One of the regions to have higher variance of the residual surface currents is the Point Loma headland, which may result from small scale variability arising from topographic effects and can be interpreted as the current components driven out of phase with the described forcing functions. The other regions are the baseline between SDBP and SDCI and the edge of the spatial coverage of the SDCI site (an angular bin at approximately 315 degrees from true north).

5.4.8 Structure of decomposed surface currents

The spatially averaged correlations of the decomposed surface currents are presented with their top views in the spatial lag space (Δx, Δy) (Figure 5.13). Three correlation terms of each decomposed component are considered: u-components ($\bar{\rho}_{uu}$, column a in Figure 5.13), v-components ($\bar{\rho}_{vv}$, column b in Figure 5.13), and the cross correlation of u and v components ($\bar{\rho}_{uv}$, column c in Figure 5.13). A set of the complement figures of the spatially averaged correlations of the decomposed surface currents is also shown in Figure 5.14.

The surface currents (Figure 5.13A) have the superposed structure of all decomposed components (Figures 5.13B–5.13G), which is slightly different from the spatial correlations presented in earlier (Figure 2.12) due to the difference in the method to extract vector current from radial velocity: optimal interpolation and un-weighted least-squares fitting (Chapter 3). The optimally interpolated surface currents have less noise and lower spatial variance due to spatial smoothing. As a result, the averaged spatial structure computed here is somewhat smoother than before. Currents related to the alongshore pressure difference in the low frequency band (Figure 5.4a), $\bar{\rho}_{vv}$ show a larger scale in the y-direction (Figure 5.13Aa) than the x-direction (Figure 5.13Ab).

The pure tide surface currents have broad spatial structure (Figure 5.13B) presumably owing to the large scale of the barotropic tidal forcing (section 5.4.1). Although the two shore station winds are local (section 5.4.2), the locally wind-driven surface currents exhibit a large scale structure in the x- and y-directions (Figure 5.13C).

The low frequency components have a directional preference in the decorrelation length scale, so that the eastward surface currents have a longer decorrelation scale in the x-direction than in the y-direction (Figure 5.13D). The diurnal band surface currents show clockwise flow with nearly uniform direction over the domain (the variance ellipses are nearly circular (not shown)), so the averaged spatial correlation shows a broad scale (Figure 5.13E). The semidiurnal band surface currents have localized and complicated features in the correlation (Figure 5.13F). The decorrelation

length scale of the residual surface currents is relatively small compared with the other components (Figure 5.13G).

The estimated correlation functions appear to be both Gaussian and exponential structures, or combination of the two with different decorrelation length scales for each decomposed component depending on physics and variability. The correlation functions of pure tide surface currents and locally wind-driven surface currents appear more Gaussian-like than exponential (Figures 5.13B and 5.13C). Large scale variability, including geostrophic and barotropic motions are expected to show more Gaussian shape, compared to exponential for turbulence ([Townsend(1980), Denman and Freeland(1985), Chereskin and Trunnell(1996), Wilkin et al.(2002)]). The other correlation functions are expected to be more exponential in shape, or perhaps large-scale Gaussian with a small-scale exponential on top (Figures 5.13D–5.13F). The cross correlation terms vary within ± 0.3 with complicated shapes and do not lend themselves to simple functional descriptions.

5.4.9 Relevance to a statistical model of surface currents

The results of decomposing the surface currents serve as building blocks for a statistical model of the surface currents for gap-filling and forecasting (equation 5.2). Future currents driven by pure tides can be computed from the estimated Fourier coefficients (section 5.3.1), and the locally wind-driven currents may have some predictability from the 6-day time interval of the TAWIRF (equation 5.7). The surface current components in the three frequency bands (equation 5.9) have predictability according to their decorrelation times, but a dynamical model is probably needed to optimize forecasts. For example, low frequency currents could be estimated from forecasts of large scale wind and atmospheric pressure.

The spatial correlation functions of each component of the surface currents are also relevant to the development of assimilation techniques for numerical ocean models, which often assume Gaussian correlation functions for lack of an improved functional relationship.

5.5 Discussion

Surface currents measured by shore-based high-frequency radar are decomposed into components using statistics informed by their driving physics: local wind, pure tides, cuspate tidal peaks at the diurnal (K1) and semidiurnal (M2) frequencies, the low frequency band ($|\omega| \leq 0.4$ cpd), and residual surface currents.

Decomposing the surface current components by their physics shows their distinct spatial structure and decorrelation length scales. The spatially averaged correlations of decomposed surface currents exhibit both Gaussian and exponential depending on the source of the variability and its scale. The complicated observed surface current decorrelation function is a superposition of all terms. The wind impulse response functions are estimated in the frequency and time domains, and are used to estimate the spectral content of the wind-forced currents and for other applications using wind

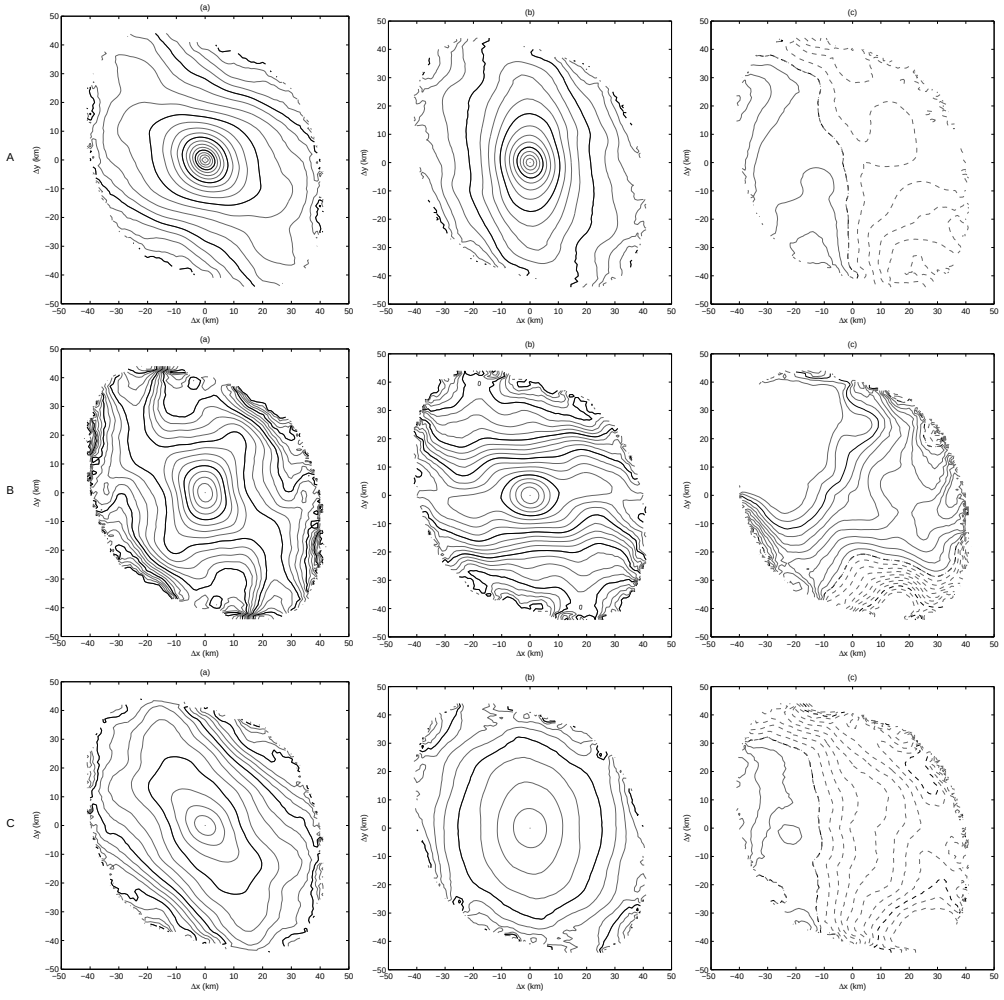

Figure 5.13: The spatially averaged correlations of decomposed surface currents are presented with top views of three components. Column (a): u-components ($\bar{\rho}_{uu}$). Column (b): v-components ($\bar{\rho}_{vv}$). Column (c): u and v components ($\bar{\rho}_{uv}$). A. Unconditioned surface currents ($\mathbf{u}$). B. Surface currents driven by pure tides ($\mathbf{u}_{\mathrm{t}}$). C. Locally wind-driven surface currents ($\mathbf{u}_{\mathrm{w}}$). D. Surface currents in the low frequency band ($\mathbf{u}_{\widehat{\mathrm{L}}}$). E. Surface currents in the frequency band centered on diurnal frequency ($\mathbf{u}_{\widehat{\mathrm{D}}}$). F. Surface currents in the frequency band centered on semidiurnal frequency ($\mathbf{u}_{\widehat{\mathrm{S}}}$). G. Residual surface currents ($\mathbf{u}_{\mathrm{r}}$). In the autocorrelation terms ($\bar{\rho}_{uu}$ and $\bar{\rho}_{vv}$), thick black contours present at 0.2, 0.4, 0.6, and 0.8 with 0.05 spacing with the gray contour. In the cross correlation term ($\bar{\rho}_{uv}$), the dash, solid, and dashdot contours indicate the negative, positive, and zero correlations.

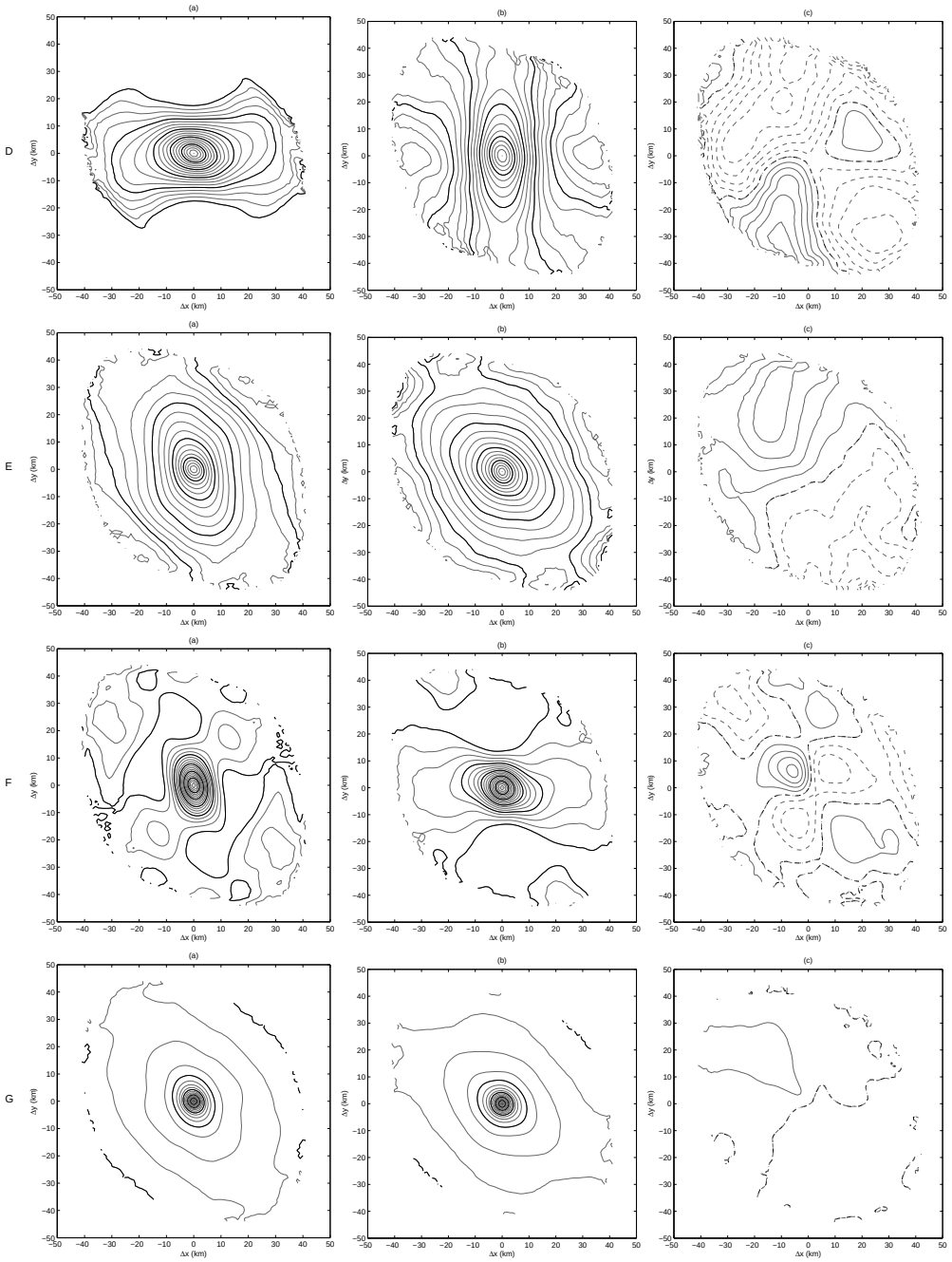

Figure 5.13: (Continued.)

wind observations and models (e.g., nowcast and forecast wind-driven current estimates, upwelling index, and etc). Weighted least-squares fitting is used to band-pass filter the surface current signal while treating missing data appropriately. The decomposition technique is applicable to both radial velocities measured by individual radars and the vector current field estimated from a radar array.

Although the baroclinic and barotropic components are indistinguishable by surface current observations alone, the spatial structure of the surface currents and the tidal ellipses may provide clues to separate the two signals in the data. The surface currents driven by M2 tides show shorter scales than those driven by K1 tides, suggesting baroclinic components such as shoreward propagating M2 internal tides. With adequate modeling, HF radar could perhaps be used to detect the surface signatures of small-scale baroclinic motions such as internal tides. The locally wind-driven surface currents were estimated from shore station winds allowing for anisotropic response and show relatively large scale structure. The magnitude of the locally wind-driven surface currents is typically 3–5% of the wind speed, and their veering angles vary 30–50 degrees to the right of the wind at the zero time lag.

In the low frequency band, the alongshore pressure difference (estimated by the SSH difference between two tide gauge stations) explains 10% of the low frequency surface currents, which presumably include both barotropic and baroclinic physics. This relatively low contribution of the shoreline SSH difference may be explained by two reasons: the shoreline SSH might not be an proxy for the alongshore pressure gradient term or the density gradients in the water column may be driving the low frequency surface currents, but does not result in an observable SSH difference. Although the contribution by coastal trapped waves are not explicitly resolved in this analysis, it might be a part of the alongshore pressure difference. The friction coefficient derived from the balance between the low frequency surface currents and the alongshore pressure difference is compared to form and bottom drag coefficients using the assumption of constant velocity throughout the water column.

5.6 Appendix

5.6.1 Stokes drift and surface layer jet

The contribution of the Stokes drift ([Kenyon(1969)]) to the observed surface currents is calculated

$$\mathbf{u}_{\text{Stokes}}(z) = \frac{1}{\rho} \iint_{\mathbf{k}} S(\mathbf{k}) \frac{\mathbf{k}}{\omega} \left[\frac{2k \cosh 2k(z+h)}{\sinh 2kh} \right] \mathrm{d}\mathbf{k}, \tag{5.18}$$

where $S(\mathbf{k}) = S(k, \theta) = A(k)B(\theta)$ is the surface gravity wave spectrum, which is the product of two independent functions – the ocean surface wave spectrum (A) and the directional distribution function (B). $\mathbf{k}$ denotes the wave number and θ is the direction of wave relative to wind ($\mathbf{k} = (k\cos\theta, k\sin\theta)$).

The directional wave spectra off San Diego are retrieved using the Maximum Entropy method ([Lygre and Korgstad(1986), Brissette and Tsanis(1994)]) using the Coastal Data Informa-

tion Program (CDIP) wave buoy observation (Point La Jolla, 093 station). The typical Stokes drift is 2–3.5 cm s^{-1} at the surface decreasing to about 1 cm s^{-1} at 1 m depth. The integration interval of the wave number is between 0.004 and 1.3552 m^{-1}, which covers the surface waves of 0.74–250 m wave length (or periods of 0.7–12.7 seconds) .

The surface current response to the wind may vary due to changes in the upper layer stratification. The magnitude of the surface layer jet, for simplicity, depends on the mixing layer (i.e., trapping depth, D_T) that the momentum penetrates, heat flux (Q), and wind stress (τ) ([Phillips(1966), Price et al.(1986)]):

$$|\mathbf{u}| \propto \frac{\tau}{D_T} \text{ and } D_T \propto \frac{\tau}{\sqrt{Q}}. \tag{5.19}$$

The seasonal and daily surface layer jets are explored with the Price-Weller-Pinkel (PWP) model ([Price et al.(1986)]) using seasonal/daily heat flux and wind stress in southern San Diego. The data are from the NCEP/NCAR heat flux reanalysis data ([Kalnay et al.(1996)]) and two wind observations (SIO and TJR). The surface layer jet shows the vertical momentum penetration from the surface in clockwise rotation. The order of magnitude of the surface layer jet is $O(2-3)$ cm s^{-1}, which is relatively small compared to the total variance of surface currents. Because the nearshore wind stress is much weaker than offshore and the diurnal winds within the land/sea breeze cell would not produce the current response of the same order as a steady wind stress ([Price et al.(1986)]). Since the seasonal variation of the wind stress is not significant in San Diego area (∼5% larger in summer), the surface layer jet is considered depending mostly on the heat flux. The heat flux in summer is approximately twice that in winter. From equation 5.19, the mixing layer in the summer is about 30% shallower than in winter and it results in 40% increase of the surface layer jet in summer.

The Stokes drift and surface layer jet are in separable in this analysis. The surface layer jet is considered to be embedded in the locally wind-driven surface currents and diurnal band surface currents as the seasonality of heat flux and the nonlinear interactions of responses to the diurnal wind (section 5.4.5), respectively.

5.6.2 Variance conservation

A time series ($\mathbf{d}$) can be regressed using the explicit basis of the sine and cosine functions ($\mathbf{G}$) on the discrete frequency domain,

$$\mathbf{d} = \mathbf{G}\mathbf{m} \tag{5.20}$$

$$d(t) = a_0 + \sum_{n=1}^{N} a_n \cos\omega_n t + b_n \sin\omega_n t \tag{5.21}$$

$$= a_0 + \frac{1}{2}\sum_{n=1}^{N} (a_n - ib_n)\, e^{i\omega_n t} + (a_n + ib_n)\, e^{-i\omega_n t}\,, \tag{5.22}$$

where a_n and b_n are the model coefficients (a_n and $b_n \in \mathcal{R}$). $\mathbf{m} = [a_1 \cdots a_n\, b_1 \cdots b_n]^\dagger$. On the other hand, the discrete Fourier transform can decompose the time series ($\mathbf{d}$) into

$$\mathbf{d} = \mathbf{G}\tilde{\mathbf{m}} \tag{5.23}$$

$$d(t) = \sum_{m=-N}^{N} \hat{d}_m e^{i\omega_m t} \tag{5.24}$$

$$= \sum_{m=-N}^{N} \left(\hat{a}_m + i\hat{b}_m\right) e^{i\omega_m t}, \tag{5.25}$$

where $\hat{a}_m$ and $\hat{b}_m$ are Fourier coefficients ($\hat{a}_m$ and $\hat{b}_m \in \mathcal{R}$, $\hat{d}_m \in \mathcal{C}$, $m \neq 0$). The variance conservation of two approaches in the frequency domain is

$$\langle \mathbf{d}(t)^2 \rangle = \frac{1}{2}\,\mathrm{trace}(\langle \mathbf{m}\mathbf{m}^\dagger \rangle) = \mathrm{trace}(\langle \tilde{\mathbf{m}}\tilde{\mathbf{m}}^\dagger \rangle), \tag{5.26}$$

where † denotes the (complex conjugate) transpose.

5.6.3 Relationship of slow least-squares fitting and discrete Fourier transform

The slow least-squares fitting is converted the regular expression of the spectral analysis ([Gonella(1972), Mooers(1973), Emery and Thomson(1997)]). The data ($\mathbf{d}$) is represented with

$$\mathbf{d}(t) = u(t) + iv(t) = \frac{1}{2}\sum_{n=1}^{N} \alpha_n e^{i\omega_n t} + \beta_n e^{-i\omega_n t}, \tag{5.27}$$

where

$$\alpha_n = (a_n + d_n) + i\,(-b_n + c_n)\,, \tag{5.28}$$

$$\beta_n = (a_n - d_n) + i\,(b_n + c_n)\,, \tag{5.29}$$

$$u(t) = \sum_{n=1}^{N} a_n \cos\omega_n t + b_n \sin\omega_n t \tag{5.30}$$

$$= \frac{1}{2}\sum_{n=1}^{N} (a_n - ib_n)\, e^{i\omega_n t} + (a_n + ib_n)\, e^{-i\omega_n t}, \tag{5.31}$$

and

$$v(t) = \sum_{n=1}^{N} c_n \cos\omega_n t + d_n \sin\omega_n t \tag{5.32}$$

$$= \frac{1}{2}\sum_{n=1}^{N} (c_n - id_n)\, e^{i\omega_n t} + (c_n + id_n)\, e^{-i\omega_n t}. \tag{5.33}$$

5.6.4 Structure of decomposed surface currents (Complement)

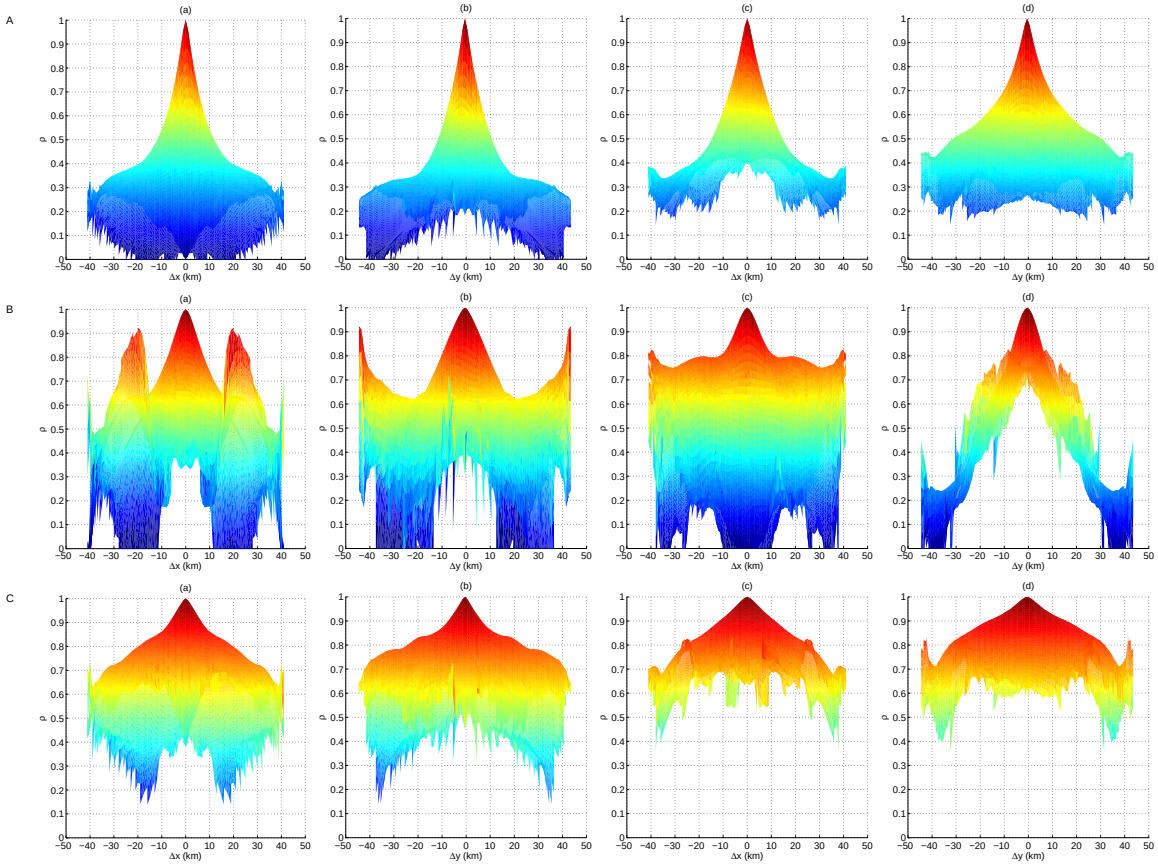

Figure 5.14: The spatially averaged correlations of decomposed surface currents are presented as the x- and y- views for each component. Column (a): Δx view of u-components ($\bar{\rho}_{uu}$). Column (b): Δy view of u-components ($\bar{\rho}_{uu}$). Column (c): Δx view of v-components ($\bar{\rho}_{vv}$). Column (d): Δy view of v-components ($\bar{\rho}_{vv}$). A. Unconditioned surface currents ($\mathbf{u}$). B. Surface currents driven by pure tides ($\mathbf{u}_{\mathrm{t}}$). C. Locally wind-driven surface currents ($\mathbf{u}_{\mathrm{w}}$). D. Surface currents in the low frequency band ($\mathbf{u}_{\widehat{\mathrm{L}}}$). E. Surface currents in the frequency band centered on diurnal frequency ($\mathbf{u}_{\widehat{\mathrm{D}}}$). F. Surface currents in the frequency band centered on semidiurnal frequency ($\mathbf{u}_{\widehat{\mathrm{S}}}$). G. Residual surface currents ($\mathbf{u}_{\mathrm{r}}$).

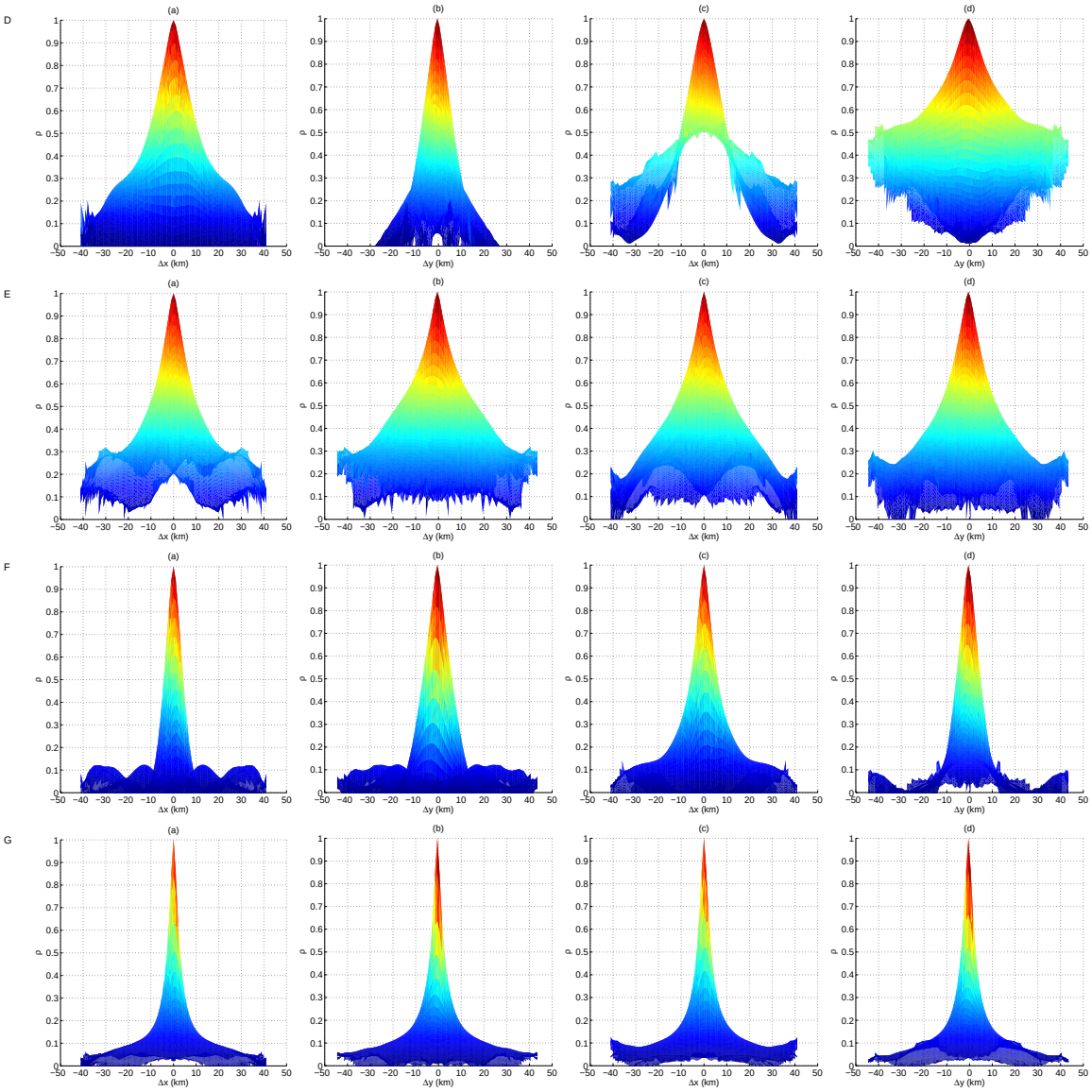

Figure 5.14: (Continued.)

This chapter, in part, has been submitted for publication of the material as it may appear in *Journal of Geophysical Research-Oceans*, 2009, Kim, S. Y., B. D. Cornuelle, and E. J. Terrill titled by 'Decomposing observations of high-frequency radar derived surface currents by their forcing mechanisms'. The dissertation author was the primary investigator and author of this paper.

Chapter 6

Assessing coastal plumes in a region of multiple discharges: the U.S.–Mexico border

Abstract

The San Diego/Tijuana border region shares similar environmental challenges with regards to assessing water quality impacts resulting from local coastal ocean discharges whose transport is not hindered by political boundaries. While an understanding of the fate and transport of these discharged plumes has a broad audience, the spatial and temporal scales of the physical processes present numerous challenges in conducting assessment with any fidelity. To address these needs, a data-driven model of the transport of both shoreline and offshore discharges is developed and operated in a hindcast mode for a four-year period to analyze regional connectivity between the discharges and the receiving of waters and the coastline. The plume exposure hindcast model is driven by surface current data generated by a network of high-frequency radars. Observations provided by both boat-based CTD measurements and fixed oceanographic moorings are used with the Roberts-Snyder-Baumgartner model to predict the plume rise height. The surface transport model outputs are compared with shoreline samples of fecal indicator bacteria (FIB), and the skill of the model to assess low water quality is evaluated using receiver operating characteristic (ROC) analysis.

6.1 Introduction

Impaired coastal water quality from point source discharges is a well-known concern for human health, degradation of marine ecosystems, and negative impacts to coastal economies when beaches are closed. At Imperial Beach located in southern San Diego, a significant number of beach closures by the San Diego County Department of Environmental Health (DEH) results from the presence of high concentrations of fecal indicator bacteria (FIB) exceeding California health standards (Assembly Bill 411). Similarly, high FIB levels are periodically reported on the Tijuana shoreline in the sparse sampling that takes place within 10 miles north and south of the Tijuana River mouth. Not only is the incidence of bacterial contamination and associated beach closures a problem, but time lags between sampling of the coastal water and completion of the analysis likely result in situations when beach waters may be clean when closed, and not clean when open. The beach closure has similar economic consequences regardless of the FIB levels.

Possible sources of bacterial contamination responsible for beach closures in this region include the Tijuana River (TJR), the South Bay International Water Treatment Plant Ocean Outfall (SBIWTP, called herein SBO), northward flow from the Punta Bandera treatment plant discharged at San Antonio de los Buenos (PBD), and local runoff from Imperial Beach. Furthermore, the tourist corridor between Tijuana and Rosarito has increased its population five-fold leading to the potential of uncontrolled residential and commercial discharge points. The multiplicity of possible sources near beaches requires that the water quality of the area be examined.

While there is political and public interest in coastal water quality, especially in the cross-border context on which this paper is based, the ocean monitoring of the physics responsible for the transport of a discharge plume has historically not been conducted at the appropriate scales required to accurately estimate its time-dependent nature. This is principally due to the high cost of continuous measurements of ocean conditions and the relatively short decorrelation length scale of a point measurement of ocean current. While the TJR flow is a likely cause for impaired water quality during the rainy season, little is known about the offshore and alongshore extent of the river plume. Likewise, impaired water quality events can occur during the dry season, indicating that plume water from one of the other two discharges may periodically impact the coastline.

Stormwater and wastewater discharges in the Southern California region have been addressed using other observational methodologies, including the application of traditional in situ oceanographic observations, analysis of historical data gathered as part of the National Pollutant Discharge Elimination System (NPDES) permit, and interpretation of intermittently obtained remote sensing data on the river discharge in the coastal area and the ocean outfall plume. The dynamics of both river and outfall plumes have a history of experimental studies which provide a basis for the approach described herein. The river plume models depend on the width of the river discharge, bottom topography, wind speed and direction, ambient current field, input flow rate, and inertial forcing ([Hill(1998), Washburn et al.(2003)]). The vertical rise and dilution of a sewage plume discharged at the seafloor has been addressed through models based on hydraulic principles

of buoyant jets in stratified and unstratified fluids, with the Roberts-Snyder-Baumgartner (RSB) model ([Roberts et al.(1989), Roberts(1999a), Roberts(1999b)]) serving as a well documented model in use by the U.S. Environmental Protection Agency (EPA) for evaluating near-field discharge plume behavior.

The approach adopted here to understand the plume transport in the coastal zone is to integrate surface current data measured by an array of high-frequency (HF) radars and produce a Lagrangian analysis of the plume trajectory. Unlike traditional discharge monitoring approaches, HF radar provides hourly surface current maps over a large spatial domain which can be used to drive a time integration of the plume position. For the U.S.–Mexico cross-border region, multiple radar sites have been maintained since 2001, providing a multi-year time series of circulation suitable for hindcast analysis of the three major discharge plumes previously described. A primary distinction of this study to previous studies is the four-year duration of a continuous hindcast analysis conducted on an hourly interval.

This chapter is organized into three sections. First, water quality, rainfall, and physical oceanographic observations of surface currents, and ocean stratification are summarized to provide a description of the study region conditions (section 6.2). Then a hindcast analysis of three regional discharges using a random walk model driven by surface current observations is described (sections 6.3 and 6.4). Lastly, we present the results of the plume exposure hindcast model including its performance using Receiver Operating Characteristic (ROC) analysis (sections 6.6 and 6.5.4) and discuss underlying assumptions used in the model including the suitability of the model when addressing transport across and within the surfzone (section 6.7). The summer and winter seasons discussed in this chapter indicate April to September and October to March, respectively.

6.2 Summary of Observations

6.2.1 Water quality sampling

The FIB sampling locations in the cross-border region are summarized in Table 6.1 ordered by a unique shore station ID as shown in Figure 6.1. These data are provided by San Diego County DEH as part of their AB411 (Assembly Bill 411, Statutes of 1997, Chapter 765) samplings and ([California Ocean Plan(1990)]) as well as the City of San Diego Wastewater District which monitors the SBO for the NPDES permit both under contract to the International Boundary Water Commission (IBWC) and for the City's co-located water reclamation plant. Although the water quality data at C1 and C14 stations are identified, they are not included in this analysis as they were sparsely sampled as compared to the other stations. The FIB sampling and processing are conducted using accepted standards and protocols on a scheduled basis except for targeted shoreline samples by the DEH during suspected contamination events.

The distribution of the bacterial levels along the shoreline is examined with the annual mean at each station over three FIB levels for ten years (January 1996 to March 2007): *Total Coliform*

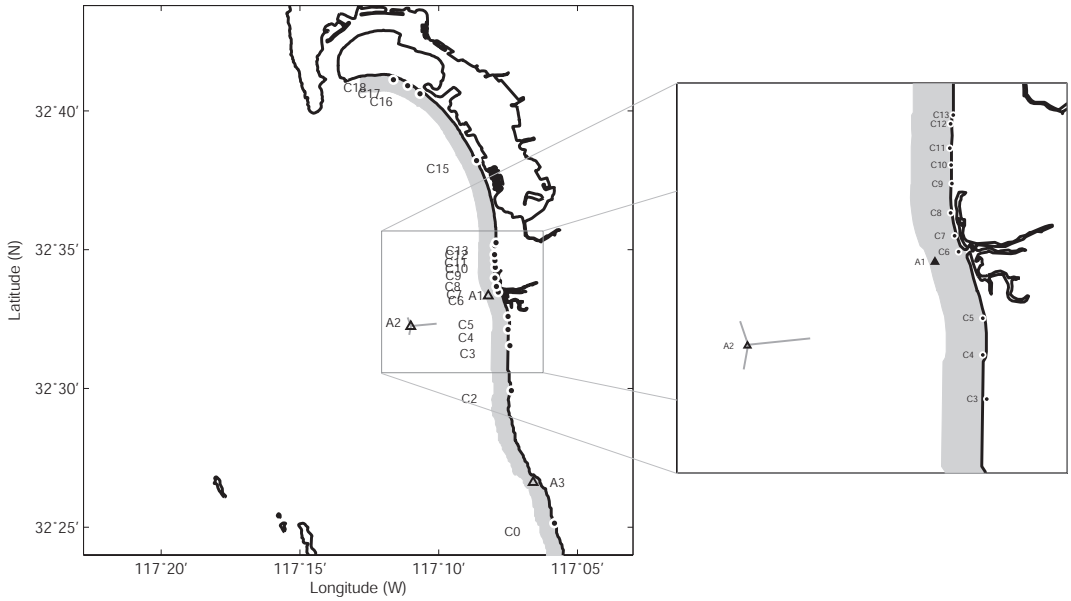

Figure 6.1: Study domain of the water quality monitoring in southern San Diego. Shoreline water quality stations (C0, C2–C13, and C15–C18 in Figure 6.1) are indicated as dots. Three potential sources of the impaired water quality are marked as triangles, and they are releasing locations of the particle trajectory model: Tijuana River (A1, TJR), the South Bay International Wastewater Treatment Plant (A2, SBO), and Punta Bandera treatment plant discharge at San Antonio de los Bueno approximately 6 miles south of the U.S.–Mexico Border (A3, PBD). The southern effluent outfall of the SBO is active, and the current and temperature profiles are observed at the SBO. The nearcoast cell is defined as the area within 1 km from the coastline (shaded area).

(TC, Figure 6.2a), *Fecal Coliform* (FC, Figure 6.2b), and *Enterococcus* (ENT, Figure 6.2c). The horizontal axis is not scaled with the physical distance between stations to avoid the overlapped plots. The highest FIB concentration is at C6 station closest to the TJR mouth. The FIB levels in the southern area of the TJR are slightly higher than the northern side. The relatively higher level of TC near the Punta Bandera discharge at Los Buenos creek is observed ([James and Groce(2006)]).

Table 6.1: A unified water quality sampling stations along the southern San Diego coastline and the number of sampling data for about eleven years (January 1996 – March 2007). The water quality data at C1 and C14 stations are reported from historical records, but they are not included in the analysis due to their sparse observations and the lack of station information.

ID	City ID	County ID	Station name	The number of samplings
C0	S0	BC-010	Playa Blanca	232
C2	S2	BC-020	El Vigia	507
C3	S3	BC-030	Playas de Tijuana	507
C4	S4	IB-010	Border Fence	1252
C5	S10	IB-020	Monument Road	1257
C6	S5	IB-030	Tijuana River Mouth	1416
C7	S11	IB-040	3/4 miles North of Tijuana River	1342
C8	S6	IB-050	End of Seacoast Drive	1447
C9		EH-010	Cortez Avenue	380
C10		EH-020	Imperial Beach Boulevard	78
C11		EH-030	Imperial Beach Pier	604
C12	S12	IB-060	Carnation Avenue	1339
C13		EH-041	Camp Surf Jetty	231
C15	S8/D2	IB-070	Silver Strand Beach	1385
C16	S9/D3	IB-080	Avenida del Sol	2042
C17		EH-050	Loma Avenue	859
C18		EH-060	Navy Fence	853

Water quality standards in the State of California Health and Safety Code (AB 411) establish a set of criteria for identifying if a human health risk is present. These criteria are based on both a single sample result for *Total Coliform* (c_1), *Fecal Coliform* (c_2), and *Enterococcus* (c_3), as well as the ratio of FC to TC:

$$g = \{g | c_1 > 10000, c_2 > 400, c_3 > 104, \left(\frac{c_2}{c_1} > 0.1\right) \cap (c_1 > 1000)\}, \tag{6.1}$$

where c_1, c_2, and c_3 indicate the amount in 100 ml, and have the units as CFU (CFU: colony forming units) for both TC and FC and as MPN (most probable number) for ENT, respectively. The exceedance relations are posed as a water quality indicator (g) with a binary state – clean (C) or contaminated (D):

$$g = g(c_1, c_2, c_3, t_d), \tag{6.2}$$

where t_d is the duration that the FIB level is valid.

The water quality sampling data along the shoreline stations for four years (April 2003 – March 2007) are shown in Figure 6.3a. All available sampling data are indicated with dots (C) and

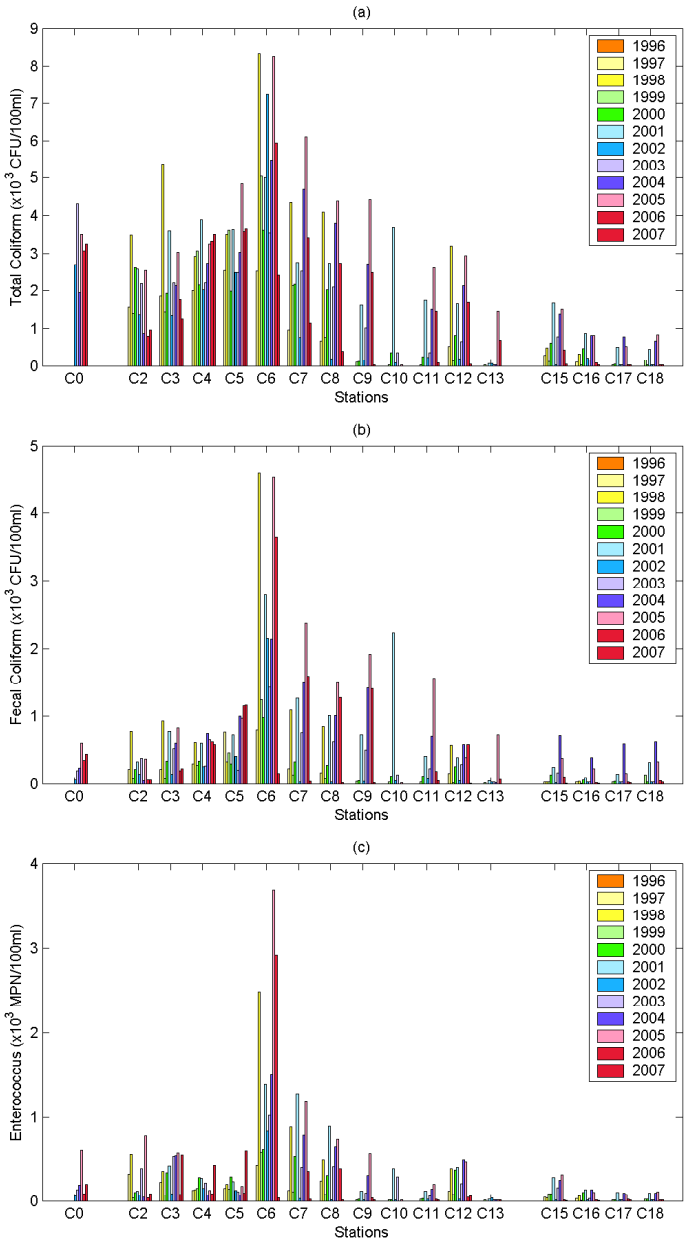

Figure 6.2: The annual mean of the water quality sampling data (January 1996 – March 2007). (a) *Total Coliform* (TC). (b) *Fecal Coliform* (FC). (c) *Enterococcus* (ENT).

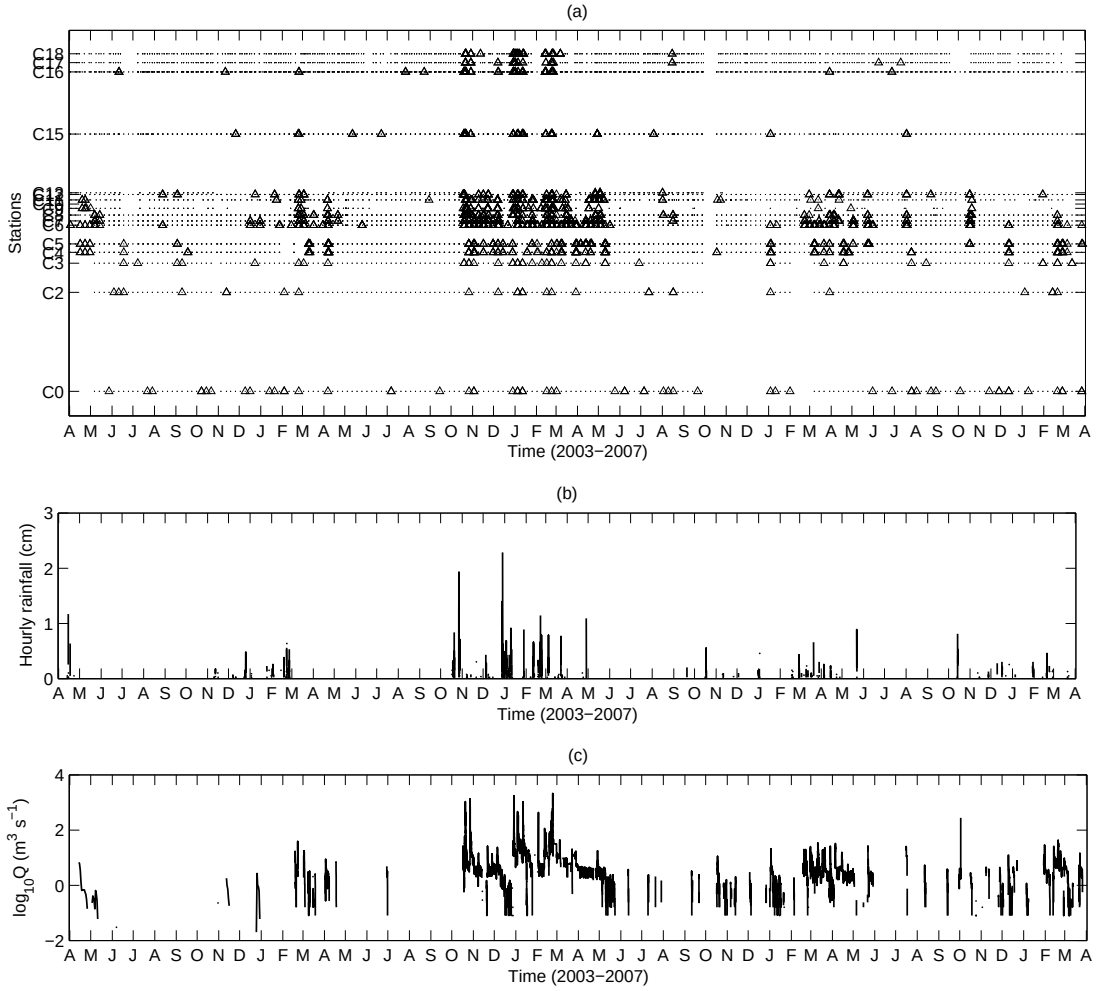

Figure 6.3: (a) Water quality sampling data along the coastline in southern San Diego. The triangles and dots, respectively, indicate the contaminated (D) and clean (C) conditions based on the FIB criteria in equation 6.1. (b) Hourly cumulative rainfall (cm) at SAN. (c) Hourly TJR flow rate ($m^3\ s^{-1}$, log scale).

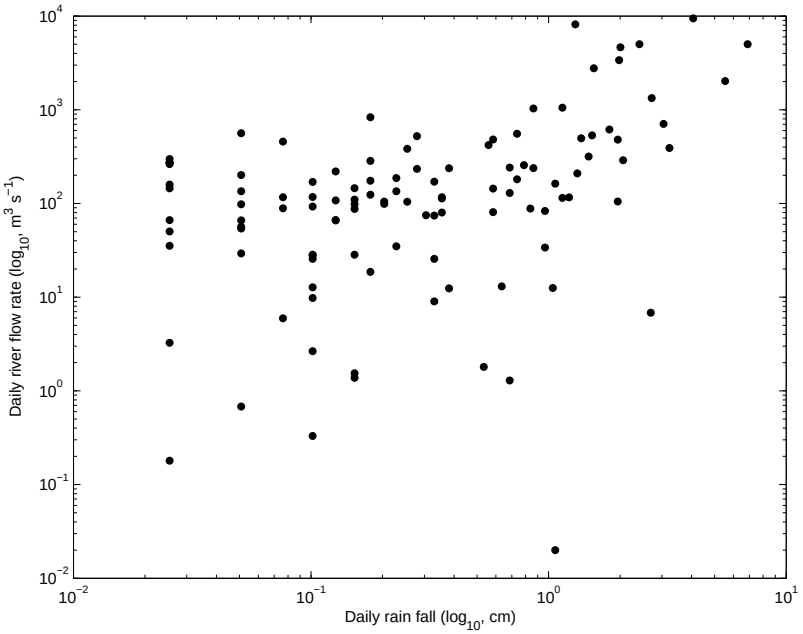

Figure 6.4: The scatter plot (log scale) of the daily rainfall at SAN and the daily TJR flow rate (2003 – 2007).

triangles (D). The D condition is highly correlated with the wet weather season (winter season), which is consistent with other studies ([Kim et al.(2004), Svejkovsky and Jones(2001)]).

6.2.2 Rainfall in San Diego and Tijuana River flow

The hourly cumulative rainfall at San Diego Lindbergh Field (SAN) and the hourly TJR flow rate are shown in Figures 6.3b and 6.3c, respectively. The rainfall in southern San Diego is concentrated during the wet season, and leads to the TJR outflows with heavy sediment and debris loads, which are potential causes of impaired coastal water quality. The river flow due to rainfall shows a time-lagged response: in the initial stage of rainfall the river flow is nearly proportional to it, then once rainfall reaches its peak, the river flow is almost steady and decreases slowly (Figure 6.4). The other local rainfall at the Tijuana River National Estuarine Research Reserve (TRNERR) and the San Diego Coastal Ocean Observing System (SDCOOS) is compared with the SAN rainfall, which is used as a proxy of the local rainfall owing to the longest record (∼10 years).

6.2.3 Surface currents

Coastal surface currents in the cross-border region used in this study are measured by an array of HF radars. While their operation is detailed in Chapter 2, we note that they provide hourly surface current maps with 1 km spatial resolution. Prior to their usage for Lagrangian trajectory computations, the surface currents are objectively mapped using a sample covariance

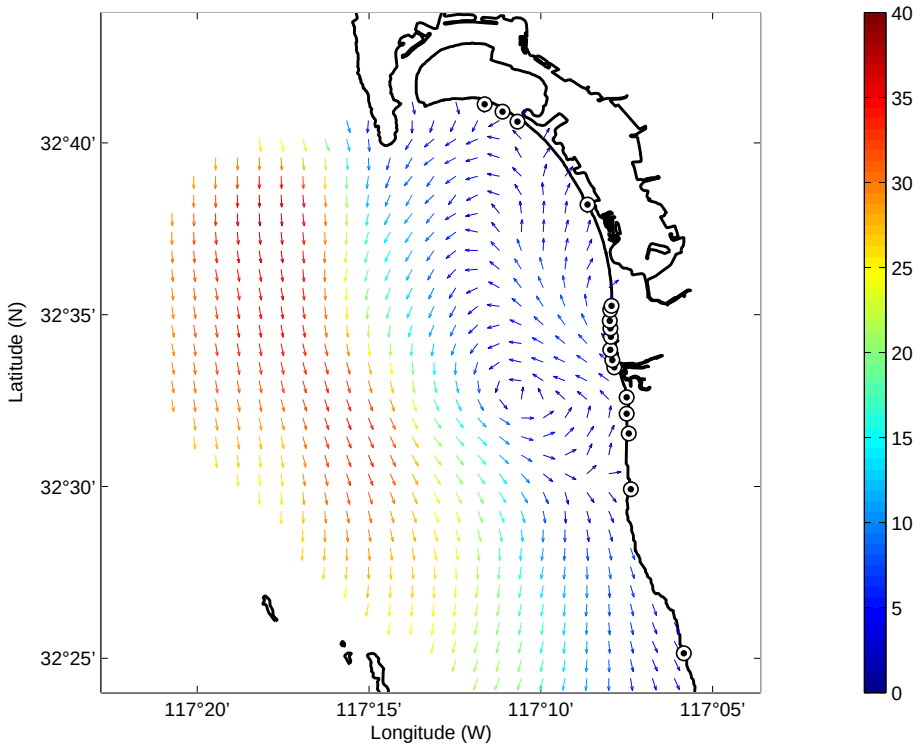

Figure 6.5: An example of the objectively mapped surface current field (May 20 1600, 2003 (GMT)).

matrix computed from four-year hourly data in order to fill in missing data (Chapter 2). The uncertainty of the estimated surface current field is about 8.6 cm s^{-1}, which is roughly consistent with reported root mean square (RMS) differences between radar-derived surface currents that are a spatial integral and in situ point observations: 5–7 cm s^{-1} (ADCP), ~5.5 cm s^{-1} (radial velocities of multiple HF radars, [Lipa et al.(2006)] and section 3.3.3), and 1–4 cm s^{-1} (GPS-tracked drifter, [Ohlmann et al.(2007)]).

The typical surface circulation pattern in the study domain is distinct between offshore (beyond 15 km from the coast) and nearshore (within 15 km from coast) regions. Persistent southeastward surface currents are observed offshore presumably due to flow around the headland or eastward flow deflected by the coastline (section 2.2.3). In the nearshore, a single eddy or dipole eddies with a diameter of 10–15 km are frequently observed near the TJR mouth and produce horizontal divergence or convergence. Figure 6.5 shows an example of the typical circulation pattern with a single counterclockwise eddy.

The dominant variance in the surface currents in this region is the low frequency band (less than 0.4 cpd) and cuspate tidal peaks at the diurnal (K1) and semidiurnal (M2) frequencies superposed on a red spectrum $\left(S(\omega) \propto \omega^{-2}\right)$ (sections 2.2.3, 4.4, and 5.2.3). Since the time integration of the surface currents is a low-pass filter $\left(S(\omega) \propto \omega^{-4}\right)$, the Lagrangian surface transport should be dominantly driven by the subinertial variability. The magnitude of the low frequency surface

currents is approximately 10 cm s^{-1}, so the Lagrangian surface transport is expected to exit the study domain (40×40 km^2) within about 5 days.

Since the numerical approach used transports plume water to the coastline, the boundary conditions at the ocean-land boundary treat the boundary currents as the projection of an alongshore vector of the measured currents from the nearby 1×1 km^2 grid. Since the coastline has significant curvature, the projection angle is computed for all discrete locations in the domain. The data suggest that the currents have less variance north of the TJR mouth (C13–C16 stations in Figure 6.1) and higher variance along the nearly straight coast south of TJR (C0–C5 stations). The alongshore currents have 40–60% more variance in the low frequency band (0.1–0.5 cpd) compared with the typical current variance in the study domain (not shown), which implies intensified 2–10 day period alongshore transport.

For a typical rain event, the surface currents are generally to the north at the start of the flow since storm events approach from the south, a pattern that was found to be consistent for over 80% of rain events when the daily averaged TJR flow rate is 10^3 m^3 s^{-1} or more.

6.2.4 Vertical ocean temperature structure

Temperature observations using a vertical array of 10 temperature probes (0.01 degree accuracy) for approximately three years at the SBO (A2 in Figure 6.1) provide a measurement of water column stratification and allow the prediction of the plume rise height which discharges at a depth of 28 m. Since the temperature probes are sampled at a 5 minute interval, high frequency fluctuations from internal tides and bores have been observed (not shown). The surfacing of the plume water occurs during weak stratification allowing the plume's buoyancy to overcome the trapping effect of the density stratification. In addition, salinity is found to be a weak influence on changes in stratification in Southern California waters ([Bratkovich(1985), Winant and Bratkovich(1981)]) including San Diego.

6.2.5 Climatological data

The NPDES permit of the SBO discharge includes monthly vertical sampling of temperature, salinity, density, and chlorophyll-a. The data are obtained using a conductivity, temperature, depth (CTD) sensor, and stations are vessel occupied both in the nearshore and offshore within 15 km from the coast including dense sampling near the SBO. Typical sampling stations are shown as dots in Figures 6.6a and 6.6b, and they are occupied in a 2–4 day window for sampling.

Examples of the TJR plume and the SBO plume detected in the salinity data from the CTD stations are shown as the linearly interpolated surface (Figure 6.6a) and bottom (Figure 6.6b) maps and vertical sections in the cross-shore direction (Figures 6.6c and 6.6d). The cross-shore sections of salinity (Figures 6.6c and 6.6d) use the salinity data within a rectangular box in Figures 6.6a and 6.6b. During a heavy rain in January 2005, a lower salinity front (less than 32.6 psu) was observed in front of the TJR mouth and reached near 12 km from the coast with a film in the

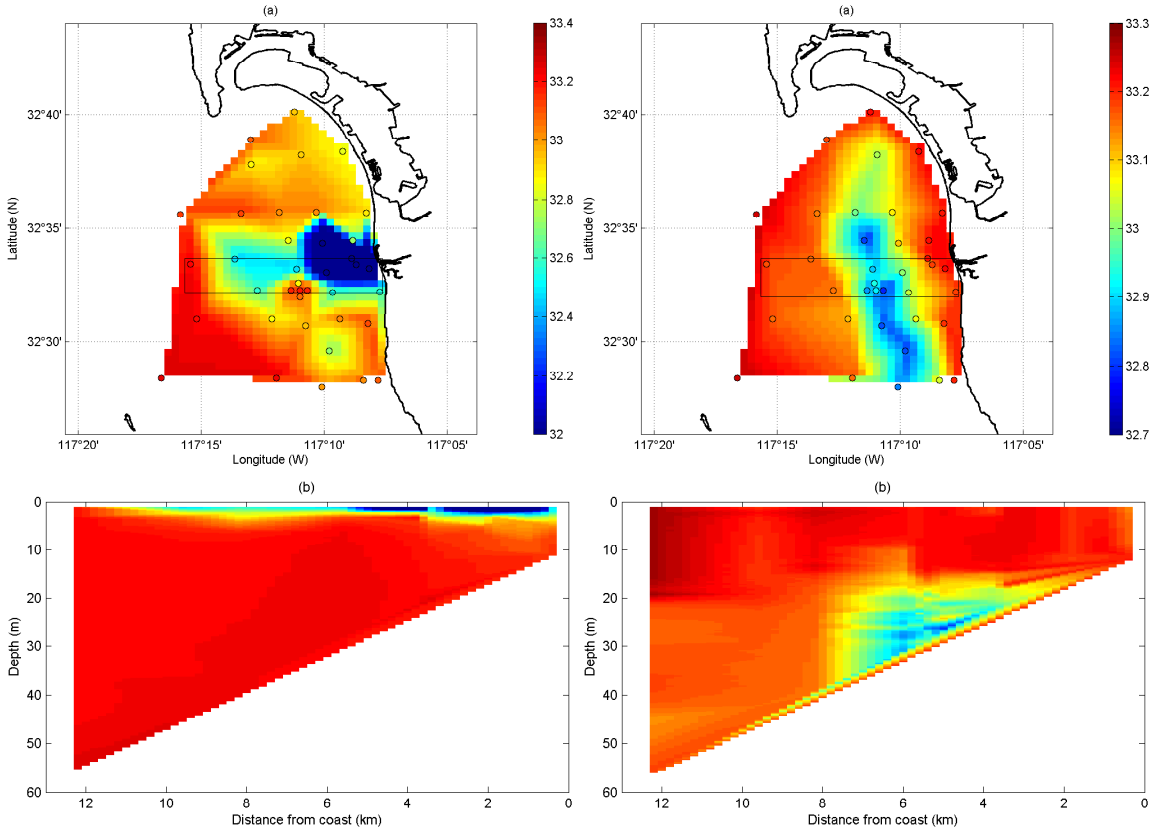

Figure 6.6: Linearly interpolated salinity (psu) surface/bottom maps and vertical section in the cross-shore direction. (a) and (c): Surface map and vertical section of salinity during the one of heavy rain events on January 2–6, 2005. (b) and (d): Bottom map and vertical section of salinity on December 16, 2003. The vertical sections of salinity ((c) and (d)) use the salinity data within the rectangular box on (a) and (b).

1–2 m upper layer (Figures 6.6a and 6.6c). This surface advected jet due to buoyancy difference is a typical flow pattern of the river plume in the coastal region ([Yankosvky and Chapman(1997), MacDonald and Geyer(2005), McCabe et al.(2008)]). On December 2003, the lower salinity water (less than 32.9 psu) near the outfall was trapped within 20 m of the bottom and spread in the alongshore direction.

6.2.6 Remote sensing data

Satellite images of total suspended matter (TSM) and chlorophyll-a (Chl-a) in the study area are used for qualitative verification of the offshore surface transport. The satellite IRS-P4 (Indian Remote Sensing Satellite or OCEANSAT-1) carries two sensors MSMR (Multichannel Sacnning Microwave Radiometer) for data collection on SST, wind speed, and atmospheric water vapour and OCM (Ocean Color Monitor) for data on atmospheric aerosols, suspended sediments, chlorophyll concentration, and reports the identical coverage of a given area every 48

hours ([Space Applications Centre (ISRO)(1997), Space Applications Centre (ISRO)(1998)]). During a storm event on January 2–6 of 2005 the higher density TSM and Chl-a were observed as a stretched tongue or a jet (Figures 6.7a and 6.7b, respectively) as the salinity surface map in Figure 6.6a.

6.3 Regional discharges

Three likely candidate discharges responsible for high FIB levels in southern San Diego are summarized by location, discharge type, and flow rate (Table 6.2). The source locations (A1, A2, and A3 in Figure 6.1) are used as source points for the particle trajectory calculation in the subsequent hindcast analysis. The TJR outflows just north of the border and drains precipitation from a watershed of 4,480 km^2, two thirds of which is in Mexico (A1 in Figure 6.1). The SBO is located 3.5 miles offshore west of the border and has discharged advanced primary-treated wastewater through an underwater outfall year round since 1999 (A2 in Figure 6.1). The City of Tijuana discharges pre-treated waters directly into the beach at San Antonio del los Buenos (6 miles south of the border) from the PBD (A3 in Figure 6.1) ([Largier et al.(2004), San Diego County(2000), Svejkovsky and Jones(2001), Orozco-Borbon et al.(2006)]).

Table 6.2: The potential sources of bacterial contamination in southern San Diego are summarized with the location, discharge type, and flow rate (MGD: Million gallons per day): Tijuana River (TJR), South Bay International Wastewater Treatment Plant (SBO), and Punta Bandera discharge (PBD).

Sources	Location		Discharge type	Flow rate ($m^3\,s^{-1}$ (MGD))
	Longitude (W)	Latitude (N)		
TJR	32.5556	117.1369	Wet season	$\sim$ 2.9 (66)
SBO	32.5373	117.1835	Plume surfacing	$\sim$ 0.9 (20)
PBD	32.4336	117.1100	Continuous	1–1.5 (22–35)

6.3.1 Coastline discharge: Tijuana River

The rainfall in southern San Diego and the TJR outflow are concentrated during the winter season (Figures 6.3b and 6.3c), and FIB exceedance at the TJR mouth (C6 station) is 93% coherent with the existence of the TJR flow. Due to the high correlation of high FIB with the TJR flow, we use flow conditions as the trigger for when to track water parcels from the TJR source.

6.3.2 Submerged discharge: South Bay International Wastewater Treatment Plant (SBIWTP)

The dynamics of the plume is controlled by the outfall design and density structure with depth in the near-field and the ocean variabilities in the far-field (e.g., winds, tides, alongshore

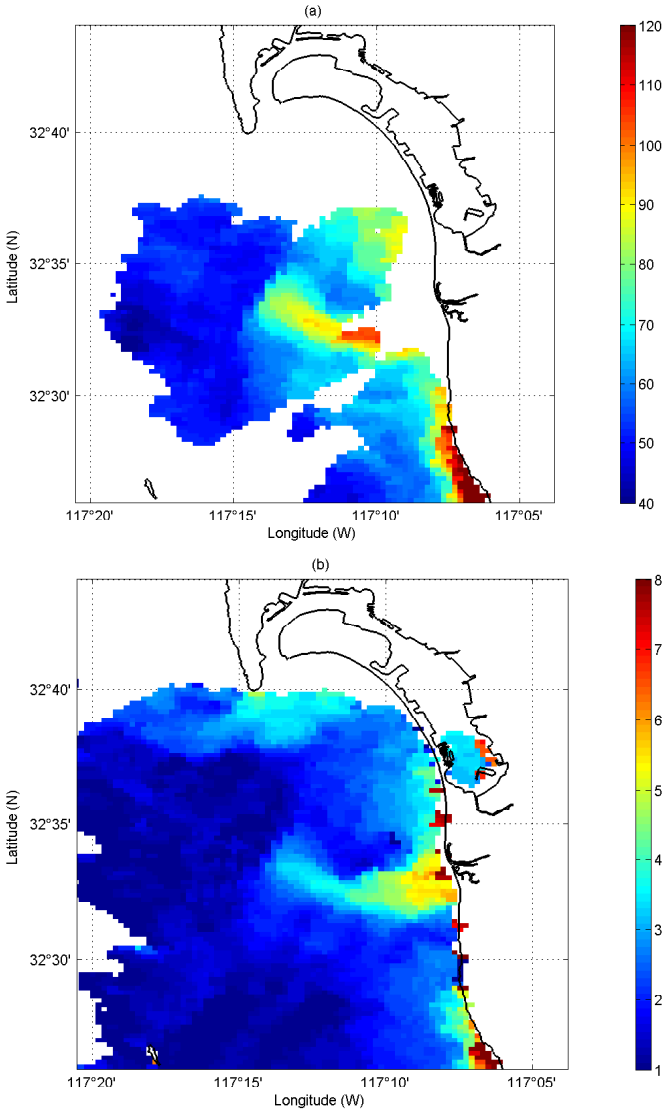

Figure 6.7: Ocean satellite images: (a) Total suspend matters (mg L^{-1}) and (b) Chlorophyll-a (mg m^{-3}) during a heavy rain event on January 6 1939, 2005 (GMT).

Table 6.3: (a) Inputs and (b) outputs of the RSB model to examine the near-field behavior of the SBO ([Roberts et al.(1989), Largier et al.(2004), San Diego County(2000)]).

(a)

Model inputs	Input data
Number of ports, n	60
Port diameter, D (m)	5
Port spacing, Δd (m)	3.66
Discharge depth, z_0 (m)	28
Diffuser orientation, θ_0 (degrees, clockwise @ N)	11.7
Effluent density, ρ_q (g cm^{-3})	0.997
Discharge amounts, q (MGD)	20
Number of points in density profile	13

(b)

Model outputs
Minimum dilution at the end of near-field, S_n
Rise height from the bottom, z_e (m)
Thickness of plume, h_e (m)
Height to level of near-field dilution, z_m (m)
Length of the near-field, x_n (m)

pressure gradient, and internal waves). The U.S. EPA Roberts-Snyder-Baumgartner (RSB) plume model ([Roberts et al.(1989), Roberts(1999a), Roberts(1999b)]) has been used to predict the height of the plume and the potential for active surfacing within the near-field. The RSB model is based on the assumptions of linear stratification between neighboring vertical observations, uniform currents, straight diffusers, and Gaussian spreading of plume water concentrations at the end of the near-field ([Roberts(1999a), Roberts(1999b), Frick et al.(2001)]). The plume height (h) is parameterized in the RSB model as

$$h = h(\rho(z), \mathbf{u}(\mathbf{x}, z_0), q;\ n, D, \Delta d, z_0, \theta_0, \rho_q), \tag{6.3}$$

where $\rho(z)$, $\mathbf{u}(\mathbf{x}, z_0)$, and q denote the ambient density profile, the current at the plume depth, and the amount of outfall flow (m^3 s^{-1}), respectively. The SBO plume specifications and the RSB model outputs are described in Figures 6.3a and 6.3b, respectively. The behavior of the plume in the near-field is estimated with the RSB model, and the transport in the far-field of the surfacing plume water is tracked with Lagrangian trajectory analysis of hourly surface current maps, which will be discussed in the following section. The surfacing of the SBO plume water is used for triggering when to tack transport.

The SBO has improved the impaired coastal water quality in southern San Diego since 1999 ([James and Groce(2006), Gersberg et al.(2008)]). However, the improvements during dry and wet seasons need to be investigated with continuous observations. ([Bratkovich(1985), Winant and Bratkovich(1981)]) found that the density stratification is closely related to the temperature rather than salinity in the Southern California Bight, which allows the density profile to be calculated from vertical temperature profile ([Millero and Poisson(1981), Fofonoff and Millard Jr.(1983)]). Due to limited observation of the current profile, the bottom cur-

rent is assumed as Gaussian variables using the mean and RMS of the ADCP observations at that location, which are 5.5 and 2.3 cm s^{-1}, respectively. The estimated plume rise height is found to be less sensitive to the bottom current.

The predicted ceiling depth (z_e) is highly dependent on the stratification: the strong stratification in summer traps the plume beneath the thermocline, and the weak stratification in winter allows the plume to surface. The RSB model outputs show the approximately one hour time lag between uplifts in isotherms and the predicted ceiling depth.

The surfacing of the SBO plume takes place ∼25% over a year. Excluding the surfacing events, the plume ceiling is on average 9.3 m (mean depth) with 3.5 m (RMS). The vertical temperature differences between top and bottom depths during surfacing and non-surfacing events are less than 1 degree and 5–6 degrees, respectively. The monthly histogram of the ceiling depth shows the frequent surfacing during winter and intermittent breakdown of the stratification during summer, which can explain the anomaly in August. The four years of temperature data (April 2003 – March 2007) have some gaps which can bias the seasonal statistics: the missing observations are 8 and 2 months for summer and winter seasons during four years, respectively, and those are 33 and 8.3% of each season.

6.3.3 Coastline discharge: Punta Bandera discharge

The Los Buenos Creek continuously discharges 0.97–1.46 $m^3\,s^{-1}$ of minimally treated sewage effluent from the San Antonio de Los Buenos Sewage Treatment Facility near Tijuana ([Svejkovsky and Jones(2001), Orozco-Borbon et al.(2006)]). [Orozco-Borbon et al.(2006)] reported the higher bacteria concentration near the PBD due to the treatment facility, and discussed the impaired water quality at the U.S.–Mexico border dominantly resulted from the TJR than the PBD. Since it is a continuous discharge, not conditional trigger for the source is necessary.

6.4 A plume exposure hindcast model and analysis

6.4.1 Trajectory analysis using random walk model (RWM)

The forward particle trajectory in the finite time domain is calculated as:

$$x(t) = \int_{t_0}^{t} (u(t') + \epsilon^u)\,\mathrm{d}t' + x(t_0) \approx \sum_k (u(t_k) + \epsilon_k^u)\,\Delta t + x(t_0), \tag{6.4}$$

$$y(t) = \int_{t_0}^{t} (v(t') + \epsilon^v)\,\mathrm{d}t' + y(t_0) \approx \sum_k (v(t_k) + \epsilon_k^v)\,\Delta t + y(t_0), \tag{6.5}$$

where $\mathbf{x}(t) = [x(t)\, y(t)]^\dagger$ and $\mathbf{u}(t) = [u(t)\, v(t)]^\dagger$ denote the location of the particle and the surface currents at the particle location at a given time (t), respectively (t_0 is the initial time of the simulation). ϵ^u and ϵ^v are the random variables with zero mean and RMS of ϵ.

In Lagrangian stochastic models, the random walk model (RWM) inherits the similarity of the Lagrangian statistics of the passive tracer in the coastal region compared to the random flight model ([Griffa et al.(1995), Griffa(1996)]). The random flight model has been used in studies of marine larvae spreading ([Siegel et al.(2003), Isaji et al.(2005), Ullman et al.(2006), Spaulding et al.(2006)]) for the active tracer simulation. The added random variable (ϵ) at time $k+1$ in the random walk and random flight models has white ($\lambda_t = \Delta t$) and red ($\lambda_t > \Delta t$) spectra, respectively, as

$$\epsilon_{k+1} = \epsilon_k \left(1 - \frac{\Delta t}{\lambda_t}\right) + \alpha\sigma\sqrt{\frac{2\Delta t}{\lambda_t}}, \tag{6.6}$$

where α is the Gaussian variable for the perturbation, λ_t is the decorrelation time scale, and σ is RMS of the current field. The shorter the decorrelation time scale is in the random flight model, the flatter its spectrum is. The RWM is used in this study in order to preserve the shape of the power spectrum of the original current field and to simulate the pollutants as the passive tracer. The diffusion parameter (ϵ^u and ϵ^v) in equations 6.4 and 6.5 represents unresolved velocities as the uncertainty in the HF radar measurements ($\epsilon = 5$ cm s^{-1}). A large number of particles are released and tracked with each time step so that their statistical distribution can be used to infer a probability exposure for a given discharge.

The RWM is applied to investigate the statistics of the particle transport for three potential sources: TJR, SBO, and PBD. For this study, all discharges are assumed to be passive with no dynamical impact on the flow, allowing the mapped surface currents to be the initial current field into which the discharge occurs. 50 particles are released hourly at each source location (A1, A2, and A3 in Figure6.1). In case that the particle crosses over the coastline boundary in a given current field, the trajectory is recalculated by applying the alongshore currents in order to constrain the particle to follow the coastline. Particles are tracked for three days, which is consistent with the estimated life time of the FIB ([Noble et al.(2000), Ackerman and Weisberg(2003), Noble et al.(2004)]). No time dependent decay of the FIB is used for the analysis since the goal is to examine the plume water exposure probability as opposed to concentration prediction.

A snapshot of the particle trajectory of the RWM and the histogram of the particle concentration within the nearcoast cell – an alongshore band extending 1 km from the coast (shaded area in Figure 6.1) – is shown in Figure 6.8, which is a part of the near real-time TJR plume tracker (`http://sdcoos.ucsd.edu/data/particles/IB/`). This histogram helps to understand upcoast/-downcoast transports in time.

The number of particles (f) arriving in the nearcoast cell is a function of several parameters:

$$f = f(l, t_p, w, n, \mathbf{x}_0, \mathbf{u}, \epsilon), \tag{6.7}$$

where l is the life time of the particle, t_p is the time span of discharge (e.g., river flood period or wet season), w is the alongshore-wide bin size of the nearcoast cell, n is the number of particles released per unit time, $\mathbf{x}_0$ is the initial position where particles are released, $\mathbf{u}$ is the surface current field, and ϵ is the diffusion parameter in the RWM.

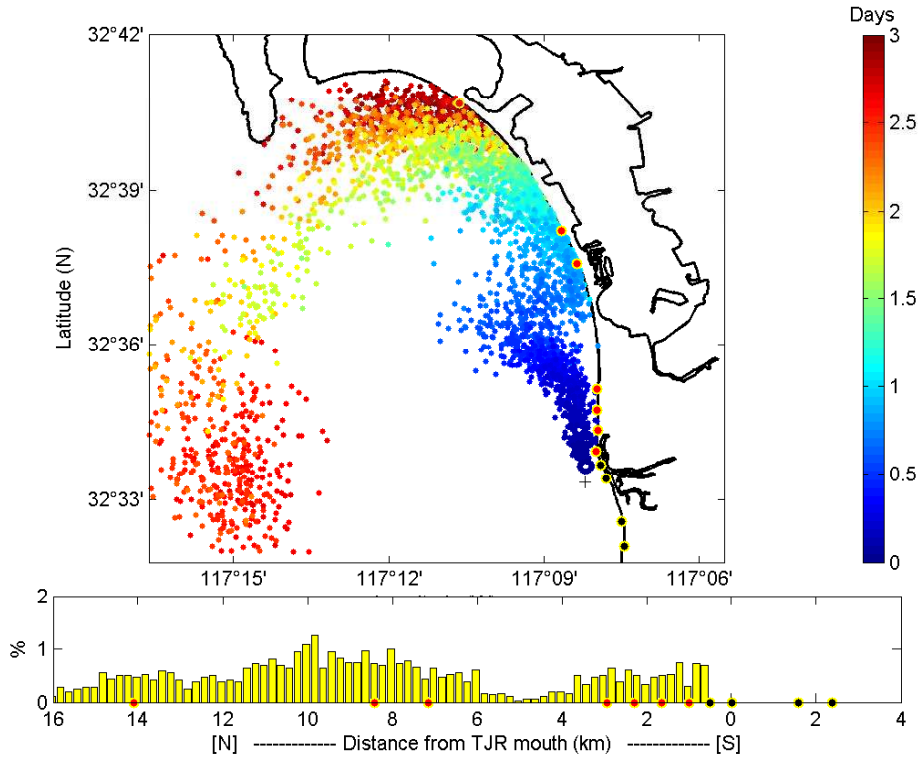

Figure 6.8: A snapshot of the TJR plume track model and the histogram of the particle concentration within the nearcoast cell. The hourly released particles at the TJR mouth are tracked for three days.

6.5 Exposure kernel

6.5.1 Coastal exposure kernel (CEK)

The coastal exposure kernel (CEK, p) of each source indicates the probability to the source location or maximum PDF resulting from the surface transport, and is calculated as

$$p_k(x,y) = \frac{N_k(x,y)}{\max(N_k(x,y))} \times 100, \tag{6.8}$$

where $N_k(x,y)$ denotes the number of particles in space (x,y) for the k-th source.

6.5.2 Shoreline exposure kernel (SEK)

In a similar way, the shoreline exposure kernel (SEK, q) is the probability to the source or maximum PDF within the nearcoast cell, and is from

$$q_k(l) = \frac{f_k(l)}{\max(f_k(l))} \times 100, \tag{6.9}$$

where $f_k(l)$ denotes the number of particles at the location l within the nearcoast cell for the k-th source (equation 6.7).

6.5.3 Scaled shoreline exposure kernel (SSEK)

In order to provide a time integrated statistic that considers the intermittency of the source, a scaled shoreline exposure kernel (SSEK, r) is defined as the SEK scaled by the number of days (δ) that each source is active over the entire period (T). T is recommended to be either annual or seasonal (summer/winter).

$$r_k(l) = q_k(l)\frac{\delta}{T} \tag{6.10}$$

The number of particles within the nearcoast cell is counted using the projection to the piece-wise coastline. The coefficients (a, b, and c) are estimated from the longitude (x) and latitude (y) of the piece-wise coastline and the distance (d) from the one end.

$$d = ax + by + c \tag{6.11}$$

$$\mathbf{d} = \mathbf{G}\mathbf{m} \tag{6.12}$$

where $\mathbf{m} = [a \;\; b \;\; c]^\dagger$. The estimated coefficients ($\hat{\mathbf{m}}$),

$$\hat{\mathbf{m}} = \left(\mathbf{G}^\dagger\mathbf{G}\right)^{-1}\mathbf{G}^\dagger\mathbf{d}, \tag{6.13}$$

is used to project the each location of the particles within the nearcoast cell into the one-dimensional axis (distance from the one end). This ad-hoc one-dimensional projection can be valid within the limited cross-shore direction (e.g., the nearcoast cell).

6.5.4 Receiver operating characteristic (ROC) analysis

A technique from statistical decision theory, the receiver (or relative) operating characteristic (ROC) analysis is used in binary classifier systems ([Metz(1978), Hanley and McNeil(1982), Hanley and McNeil(1983), Swets(1988)]). In the ROC analysis, the diagnosis (the model outputs) and the event (the observations) are used, and the positive and negative cases are typically considered as signal and noise events, respectively. All possible cases fall into four categories in the contingency table (Table 6.4 and [Swets(1988)]). When the diagnosis and the event agree, true-positive (TP) and true-negative (TN) are claimed, and if they disagree, false-positive (FP) and false-negative (FN) are claimed. The beach closure is evaluated with the diagnosis based on the RWM (f in equation 6.7) and the event from the FIB level ($g = \mathsf{C}$ or D in equation 6.1).

Table 6.4: A contingency table for two alternative events and two diagnosis. The positive and negative represent the D and C conditions, respectively.

		Event	
		Positive	Negative
Diagnosis	Positive	True-Positive (TP)	False-Positive (FP)
	Negative	False-Negative (FN)	True-Negative (TN)

The TP proportion (sensitivity, α) and the FP proportion (1–specificity, β) are a function of the threshold value (λ) as shown in Figure 6.9:

$$\alpha(\lambda) = \frac{\mathrm{TP}}{\mathrm{TP} + \mathrm{FN}} = P(g \equiv \mathsf{D} \mid f \leq \lambda) \tag{6.14}$$

and

$$\beta(\lambda) = \frac{\mathrm{FP}}{\mathrm{FP} + \mathrm{TN}} = P(g \equiv \mathsf{C} \mid f \leq \lambda). \tag{6.15}$$

Each point of the ROC curve represents a pair of α and β in a given threshold (λ). The area (A) under the ROC curve indicates how well the diagnosis system distinguish between positive and negative cases as the discriminator:

$$A = \int_0^1 \alpha \, \mathrm{d}\beta \approx \sum_k \alpha(\beta_k) \Delta\beta. \tag{6.16}$$

The area under the ROC curve of the binary classifier systems under random variables is equal to 0.5.

6.6 Results

A time-averaged synthesis of the particle trajectories is used to construct three probability kernels for the surface transport of regional discharges: coastal exposure kernel (CEK, section 6.5.1),

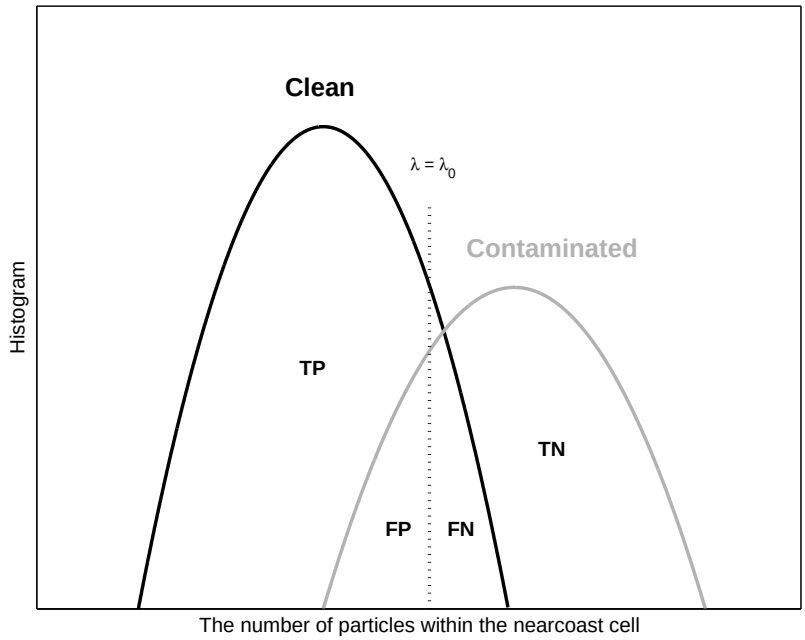

Figure 6.9: Variables in the Receiver Operating Characteristic (ROC) analysis are a function of threshold (λ) : true-positive (TP), false-negative (FN), false-positive (FP), and true-negative (TN).

shoreline exposure kernel (SEK, section 6.5.2), and scaled shoreline exposure kernel (SSEK, section 6.5.3). The bin size of probability kernels is a square box of 0.2×0.2 km^2 (CEK) and a rectangular box of 0.2×1 km^2 (SEK and SSEK, $w = 200$ m in equation 6.7), respectively. The CEK and SEK are normalized to a maximum of 1 allowing the kernel to represent a statistical assessment of the resulting exposure during a discharge. The kernels are contoured at 100, 90, 80, 70, 50, 25, 10, 5, 2.5, 1%, and minor percentages. These procedures are intended to allow rapid examination of how a discharge may expose itself along the coast, but should be used with caution if relative impacts of different sources are desired since their flow rates and concentrations of contaminants can vary. To provide a simple comparison between sources, the SEK is scaled by the percentage of time it is active, providing a time integrated statistic that can be used to assess how often a particular source may be transported to a particular shoreline location relative to another. The units in the CEK and SEK are the source exposure probabilities (%) if the source is active, and the SSEK (%) considers the source statistics for a given time period (either annual or seasonal). The number of particles within the nearcoast cell for the SEK is counted using an ad-hoc method which considers the curvature of the coastline.

In order to examine the typical surface transport pattern in southern San Diego, the CEK by each steady source regardless of discharge type (Table 6.2) is considered with three cases: year-round (Figure 6.10), season (summer/winter, Figure 6.11), and selected by nearshore current direction (upcoast/downcoast, Figure 6.12). Then, the CEK is considered while each source is active (Figure

6.14), and its SEK is evaluated with FIB data using ROC analysis (Figure 6.15 and section 6.5.4). For the RWM, the number of tracers released and tracked are constant regardless of the time-dependent nature of the discharge flow rate.

6.6.1 Regional exposure kernel

The TJR plume statistics exhibit a broad distribution in the near the coast, with the influence of the eddy flows presenting itself in the northern and southern edges of the domain (Figure 6.10a). The SBO surface transport is slightly oval due to stronger alongshore currents than cross-shore currents. The relatively high probabilities in the nearcoast cell result from a trapping of plume water at the coastline in the simulation (Figure 6.10b). Most tracers from PBD plume water are transported south and spread along the coastline. Upcoast transports from the PBD cross the U.S–Mexico border intermittently – 56 times for 234 days (∼16%) over four years –, and their probabilities are less than 2.5% compared with those in the PBD area (Figure 6.10c). The plume probability decays exponentially in the cross-shore direction with 1–2 km length scale. The alongshore probability distribution is addressed with the SEK (Figure 6.15).

The seasonal CEKs of the three sources are shown as Figures 6.11A, 6.11B, and 6.11C. The summer CEK has more alongshore spreading of the plume water, and the winter CEK shows the more offshore extend of it. For example, 10% contours of the seasonal TJR CEKs cover approximately 20 and 12 miles centered by the TJR for summer and winter, respectively (Figures 6.11Aa and 6.11Ab). The summer SBO CEK shows the significant alongshore transport to reach the most of shoreline stations (Figure 6.11Ba). The winter PBD CEK exhibits the dominant offshore stretch of plume statistics (Figure 6.11Cb). The seasonal upcoast events which the PBD plume crosses the border occur 17 times during 66 days (summer) and 28 times during 120 days (winter).

The CEKs of the three sources under two current directions (upcoast and downcoast) are shown in Figures 6.12A, 6.12B, and 6.12C, respectively. The upcoast and downcoast directions are defined as the averaged alongshore surface currents within the nearcoast cell. The spreading of the plume water under the unidirectional currents and the relatively longer residence time at the shoreline boundary are simulated.

The SEKs of the three sources for four years are shown in Figure 6.13a. Each SEK represents the relative probability along the coast generated by each source. Two shoreline sources (TJR and PBD) exhibit slightly different distribution: nearly similar shape centered by the TJR (TJR SEK) and the abrupt decay of the concentration in the north of the PBD (PBD SEK). These differences result from spatial variations of the circulation observed in the region. The offshore source generates nearly uniform probability along the coast (SBO SEK). The SBO SEKs in both seasons are very similar except the probability in the northern area of C13 station (Figures 6.13b and 6.13c).

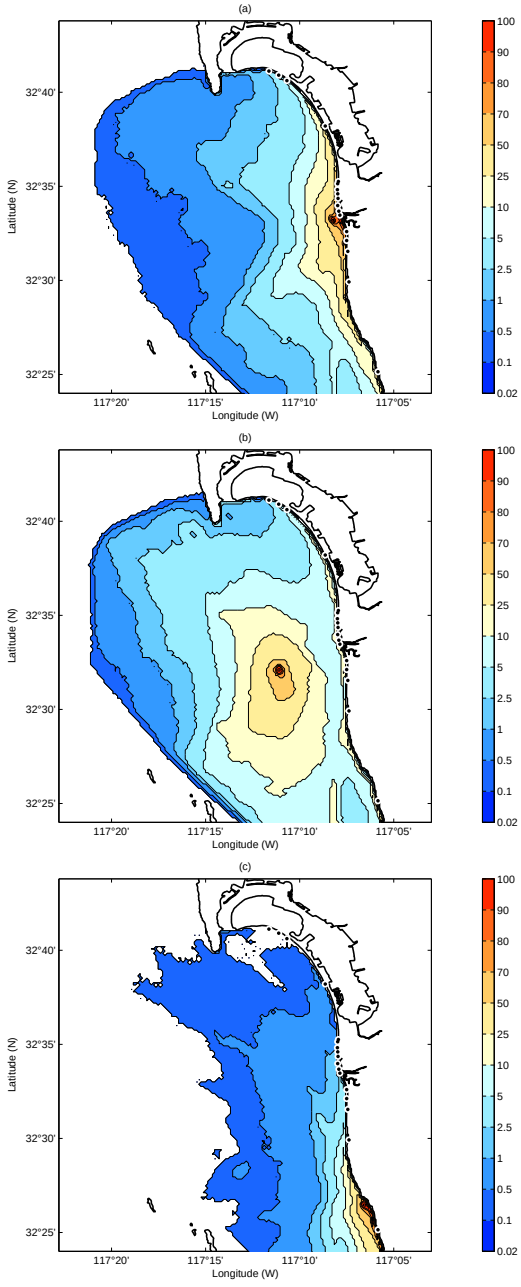

Figure 6.10: Coastal exposure kernels (CEKs) for each local discharge derived from the RWM using surface current observations for four years. The concentration in a given 0.2×0.2 km^2 square box is normalized with the maximum concentration, which is typically the value at the source location. The contours indicate 100, 90, 75, 50, 25, 10, 5, 2.5, 1, and minor percentages. (a) TJR. (b) SBO. (c) PBD.

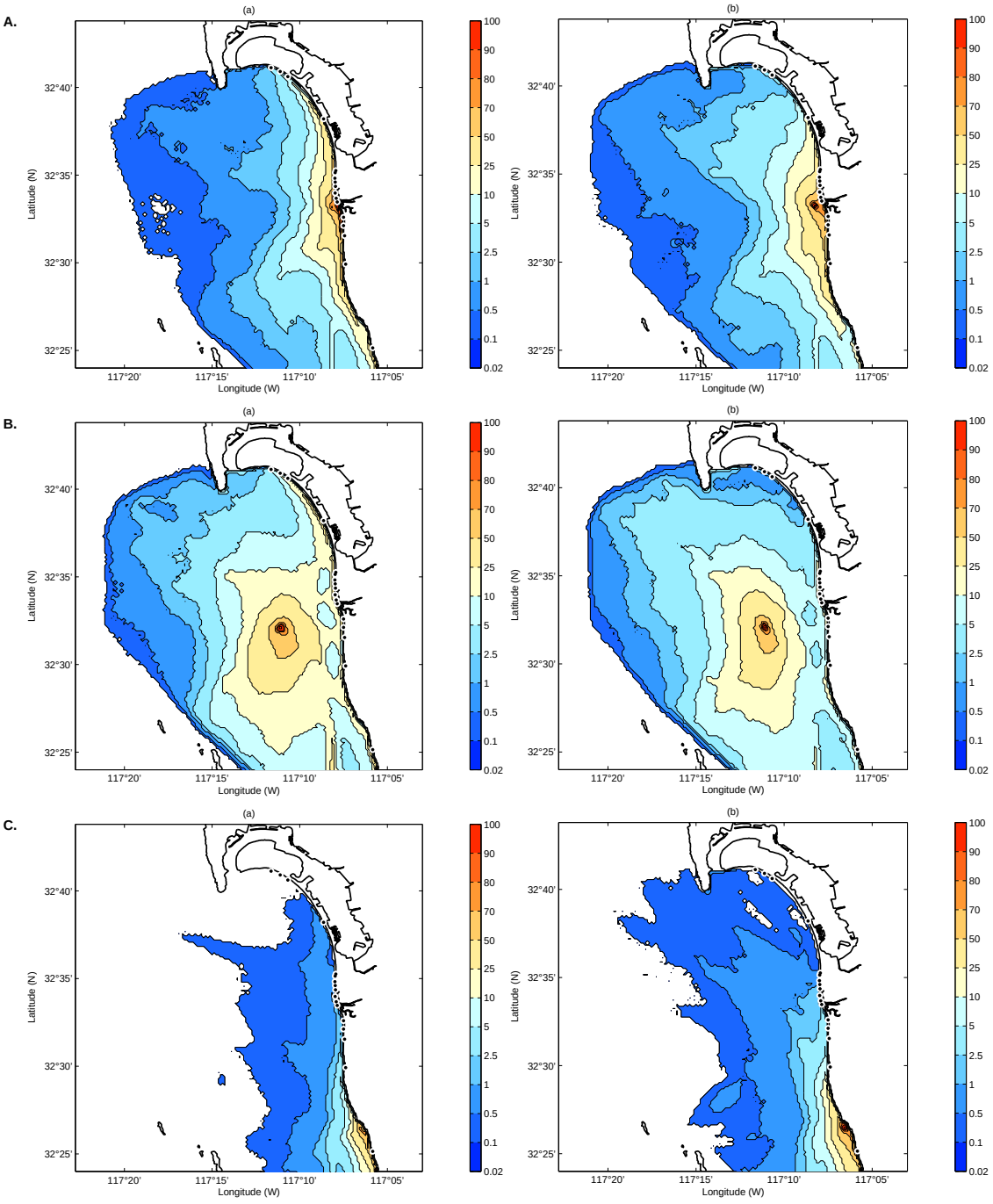

Figure 6.11: Seasonal CEKs for each local discharge. A. TJR. B. SBO. C. PBD. (a) Summer. (b) Winter.

Table 6.5: The number of days (δ) that each source is active.

Sources	All season	Summer	Winter
TJR	369	71	298
SBO	420	2	418
PBD	1461	732	729

6.6.2 Regional exposure kernel while sources are active

While the previous section illustrated the potential connectivity between discharge sites for all times, regardless if the discharge was active, this section examines the resultant exposure only when a site is an active discharge. The RWM starts and stops according to the type of three local discharges (Table 6.3). A CEK and SEK are conditionally computed only with the discharge source active. Although the TJR flow rate is nearly zero, the residual flow after a flood event may last several days and the discharge may take several days to be flushed out of the estuary. For this study, we assume the TJR is active for 7 days after rain event. The surfacing of the SBO serves as the trigger for the SBO CEK. Since the PBD is continuous discharge (Figures 6.10c and 6.11C), only TJR CEK and SBO CEK are considered. The number days that each source is active is summarized in Table 6.5.

The active CEKs for four years, summer, and winter are shown in Figures 6.14A, 6.14B, and 6.14C, respectively. Due to the sparse rain and strong ocean stratification during summer, they are similar to the winter CEKs (Figures 6.11Ab and 6.11Bb) and the active winter CEKs (Figures 6.14Ca and 6.14Cb).

The active SEKs for four years, summer, and winter are shown in Figures 6.15Aa, 6.15Ba, and 6.15Ca, respectively. The spreading pattern along the shore in the active SEKs is nearly the same as the SEKs (Figure 6.13).

The SSEKs for four years, summer, and winter are shown in 6.15Ab, 6.15Bb, and 6.15Cb, respectively. The SSEK can be interpreted as the time-averaged probability that plume water from a particular source may be present along the coast. At the source locations for the coastline discharges, the annual probabilities are 100, 28.2, and 4.8% for PBD, TJR, and SBO, respectively. The daily probability of the SBO is 2.3 relative to the PBD, which means the daily (highest) probability of finding SBO plume water somewhere on the northern coast of U.S.–Mexico border is 2.3 time higher than the probability of the PBD plume water. For the dry season (April - October), the daily probability of the SBO is almost zero, while during the wet season, the daily probabilities for TJR and SBO are 22.7 and 5.3 times relative to the PBD.

6.6.3 ROC analysis

The receiver operating characteristic (ROC) analysis is applied to several rain events during the wet season. The number of particles within the nearcoast cell is plotted against the observed FIB levels. FP and TP are calculated as a function of the number of particles (λ in Figure 6.9).

An example of ROC analysis is shown in Figure 6.16, of which area is about 0.72. Using four years water quality samplings and the RWM during several rain events, the average accuracy of the plume exposure hindcast model is about 70%, which is a reasonable classification. A random classifier would have 0.5 skill.

6.7 Discussion

A framework for combining FIB samplings with integrated coastal observations – surface currents, temperature and current profiles, rain fall and river flow measurements, CTD cast data, and satellite images – is presented. The framework leads to a plume exposure hindcast statistical model for coastal water quality prediction. A Lagrangian particle trajectory model (random walk) using hourly surface current maps applied to three discharge sites provides a regional (spatial) plume water exposure kernel as well as the shoreline exposure kernel for two shoreline sources (TJR and PBD) and one offshore outfall (SBO). The data-driven model is compared to the FIB samplings using ROC analysis for several rain events, and found to have 70% accuracy.

The surface transport of the passive tracer is simulated with the random walk rather than the random flight model, which preserves the shape of the power spectrum of the surface current field. The power spectrum of the time-integrated surface currents exhibits variance dominated by the low frequency band (less than 0.4 cpd), which may result from the alongshore pressure gradient and local pressure setup by wind.

As the plume is trapped and transported along the shoreline, an assumption is made that the shoreline currents are simply the along-coast projection of currents measured 1 km offshore. As a result, the model ignores the important role of wave-driven currents in the surfzone and the exchange of water across the breaking surf. A logical next step to improve the fidelity of the hindcast approach presented is to include effects of surfzone currents and surfzone exchange.

The Lagrangian trajectory model framework using HF radar-derived surface currents has been applied to other applications including tracking a coastal river plume, water quality, oil spill, search and rescue, and biological larvae spreading ([Spaulding et al.(1993), Ullman et al.(2006), Coulliette et al.(2007), Kohut et al.(2008)]). The near real-time TJR plume tracking model has been used the San Diego County DEH for decision making and guiding the posting of beach advisories.

This chapter has been submitted for publication of the material as it my appear in *Environmental Science & Technology*, 2009, Kim, S. Y., E. J. Terrill, and B. D. Cornuelle titled by 'Assessing coastal plumes in a region of multiple discharges: the U.S.–Mexico border'. The dissertation author was the primary investigator and author of this paper.

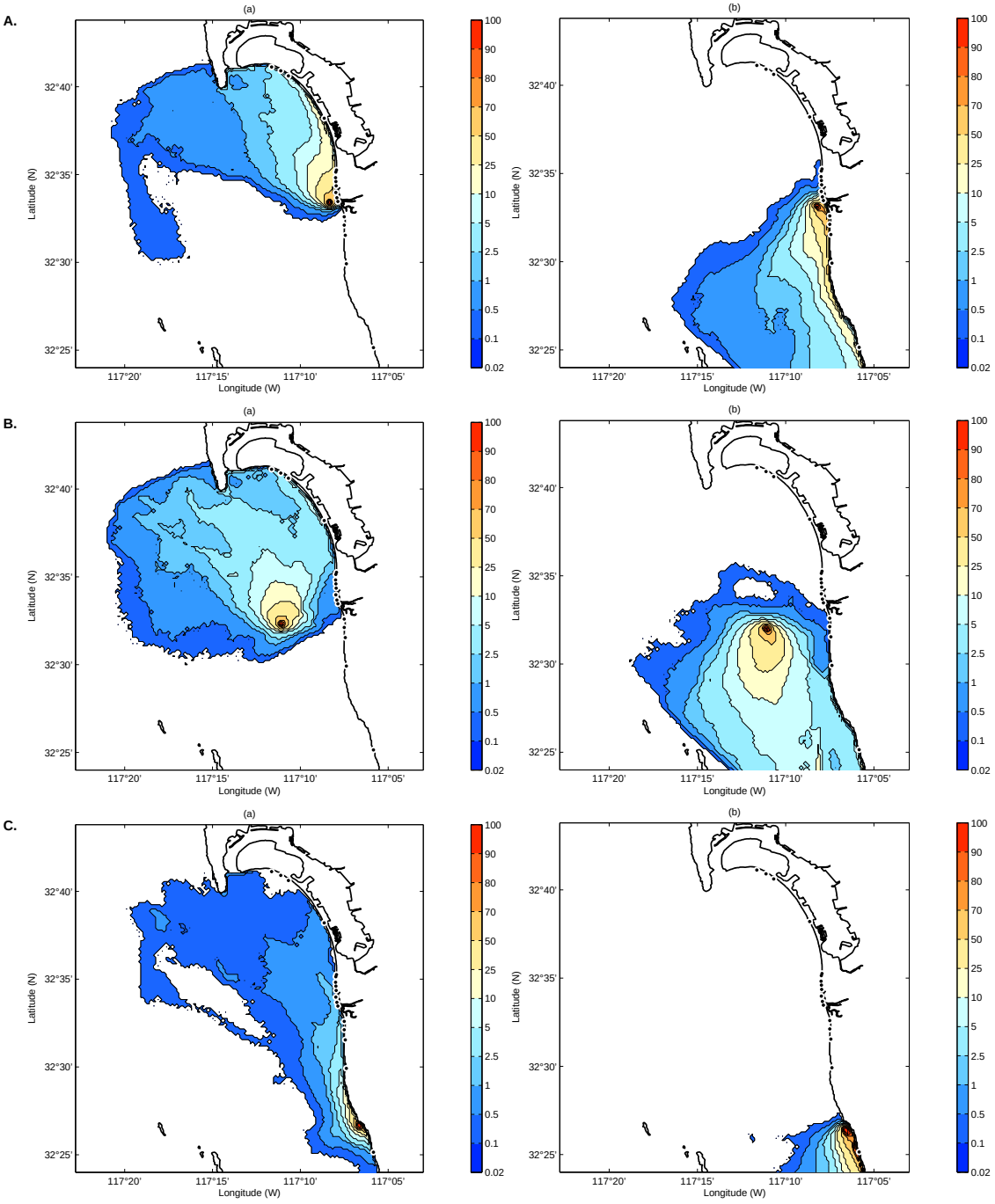

Figure 6.12: CEKs for each local discharge under the current directions. A. TJR. B. SBO. C. PBD. (a) Upcoast currents. (b) Downcoast currents. The direction of the upcoast and downcoast currents is determined by the sign of the averaged alongshore current within the nearcoast cell.

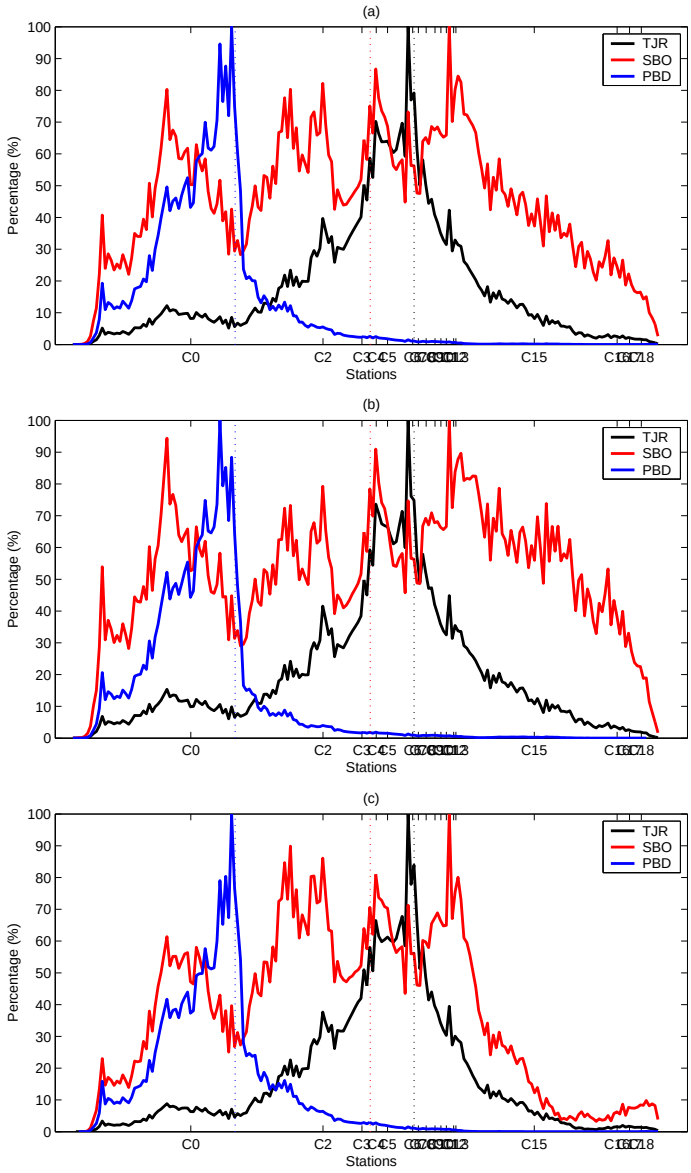

Figure 6.13: Shoreline exposure kernels (SEKs) for three local discharges based on the four year RWM outputs. (a) All season. (b) Summer. (c) Winter.

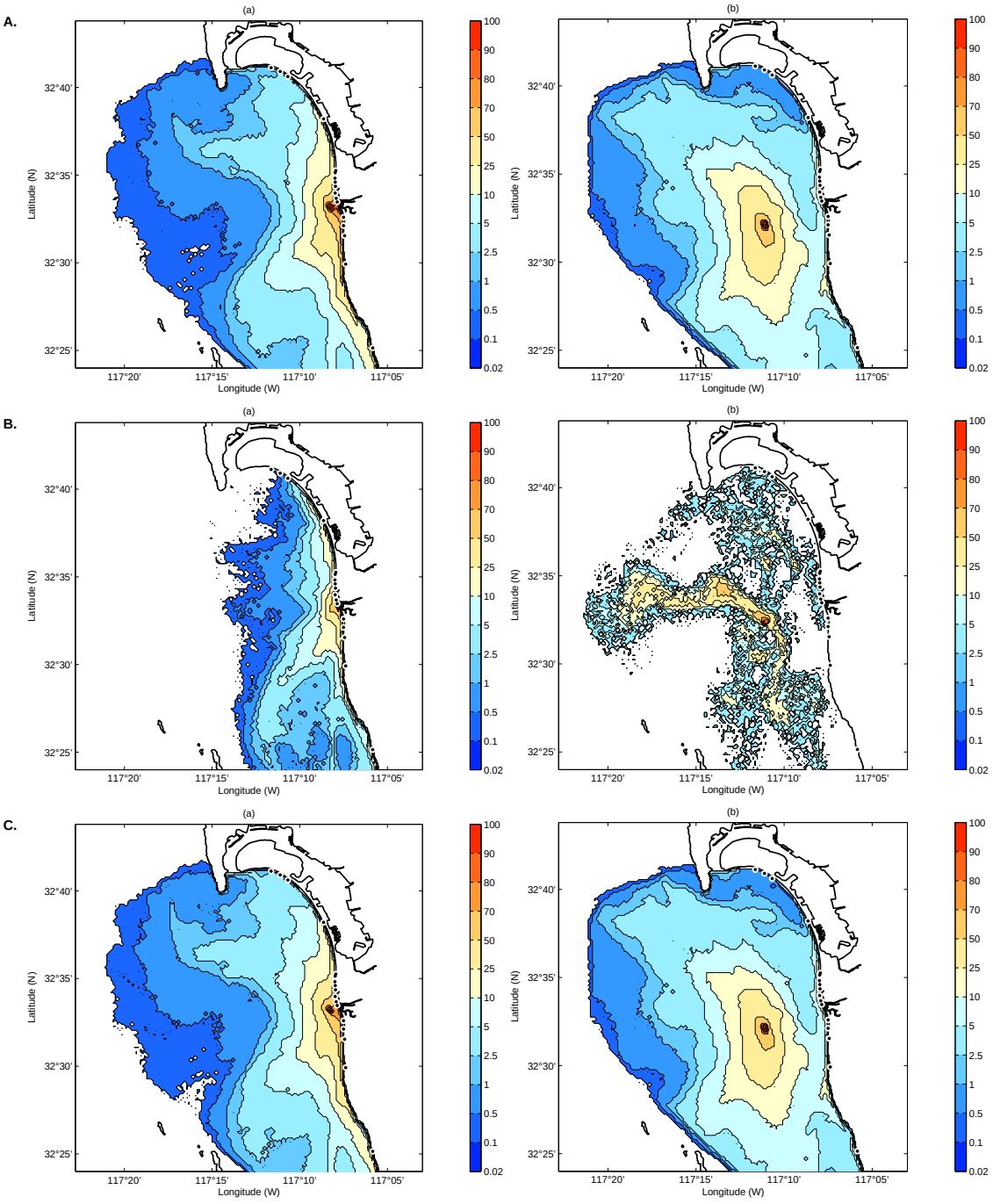

Figure 6.14: Active CEKs for each local discharge. A. All season. B. Summer. C. Winter. (a) TJR. (b) SBO.

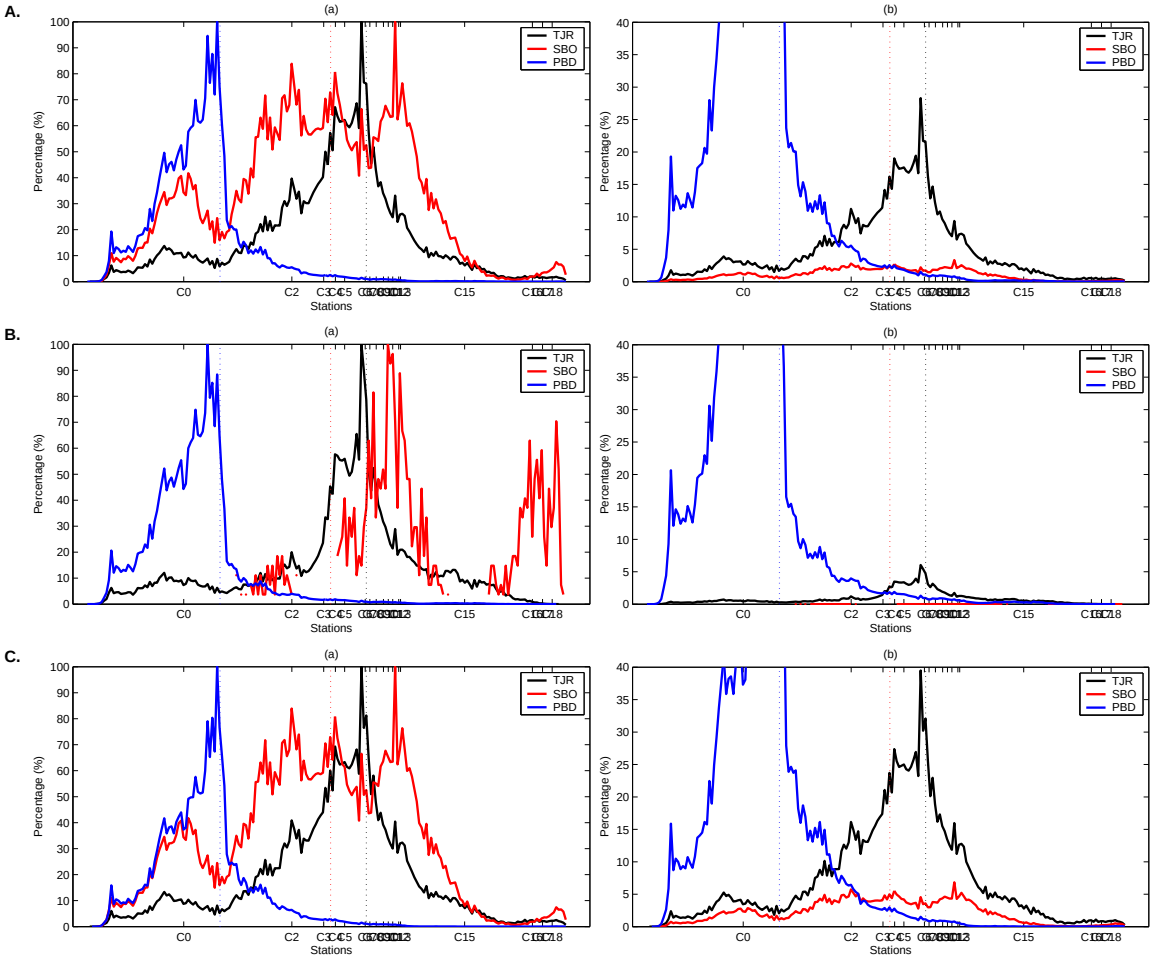

Figure 6.15: Active SEKs and SSEKs for each local discharge (TJR, SBO, and PBD). A. All season. B. Summer. C. Winter. (a) SEK. (b) SSEK (zoomed in).

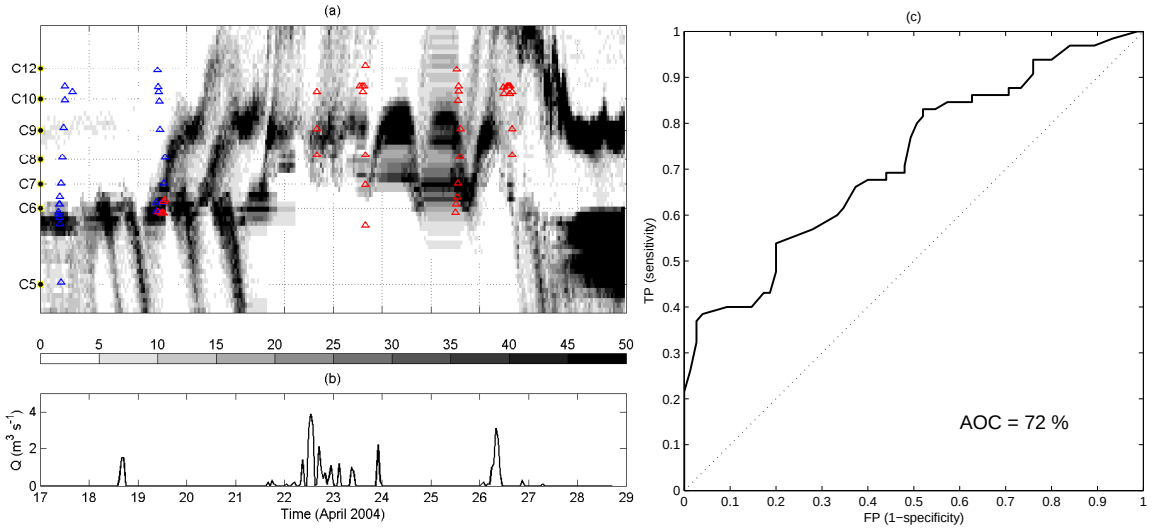

Figure 6.16: An example of the RWM evaluation using ROC analysis. (a) The time series of the SEK superposed with FIB samplings. Red and blue triangles indicate the contaminated (D) and clean (C) conditions, respectively. (b) Hourly TJR flow rate ($m^3\,s^{-1}$). (c) ROC curve.

Chapter 7

Conclusion

The dissertation addressed coastal ocean studies in southern San Diego using high-frequency-radar-derived surface currents including low-level HF radar data processing, data analysis using statistical techniques and physical interpretation, and coastal environmental applications. Optimal interpolation shows better performance – concrete uncertainty estimates, reduced spurious currents, direct calculation of dynamic quantities, and use of prior information – than more commonly used un-weighted least-squares fitting. The surface currents observed in southern San Diego are decomposed into the currents driven by the pure tides, local winds, low frequency pressure gradient, and several continuous frequency bands. Once the locally wind-driven surface currents are removed by regression of observed winds on surface currents, the filter by weighted least-squares fitting assuming three colored signals and white noise is applied. The frictional momentum balance is examined with the atmospherically-adjusted sea-surface difference and the surface currents within a distinctive low frequency band. The spatial correlations of each part of the decomposed surface currents exhibit Gaussian and exponential shapes with varying decorrelation length scales. The impaired water quality in the border region coastlines of San Diego and Tijuana is monitored by a data-driven model to understand the transport of shoreline and offshore discharges. The surface transport model outputs are compared with shoreline samples of fecal indicator bacteria, and the skill of the model to assess low water quality is evaluated using receiver operating characteristic analysis.

The techniques discussed in the dissertation are applicable to the surface current data in other study domains. For example, the U.S. National HF radar network may enable us to examine poleward propagating surface currents or coastally trapped waves, locally wind-driven currents along the U.S. West Coast, and the proxies for climate signals (Figure 7.1). Moreover, the spatial correlation function and decorrelation length scales, the large scale surface circulation, and the biological connectivity (e.g., Lyapunov exponents, the random walk/flight models) can be explored. On the other hand, the horizontal and vertical continuity of the current field can be examined with other in-situ observations such as the altimetry-derived geostrophic current, the moored current profile, and Lagrangian observations (e.g, autonomous unmanned vehicle, glider, and ship transects). The high-density HF radar-derived surface current maps can be used as a potential resource of the numerical ocean model and the data assimilation. Although the baroclinic and barotropic components are not distinguishable by surface current measurements alone, the spatial structure and its continuity would play in a role of detecting the surface features of internal waves/tides. The link between the surfzone and the nearcoast area will be a subject for future work.

Observations of coastal surface currents using HF radar provide the infrastructure of the national and regional coastal ocean observing system, and are growing in use world wide (Figures 7.1B and 7.2).

A

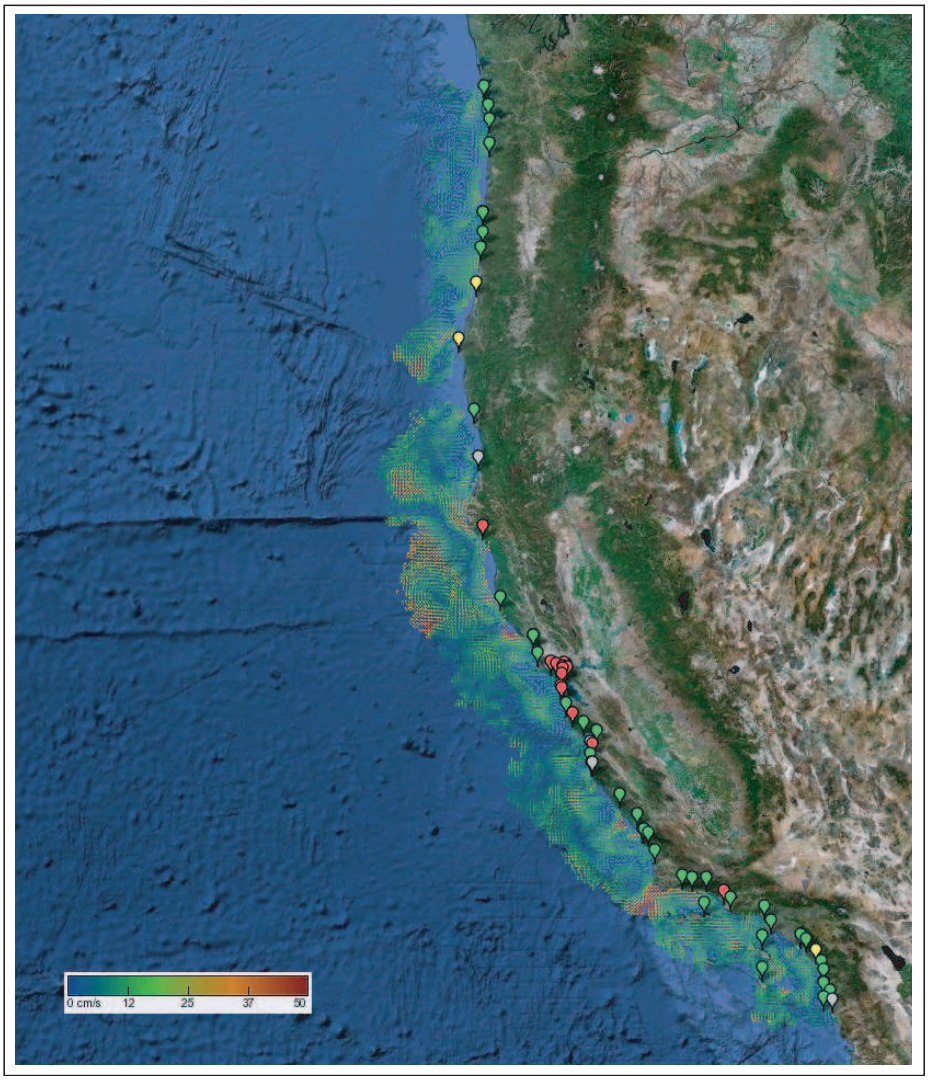

Figure 7.1: An example of the surface current map created by (A) U.S. West Coast HF radar network and (B) U.S. National HF radar network superposed on the Google map (a courtesy of http : //www.cordc.ucsd.edu). The balloon indicates the location of the HF radar, and its color represents the status of HF radar as green (online), yellow (temporary delay), red (temporary shutdown), and gray (offline).

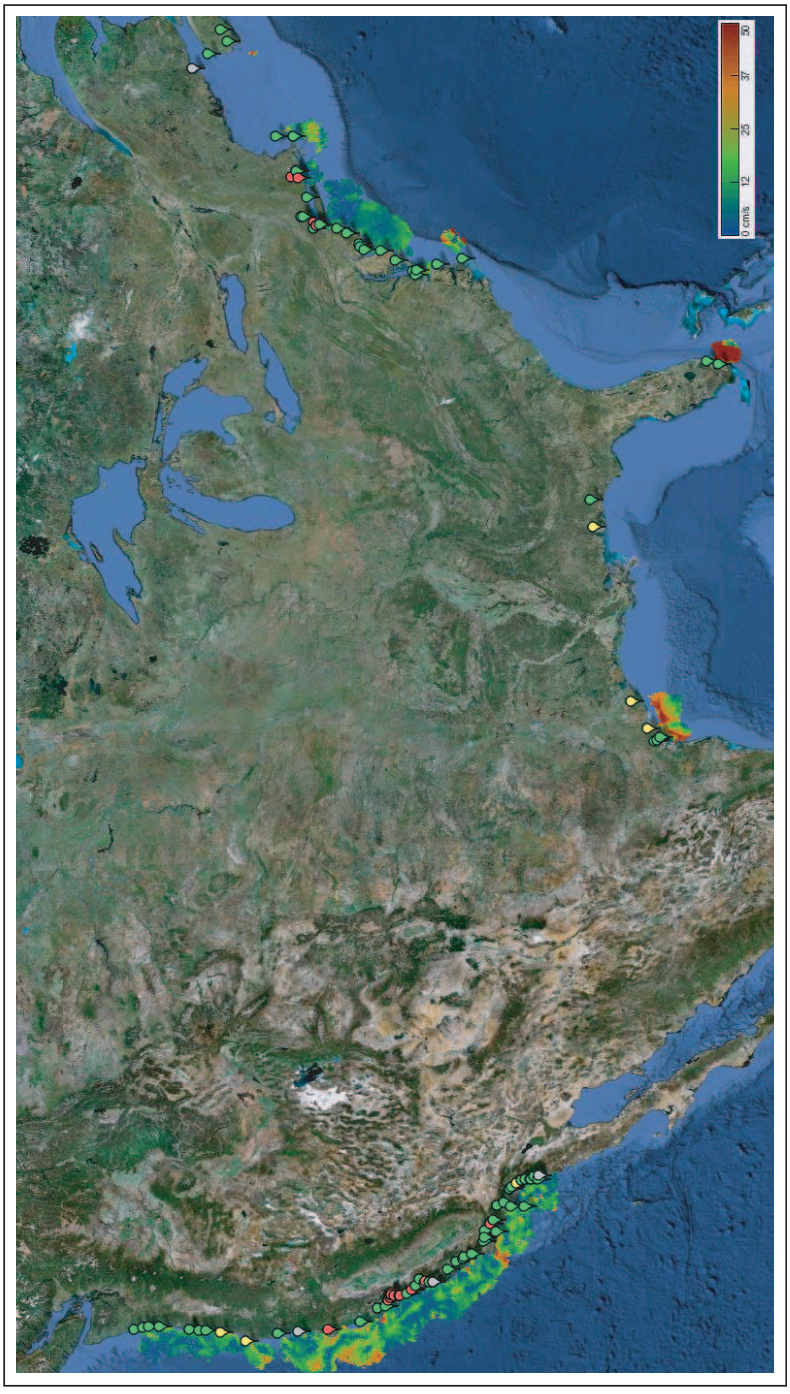

Figure 7.1: (Continued.)

Figure 7.2: National and regional coastal ocean observing systems built in the HF radars.

Bibliography

[Ackerman and Weisberg(2003)] Ackerman, D. and S. B. Weisberg, 2003: Relationship between rainfall and beach bacterial concentrations on Santa Monica Bay beaches. *J. Water and Health*, 85–89.

[Allen(1980)] Allen, J. S., 1980: Models of wind-driven currents on the continental shelf. *Annu. Rev. Fluid Mech.*, **12**, 389–433.

[Allen and Denbo(1984)] Allen, J. S. and D. W. Denbo, 1984: Statistical characteristics of the large-scale response of coastal sea level to atmospheric forcing. *J. Phys. Oceanogr.*, **14**, 1079–1094.

[Alpers(1985)] Alpers, W., 1985: Theory of radar imaging of internal waves. *Nature*, **314**, 245–247.

[Alvera-Azcarate et al.(2005)] Alvera-Azcarate, A., A. Barth, M. Rixen, and J. Beckers, 2005: Reconstruction of incomplete oceanographic data sets using empirical orthogonal functions: Application to the Adriatic Sea surface temperature. *Ocean Model.*, **9**, 325–346.

[Barrick et al.(1977)] Barrick, D. E., M. W. Evans, and B. L. Webber, 1977: Ocean surface currents mapped by radar. *Science*, **198 (4313)**, 138–144.

[Barrick and Lipa(1996)] Barrick, D. E. and B. J. Lipa, 1996: Phase 1 SBIR Final Report: Comparison of direction-finding and beam-forming in HF radar ocean surface current mapping. Tech. rep., National Oceanic and Atmospheric Administration (NOAA), Rockville, MD.

[Barrick and Lipa(1997)] Barrick, D. E. and B. J. Lipa, 1997: Evolution of bearing determination in HF current mapping radars. *Oceanography*, **10 (2)**, 72–75.

[Beardsley et al.(1987)] Beardsley, R. C., C. E. Dorman, C. A. Friehe, L. K. Rosenfeld, and C. D. Winant, 1987: Local atmospheric forcing during the Coastal Ocean Dynamics Experiment 1: A description of the marine boundary layer and atmospheric conditions over a Northen California upwelling region. *J. Geophys. Res.*, **92**, 1467–1488.

[Beckenbach and Washburn(2004)] Beckenbach, E. and L. Washburn, 2004: Low-frequency waves in the Santa Barbara Channel observed by high-frequency radar. *J. Geophys. Res.*, **109**, C02010, doi:10.1029/2003JC001999.

[Beckers and Rixen(2003)] Beckers, J. M. and M. Rixen, 2003: EOF calculations and data filling from incomplete oceanographic datasets. *J. Atmos. Oceanic Technol.*, **20**, 1839–1856.

[Bendat and Piersol(2000)] Bendat, J. and A. G. Piersol, 2000: *Random data analysis and measurement procedures*. 3rd ed., John Wiley & Sons, Inc.

[Blackford(1978)] Blackford, B. L., 1978: Wind-driven inertial currents in the Magdalen Shallows, Gulf of St. Lawrence. *J. Phys. Oceanogr.*, **8**, 653–664.

[Boyd et al.(1994)] Boyd, J. D., E. P. Kennelly, and P. Pistek, 1994: Estimation of EOF expansion coefficients from incomplete data. *Deep-Sea Research I*, **41 (10)**, 1479–1488.

[Brankart and Brasseur(1996)] Brankart, J. M. and P. Brasseur, 1996: Optimal analysis of in situ data in the western Mediterranean using statistics and cross-validation. *J. Atmos. Oceanic Technol.*, **13**, 477–491.

[Bratkovich(1985)] Bratkovich, A., 1985: Aspects of the tidal variability observed on the Southern California continental shelf. *J. Phys. Oceanogr.*, **15 (3)**, 225–239.

[Bretherton et al.(1976)] Bretherton, F. P., R. E. Davis, and C. B. Fandry, 1976: A technique for objective analysis and design of oceanographic experiment applied to MODE-73. *Deep Sea Res.*, **23**, 559–582.

[Brink(1991)] Brink, K. H., 1991: Coastal-trapped waves and wind-driven currents over the continental shelf. *Annu. Rev. Fluid Mech.*, **23**, 389–412.

[Brink et al.(1987)] Brink, K. H., D. C. Chapman, and G. R. Halliwell, Jr., 1987: A stochastic model for wind-driven currents over the continental shelf. *J. Geophys. Res.*, **92 (C2)**, 1783–1797.

[Brissette and Tsanis(1994)] Brissette, F. P. and I. K. Tsanis, 1994: Estimation of wave directional spectra from pitch-roll buoy data. *J. Waterway, Port, Coastal and Ocean Engineering*, **120 (1)**, 93–115.

[Bye(1965)] Bye, J. A. T., 1965: Wind-driven circulation in unstratified lakes. *Limnol. Oceanogr.*, **10**, 451–458.

[Bye(1967)] Bye, J. A. T., 1967: The wave-drift current. *J. Mar. Res.*, **25**, 95–102.

[Cacchione and Wunsch(1974)] Cacchione, D. and C. Wunsch, 1974: Experimental study of internal waves over a slope. *J. Fluid Mech.*, **66**, 223–239.

[Cacchione et al.(2002)] Cacchione, D. A., L. F. Pratson, and A. S. Ogston, 2002: The shaping of continental slope by internal tides. *Science*, **296**, 724–727.

[California Ocean Plan(1990)] California Ocean Plan, 1990: Water quality control plan for ocean waters of California. State Water Resources Control Board, Sacramento, CA.

[Chapman(1983)] Chapman, D. C., 1983: On the influence of stratification and continental shelf and slope topography on the dispersion of subinertial coastally trapped waves. *J. Phys. Oceanogr.*, **13 (9)**, 1641–1652.

[Chapman et al.(1997)] Chapman, R. D., L. K. Shay, H. Graber, J. B. Edson, A. Karachintsev, C. L. Trump, and D. B. Ross, 1997: On the accuracy of HF radar surface current measurements: Intercomparisons with ship-based sensors. *J. Geophys. Res.*, **102(C8)**, 18 737–18 748.

[Chelton and Davis(1982)] Chelton, D. B. and R. E. Davis, 1982: Monthly mean sea-level variability along the west coast of North America. *J. Phys. Oceanogr.*, **12**, 757–784.

[Chelton and Enfield(1986)] Chelton, D. B. and D. B. Enfield, 1986: Ocean signals in tide gauge records. *J. Geophys. Res.*, **91 (B9)**, 9081–9098.

[Chereskin(1995)] Chereskin, T. K., 1995: Direct evidence for an Ekman balance in the California Current. *J. Geophys. Res.*, **100 (C9)**, 18 261–18 269.

[Chereskin and Trunnell(1996)] Chereskin, T. K. and M. Trunnell, 1996: Correlation scales, objective mapping, and absolute geostrophic flow in the California current. *J. Geophys. Res.*, **101 (C10)**, 22 619–22 629.

[Choi and Wilkin(2007)] Choi, B.-J. and J. L. Wilkin, 2007: The effect of wind on the dispersal of Hudson river plume. *J. Phys. Oceanogr.*, **37**, doi:10.1175/JPO3081.1.

[Churchill and Csanady(1983)] Churchill, G. H. and G. T. Csanady, 1983: Near-surface measurements of quasi-Lagrangian velocities in open water. *J. Phys. Oceanogr.*, **13**, 1669–1680.

[Coulliette et al.(2007)] Coulliette, C., F. Lekien, J. D. Paduan, G. Haller, and J. E. Marsden, 2007: Optimal pollution mitigation in Montrey Bay based on coastal radar data and nonlinear dynamics. *Environ. Sci. Technol.*, **41**, 6562–6572, doi:10.1021/es0630691.

[Crombie(1955)] Crombie, D. D., 1955: Doppler spectrum of sea echo at 13.56 Mc./s. *Nature*, **175**, 681–682.

[Cronin and Kesseler(2008)] Cronin, M. F. and W. S. Kesseler, 2008: Near-surface shear flow in the tropical Pacific cold tongue front. *J. Phys. Oceanogr.*, doi:10.1175/2008JPO04064.1.

[Csanady(1982)] Csanady, G. T., 1982: *Circulation in the coastal ocean*. D. Reidel Pub. Co.

[Daley(1993)] Daley, R., 1993: Estimating observation error statistics for atmospheric data assimilation. *Ann. Geophysicae*, **11**, 634–647.

[Davis(1985)] Davis, R. E., 1985: Objective mapping by least squares fitting. *J. Geophys. Res.*, **90(C7)**, 4773–4778.

[de Paolo and Terrill(2007a)] de Paolo, T. and E. Terrill, 2007a: Properties of HF radar compact antenna arrays and their effect on the MUSIC algorithm. *Oceans 2007*, 1–10, doi:10.1109/OCEANS.2007.4449265.

[de Paolo and Terrill(2007b)] de Paolo, T. and E. Terrill, 2007b: Skill assessment of resolving ocean surface current structure using compact-antenna-style HF radar and the MUSIC direction-finding algorithm. *J. Atmos. Oceanic Technol.*, **24**, 1277–1300, doi:10.1175/JTECH2040.1.

[Denman and Freeland(1985)] Denman, K. L. and H. J. Freeland, 1985: Correlation scales, objective mapping and a statistical test of geostrophy over the continental shelf. *J. Mar. Res.*, **43**, 517–539.

[Efron and Gong(1983)] Efron, B. and G. Gong, 1983: A leisurely look at the bootstrap, the Jackknife, and the cross-validation. *The American Statistician*, **37 (1)**, 36–48.

[Ekman(1905)] Ekman, V. W., 1905: On the influence of the Earth's rotation on ocean-currents. *Ark. Mat. Astron. Fys.*, **2**, 1–49.

[Emery and Thomson(1997)] Emery, W. J. and R. E. Thomson, 1997: *Data analysis methods in physical oceanography*. Elsevier.

[Enfield and Allen(1980)] Enfield, D. B. and J. S. Allen, 1980: On the structure and dynamics of monthly mean sea level anomalies along the Pacific coast of North and South America. *J. Phys. Oceanogr.*, **10**, 557–578.

[Essen(1993)] Essen, H.-H., 1993: Ekman portion of surface currents as measured by radar in different areas. *Dt. Hydrogr. Z.*, **45 (2)**, 57–85.

[Essen et al.(1983)] Essen, H.-H., K.-W. Gurgel, and F. Schirmer, 1983: Tidal and wind-driven parts of surface currents as measured by radar. *Dt. Hydrogr. Z.*, **36 (3)**, 81–96.

[Ewing(1950)] Ewing, G. C., 1950: Relation between band slicks at the surface and internal waves in the sea. *Science*, **111 (2874)**, 91–94.

[Fernandez et al.(1996)] Fernandez, D. M., J. F. Vesecky, and C. C. Teague, 1996: Measurements of upper ocean surface current shear with high-frequency radar. *J. Geophys. Res.*, **101 (C12)**, 28 615–28 625.

[Fofonoff and Millard Jr.(1983)] Fofonoff, N. P. and R. C. Millard Jr., 1983: Algorithms for computation of fundamental properties of seawater. UNESCO Technical Papers in Marine Science, UNESCO, Place de Fontenoy, 75700 Paris, France.

[Frick et al.(2001)] Frick, W. E., P. J. W. Roberts, L. R. Davis, J. Keyes, D. J. Baumgartner, and K. P. George, 2001: *Dilution models for effluent discharges (Visual Plumes)*. Standard and Applied Science Division Office of Science and Technology, 4th ed.

[Gersberg et al.(2008)] Gersberg, R., J. Tiedge, D. Gottstein, S. Altmann, K. Watanabe, and V. Luderitz, 2008: Effect of the South Bay Ocean Outfall (SBOO) on ocean beach water quality near the USA-Mexico border. *Int. J. Environ. Health Res.*, **18 (2)**, 149–158.

[Golub et al.(1979)] Golub, G. H., M. Heath, and G. Wahba, 1979: Generalized cross-validation as a method for choosing a good ridge parameter. *Technometrics*, **21 (2)**, 215–223.

[Golub and Van Loan(1996)] Golub, G. H. and C. Van Loan, 1996: *Matrix computations*. 3rd ed., Johns Hopkins University Press, Baltimore, MD.

[Golub and Van Loan(1980)] Golub, G. H. and C. F. Van Loan, 1980: An analysis of the total least squares problem. *SIAM J. Numer. Anal.*, **17**, 883–893, doi:10.1137/0717073.

[Gonella(1971)] Gonella, J., 1971: The drift current from observations made on the Bouee Laboratoire. *Cah. Océanogr.*, **23 (1)**, 1–15.

[Gonella(1972)] Gonella, J., 1972: A rotary-component method for analysis in meteorological and oceanographic vector time series. *Deep Sea Res.*, **19**, 833–846.

[Graber et al.(1997)] Graber, H. C., B. K. Haus, R. D. Chapman, and L. K. Shay, 1997: HF radar comparisons with moored estimates of current speed and direction: Expected differences and implications. *J. Geophys. Res.*, **102(C8)**, 18 749–18 766.

[Grant et al.(1984)] Grant, W. D., A. J. Williams, III, and S. M. Glenn, 1984: Bottom stress estimates and their prediction on the Northern California continental shelf during CODE-1: The importance of wave-current interaction. *J. Phys. Oceanogr.*, **14**, 506–527.

[Griffa(1996)] Griffa, A., 1996: *Stochastic modeling in physical oceanography*, chap. Applications of stochastic particle models to oceanographic problems, 114–140. Progress in Probability, Birkhäuser, Cambridge, MA.

[Griffa et al.(1995)] Griffa, A., K. Owens, L. Piterbarg, and B. Rozovskii, 1995: Estimates of turbulence parameters from Lagrangian data using a stochastic particle model. *J. Mar. Res.*, **53**, 371–401.

[Gurgel(1994)] Gurgel, K.-W., 1994: Shipborne measurements of surface current fields by HF radar. *L'Onde Electr.*, **74 (5)**, 54–59.

[Ha(1979)] Ha, E. C., 1979: High-frequency radar measurements of coastal ocean surface currents. Ph.D. thesis, Stanford University, Stanford, California.

[Hanley and McNeil(1982)] Hanley, J. A. and B. J. McNeil, 1982: The meaning and use of the area under the receiver operating characteristic (ROC) curve. *Radiology*, **143**, 29–36.

[Hanley and McNeil(1983)] Hanley, J. A. and B. J. McNeil, 1983: A method of comparing the areas under receiver operating characteristic curves derived from the same cases. *Radiology*, **148**, 839–843.

[Hendershott and Munk(1970)] Hendershott, M. and W. Munk, 1970: Tides. *Annu. Rev. Fluid Mech.*, **2**, 205–224, doi:10.1146/annurev.fl.02.010170.001225.

[Hendershott(1973)] Hendershott, M. C., 1973: Ocean tides. *EOS Trans.*, **54**, 76–86.

[Hill(1998)] Hill, A. E., 1998: *The Sea: The Global Coastal Ocean*, Vol. 11, chap. 2. Buoyant effects in coastal shelf seas, 21–62. John Wiley & Sons, Inc., New York.

[Hoerl and Kennard(1970)] Hoerl, A. E. and R. W. Kennard, 1970: Ridge regression: Biased estimation for nonorthogonal problems. *Technometrics*, **12 (1)**, 55–67.

[Hollingsworth and Lönnberg(1986)] Hollingsworth, A. and P. Lönnberg, 1986: The statistical structure of short-range forecast errors as determined from radiosonde data. Part I: The wind field. *Tellus, Ser. A*, **38**, 111–136.

[Houseago-Stokes and Challenor(2004)] Houseago-Stokes, R. E. and P. G. Challenor, 2004: Using PPCA to estimate EOFs in the presence of missing values. *J. Atmos. Oceanic Technol.*, **21**, 1471–1480.

[Huyer and Kosro(1987)] Huyer, A. and P. M. Kosro, 1987: Mesoscale surveys over the shelf and slope in the upwelling region near Pt. Arena, California. *J. Geophys. Res.*, **92**, 1655–1681.

[Hyder et al.(2002)] Hyder, P., J. H. Simpson, and S. Christopoulos, 2002: Sea-breeze forced diurnal surface currents in the Thermaikos Gulf, North-West Aegean. *Cont. Shelf Res.*, **22**, 585–601.

[Ingram and Chu(1987)] Ingram, R. G. and V. H. Chu, 1987: Flow around islands in Rupert Bay: An investigation of the bottom friction effect. *J. Geophys. Res.*, **92 (C13)**, 14 521–14 533.

[Isaji et al.(2005)] Isaji, T., M. L. Spaulding, and A. A. Allen, 2005: Stochastic particle trajectory modeling technique for spill and search and rescue models. *Estuarine and Coastal Modelling*, 537–547.

[Jackson(2004)] Jackson, C. R., 2004: *An atlas of internal solitary-like waves and their properties*. 2nd ed., N00014-03-C-0176, Global Ocean Associates, 6220 Jean Louise Way, Alexandria, VA 22310.

[James and Groce(2006)] James, D. and A. Groce, 2006: Water quality in the South Bay region off San Diego, Southern California spatial and temporal trends in bacteria levels. California and the World Ocean 2006.

[Johnson and Dudgeon(1993)] Johnson, D. H. and D. E. Dudgeon, 1993: *Array signal processing: Concepts and technique*. Prentice-Hall PTR, 512 pp.

[Johnson and O'Brien(1990)] Johnson, M. A. and J. J. O'Brien, 1990: The Northest Pacific Ocean response to the 1982-1983 El Nino. *J. Geophys. Res.*, **95 (C5)**, 7155–7166.

[Kalnay et al.(1996)] Kalnay, E., M. Kanamitsu, R. Klstler, W. Collins, D. Deaven, L. Gandin, M. Iredell, S. Saha, G. Whitle, J. Woollen, Y. Zhu, M. Chellah, W. Ebisuzaki, W. Higgins, J. Janowak, K. Mo, C. Ropelewski, J. Wang, R. R. A. Leetmaa, R. Jenne, and D. Joseph, 1996: The NCEP/NCAR 40-year reanalysis project. *Bull. Amer. Meteor. Soc.*, **77 (3)**, 437–471.

[Kaplan and Lekein(2007)] Kaplan, D. M. and F. Lekein, 2007: Spatial interpolation and filtering of surface current data based on open-boundary modal analysis. *J. Geophys. Res.*, **112**, C12007, doi:10.1029/2006JC003984.

[Kenyon(1969)] Kenyon, K. K., 1969: Stokes drift for random gravity waves. *J. Geophys. Res.*, **74**, 6691–6694.

[Kim et al.(2004)] Kim, J. H., S. B. Grant, C. D. Mcgee, B. F. Sanders, and J. L. Largier, 2004: Locating sources of surf zone pollution: A mass budget analysis of fecal indicator bacteria at Huntington Beach, California. *Environ. Sci. Technol.*, **38**, 2626–2636.

[Kirincich et al.(2005)] Kirincich, A. R., J. A. Barth, B. A. Grantham, B. A. Menge, and J. Lubchenco, 2005: Wind-driven inner-shelf circulation off central Oregon during summer. *J. Geophys. Res.*, **110**, C10S03, doi:10.1029/2004JC002611.

[Kohut et al.(2008)] Kohut, J., H. Roarty, S. Licthenwalner, S. Glenn, D. Barrick, B. Lipa, and A. Allen, 2008: The Mid-Atlantic regional coastal ocean observing system: Serving coast guard needs in the Mid-Atlantic Bight. *IEEE/OES*, doi:10.1109/BALTIC.2008.4625502, US/EU-Baltic International Symposium.

[Kundu(1984)] Kundu, P. K., 1984: Generation of coastal inertial oscillations by time-varying wind. *J. Phys. Oceanogr.*, **14**, 1901–1913.

[Large and Pond(1981)] Large, W. G. and S. Pond, 1981: Open ocean momentum flux measurements in moderate to strong winds. *J. Phys. Oceanogr.*, **11**, 324–336.

[Largier et al.(2004)] Largier, J., L. Rasmussen, M. Carter, and C. Scearce, 2004: Evaluation of the South Bay international waste-water treatment plant receiving water quality monitoring program to determine its ability to identify source(s) of recorded bacterial exceedances. Final Report, Scripps Institution of Oceanography, University of California, San Diego, CA.

[LeBlanc and Tibshirani(1996)] LeBlanc, M. and R. Tibshirani, 1996: Combining estimates in regression and classification. *J. Amer. Stat. Assoc.*, **91 (436)**, 1641–1650.

[Leibovich(1977)] Leibovich, S., 1977: On the evolution of the system of wind drift currents and Langmuir circulation in the ocean. Part 1. Theory and averaged current. *J. Fluid Mech.*, **79**, 715–743.

[Lentz(2001)] Lentz, S. J., 2001: The influence of stratification on the wind-driven cross-shelf circulation over the north Carolina shelf. *J. Phys. Oceanogr.*, **31**, 2749–2760.

[Lentz and Winant(1986)] Lentz, S. J. and C. D. Winant, 1986: Subinertial currents on the southern California shelf. *J. Phys. Oceanogr.*, **16**, 1737–1750.

[Levanon(2000)] Levanon, N., 2000: Lowest GDOP in 2-D scenarios. *IEE Proc. Radar, Sonar Navig.*, **147**, 149–155.

[Lewis and Belcher(2004)] Lewis, D. M. and S. E. Belcher, 2004: Time-dependent, coupled, Ekman boundary layer solutions incorporating Stokes drift. *Dynam. Atmos. Oceans*, **37**, 313–351.

[Li and Weisberg(1999)] Li, Z. and R. H. Weisberg, 1999: West Florida shelf response to upwelling favorable wind forcing: Kinematics. *J. Geophys. Res.*, **104 (C6)**, 13 507–13 527.

[Lipa et al.(2006)] Lipa, B., B. Nyden, D. S. Ullman, and E. Terrill, 2006: SeaSonde radial velocities: Derivation and internal consistency. *IEEE J. Oceanic Eng.*, **31 (4)**, 850–861, doi:10.1109/JOE.2006.886104.

[Lipa(2003)] Lipa, B. J., 2003: Uncertainties in SeaSonde current velocities. *IEEE/OES Seventh Working Conference on Current Measurement Technology*, Inst. of Electr. and Electron. Eng., San Diego, Calif., 95–100.

[Lipa and Barrick(1983)] Lipa, B. J. and D. E. Barrick, 1983: Least-squares methods for the extraction of surface currents from CODAR crossed-loop data: Application at ARSLOE. *IEEE J. Oceanic Eng.*, **OE-8 (4)**, 226–253.

[Lipphardt Jr. et al.(2000)] Lipphardt Jr., B. L., A. D. Kirwan Jr., C. E. Grosch, J. K. Lewis, and J. D. Paduan, 2000: Blending HF radar and model velocities in Monterey Bay through normal mode analysis. *J. Geophys. Res.*, **105 (C2)**, 3425–3450.

[Lorenc(1986)] Lorenc, A., 1986: Analysis methods for numerical weather prediction. *Q. J. Roy. Meteorol. Soc.*, **112**, 1117–1194.

[Lygre and Korgstad(1986)] Lygre, A. and H. E. Korgstad, 1986: Maximum entropy estimation of the directional distribution in ocean wave spectra. *J. Phys. Oceanogr.*, **16**, 2052–2060.

[MacDonald and Geyer(2005)] MacDonald, D. G. and W. R. Geyer, 2005: Hydraulic control of a highly stratified estuarine front. *J. Phys. Oceanogr.*, **35 (3)**, 374–387.

[Marquardt(1970)] Marquardt, D. W., 1970: Generalized inverses, ridge regression, biased linear estimation, and nonlinear estimation. *Technometrics*, **12 (3)**, 591–612.

[McCabe et al.(2008)] McCabe, R. M., B. M. Hickey, and P. MacCready, 2008: Observational estimates of entrainment and vertical salt flux in the interior of a spreading river plume. *J. Geophys. Res.*, **113**, C08027, doi:10.1029/2007JC004361.

[McCabe et al.(2006)] McCabe, R. M., P. MacCready, and G. Pawlak, 2006: Form drag due to flow separation at a headland. *J. Phys. Oceanogr.*, **36**, 2136–2152.

[Metz(1978)] Metz, C. E., 1978: Basic principles of ROC analysis. *Semin. Nucl. Med.*, **8**, 283–298.

[Millero and Poisson(1981)] Millero, F. J. and A. Poisson, 1981: International one-atmosphere equation of state of seawater. *Deep Sea Res.*, **28A (6)**, 625–629.

[Mooers(1973)] Mooers, C. N. K., 1973: A technique for the cross spectrum analysis of pairs of complex-valued time series, with emphasis on properties of polarized components and rotational invariants. *Deep Sea Res.*, **20**, 1129–1141.

[Munk and Cartwright(1966)] Munk, W. H. and D. E. Cartwright, 1966: Tidal spectroscopy and prediction. *Philos. Trans. Ser. A Math. Phys. Sci.*, **259 (1105)**, 533–581.

[Munk et al.(1970)] Munk, W. H., F. Snodgrass, and M. Wimbush, 1970: Tides off-shore: Transition from California coastal to deep-sea waters. *Geophys. Fluid Dynm.*, **1**, 161–235.

[Munk et al.(1965)] Munk, W. H., B. Zetler, and G. W. Groves, 1965: Tidal cusps. *Geophys. J.*, **10**, 211–219.

[Ng(1993a)] Ng, B., 1993a: The prediction of nearshore wind-induced surface currents from wind velocities measured at nearby land stations. *J. Phys. Oceanogr.*, **23**, 1609–1617.

[Ng(1993b)] Ng, B., 1993b: Tidal current predictions using rotary empirical orthogonal functions. *J. Atmos. Oceanic Technol.*, **10**, 868–879.

[NOAA(2006)] NOAA, 2006: *Harmonic Constituents*. National Oceanic and Atmospheric Administration (NOAA), National Ocean Service, Center for Operational Oceanographic Products and Services, http://www.co-ops.nos.noaa.gov.

[Noble et al.(2004)] Noble, R. T., I. M. Lee, and K. C. Schiff, 2004: Inactivation of indicator microorganisms from various sources of fecal contamination in sea water and freshwater. *J. Appl. Microbio.*, **96**, 464–472, doi:10.1111/j.1365-2672.2004.02155.

[Noble et al.(2000)] Noble, R. T., M. K. Leecaster, C. D. McGee, D. F. Moore, V. Orozco-Borbon, K. Schiff, P. Vainik, and S. B. Weisberg, 2000: Southern California Bight 1998 Regional Monitoring Program Volume III: Storm event shoreline microbiology. Tech. rep., Southern California Coastal Wate Research Project, 65 pp., Westerminster, CA 92683.

[Ohlmann et al.(2007)] Ohlmann, C., P. White, L. Washburn, E. Terrill, B. Emery, and M. Otero, 2007: Interpretation of coastal HF radar-derived surface currents with high-resolution drifter data. *J. Atmos. Oceanic Technol.*, **24**, 666–680.

[Orchard and Woodbury(1972)] Orchard, T. and M. A. Woodbury, 1972: A missing information principle: Theory and applications. *6th Berkeley Symposium on Mathematics, Statistics, and Probability*, California,.

[Orozco-Borbon et al.(2006)] Orozco-Borbon, M. V., R. Rico-Mora, S. B. Weisberg, R. T. Noble, J. H. Dorsey, M. K. Leecaster, and C. D. McGee, 2006: Bacteriological water quality along the Tijuana-Ensenada, Baja Calilfornia, Mexico shoreline. *Marine Pollution Bulletin*, **52**, 1190–1196, doi:10.1016/j.marpolbul.2006.02.005.

[Overland and Pease(1988)] Overland, J. E. and C. H. Pease, 1988: Modeling ice dynamics of coastal seas. *J. Geophys. Res.*, **93 (12)**, 15 619–15 637.

[Pedlosky(1992)] Pedlosky, J., 1992: *Geophysical Fluid Dynamics*. 2nd ed., Springer.

[Phillips(1966)] Phillips, O. M., 1966: *The dynamics of the upper ocean*. Cambridge University Press, London.

[Pidgeon and Winant(2005)] Pidgeon, E. J. and C. D. Winant, 2005: Diurnal variability in currents and temperature on the continental shelf between central and southern California. *J. Geophys. Res.*, **110**, C03024, doi:10.1029/2004JC002321.

[Prandle(1987)] Prandle, D., 1987: The fine-structure of nearshore tidal and residual circulations revealed by HF radar surface current measurements. *J. Phys. Oceanogr.*, **17**, 231–245.

[Prandle and Player(1993)] Prandle, D. and R. Player, 1993: Residual currents through the Dover Strait measured by HF radar. *Esturaine, Coastal and Shelf Science*, **37**, 635–653.

[Price et al.(1986)] Price, J. F., R. A. Weller, and R. Pinkel, 1986: Diurnal cycling: Observations and models of the upper ocean response to diurnal heating, cooling, and wind mixing. *J. Geophys. Res.*, **91 (C7)**, 8411–8427.

[Price et al.(1987)] Price, J. F., R. A. Weller, and R. R. Schudlich, 1987: Wind-driven ocean currents and Ekman transport. *Science*, **238 (4833)**, 1534–1538.

[Rabinovich et al.(2006)] Rabinovich, A. B., G. V. Shevchenko, and R. E. Thomson, 2006: Sea ice and current response to the wind: A vector regressional analysis approach. *J. Atmos. Oceanic Technol.*, **24**, 1086–1101, doi:101175/JTECH2015.1.

[Rio and Hernandez(2003)] Rio, M.-H. and F. Hernandez, 2003: High-frequency response of wind-driven currents measured by drifting buoy and altimetry over the world ocean. *J. Geophys. Res.*, **108 (C8)**, 3238, doi:10.1029/2002JC001655.

[Roberts(1999a)] Roberts, P. J. W., 1999a: Modeling Mamala Bay outfall plumes. I: Near field. *J. Hydr. Engr. ASCE*, **126 (6)**, 564–573.

[Roberts(1999b)] Roberts, P. J. W., 1999b: Modeling Mamala Bay outfall plumes. II: Far field. *J. Hydr. Engr. ASCE*, **126 (6)**, 574–583.

[Roberts et al.(1989)] Roberts, P. J. W., W. H. Snyder, and D. J. Baumgartner, 1989: Ocean outfalls. I: Submerged wastefield formation. *J. Hydr. Engr. ASCE*, **115 (1)**, 1–25.

[San Diego County(2000)] San Diego County, 2000: *California Regional Water Quality Control Board San Diego Region, Order No. 2000-129*. City of San Diego.

[Santiago-Mandujano and Firing(1990)] Santiago-Mandujano, F. and E. Firing, 1990: Mixed layer shear generated by wind stress in the central equatorial Pacific. *J. Phys. Oceanogr.*, **20**, 1576–1582.

[Schmidt(1986)] Schmidt, R. O., 1986: Multiple emitter location and signal parameter estimation. *IEEE Trans. Antennas and Propagation*, **34 (3)**, 276–280.

[Schneider(2001)] Schneider, T., 2001: Analysis of incomplete climate data: Estimation of mean values and covariance matrices and imputation of missing values. *J. Clim.*, **14**, 853–871.

[Schudlich and Price(1998)] Schudlich, R. R. and J. F. Price, 1998: Observations of seasonal variation in the Ekman layer. *J. Phys. Oceanogr.*, **28**, 1187–1204.

[Scott(1979)] Scott, D., 1979: On optimal and data-based histograms. *Biometrika*, **3 (66)**, 605–610.

[Shay et al.(1995)] Shay, L. K., H. C. Graber, D. B. Ross, and R. D. Chapman, 1995: Mesoscale ocean surface current structure detected by high-frequency radar. *J. Atmos. Oceanic Technol.*, **12**, 881–900.

[Siegel et al.(2003)] Siegel, D. A., B. P. Kinlan, B. Gaylord, and S. D. Gaines, 2003: Lagrangian descriptions of marine larval dispersion. *Mar. Ecol. Prog. Ser.*, **260**, 83–96.

[Simpson et al.(2002)] Simpson, J. H., P. Hyder, T. P. Rippeth, and I. M. Lucas, 2002: Forced oscillations near the critical latitude for diurnal-inertial resonance. *J. Phys. Oceanogr.*, **32**, 177–187.

[Smith(1959)] Smith, D. E., 1959: *A source book in mathematics*. Dover Publications, Inc., New York.

[Snee(1977)] Snee, R. D., 1977: Validation of regression models: Methods and examples. *Technometrics*, **19 (4)**, 415–428.

[Space Applications Centre (ISRO)(1997)] Space Applications Centre (ISRO), 1997: Indian Remote Sensing Satellite IRS-P4 utilisation plan. Tech. Rep. SAC-RSA/IRS-P4-UP/PP-02/97, Space Applications Centre (ISRO), Ahmedabad 380 053, India.

[Space Applications Centre (ISRO)(1998)] Space Applications Centre (ISRO), 1998: Detailed Design and Analysis report on IRS-P4 Ocean colour monitor. Tech. Rep. SAC/IRS-P4/01/05/98, Space Applications Centre (ISRO), Ahmedabad 380 053, India.

[Spaulding(1999)] Spaulding, M., 1999: *Wind-Over-Wave Couplings*, chap. Drift current under the action of wind and waves, 243–256. Clarendon, Oxford, U. K.

[Spaulding et al.(1993)] Spaulding, M. L., E. L. Anderson, T. Isaji, and E. Howlett, 1993: Simulation of the oil trajectory and fate in the Arabian Gulf from the Mina Al Ahmadi spill. *Marine Environ. Res.*, **36**, 75–115.

[Spaulding et al.(2006)] Spaulding, M. L., T. Isaji, P. Hall, and A. A. Allen, 2006: A hierarchy of stochastic particle models for search and rescue (SAR): Application to predict surface drifter trajectories using HF radar current forcing. *J. Marine Env. Eng.*, **8 (3)**, 181–214.

[Stewart and Joy(1974)] Stewart, R. H. and J. W. Joy, 1974: HF radio measurements of surface currents. *Deep Sea Res.*, **21**, 1039–1049.

[Svejkovsky and Jones(2001)] Svejkovsky, J. and B. Jones, 2001: Detection of coastal urban stormwater and sewage runoff with synthetic aperture radar satellite imagery. *EOS*, **82 (50)**, 621, 624–625, and 630.

[Sverdrup(1938)] Sverdrup, H. U., 1938: On the process of upwelling. *J. Mar. Res.*, **1**, 155–164.

[Swets(1988)] Swets, J. A., 1988: Measuring the accuracy of diagnostic systems. *Science*, **240 (4857)**, 1285–1293.

[Townsend(1980)] Townsend, A. A., 1980: *The Structure of Turbulent Shear Flow*. 2nd ed., Cambridge University Press.

[Trenberth and Hurrell(1994)] Trenberth, K. E. and J. W. Hurrell, 1994: Decadal atmosphere-ocean variations in the Pacific. *Clim. Dynam.*, **9**, 303–319.

[Ullman et al.(2006)] Ullman, D. S., J. O'Donnell, J. Kohut, T. Fake, and A. Allen, 2006: Trajectory prediction using HF radar surface currents: Monte Carlo simulations of prediction uncertainties. *J. Geophys. Res.*, **111**, C12005, doi:10.1029/2006JC003715.

[Van Huffel and Vandewalle(1991)] Van Huffel, S. and J. Vandewalle, 1991: *The Total Least Squares Problem: Computational Aspects and Analysis*. SIAM, 314 pp.

[Warner and MacCready(2008)] Warner, S. and P. MacCready, 2008: Dissecting the pressure field in tidal flow past a headland: When is form drag real? *J. Phys. Oceanogr.*, submitted.

[Washburn et al.(2003)] Washburn, L., K. A. McClure, B. H. Jones, and S. M. Bay, 2003: Spatial scales and evolution of stormwater plumes in Santa Monica Bay. *Marine Environ. Res.*, **56**, 103–125, doi:10.1016/S0141-1136(02)00327-6.

[Weber(1983)] Weber, J. E., 1983: Steady wind- and wave-induced currents in the open ocean. *J. Phys. Oceanogr.*, **13**, 524–530.

[Weisberg et al.(2001)] Weisberg, R. H., Z. Li, and R. Muller-Karger, 2001: West Florida shelf response to local wind forcing: April 1998. *J. Geophys. Res.*, **106 (C12)**, 31 239–31 262.

[Weller(1981)] Weller, R. A., 1981: Observations of the velocity response to wind forcing in the upper ocean. *J. Geophys. Res.*, **86 (C3)**, 1969–1977.

[Weller and Plueddemann(1996)] Weller, R. A. and A. J. Plueddemann, 1996: Observations of the vertical structure of the oceanic boundary layer. *J. Geophys. Res.*, **101**, 8789–8806.

[Wilkin et al.(2002)] Wilkin, J. L., M. M. Bowen, and W. J. Emery, 2002: Mapping mesoscale currents by optimal interpolation of satellite radiometer and altimeter data. *Ocean Dynamics*, **52**, 95–103, doi:10.1007/s10236-001-0011-2.

[Winant(2004)] Winant, C. D., 2004: Three-dimensional wind-driven flow in an elongated rotating basin. *J. Phys. Oceanogr.*, **34**, 462–476.

[Winant and Bratkovich(1981)] Winant, C. D. and A. W. Bratkovich, 1981: Temperature and currents on the southern California shelf: A description of the variability. *J. Phys. Oceanogr.*, **11**, 71–86.

[Wu(1975)] Wu, J., 1975: Wind-induced drift currents. *J. Fluid Mech.*, **68**, 49–70.

[Wu(1983)] Wu, J., 1983: Sea-surface drift currents induced by wind and waves. *J. Phys. Oceanogr.*, **13**, 1441–1451.

[Wunsch(1996)] Wunsch, C., 1996: *The ocean circulation inverse problem*. Cambridge University Press, New York.

[Wunsch and Stammer(1997)] Wunsch, C. and D. Stammer, 1997: Atmospheric loading and the oceanic 'inverted barometer' effect. *Rev. Geophys.*, **35**, 79–107, 96RG03037.

[Yankosvky and Chapman(1997)] Yankosvky, A. E. and D. C. Chapman, 1997: A simple theory for the fate of buoyant coastal discharge. *J. Phys. Oceanogr.*, **27**, 1386–1401.

[Zelenke(2005)] Zelenke, B. C., 2005: An empirical statistical model relating winds and ocean surface currents: Implications for short-term current forecasts. http://hdl.handle.net/1957/2166, Oregon State University, Corvallis, OR 97331-4501.